LEABHARLANN CHOLÁISTE NA TRÍONÓIDE, BAILE ÁTHA CLIATH
Ollscoil Átha Cliath

TRINITY COLLEGE LIBRARY DUBLIN
The University of Dublin

**Terms and Conditions of Use of Digitised Theses from Trinity College Library Dublin**

**Copyright statement**

All material supplied by Trinity College Library is protected by copyright (under the Copyright and Related Rights Act, 2000 as amended) and other relevant Intellectual Property Rights. By accessing and using a Digitised Thesis from Trinity College Library you acknowledge that all Intellectual Property Rights in any Works supplied are the sole and exclusive property of the copyright and/or other IPR holder. Specific copyright holders may not be explicitly identified. Use of materials from other sources within a thesis should not be construed as a claim over them.

A non-exclusive, non-transferable licence is hereby granted to those using or reproducing, in whole or in part, the material for valid purposes, providing the copyright owners are acknowledged using the normal conventions. Where specific permission to use material is required, this is identified and such permission must be sought from the copyright holder or agency cited.

**Liability statement**

By using a Digitised Thesis, I accept that Trinity College Dublin bears no legal responsibility for the accuracy, legality or comprehensiveness of materials contained within the thesis, and that Trinity College Dublin accepts no liability for indirect, consequential, or incidental, damages or losses arising from use of the thesis for whatever reason. Information located in a thesis may be subject to specific use constraints, details of which may not be explicitly described. It is the responsibility of potential and actual users to be aware of such constraints and to abide by them. By making use of material from a digitised thesis, you accept these copyright and disclaimer provisions. Where it is brought to the attention of Trinity College Library that there may be a breach of copyright or other restraint, it is the policy to withdraw or take down access to a thesis while the issue is being resolved.

**Access Agreement**

By using a Digitised Thesis from Trinity College Library you are bound by the following Terms & Conditions. Please read them carefully.

I have read and I understand the following statement: All material supplied via a Digitised Thesis from Trinity College Library is protected by copyright and other intellectual property rights, and duplication or sale of all or part of any of a thesis is not permitted, except that material may be duplicated by you for your research use or for educational purposes in electronic or print form providing the copyright owners are acknowledged using the normal conventions. You must obtain permission for any other use. Electronic or print copies may not be offered, whether for sale or otherwise to anyone. This copy has been supplied on the understanding that it is copyright material and that no quotation from the thesis may be published without proper acknowledgement.

# Electronic Structure, Bonding and Dichroism in Rutile Compounds

## An X-Ray Spectroscopic Study

A thesis submitted for the degree of
*Doctor of Philosophy*
2012

Declan Cockburn
School of Physics
The University of Dublin
Trinity College

TRINITY COLLEGE
2 4 MAY 2013
LIBRARY DUBLIN

Thesis 9877

I, the undersigned, declare that this thesis has not been submitted as an exercise for a degree at this or any other university and, with the exception of the assistance noted in the acknowledgements, it is entirely my own work.

I agree to deposit this thesis in the University's open access institutional repository or allow the library to do so on my behalf, subject to the Irish Copyright Legislation and Trinity College Library conditions of use and acknowledgement.

[redacted]

To my parents Anna and Peter Cockburn,
on their 30th wedding anniversary.
*For being there for me.*

# Acknowledgements

First and foremost I would like to thank my supervisor, Dr. Cormac McGuinness. One of the most scientifically passionate and knowledgeable people I've ever had the pleasure to know. To his students and to the pursuit of knowledge, he is dedicated to a fault. I would feel thoroughly confident recommending him as a supervisor to any prospective student.

My parents have offered significant moral support, maintaining a hands off approach allowing me the space to follow my own path, as well as never rescinding the offer of accommodation or financial support should I ever require it. For this and other things (like existence etc.) I thank them.

Science Foundation Ireland for funding my education as well as my living; allowing me the opportunity to pursue this research, performing experiments in distinguished facilities world-wide, and not starve while doing it. To the Irish tax-payer, burdened as you are, I appreciate it.

A person who warrants strong mention is Brian Kennedy, he paved the way as it were in this, showing what and what not to do. As well as being a close colleague providing such guidance, I can also count him as a good friend. Nikolaos Peltekis, for (eventually) breaking the seal, showing that a PhD thesis in this group could be completed.

Others members past and present of the surface science and related groups, for whom I'm grateful for their help at various stages, include: Daniel McNally, Brendan Arnold, Martin "get in there" Duignan, Stephen Callaghan, Niall McAlindin, John Cunniffe, Lina Persechini, Nina Berner, Chris Smith, Zhi Ming Wang, Karsten Rhode, Karsten Fleischer, Jonathan Alaria, Satheesh Krishnamurthy. Prof. James Lunney also deserves mention for his helpful advice and encouragement in choosing this PhD.

To the beamline scientists who dedicated an inordinate amount of their time to training and collaborating: Franz Hennies and Annette Pietzsch at MAX-lab, Jonathan Denlinger, Wanli Wang, Jinghua Guo and Per-Anders Glans at the ALS, the BU Smith group at the NSLS, and Mikhail Yablonskikh in ELETTRA. Our other collaborators: Prof. Russ Egdell, Prof. Kevin Smith, Louis Piper. The material scientists who were kind enough to let us "borrow" the crystals used in this research: Hirohiko Sato, Ying-Sheng Huang, Frank Imbusch and Matthias Klemm. To the retired Prof. R. K. Pomeroy of B.C. Canada who on a chemistry internet forum, helped me overcome a significant roadblock in my inorganic chemistry understanding.

For moral support I needn't have looked further than my own home. My flatmate of numerous years Colman O'Sullivan who like a master chef, innately knew the exact combination of encouragement and peer pressure apply in this process. Other comrades who wouldn't shy from a pep talk include Rob Lennox, whom I've yet to help deadlift, Joe Roche whose charm and pleasant demeanour bespeaks his character, Yuki Utsumi, and the numerous close friends who've stood by in patient understanding of the necessary hermitation required to finish this thing off.

I would also like to thank my internal examiner Iggy McGovern, and my external examiner whoever that may be, for taking the time to read what turned out to be a larger-than-anticipated thesis. The knowledge that this work would be held up to your independent and presumably expert scrutiny kept me endeavouring for honesty and accuracy throughout its writing, leaving me a composition I genuinely feel proud to have authored.

Lastly I acknowledge the memory of Tom Quinlan, who I have no doubt would have been here graduating beside us. I'm guessing he'd have felt awful incongruous in those red and golden robes, yet at the same time proud as punch.

# Abstract

Rutile-type transition-metal compounds are a continually rewarding area of research, of both technological and fundamental importance due to their exhibiting a wide variety of physical properties, lending to numerous potential applications. They range from wide bandgap insulators such as $MgF_2$ and $TiO_2$, to semiconducting $SnO_2$, metallic $IrO_2$, and compounds like $VO_2$ and $NbO_2$ which undergo a temperature dependent metal-to-insulator transition. These crystals straddle the boundary between ionic and covalent bonding, exhibiting an anisotropy in their orbital overlapping, and thus electronic structure and hybridisation which has not been fully explored. To this end, element selective X-ray absorption spectroscopy (XAS) and resonant X-ray emission spectroscopy (RXES) are demonstrated to be valuable tools for studying the electronic structure and bonding of bulk compounds. Further, by utilising a novel application of polarisation-dependent RXES, the symmetry- and state-selective nature of this technique can be de-coupled, allowing an axis-projected measurement of specifically selected occupied states. The rutile structure is particularly amenable to this analysis. This thesis presents a systematic study of a range of rutile-type compounds: $IrO_2$, $MnO_2$, $WO_2$, $MoO_2$ and $VO_2$ at the O $K$-edge, $MgF_2$ and $MnF_2$ at the F $K$-edge, as well as $TiO_2$ and its anatase structural polymorph – at the Ti $L$-edge. In all cases XAS and RXES were exploited as an energy selective probe of the partial density of states (PDOS) in the bonding anion or cation, projected either along selected axes in the conduction band, or onto planes in the valence band respectively. The majority of the materials presented exhibited a pronounced natural linear dichroism, subsequently discussed from a molecular orbital theory perspective. For these compounds, particularly with respect to emission, this thesis constitutes the first reported account of soft X-ray dichroism; from which an expanded knowledge of their fundamental bonding nature was acquired. In selected cases, a comparison was made with original axes-projected PDOS, calculated via density functional theory (DFT), which contributed significantly to conclusions drawn. In $IrO_2$ and $MgF_2$ especially, it was possible to identify and experimentally isolate the PDOS of individual orthogonal component states, dramatically extending current understanding of their electronic structure.

# Contents

1 **Introduction** 1

2 **X-ray Spectroscopic Methods** 5

2.1 Introduction . . . . . 5

2.2 X-ray Absorption Spectroscopy . . . . . 6

2.2.1 Natural Linear Dichroism . . . . . 9

2.3 Soft X-ray Emission Spectroscopy . . . . . 10

2.3.1 Theoretical Background . . . . . 10

2.3.2 NXES and RXES . . . . . 12

2.3.3 RXES and RIXS . . . . . 14

2.3.4 State and Symmetry Selectivity of RXES . . . . . 14

2.3.5 Natural Linear Dichroism in XES . . . . . 18

2.3.6 Crystal Momentum Selectivity . . . . . 18

2.4 Synchrotrons and Beamlines . . . . . 20

2.4.1 The Synchrotron . . . . . 20

2.4.2 Soft X-ray Spectrometer . . . . . 21

2.4.3 Beamlines . . . . . 24

2.4.3.1 Beamline 8.0.1 at the ALS . . . . . 24

2.4.3.2 Beamline 7.0.1 at the ALS . . . . . 26

2.4.3.3 I511-3 at MAX-lab . . . . . 26

2.4.3.4 X1B at the NSLS . . . . . 27

3 **Rutile Structure** **29**

3.1 Introduction . . . . . 29

3.2 Rutile Structure . . . . . 30

3.2.1 Bonding . . . . . 32

3.2.2 Electronic Structure . . . . . 33

3.3 Distorted Rutile Structure . . . . . 36

3.3.1 Electronic Structure . . . . . 37

3.4 Electronic Structure Calculations . . . . . 38

3.4.1 Electronic Structure Methods . . . . . . . . . . . . . . . . . . . . . . 38
3.4.2 Simulating X-Ray Spectra, NXES and RXES . . . . . . . . . . . . . 39
3.5 Summary . . . . . . . . . . . . . . . . . . . . . . . . . . . . . . . . . . . 40

**4 $IrO_2$ and $MnO_2$** **43**
4.1 Introduction . . . . . . . . . . . . . . . . . . . . . . . . . . . . . . . . . 43
4.2 Physical and Electronic Structure of $IrO_2$ . . . . . . . . . . . . . . . . . . . . 44
4.2.1 Electronic Structure Calculations . . . . . . . . . . . . . . . . . . . 45
4.3 Physical and Electronic Structure of $MnO_2$ . . . . . . . . . . . . . . . . . . 49
4.4 Experimental Measurements . . . . . . . . . . . . . . . . . . . . . . . . 50
4.4.1 Sample Preparation . . . . . . . . . . . . . . . . . . . . . . . . . . 50
4.4.2 Sample Mounting for polarisation-dependent study . . . . . . . . . . 51
4.4.2.1 $IrO_2$ Mounting . . . . . . . . . . . . . . . . . . . . . . . 52
4.4.2.2 $MnO_2$ Mounting . . . . . . . . . . . . . . . . . . . . . . 53
4.4.3 Experimental details . . . . . . . . . . . . . . . . . . . . . . . . . . 54
4.5 Results and Discussion . . . . . . . . . . . . . . . . . . . . . . . . . . . 55
4.5.1 O *K* Edge X-Ray Absorption Spectroscopy of $IrO_2$ . . . . . . . . . . 55
4.5.2 O *K* Edge X-Ray Absorption Spectroscopy of $MnO_2$ . . . . . . . . . 58
4.5.3 Polarisation Dependent XES of $IrO_2$ . . . . . . . . . . . . . . . . . . 60
4.5.3.1 Normal X-ray Emission . . . . . . . . . . . . . . . . . . . 60
4.5.3.2 Resonant X-ray Emission Spectra . . . . . . . . . . . . . . 62
4.5.3.3 Difference Spectra . . . . . . . . . . . . . . . . . . . . . . 69
4.5.4 Polarisation Dependent XES of $MnO_2$ . . . . . . . . . . . . . . . . . 73
4.6 Summary and Conclusions . . . . . . . . . . . . . . . . . . . . . . . . . 78

**5 $MgF_2$ and $MnF_2$** **81**
5.1 Introduction . . . . . . . . . . . . . . . . . . . . . . . . . . . . . . . . . 81
5.1.1 Transition Metal Fluorides . . . . . . . . . . . . . . . . . . . . . . . 82
5.2 Physical Structure . . . . . . . . . . . . . . . . . . . . . . . . . . . . . . 82
5.3 Electronic Structure . . . . . . . . . . . . . . . . . . . . . . . . . . . . . 83
5.4 Electronic Structure Calculations . . . . . . . . . . . . . . . . . . . . . . 85
5.4.1 $MgF_2$ Calculations . . . . . . . . . . . . . . . . . . . . . . . . . . 85
5.4.2 $MnF_2$ Calculations . . . . . . . . . . . . . . . . . . . . . . . . . . 87
5.5 Experimental Measurements . . . . . . . . . . . . . . . . . . . . . . . . 90
5.5.1 Sample Preparation and Mounting . . . . . . . . . . . . . . . . . . 90
5.5.2 Experimental Setup . . . . . . . . . . . . . . . . . . . . . . . . . . 90
5.6 Results and Discussion . . . . . . . . . . . . . . . . . . . . . . . . . . . 92
5.6.1 F *K*-Edge X-Ray Absorption Spectroscopy . . . . . . . . . . . . . . 92
5.6.1.1 XAS of $MgF_2$ . . . . . . . . . . . . . . . . . . . . . . . 92

5.6.1.2 XAS of $MnF_2$ . . . 95
5.6.2 Polarisation Dependent NXES and RXES of $MgF_2$ . . . 98
5.6.3 Polarisation Dependent RXES and NXES of $MnF_2$ . . . 105
5.7 Summary and Conclusions . . . 112

6 $WO_2$ and $MoO_2$ 115
6.1 Introduction . . . 115
6.2 Physical and Electronic Structure . . . 116
6.2.1 $WO_2$ . . . 118
6.2.2 Electronic Structure Calculations of $WO_2$ . . . 119
6.2.3 $MoO_2$ . . . 122
6.2.4 Electronic Structure Calculations of $MoO_2$ . . . 124
6.3 Experimental Measurements . . . 124
6.3.1 $WO_2$ Measurements . . . 125
6.3.2 $MoO_2$ Measurements . . . 126
6.4 Results and Discussion . . . 126
6.4.1 Polarisation Dependent XAS of $MoO_2$ . . . 126
6.4.2 Polarisation Dependent XAS of $WO_2$ . . . 131
6.4.3 Polarisation Dependent RXES of $MoO_2$ . . . 133
6.4.4 Polarisation Dependent RXES of $WO_2$ . . . 138
6.5 Summary and Conclusions . . . 143

7 $VO_2$ 145
7.1 Introduction . . . 145
7.1.1 Metal-Insulator Transition . . . 146
7.2 Physical and Electronic Structure . . . 146
7.3 Experimental Measurements . . . 151
7.3.1 Sample Preparation and Mounting . . . 152
7.3.2 Experimental Setup . . . 152
7.4 Results and Discussion . . . 153
7.4.1 XAS of $VO_2$ . . . 153
7.4.2 Polarisation Dependent RXES of $VO_2$ . . . 155
7.5 Conclusions . . . 165

8 Rutile and Anatase $TiO_2$, Ti $L$-edge 167
8.1 Introduction . . . 167
8.1.1 Previous Work and Motivation . . . 168
8.2 Applications of Rutile and Anatase $TiO_2$ . . . 172
8.2.1 Memristors . . . 172

8.3 Physical and Electronic Structure . . . 173
8.3.1 Bonding in $TiO_2$ . . . 175
8.4 Ti $L$-edge Spectroscopy and Analysis . . . 178
8.4.1 Dichroism at the Ti $L$-edge . . . 179
8.4.2 Self Absorption Correction . . . 180
8.5 Experimental Measurements . . . 184
8.6 Samples and Mounting . . . 185
8.7 Results and Discussion . . . 185
8.7.1 XAS of $TiO_2$ . . . 185
8.7.2 Resonant X-ray Emission of $TiO_2$ $L$-edge . . . 190
8.7.2.1 Rutile RXES . . . 190
8.7.2.2 Anatase RXES . . . 196
8.8 Summary and Conclusions . . . 199

**9 Conclusions** **201**

**A Appendix** **207**
A.1 Excitation Nomenclature . . . 207
A.2 Emission Nomenclature . . . 208
A.3 $VO_2$ RXES, O $K$ Peak Normalisation . . . 209
A.4 $VO_2$ RXES, Contaminated . . . 210
A.5 $WO_2$ O1 Weighted Bandstructures . . . 211
A.6 $WO_2$ O2 Weighted Bandstructures . . . 212
A.7 $WO_2$ W $5d$ $t_{2g}$ Weighted Bandstructures . . . 213
A.8 $WO_2$ W $5d$ $e_g$ Weighted Bandstructures . . . 214
A.9 Rutile $TiO_2$ PDOS . . . 215
A.10 Anatase $TiO_2$ PDOS . . . 216

**List of Abbreviations** **217**

**Presentations and Publications** **224**

**List of Figures** **237**

**References** **258**

# 1 Introduction

Transition metal (TM) compounds, particularly oxides, straddle that subtle boundary between covalent, ionic, and metallic bonding. They exhibit a bountiful range of physical phenomena, from high-$T_c$ superconductivity in layered cuprates, colossal magnetoresistance (CMR) in perovskite manganites, as well as the coexistence of magnetism and ferroelectricity, or multiferroicity. [1] Less extreme properties that are of significant application include catalysis, where TM oxides are the most important classes of metal oxides in this context. Electrochromism is a property of $TiO_2$, $WO_3$ and other TM based materials, with applications in dynamic "smart" windows, e-paper and perhaps in the near future, digital displays. $VO_2$ undergoes an metal-to-insulator transition (MIT) and is one of the most investigated of the TM oxides, with $VO_2$ based materials currently finding application in spectrally selective windows, extremely fast optical shutters, optical modulators and may in the future play a role in camera and data storage technology. Perhaps the most topical of TM oxide applications comes in the form of electromigration properties of titanates and their impending commercial implementation by Hewlett Packard (HP) as the (formerly missing) fourth fundamental circuit element, i.e. the memristor.

The fundamental question posed in the original funding proposal for this research project that enabled the research presented in this thesis was:

*"Can we extend our understanding of both the electronic structure of, and bonding within, selected single crystal structures by exploring their symmetry and state selective characteristics through element-selective X-ray spectroscopic techniques?"*

It was anticipated this was a rhetorical question. Clearly additional insight would be gained, the point however was that this had not been applied to tetragonal binary systems which exhibit natural linear dichroism. Thus the research presented here is in some senses a clear demonstration of the breadth by which our knowledge of the chemical bonding and electronic structure of these systems can be extended.

The significance of the insight gained goes beyond extending our knowledge of the specific crystals investigated. This becomes clear when considering the variety of properties and technological applications of TM compounds delved into above. This breadth is partially due to the range of structures these compounds form, arising from the multitude of TM oxidation states available. So as a focal point one particular class was chosen; that of the $MA_2$ formula unit, of which most crystallise in a rutile tetragonal or very similar distorted rutile monoclinic structure, making this structure the basis of the investigations presented here. This structural motif was chosen as a result of the $sp^2$ bonding of the anion in the $M_3A$ environment within the rutile $MA_2$ crystal. In rutile $MA_2$ crystals these $M_3A$ planes generally result in a natural linear-dichroism at the anion $K$-edge which is exploited here and explained briefly below.

The restriction to the undoped rutile class does not limit the potential of such a project. On the contrary, even among this class alone, the catalogue of properties and applications is impressive. Further, there are ongoing worldwide investigations into, for example, developing useful dilute magnetic semiconductors (DMSs) that are based upon substitutionally doped wide bandgap TM oxides. Two of the most promising DMS systems that have been studied in recent years are TM doped $TiO_2$ [2] and $SnO_2$ [3,4] both of which possess a rutile-tetragonal structure. Doping of transition-metal materials is in general for the purpose of enhancing, modulating or otherwise altering the electronic, structural or behavioural properties of a compound. In order to understand and predict the effects of substitutional doping on a material, it is necessary to understand the physical properties of that material in the first place. This is especially the case when using advanced spectroscopic techniques.

The theme of interest in rutile TM compounds is enduring; half-metallic $CrO_2$ for example is the basis for many magnetic device components, including spin-injection for spintronic devices. $RuO_2$ is being evaluated for use in integrated circuits; $IrO_2$ for an electrode material in advanced ferroelectric memory technologies. Rutile lead dioxide $\beta$-$PbO_2$ is ubiquitous in lead battery technology, a $36 billion industry; the metallic nature of which we have only recently come to understand. Even without regard to technological significance, it should not be overlooked that such an investigation provides significant opportunity for gaining deeper insight into the nature of bonding in these undoped systems.

The proposed question is addressed by novel, element-selective, symmetry, polarisation and state resolved investigations into the chemical bonding of these compound. This was achieved using synchrotron based soft X-ray spectroscopic techniques, with a focus on the anion (oxygen or fluorine) $K$-edge. Element selective X-ray spectroscopies such as polarisation dependent XAS and RXES spectroscopy can directly measure the chemical bonding between one element and the next within an oriented single crystal, and in fact can select specific bonds and states or molecular orbitals (MOs) by the polarisation dependence with respect to the crystal axes and energy dependence of these spectroscopies. Though many studies have been made of oxygen and fluorine $K$-edge X-ray emission in a number of rutile-type materials, no attention has been paid to the symmetry selection or polarisation dependence. Neither has such a polarisation dependent study been done extensively for cation metal edge RXES spectra, excepting the case of the Ti $L_{2,3}$ edge in $TiO_2$.

Rutile type compounds possess a structure that is particularly amenable to this approach. A detailed discussion of the crystal structure is made later in Chapter 3, but to put briefly: structural anisotropy of the tetragonal bonding means that the trigonally-coordinated anion $M_3A$ planes formed in this structure all lie parallel to the rutile $c$-axis. The trigonal coordination requires $sp^2$ hybridisation of the anion valence orbitals. Thus, as we define the local coordinate geometry with the anion $z$-axis directed towards the central cation, the $p_x$ and $p_z$ orbitals of the anion lie in the trigonal plane, while the $p_y$ orbital lies perpendicular to it. In this $x - z$ plane a direct overlap of anion derived $sp^2$ orbitals will occur with the metal valence $d\ e_g$ orbitals resulting in $\sigma$ bonding arrangements parallel their local $M_3A$ trigonal plane, which in turn are parallel to the rutile $c$-axis. While any overlap of the $p_y$ with the metal orbitals, when it does occur, will be in the plane orthogonal to the rutile $c$-axis. Due to the type of side-on overlap these states are considered to be of $\pi$-character, hybridising with the metal $t_{2g}$ ($d_{z(y-x)}$ in most cases).

This geometric separation of $\pi$ and $\sigma$ states in rutile-type compounds coupled with the dipole selection rule for excitation, means there is a natural linear dichroism (polarisation dependence) observed in anion $K$-edge XAS. It can be simply described as deriving from whether the linear electric field vector is parallel or perpendicular to the rutile $c$-axis, i.e. it will preferentially excite a $1s$ core electron into the anion $2p_y$ states when perpendicular, but cannot do so when parallel.

In RXES, where the emitted photon is observed, this natural linear dichroism, coupled with the dipole, state, space, and symmetry selection rules of RXES allows it to measure, and in some cases isolate, occupied anion $2p$ $\pi$ and $\sigma$ molecular orbitals. The preference for which depends upon the symmetry, geometry and excitation energy by selection of either unoccupied $\sigma^*$ or $\pi^*$ molecular orbitals in absorption. The observed RXES spectrum can thus directly measure the occupied anion $2p$ PDOS of specific bonding orbitals that form the valence band of the material, as well as the hybridised contribution of the metal cation orbitals to these states. This symmetry selective energy dependence of RXES can also be seen in other materials, but in single crystal rutile-type crystal structures the symmetry selection can be entirely decoupled from the photon energy dependence, allowing separate measurements of the occupied $\sigma$ and $\pi$ states.

No such symmetry selective, elementally resolved, polarisation dependent measurement of the anion $2p$ PDOS through RXES for any pure host materials, let alone doped or rutile-type materials, has been attempted on any systematic basis. This thesis presents the first such report, an overview of which will be given in the following paragraphs.

Chapter 2 describes the forms of soft X-ray spectroscopic techniques utilised in these experiments, the theory, methods and apparatus employed in the spectroscopy, as well as a discussion of the particular characteristics of resonant soft X-ray scattering that govern the polarisation dependent study of the anisotropic materials measured.

Chapter 3 gives an in depth overview of the physical rutile structure, as well as its bonding and electronic structure. The distorted rutile-like monoclinic structure is also discussed, and an introduction to the density of states (DOS) calculations performed using DFT methods to map the electronic structure is outlined.

Chapter 4 is the first chapter that presents and discusses the results of a spectroscopic study. Here the iso-structural tetragonal rutile compounds $IrO_2$ and $MnO_2$ were studied with the methods described, for polarisation dependent measurements on bulk single-crystals at the oxygen $K$-edge.

Chapter 5 continues the presentation of spectroscopic results, describing the similarly iso-structural rutile fluorides $MgF_2$ and $MnF_2$, this time at the fluorine $K$-edge.

Chapter 6 introduces the first results from distorted-rutile (monoclinic) TM dioxides, $WO_2$ and $MoO_2$, investigated in a similar fashion as the previous compounds, at the O $K$-edge.

Chapter 7 is assigned to the polarisation dependent bulk spectroscopic investigation $VO_2$ at the O $K$-edge, in both its rutile conducting phase ($> 340$ K) and its semiconducting distorted-rutile (monoclinic) phase ($< 340$ K).

Chapter 8 takes a different tack to the previous chapters, exploring the metal side of the bonding and hybridisation in rutile-type systems by analysing the polarisation dependence of $TiO_2$ at the Ti $L$-edge. Two separate crystal phases of this structural unit were utilised in this study, the rutile phase and the non-rutile but nevertheless analogous tetragonal anatase structural phase. This was expanding upon the previous polarisation dependent O $K$-edge work done on these compounds by Kennedy for his PhD thesis [5].

Chapter 9, the final chapter, concludes this work by summarising the results of the investigations undertaken and conclusions the author has drawn. There is also a discussion of, and suggestion for further work that may continue to exploit such powerful techniques as polarisation dependent resonant soft X-ray emission spectroscopy. Supplementary information is then presented in the appendix, followed by the list of abbreviations used in this work, a list of figure captions and finally references.

# 2 X-ray Spectroscopic Methods

## 2.1 Introduction

Broadly speaking, spectroscopic techniques utilise the interaction between photons and matter to probe the electronic structure of materials; be they atoms, molecules or solid state materials. They measure the distribution in energy of electronic states by giving a direct determination of the energy difference and transition probability between these states. This makes these techniques some of the most powerful tools in modern physics.

The valence orbitals of atomic systems are the least tightly bound, thus they are responsible for bonding in molecules and solids. The electron density distribution formed by the chemical bonding has a large influence on the chemical, electronic, magnetic and structural properties of the resulting compound. The transition energy of a core hole electron to the valence or conduction bands for many light atoms falls within the 20 eV to approximately keV range, which is the soft X-ray region. The core states of an atom are localised in space for a specific atom and do not take part in bonding, thus core states of differing elements, whether bonded or not, have specific binding energies that are individually identifiable due to their discrete energy separation. Core hole excited X-ray spectroscopies are therefore element selective. Thus soft X-rays are extremely useful for studying the electronic structure of materials, that is the valence and conduction bands, by way of these electronic transitions.

Soft X-ray spectroscopic techniques used in this thesis can be divided into three main types: X-ray photoemission spectroscopy (XPS), X-ray absorption spectroscopy (XAS), X-ray emission spectroscopy (XES). The latter two are performed at synchrotrons and will be the basis of this chapter, as well as the experimental work in this thesis at large. Though laboratory based XPS usually uses a fixed monochromatic source of X-rays that does not require a synchrotron, a variation of it known as soft X-Ray photoelectron spectroscopy (SXPS) does. In photoemission spectroscopy (PES) lower energy, often ultra-violet (UV) region photons are used so that core electrons are not excited. This makes it a very similar technique to ultra-violet photoelectron spectroscopy (UPS).

Both XAS and XES create core holes, and as mentioned element specific core states are well defined and separated, while valence and conduction band states have a much more non-localised character. However, excitation or decay of electrons between the core states and the conduction or valence bands allows the distribution of energy levels of these bands to be studied in a localised fashion. The information yielded will thus be specific to the excited core hole within the atomic site studied.

## 2.2 X-ray Absorption Spectroscopy

XAS is an umbrella term for all X-ray absorption spectroscopies, but can be divided further into physically related techniques that probe different areas above the Fermi level. One type is extended X-ray absorption fine structure (EXAFS), which probes at energies above the ionisation continuum, ejecting the core electron. The measured absorption coefficient will tend to oscillate with incident photon energy as a result of interference. This can be understood if the ejected photoelectron is taken to have a wave-like nature, where forward propagating waves interfere with backscattered electrons. EXAFS is a structural probe, allowing the radial distribution function to be reconstructed from the oscillations, hence the nearest neighbour distance and number of nearest neighbours in the first and subsequent coordination shells can be determined. The latter is particularly useful due to the technique's element selectivity. The other type is near edge X-ray absorption fine structure (NEXAFS). This is typically taken for energies between the Fermi-edge or beginning of the conduction band until just beyond the beginning of the ionisation continuum threshold, and is an indirect measure of the partial density of states (PDOS) of the conduction band. All of the XAS spectra presented in this thesis are primarily of a NEXAFS nature, and were excited using soft X-ray photons less than 1 keV in energy, or >1 nm in wavelength.

X-ray Absorption Spectroscopy (XAS) is a measurement of the transition probabilities from the core level to the unoccupied states of a material [6]. An approximation of the transition probability can be attained by using Fermi's Golden Rule, this gives the transition rate from one energy eigenstate into a continuum of energy eigenstates due to a perturbation. The transition probability per unit time $T_{i\to f}$, from the ground state $|i\rangle$ to the final state $|f\rangle$ can be written as follows:

$$T_{i\to f} = \frac{2\pi}{\hbar}\left|\langle f|H'|i\rangle\right|^2 \rho \qquad (2.1)$$

Where $\rho$ is the density of final states (the final state in XAS is the excited state). $H'$ is the time-dependent perturbation at a frequency $\omega$, where $\hbar\omega$ would the energy difference between the initial and final states.

For $K$-edge X-ray absorption in the absence of an external magnetic field, the $1s$ core shell has zero orbital angular momentum and thus no spin-orbit coupling. As a result for increasing $\hbar\omega$, the matrix element can usually be considered constant. Hence the absorption spectrum is a direct measure of $\rho(\epsilon_f)$, or the unoccupied PDOS. For $L$-edge absorption it is not so straightforward to attempt such a comparison, as the matrix element is a strong function of the radial overlap of the $2p$ core electron and empty $d$ orbital, whereby atomic-like multiplet effects are strongly favoured, even apart from the spin-orbit splitting of the $2p$ core levels. This will be discussed further in Chapter 8.

XAS can be viewed as a one-step single photon, one electron spectroscopy, in that a photon excites a core electron into the unoccupied conduction band states, creating a core hole. While the route of decay of this core hole is not theoretically important, the resulting decay process is indirectly utilised to measure absorption, and the lifetime of the final state will broaden the observed transition. There are two primary methods by which a core hole decays. It may be filled by another local electron, the excess energy fuelling emission of an Auger electron, Figure 2.1. The second decay route also illustrated in 2.1 is by fluorescence, where the transition of a valence electron or excited conduction-band electron coupled to the core hole results in the emission of a photon (elastic decay). Auger emission will result in a net drain current from the sample, assuming it is grounded and conductive, that is directly proportional to absorption or to the number of core holes created. The intensity of fluorescent emission is similarly proportional and can be measured via a variety of photodetectors such as a photodiode, channeltron or microchannel plate (MCP). Commonly these measurements are known as total electron yield (TEY) and total fluorescence yield (TFY). TEY is far more surface sensitive than TFY due to the reduced escape depth of electrons compared to photons at sub 1 keV energies, thus adsorbed surface contamination or stoichiometric differences in surface chemistry can reduce the efficacy of a TEY measurement.

The physical process of measuring an absorption spectrum is undertaken in the form of a scan. A particular energy of monochromatised X-ray photons is selected, directed onto the sample, and absorption is measured via the above methods for a discrete amount of time depending on the signal. The incident photon energy is then usually incremented and the process is repeated in this stepwise fashion for a selected energy range. Factors that affect the detail and resolution of such a scan include: the resolution of the monochromatised incident beam, the flux of said beam, the distance between steps and the counting time taken for each step. To complete a scan, the entire process in most cases is only in the order of minutes.

As well as being element and site selective, as qualitatively described, XAS has other parameters that require a slightly more in-depth qualification. The first is the orbital dipole

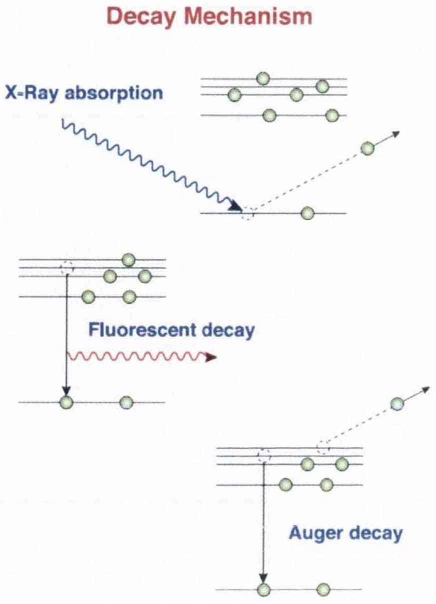

Figure 2.1: After absorption of an X-ray photon the excited core hole will undergo decay. Two primary routes are shown. For low Z elements Auger decay is dominant, while for high Z elements fluorescent decay is dominant. Adapted from [7]

(Laporte) selection rule for radiative transitions:

$$\Delta l = \pm 1 \tag{2.2}$$

Thus for $K$-edge absorption, only transitions between $s$ and $p$ are allowed, and for $L$-edge only between $p$ and $d$ or $p$ and $s$. Thus XAS will only probe the unoccupied PDOS selected by the dipole transition. Further, a second total angular momentum selection rule of $\Delta j = 0, \pm 1$ must also be satisfied. Where $j$ is the vector addition of the orbital angular momentum of the electron with its spin, which can be either aligned or anti-aligned causing a spin-orbit splitting effect. Though for the oxygen or fluorine $K$-edge absorption the spin orbit splitting usually need not be considered. It is discussed further in Section 8.4 in the Ti $L$-edge chapter.

As will be explained in detail in Section 2.4.1, undulator radiation from a synchrotron is polarised, usually linearly for XAS/XES set-ups. This adds another parameter to the final absorption spectrum; polarisation dependence. Apart from $s$ orbitals, most atomic orbitals in a molecular structure do not retain a spherically symmetric charge distribution. $p$ orbitals for example are dumbbell shaped, oriented parallel to their local $x$, $y$ and $z$ axes. The polarisation vector of the incident light $\mathbf{E}$ is included in the matrix element of $H'$ in equation 2.1 along with $\mathbf{p}$, the momentum vector of the state involved in the transition. Thus in an oriented bulk solid, their dot product will result in a polarisation dependence being present in any XAS spectrum. This becomes important particularly for bulk samples that possess a structural anisotropy. Unoriented powder samples clearly cannot exhibit dichroism in absorption, due to the random orientation of the crystal axes of each grain.

### 2.2.1 Natural Linear Dichroism

As alluded to in the previous subsection, X-ray absorption using linearly polarised light acts as a "search light" of individual orbitals. Or in other words, the polarisation vector **E** probes the direction of the maximum and minimum number of empty valence states. Stöhr [8] introduces the concept of charge anisotropy: "It is clear that the charge distribution of the individual $p$ and $d$ orbitals is asymmetric in space, and therefore as the symmetry is lowered below cubic, transitions to individual $p$ and $d$ orbitals will depend on the orientation of the **E**-vector relative to the $x$, $y$, $z$ coordinate system of the crystal." He goes on further to define natural linear dichroism in terms of anisotropic charge distribution.

"The term 'linear dichroism' describes angle dependent effects when the direction of the linear polarised **E** vector is changed relative to the sample. In non-magnetic systems the anisotropy arises from an anisotropic charge distribution about the absorbing atom caused by bonding... If the origin of the charge anisotropy is due to bonding alone we speak of 'natural' linear dichroism."

The transition intensity is directly proportional to the number of valence states in the **E** direction [8]. This search-light effect is most clearly described by considering the transition from a specific core to valence level. Let us consider the polarisation core to valence transition intensities for **E** along the principal coordinate axes for the $K$-edge, or $s \rightarrow p_i$ $(i = x, y, z)$ which result from the square of the transition matrix element given by equation 2.3 for polarisation-dependent transition intensities, assuming $\mathbf{E} \| x, y, z$.

$$|\langle 2p_n|\frac{P_\alpha^q}{r}|1s\rangle|^2 \tag{2.3}$$

Here the notation from Stöhr [8] is used. $P_\alpha^q$ is the polarisation dependent dipole operator, with the X-ray propagation direction $\alpha = x, y$ or $z$, $q$ represents the angular momentum of the light, which for natural or circularly polarised light would be $q = \pm 1$, however here $q = 0$ for linearly polarised light. For all $K$-edge $(s \rightarrow p_i)$ transitions, the transition intensity is $1/3$ when **E** is parallel to $i$ the axis of the orbital lobe, and zero otherwise. Thus the averaged intensity per $p_i$ orbital is $\langle I \rangle = 1/9$. For $L$-edge $p \rightarrow d_{i,j}$ transitions the case is a little different for the cloverleaf and $d_{3z^2-r^2}$ shaped orbitals, this is elaborated upon in Chapter 8 for the Ti $L$-edge polarisation dependent study.

Of course **E** cannot be presumed parallel to a lobe axis all of the time. As such an angle dependent $\cos^2$ dependence is observed. The intensity of which is given by equation 2.4 [8], where $\theta$ is the angle of the **E** vector with respect to the symmetry axis labelled by $\|$ and $\langle I \rangle$ is the averaged intensity for all angles.

$$I(\theta) = I_{\|} \cos^2 \theta = 3\langle I \rangle \cos^2 \theta \tag{2.4}$$

## 2.3 Soft X-ray Emission Spectroscopy

There are many acronyms by which XES is also known, broadly speaking the techniques are identical, but it is worth noting the distinction. For consistency the acronym "XES" will be maintained for all fluorescent emission described in this thesis, and further on in this section the distinction between normal XES (NXES) and resonant X-ray emission spectroscopy (RXES) will be explained. The variety of acronyms used for XES, especially RXES, comes partly from the variety of means used to describe the process; resonant inelastic X-ray scattering (RIXS) is perhaps the most popular of these. Since the technique is a photon in / photon out process, where the momentum and energy change of the outgoing X-ray photon is measured, it can justifiably be considered an inelastic scattering technique, hence RIXS. Similarly it is sometimes known as resonance Raman (RR) spectroscopy though the differences between this and RXES is not distinct. Other denoting names for XES include soft X-ray fluorescence (SXF) and soft X-ray emission (SXE).

XES and in particular RXES has a number of unique features that differentiates it from other scattering techniques. RXES like XAS (and in which an absorption step is required) is element and orbital specific, and can differentiate between the same chemical elements in different bonding environments. RXES is also bulk sensitive, ranging in penetration depth from hundreds of nanometres in the soft X-ray region to micrometres for keV hard X-rays. For XES measurements only a small sample volume is required, unlike with neutron scattering, as the interaction strength is considerably greater. Photon sources such as 3rd generation synchrotrons may also produce a particle flux many orders of magnitude greater than typical neutron sources, focused on a much smaller beamspot, allowing the study of low volume samples such as nanoparticles and thin films. RXES differs from NXES (which will be explained in the proceeding subsection) primarily in its ability to resolve the electronic structure by consideration of the crystal momentum, i.e. it is a $k$-selective process. Resonant excitations are also significantly more symmetry selective, as discussed in detail by Gel'mukhanov and Ågren [9].

### 2.3.1 Theoretical Background

Unlike XAS, XES is a coherent second order optical process, where absorption is first order. The final state $|f\rangle$ of absorption becomes the intermediate state $|m\rangle$ in emission. The cross-section of scattering is described by the Kramers-Heisenberg equation (2.5) [10] for a radiative transition from an initial state $|i\rangle$ to a final state $|f\rangle$ through the intermediate state $|m\rangle$.

$$F(\Omega,\omega) = \sum_f \left| \sum_m \frac{\langle f|T|m\rangle\langle m|T|i\rangle}{E_i + \Omega - E_m - i\Gamma_m} \right|^2 \times \delta(E_i + \Omega - E_f - \omega) \tag{2.5}$$

Here the operator $T$ represents the radiative transition. $\Omega$ and $\omega$ are the incident and radiated photon energies respectively while $E_i$, $E_m$ and $E_f$ are the energies of the initial, intermediate and final states. The intermediate state $E_m$ has a finite lifetime ($\tau_m = \hbar/\Gamma_m$) due to the lifetime of the core hole, and thus the energy $E_m$ is fully given by the complex number $E_m + i\Gamma_m$, where $\Gamma_m$ is the spectral broadening due to the core-hole liftetime in the intermediate state.

In soft XES, the core hole excited intermediate states decay by the radiative transition of an electron, simultaneously filling the core hole and emitting a soft X-ray photon of energy $\omega$. When the core hole is filled by a valence band electron, and there are a variety of valence band states available, a spectrum of emitted photons is obtained via the coupling of the core hole and valence states through the fluorescence channel. Just as in absorption, the dipole approximation governs radiative decay emission. Thus the creation of an O or F $1s$ core hole may lead to the decay of an occupied O or F state of $2p$ character. Similarly other properties described for XAS in Section 2.2 apply to XES i.e. element selectivity, symmetry selectivity, polarisation dependence and a probe of the local partial density of states; this time however it is the valence band PDOS that are probed.

As can be seen in Figure 2.2, for low $Z$ elements such as oxygen and fluorine (the primary elements studied in this work), Auger emission is the significantly more likely route of decay for $K$-shell excitation. Fluorescence yield is as little as 0.7% [12]. Thus the technique is only practical at ultra-bright synchrotron X-ray sources in combination with efficient emission detectors. As a result of many such $3^{\text{rd}}$ generation synchrotrons being built in recent years, this powerful technique has seen an explosion of popularity among research scientists within the past 15 years. [9,10]

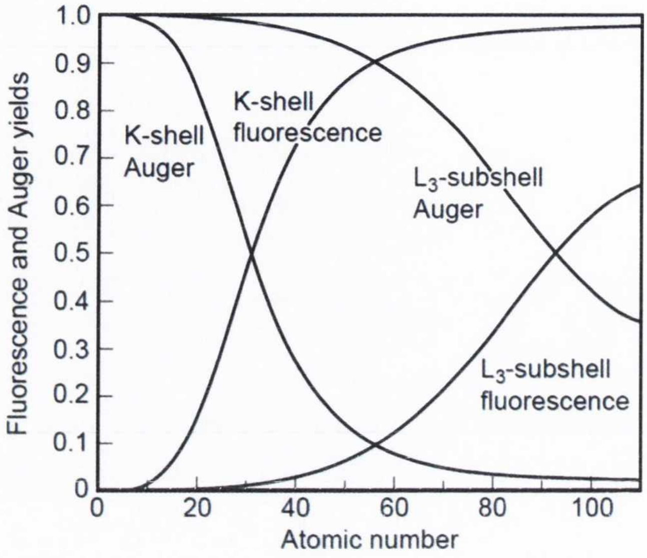

Figure 2.2: Non radiative and radiative transition rates as a function of atomic number Z from page 6 in Attwood [11]

### 2.3.2 NXES and RXES

If the core electron is resonantly excited into states just above or at the absorption threshold by the exciting photon, this is denoted RXES. Here the resulting emission spectrum is highly dependent upon $\Omega$, the incident photon energy and the transition intensity due to the coupling between intermediate states. On the other hand if the system is excited well above the absorption threshold, into the ionisation continuum such as in the final state of XPS, the resulting spectral shape no longer has a $\Omega$ dependency. This latter type of emission spectrum is denoted NXES, and will reflect, at least in the case of $K$-shell excitation, the $2p$ occupied PDOS as previously stated.

In RXES the spectral features may be further subdivided into two distinct categories, elastic scattering where $\omega = \Omega$, and inelastic where $\omega \neq \Omega$. The former is simply participator decay, where the participating excited core electron subsequently transitions back, reoccupying the core level from which it was excited. The latter spectral features are "RIXS" (or RXES) features, and are described by equation 2.5.

While equation 2.5 describes RXES (and RIXS), it can also be used to describe NXES. In following the derivation done by Kotani and Shin [10], by taking $\Omega$ as sufficiently large as to excite the core electron into a high energy continuum (photoelectron) state described as $|\phi_\epsilon\rangle$, with energy $\epsilon$, it can be treated as independent of the other electrons. Then by setting the equalities 2.6 and 2.7:

$$|m\rangle = |\phi_\epsilon\rangle|m'\rangle, \qquad E_m = E_{m'} + \epsilon, \tag{2.6}$$

$$|f\rangle = |\phi_\epsilon\rangle|f'\rangle, \qquad E_f = E_{f'} + \epsilon, \tag{2.7}$$

And inserting them into 2.5, we get equation 2.8, a version of the formula for NXES.

$$\begin{aligned} F(\Omega,\omega) = \sum_{f'} \int d\epsilon\ \rho(\epsilon) t^2 \left| \sum_{m'} \frac{\langle f'|T|m'\rangle\langle m'|a_c|i\rangle}{E_i + \Omega - E_{m'} - \epsilon - i\Gamma_{m'}} \right|^2 \\ \times\delta(E_i + \Omega - E_{f'} - \epsilon - \omega) \end{aligned} \tag{2.8}$$

Here $t$ is the dipole transition amplitude from a core state to the photoelectron state and is approximately constant, $a_c$ is the annihilation operator of the core electron, and $\rho_\epsilon$ is the density of states (DOS) of the photoelectron. Integrating over $\epsilon$ while setting $\rho(\epsilon) \sim$ constant gives equation 2.9.

$$F(\Omega,\omega) = \rho t^2 \sum_{f'} \left| \sum_{m'} \frac{\langle f'|T|m'\rangle\langle m'|a_c|i\rangle}{E_{f'} - E_{m'} - \omega - i\Gamma_{m'}} \right|^2 \tag{2.9}$$

While still a coherent second order optical process, where a core-hole creation is correlated with the emission of an X-ray [13], it is found that $F(\Omega,\omega)$ of NXES does not depend on $\Omega$. Assuming then that the numerator is approximately constant and $\Gamma_m$ is infinitesimally small, the NXES spectrum becomes proportional to the DOS of the occupied states at $m$. In reality the NXES spectrum gives the PDOS since it is symmetry selected by the dipole transition and broadened by the core-hole lifetime broadening factor $\Gamma_m$ in the intermediate state. From equation 2.8 it is noted that if $\Omega$ is decreased down to the absorption threshold, $t$ is no longer constant since the excited core electron now couples with other electrons in the system and the spectrum given by $F(\Omega,\omega)$ becomes increasingly dependent on $\Omega$. It can thus be seen that RXES and NXES are two aspects of the same process, XES, caused by different types of intermediate states based in the choice of $\Omega$. The distinction between them is gradual and it is possible to have in-between "NXES-like" RXES where the resulting spectrum has very little dependence upon $\Omega$. RXES is often used interchangeably with RIXS. The process is essentially the same. For consistency, subsequent chapters of this work will refer to the term as RXES.

For a more detailed discussion and derivation of the RXES and NXES processes please refer to the review paper by Kotani and Shin [10] as well as the more recent review paper by Ament *et al.* [14]

### 2.3.3 RXES and RIXS

As resonant X-ray emission spectroscopy (RXES) and resonant inelastic X-ray scattering (RIXS) belong to a new field, their terminology has not as yet been fully established. It has been suggested by A. Kotani and F. M. F. de Groot [XAFS13, Stanford 2006] that RIXS should be used for experiments where the emitted energy is not tuned to a fluorescence energy but to small energy transfers of a few eV. Whereas measurements of fluorescence lines after resonant excitation should be referred to as RXES.

While both RXES and RIXS are terms used to describe resonant photon-in and photon-out processes, strictly speaking RXES includes more processes than RIXS; in that RIXS is part of RXES and disperses linearly with the incident photon energy. In this sense RIXS features can be described in terms of their constant Raman shift. The term RXES on the other hand includes resonant elastic X-ray scattering with zero energy loss (elastic peak) as well as "fluorescence" spectroscopy, with an approximately constant X-ray emission energy. [15]

Thus RIXS measurements will often be plotted as a loss graph, with respect to the elastic de-excitation feature, if it exists. Whereas RXES measurements tend to be plotted with respect to the fluorescent energy of the detected photons. There is still some overlap though as RIXS and RXES coincide in valence band RXES, where elementary excitations in the valence electron states corresponds to the Raman shift.

### 2.3.4 State and Symmetry Selectivity of RXES

As briefly discussed earlier in the chapter, selection rules govern allowed transitions of a single electron. Taking Fermi's Golden Rule in equation 2.1, which gives the transition rate from one energy eigenstate to another due to a first order perturbation, the dipole matrix element requires the initial and final states to be of opposite parity, otherwise it is zero [16]. This leads to the selection rules mentioned earlier in the absence of an external magnetic field: $\Delta l = \pm 1$,[†] $\Delta j = 0, \pm 1$ and $\Delta s = 0$. For example a $1s$ core electron transition in a system with vacant $n = 2$ states is forbidden from interacting with the $2s$ states. Given the narrow energy width of a $1s$ state in this system, any spectroscopy involving such a transition would yield a study of the $2p$ PDOS, alone. Since these selection rules limit the specific excitations that can occur between subshells, both XAS and XES are thus extremely powerful tools for the study of the DOS of materials.

---

[†] There are exceptions to the Laporte selection rule: $\Delta l = \pm 1$. $d - d$ transitions for example may be weakly allowed due to vibronic coupling.

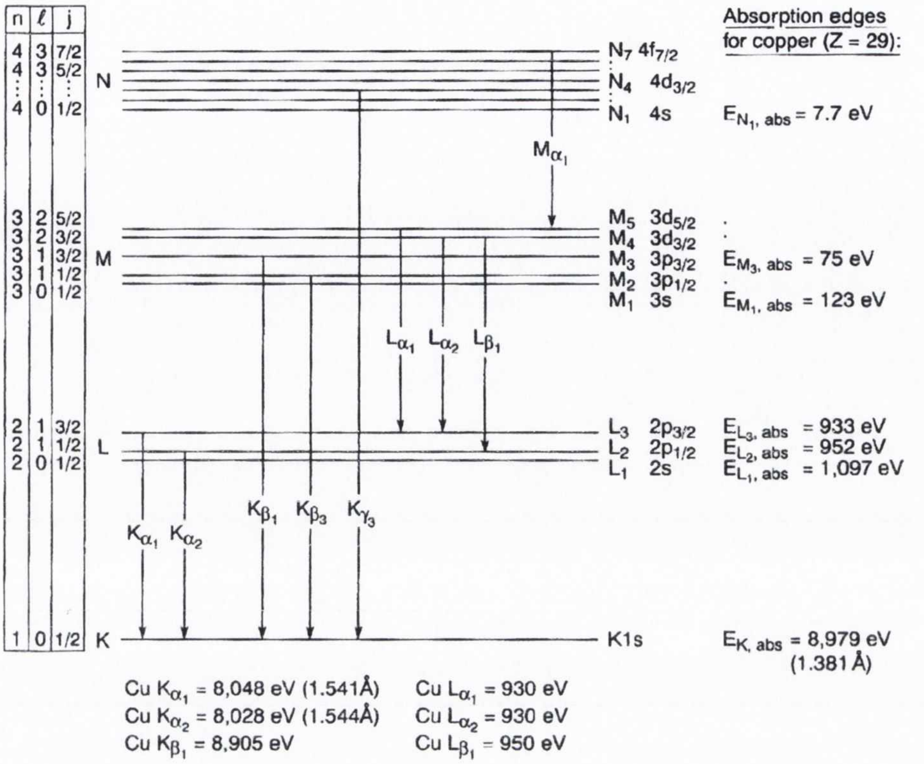
n ℓ j
4 3 7/2
4 3 5/2
4 0 1/2
N
3 2 5/2
3 2 3/2
3 1 3/2
3 1 1/2
3 0 1/2
M
2 1 3/2
2 1 1/2
2 0 1/2
L
1 0 1/2
K
N7 4f7/2
N4 4d3/2
N1 4s
M5 3d5/2
M4 3d3/2
M3 3p3/2
M2 3p1/2
M1 3s
L3 2p3/2
L2 2p1/2
L1 2s
K1s
Mα1
Lα1 Lα2 Lβ1
Kα1 Kα2
Kβ1 Kβ3 Kγ3
Absorption edges for copper (Z = 29):
EN1, abs = 7.7 eV
EM3, abs = 75 eV
EM1, abs = 123 eV
EL3, abs = 933 eV
EL2, abs = 952 eV
EL1, abs = 1,097 eV
EK, abs = 8,979 eV (1.381 Å)
Cu Kα1 = 8,048 eV (1.541Å)
Cu Kα2 = 8,028 eV (1.544Å)
Cu Kβ1 = 8,905 eV
Cu Lα1 = 930 eV
Cu Lα2 = 930 eV
Cu Lβ1 = 950 eV

Figure 2.3: Energy level diagram for copper showing spectroscopic notation for transitions allowed by the selection rules $\Delta l = \pm 1$ and $\Delta j = 0, \pm 1$. $n$ is the principal quantum number, $l$ is the orbital angular momentum quantum number and $j$ is the total angular momentum quantum number from the vector combination of spin and orbital angular momentum. Absorption edge nomenclature is shown to the right. From page 17 Attwood [11].

The atomic electronic configuration is referred to by different nomenclature in the context of spectroscopy. Figure 2.3 gives an energy level diagram illustrating the allowed transitions for copper. The subshells are further subdivided by the spin-orbit effect ($j$ value). On the left the quantum numbers $n, l, j$ are given for each subshell. Right of each subshell is its designated edge in spectroscopic notation. So for example the $n = 2$ shell is designated as the $L$-shell, where its subshell divisions $s$ and $p$ are differentiated by numerical subscripts. The spin-orbit split $2p_{1/2}$ and $2p_{3/2}$ levels are further differentiated by these subscripts, giving the $L_1, L_2$, and $L_3$ edges. Emission on the other hand will always involve a transition between two levels and thus cannot be described solely by this notation, and instead uses Siegbahn notation. The most highly bound level is used as the basis of this notation, where Greek subscripts then refer to the specific transition. Unfortunately these subscripts do not follow a systematic pattern. Since the Siegbahn notation is in overwhelmingly common use, they will be referred to as standard in this thesis. Table A.2 on page 208 compares the systematic International Union of Pure and Applied Chemistry (IUPAC) designations for these transitions, and can be used as a reference for more arbitrary Siegbahn notation.

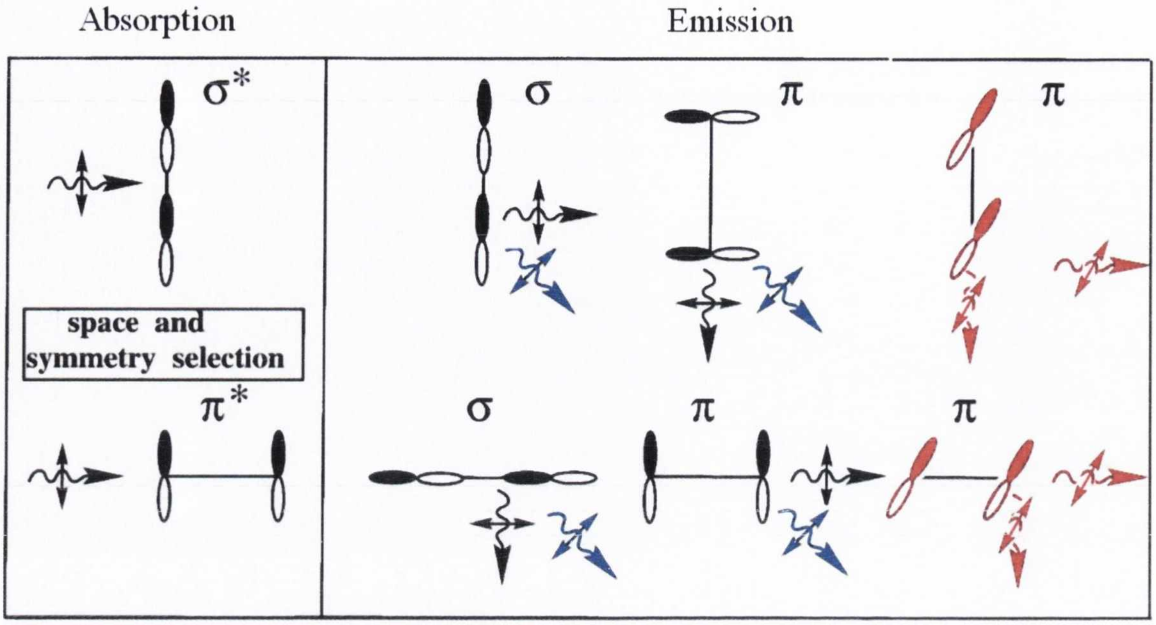

Figure 2.4: Orbital symmetry selectivity in X-ray emission due to varying spectrometer position with respect the polarisation of the exciting photons. Geometries of maximum absorption and emission are illustrated for $p$ orbitals with either $\sigma$ or $\pi$ bonding symmetry in the left and right panel respectively. Black has orbital axis (**k**-vector) and bond direction (**E**-vector) in the plane of the page, for red the orbital axis (**E**-vector) alone is orthogonal to the page. Blue applies only to the photon, where **E** is parallel to the page but the **k** is orthogonal. Adapted from Gel'mukhanov and Ågren (Figure 32) [9].

While the Kramers-Heisenberg equation 2.5 gives the total transition rate for RXES, it does not detail the energy dependent state-selectivity of resonant emission. Figure 2.4 adapted from Gel'mukhanov and Ågren [9] indicates the molecular symmetry and spatial selection for resonant excitation into unoccupied orbitals or states of either $\pi$ or $\sigma$ character on the left, and the resulting angle dependent character selection of the inelastically scattered photons on the right. The figure is most appropriate when considering homogeneous or heterogeneous diatomic molecules, as this was the context in which this picture was introduced. [8] The viewpoint is from above an in-plane scattering geometry[†], assuming the measurement device (XES spectrometer) in this case is toward the bottom of the figure. Two bonding types are portrayed showing $p$ orbital lobes hybridised (orbital overlapping) as either $\pi$ or $\sigma$ arrangements, with the upper now showing the diatomic internuclear axis being parallel to the incoming polarisation vector, and the lower now showing the internuclear axis as being perpendicular to the incoming polarisation. The orbitals oriented with their axis of symmetry in the plane of the page are in black, while those perpendicular to the plane of the page are represented in red. The arrows are coloured in a similar arrangement, where the curly single-ended arrows represent the direction of propagation, while the double ended indicate the polarisation. Black has both in the plane of the page, red is with the polarisation alone orthogonal, the blue arrows on the other hand propagate perpendicular to the page while the **E** vector remains in the plane of the page. As will be discussed in the following section, the angle between the electric polarisation vector and the projection of the orbital angular momentum follows a $\cos^2$ dependence, being at a maximum when the two are parallel. Thus each arrow represents where this is a maximum, for both absorption on the left, and emission on the right.

---

[†] i.e. when the plane of scattering is parallel to the polarisation vector **E**

The polarisation vector of the incident light **E** can excite specific unoccupied molecular orbitals (MOs) with the same symmetry if its photon energy is tuned resonant with those orbital states.

Figure 2.4 illustrates symmetry selectivity in the specific case of $\sigma$ and $\pi$ bonding in a diatomic molecule. When absorption occurs resonantly into $\sigma^*$ states, as is the case in the upper half of the diagram, emission at a 90° scattering geometry *within the plane* will be of $\pi$ character. The crux of the diagram illustrates that emitted photons radiate in a dipole fashion with respect to the orbital lobe axis symmetry and not the bond axis, and the polarisation vector of the emitted photons is also subject to the orbital symmetry. For a 90° scattering geometry, emitted photons are polarised parallel to the plane of the page (first and second column of the emission panel in Figure 2.4) and perpendicular to the plane of the page (third column). Thus when the polarisation and energy resonantly excites an unoccupied $\sigma^*$ orbital as in the upper half of the figure, the emission observed from occupied MOs in a 90° *in-plane* scattering geometry consists of occupied $\pi$ orbitals, where the polarisation **E** is given by the second and third column, parallel and perpendicular to the page respectively. By contrast, resonant excitation to the $\pi^*$ MO, for the same 90° in-plane geometry, gives a $\sigma$ MO contribution polarised within the plane of scattering, and a $\pi$ MO contribution polarised perpendicular to this plane.

For a 90° *out-of-plane* scattering geometry, the state and symmetry selectivity differs a little further; here both $\sigma^*$ excitations produce $\pi$ and $\sigma$ emission while $\pi^*$ excitation will give $\sigma$ and $\pi$ emission respectively. It should be noted that this discussion applies specifically for the case of diatomic molecules with $p-p$ hybridisation, as opposed to the M–A MO of materials studied in this thesis, which are either $e_g - sp^2$ $\sigma$ or $t_{2g} - p$ $\pi$ in the rutile structure. However this more simplified example is nevertheless highly instructive in the analysis of emission spectra from these materials.The polarisation vector of fluorescence $\mathbf{E}'$ will be the same as **E** for occupied MOs of $\sigma$ symmetry, but will be polarised mainly perpendicular to **E** for occupied MOs with $\pi$ symmetry.

### 2.3.5 Natural Linear Dichroism in XES

Further to this state selectivity dependent upon the resonant energy and scattering angle, as described previously, there is another polarisation factor, that of natural linear dichroism independent of resonance. While the individual atomic $p$ and $d$ orbitals are anisotropic, when summed however they are spherically symmetric. The same is true for split $d$-orbitals in a crystal field. The individual orbitals within $t_{2g}$ and $e_g$, when summed make each spherically symmetric. As explained in Section 2.2.1, XAS acts as a search light for individual orbitals. Much in the same way that natural linear dichroism is explained in that section, in the context of X-ray absorption, applies similarly to the transition from a valence to core state, which may result in emission. Since fluorescence is usually measured propagating in one direction, and the polarisation of the photon is intrinsically orthogonal to that, the non-resonant transition intensity measured is dependent upon the crystal orientation with respect to the measurement device. In other words the natural linear dichroism observed in absorption will also be observed in normal emission, and indeed is a factor in resonant emission. It can be thought of as the reverse of the absorption process. Hence this is why NXES spectra can exhibit natural linear dichroism, where the only variable is a rotation of an anisotropic bulk solid.

### 2.3.6 Crystal Momentum Selectivity

Another feature of RXES is the crystal momentum selective nature of the technique. Simply put, for resonant emission at soft x-ray energies the crystal momentum of the selected conduction band states is conserved in emission. An excellent demonstration of this was provided in an experiment by Carlisle *et al.* [17] summarised in Figure 2.5, which concerned $sp^2$ bound graphite. In the emission spectrum part of this figure, the numbered dispersive features in the resonant spectra are associated with those of the graphite bandstructure. The direction of dispersion is indicated by the dashed lines in both cases. At the very threshold energies above the Fermi energy, only a very small range of crystal momentum is selected in the conduction band, as observed at the Brillouin zone K-point, corresponding to the conduction band minimum. The non elastic emission features at these threshold energies correspond to emission energies where the valence bands intersect with this narrow range of selected **k**-points (crystal momentum). Formally the momenta of the incoming and outgoing photons (and hence scattering angle) must be taken into account and is non negligible, but for soft X-ray photons the photon momentum is a small fraction of the span of the Brillouin zone, at least for small unit cells e.g. O $K$-edge and energies of $\sim 530$ eV and $\mathbf{k} \sim 0.268$ Å$^{-1}$. As the excitation energy is increased the features begin to disperse in a manner not related to the increase of energy. Further, new features begin to appear at energies as others fade.

The correlation between the resonant evolution of these features and the direction of the bands at varying crystal momentum is unmistakeable. For example, as the excitation energy reaches 285 eV, the unoccupied states in the M region are strongly favoured for absorption. At the same crystal momentum the band indicated by arrow 4 also shows an inflection point, indicating a concentration of states at this energy. The emission spectrum at 285 eV indeed shows a prominent feature at the same $\Delta$ eV below the Fermi level. Other dispersing features appear to follow the valence bands at the varying crystal momentum selected by the energy excitation in the conduction band (CB).

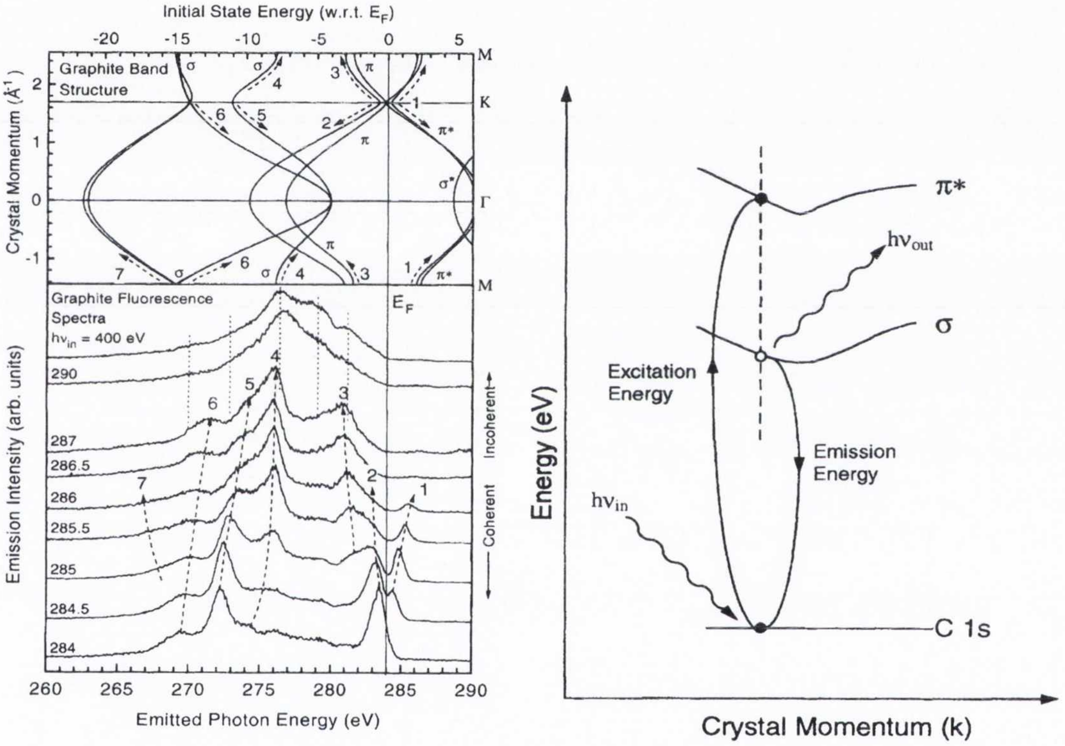

Figure 2.5: Resonant and non resonant emission spectra from oriented graphite. Upper left panel is bandstructure aligned such that the energy axes match. The right panel is a schematic representation of the coherent resonant fluorescence. Only emission from the occupied states with the same crystal momentum (vertical line) is allowed. Adapted from Carlisle *et al.* [17]

As the excitation energy increases towards the ionisation continuum, the features become less dependent upon $\Omega$, energy of the incident photon. A far wider range of crystal momentum is selected, and as well the excited core electron coupling with the valence band (VB) becomes less apparent. Thus $\mathbf{k}$ is no longer conserved and the states selected correspond to an average PDOS over the full span of crystal momentum, or over the entire Brillouin zone. This k-unselective spectrum is the NXES spectrum.

## 2.4 Synchrotrons and Beamlines

X-ray emission as a synchrotron radiation technique has been around for more than half a century, in its earliest form the excitation source was supplied by electrons accelerated towards conventional X-ray targets. Synchrotron sources however produce a continuously tunable X-ray source, which in turn allowed new techniques such as XAS and RXES to be performed, but as these techniques are extremely photon hungry, they were not considered a very feasible method of analysis compared with other techniques available. With the advent of third generation synchrotrons offering far greater brightness, these techniques have undergone a revival since the late 1980s. The developments made since this time have continued the pace of this revival to the present day. This section will present a brief introduction of synchrotrons and soft X-ray beamlines, as well as outlining the specific instruments utilised for the experimental work presented in this thesis.

### 2.4.1 The Synchrotron

An accelerated charged particle, such as an electron travelling on a curved trajectory, is known to emit radiation described as synchrotron radiation. Generally a synchrotron consists of an evacuated storage ring in which thermally generated electrons are accelerated up to relativistic velocities. Bending magnets are used to maintain the circular trajectory. These magnets cause electrons at such velocities to emit light radiated in a narrow cone tangential to the trajectory, and was the source utilised in early synchrotrons. Third generation synchrotrons make use of two other types of magnets, or insertion devices, to produce far more brilliant, collimated, and tunable radiation: wigglers and undulators. A wiggler is not unlike a bending magnet but consists of a series of magnets designed to laterally deflect the electron current in a periodic (wiggling) fashion. The flux of light produced is much higher than that of a bending magnet however, due to its many magnetic dipoles. It produces very broadband, and very brilliant light. Figure 2.6 illustrates the fundamental layout of a synchrotron storage ring.

In all synchrotron experiments undertaken for this thesis, radiation from an undulator insertion device was used. An undulator, like a wiggler, is a series of magnets designed to periodically deflect (undulate) the passing electrons. An undulator instead uses a periodic structure of dipole magnets whose static magnetic field alternates along the length of the undulator with a wavelength $\lambda_u$. The length of this period distinguishes it from a wiggler, the smaller oscillations from an undulator causes constructive interference of the resultant radiation, leading to the production of intense narrow energy bands. Further, the distance (or gap) between the dipole magnets above and below the electron beam can be altered

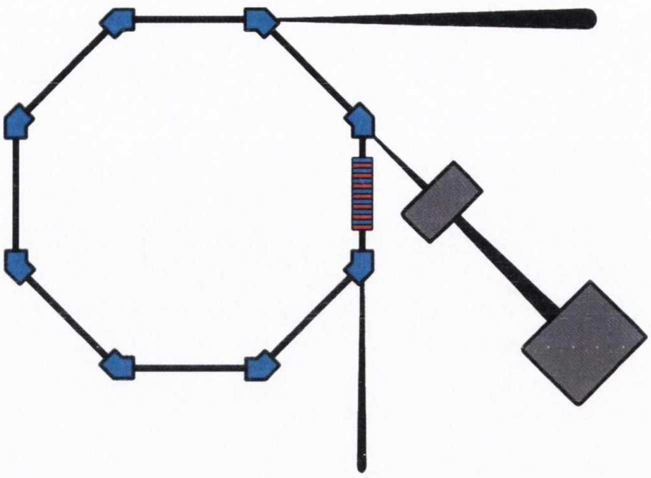

Figure 2.6: Sketch of a synchrotron storage ring and a beamline. Bending magnets are shown at corners, while a straight-line section houses an undulator storage device. The tangential cone-shaped trajectory of the of light is also indicated.

to change the frequency of the harmonic energy bands produced. The flux of the resulting radiation is dependent upon the number of magnetic periods in the structure and inversely proportional to the gap.

Though narrow band frequency ranges are produced, they are not monochromatic. Therefore a suitable monochromator comprising of a diffraction grating and slits is used to select the desired photon energy. The width of these slits are used to further select the resolution of this energy. Simultaneously the peak intensity of the chosen undulator harmonic is varied to maximise the flux at the desired energy.

Another characteristic of undulator energy is its polarisation. This matches the direction of deviation of the electrons by the undulator field. If the dipole magnets are aligned directly over each other perpendicular to the orbit, the undulation will be linear and in the plane of the orbit and result in linearly polarised light. If the dipole magnets are aligned with an offset, they may produce left or right circularly or elliptically polarised.

### 2.4.2 Soft X-ray Spectrometer

This section describes the general set up for soft X-ray fluorescence spectrometers. Specific details differ between spectrometers used at various beamlines so the Nordgren type design[†] will be used as a blueprint, since it was on this type that the majority of emission spectra presented in this thesis was recorded. [18] For details regarding types used on other beamlines, please refer to the latter sections in this chapter detailing those specific beamlines.

---

[†] For example the XES300 manufactured by Gammadata and developed by the group of Josef Nordgren and collaborators at Uppsala University. [18]

SXF spectrometers, as they are often called, rely on grazing incidence optics. This is due to the low reflectivity of soft X-rays for materials, and thus total external reflection is utilised. To achieve diffraction spherical diffraction gratings are used in the spectrometers, the optics of which can be understood via Rowland circle geometry.

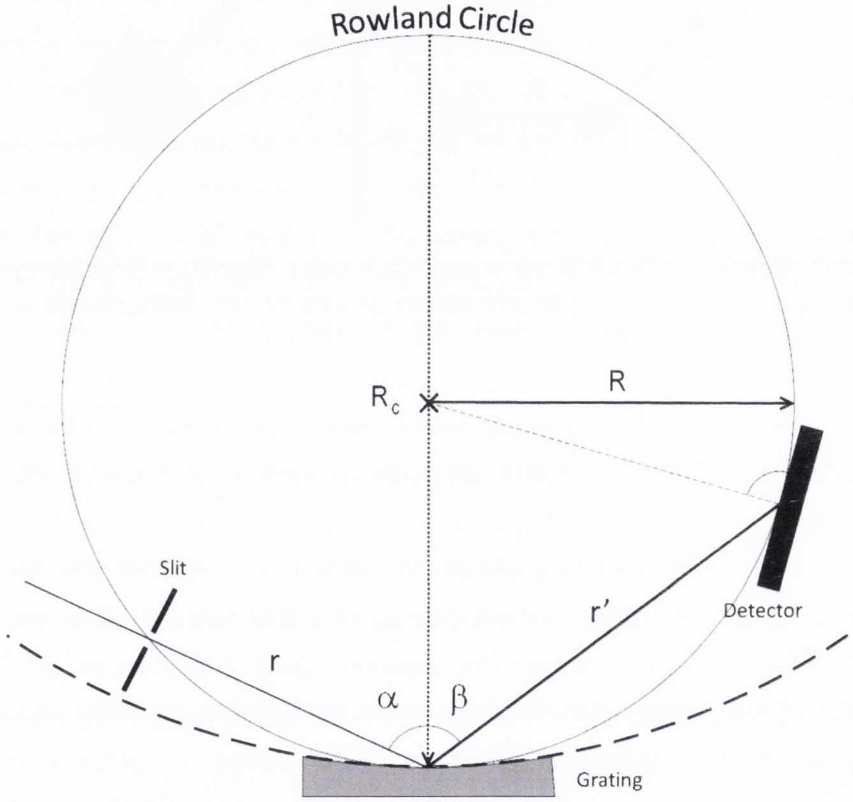

Figure 2.7: Grazing incidence Rowland circle focusing geometry for a concave spherical grating, in a SXF spectrometer. Radius of Rowland circle 2R is defined as the radius of curvature of the grating positioned at its centre point: $2\mathrm{R} = \mathrm{R}_c$. Entrance slit and detector are also indicated lying on the circumference for optimal focus.

A sketch of the Rowland circle in a spectrometer mounting is given in Figure 2.7. The diameter of a Rowland circle is equal to the principal radius of curvature of the grating. The focusing condition is satisfied in the Rowland circle geometry when each component, slit, grating and detector, lie on the circumference of the circle [19]. The diffraction equation is then given by $m\lambda = d(\sin\alpha + \sin\beta)$, where $m$ is the order of diffraction, $\lambda$ is the wavelength of light, $d$ is the grating groove spacing and $\alpha$ and $\beta$ are the angles indicated in the Figure.

For the application of such optical geometry in a soft X-ray spectrometer see Figure 2.8 which illustrates the Nordgren type [18]. Part (A) of the figure shows three fixed-position spherical gratings with varying groove density and blaze angle attuned for maximum operating efficiency in specific energy regions. Each of these can be selected via the grating selector flags, which form an aperture to illuminate only the selected grating. The optical axis of the spectrometer is defined by the line between the slit and the centre of the selected grating, shown in part (C) of Figure 2.8. In the Nordgren style design the optical axis is allowed to rotate about an orthogonal axis parallel to the direction of the rulings of the grating. The spherical gratings diffract the emitted X-rays, separating them by energy in a crescent-like two-dimensional shape on the detector. This crescent aberration is usually corrected after recording by a fitting adjustment of adjacent horizontal slices of the detector, after which an addition of the slices can be made forming a normal one-dimensional spectrum.

Part (B) of Figure 2.8 gives a detailed cross section of the detector which consists of two stacks of MCP electron multipliers. These are arranged in a chevron, or zig-zag arrangement under a deflector plate that is maintained a ~keV range negative potential with respect to the MCP detector array. Each stack creates a seed-shower of secondary electrons upon photon incidence which is then amplified by $\sim 10^8$ in a cascade effect as they pass through the MCPs [20]. The potential on the detector directs these secondary electrons back towards the detector to contribute to this shower, which then arrives at the resistive anode encoder (RAE). The spatial position of the arrival on the RAE is determined by current measurement at each of its corners by a position analyser; it is then recorded and added to the counts for that specific pixel. Another method of detection, currently employed on beamline I511-3 at MAX-lab, is via a phosphor screen and CCD camera. The scale of the detector is calibrated post processing using well defined emission lines.

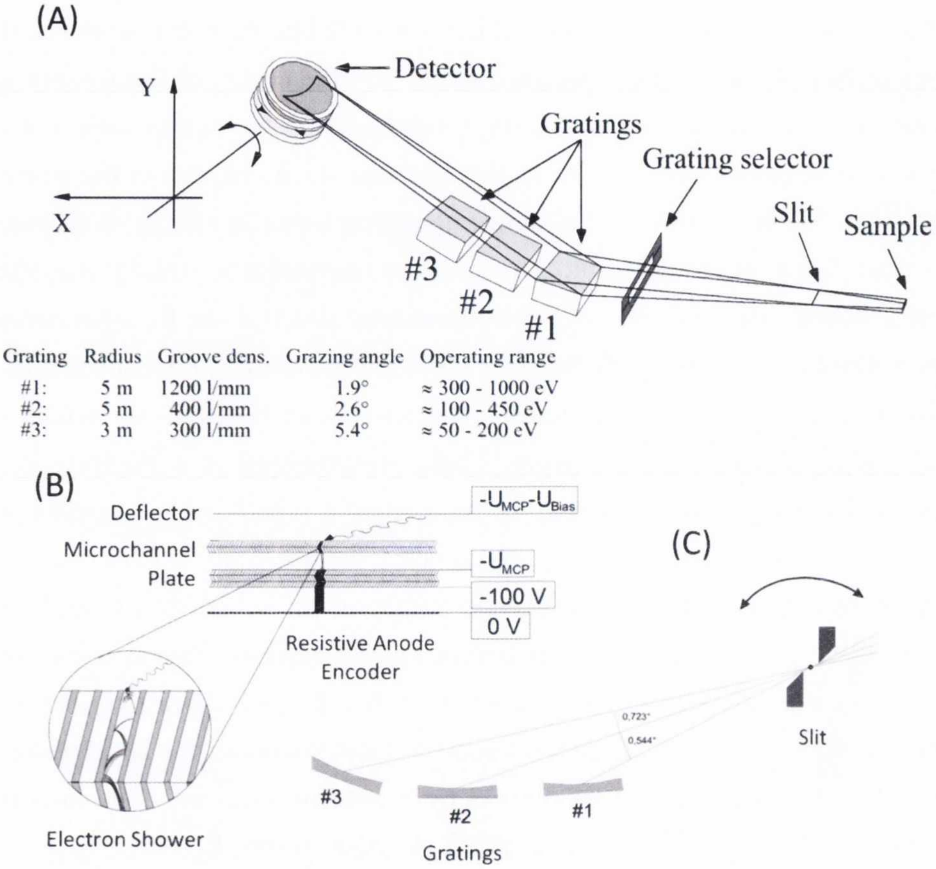
(A)
Detector
Y
X
Gratings
Grating selector
Slit
Sample
#3
#2
#1
(B)
Deflector
Microchannel Plate
Resistive Anode Encoder
Electron Shower
-U_MCP-U_Bias
-U_MCP
-100 V
0 V
(C)
0.723°
0.544°
Slit
#3
#2
#1
Gratings

| Grating | Radius | Groove dens. | Grazing angle | Operating range |
|---|---|---|---|---|
| #1: | 5 m | 1200 l/mm | 1.9° | ≈ 300 - 1000 eV |
| #2: | 5 m | 400 l/mm | 2.6° | ≈ 100 - 450 eV |
| #3: | 3 m | 300 l/mm | 5.4° | ≈ 50 - 200 eV |

Figure 2.8: Gammadata XES300/350 SXF Nordgren type spectrometer. (A) shows the sample, slit, grating-selector, gratings and detector layout. (B) details the detector; showing the deflector, MCP as well as the RAE. (C) gives the relative orientation of the spherical gratings with respect to the slit. Diagram from Nordgren *et al.* [18]

### 2.4.3 Beamlines

In this section a brief overview of the experimental stations (beamlines) utilised for the measurements presented in this thesis will be given.

#### 2.4.3.1 Beamline 8.0.1 at the ALS

Beamline 8.0.1 (BL8) of the Advanced Light Source (ALS) is part of Lawrence Berkeley National Laboratory (LBNL) in Berkeley, California. It contains a U5.0 undulator together with a high throughput spherical grating monochromator (SGM) with good resolution in the sub-keV photon energy range. Parameters from this beamline are quoted from Jia *et al.* [21] The undulator has 89 poles at a 5 cm period, possessing useful first, second and third harmonics, allowing an intense photon flux of up to $10^{13}$ photons per second in the 70–1200 eV range with continuous adjustment of the undulator gap. The coherent radiation from the undulator is focused onto a water-cooled moveable entrance slit. The light then enters the grating tank where three holographically ruled laminar gratings of 150, 380 and 925 lines grooves per millimetre (gpm) are housed. These are mounted on a horizontal linear slide parallel to each other. After passing through the exit slit, the monochromatised light falls onto horizontal refocusing mirror designed to narrow the spot size. The spot size is of the order of a $100\mu$m × $100\mu$m, and the maximum resolving power is about 10,000 for O $K$-edge measurements using the 380 gpm medium energy grating (MEG) in the $3^{\text{rd}}$ harmonic.

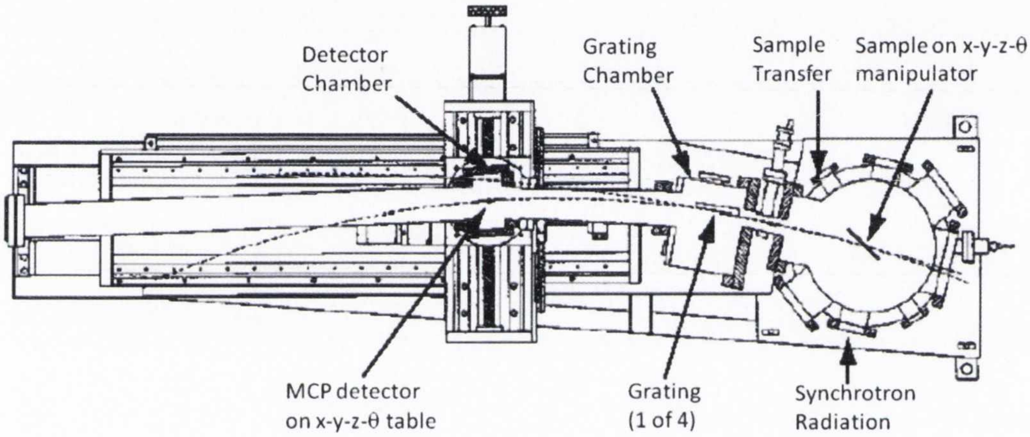

Figure 2.9: End station and SXF spectrometer at the ALS beamline 8.0.1. Diagram adapted from Jia [21].

The soft X-ray spectrometer, designed by the Tennessee/Tulane groups [21] and shown in Figure 2.9 in a cross section view from above, has its Rowland circle in the horizontal plane. The position of the entrance slit is fixed, and its width is adjusted by varying the voltage applied to a piezoelectric crystal in the slit mechanism. There are four spherical diffraction gratings in the spectrometer which cover a range from 40–1000 eV. For emission measurements presented in this thesis the grating used possessed 1500 gpm, and had a radius of curvature of 10 m. Otherwise it bears similarity to the Gammadata XES300/350, possessing a similar MCP stack detector system.. The beamline allows both TEY recording using drain current, and TFY via a channeltron. The manipulator housing is set up for simultaneous resistive heating of a specifically designed sample plate, as well as isolated thermocouple measurement of the temperature, and can do these simultaneously with TEY measurements.

#### 2.4.3.2 Beamline 7.0.1 at the ALS

This beamline is very similar to that of BL8, also containing a U5 undulator with a 89×5 cm periods dipole magnets. These provide light from 60 to 1200 eV using the first, third and fifth harmonics according Hoyer *et al.* [22]. A schematic of the optics of the beamline is given in Figure 2.10, and matches that of BL8 very closely. A maximum resolving power of 8,000 is achieved for the incident light onto the sample. The 380 gpm SGM was used together with the third order harmonic of the undulator for the O $K$-edge spectra recorded at this beamline. The beamline consists of a number of endstations, light is directed into the chosen endstation via the selection mirror depicted in Figure 2.10. The focal length of the reflected beam is adjustable depending on the desired endstation. Optimisation for the SXF endstation produces a spot approximately 50–100 $\mu$m in size.

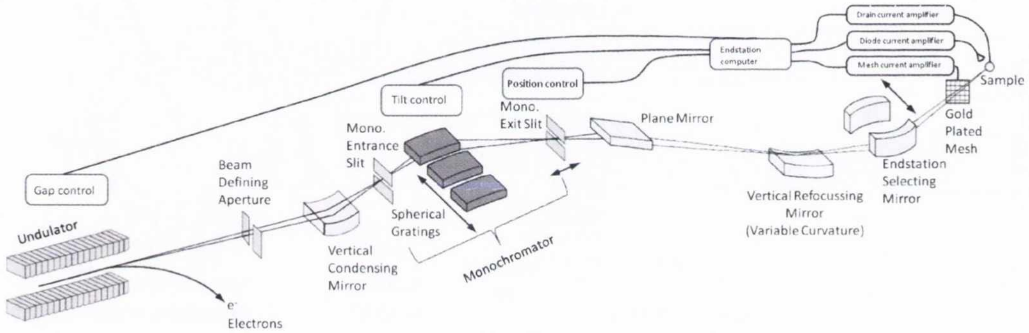
Drain current amplifier
Diode current amplifier
Mesh current amplifier
Endstation computer
Sample
Position control
Tilt control
Mono. Exit Slit
Plane Mirror
Gold Plated Mesh
Mono. Entrance Slit
Beam Defining Aperture
Gap control
Endstation Selecting Mirror
Vertical Refocussing Mirror (Variable Curvature)
Spherical Gratings
Undulator
Vertical Condensing Mirror
Monochromator
e⁻
Electrons

Figure 2.10: End station and SXF spectrometer at the ALS beamline 8.0.1. Diagram adapted from Jia [21].

The endstation contains a Nordgren type, Gammadata XES300 SXF grazing incidence spectrometer installed by the University of Uppsala group [23], similar to that used in I511-3 at MAX-lab. As with BL8, the X-ray emission spectrometer is mounted at 90° to the incident X-ray beam, with the dispersive plane perpendicular to the scattering plane.

#### 2.4.3.3 I511-3 at MAX-lab

Beamline I511-3 is part of the MAX-II synchrotron at MAX-lab in Lund, Sweden. This beamline, like those that were discussed for the ALS has a U5 undulator. Detailed specifics of this beamline have been reported by Denecke *et al.* [24], but will be summarised here. The undulator is composed of 49 periodic dipoles spaced at 52 mm, producing a linearly polarised flux of photons in the horizontal plane of the synchrotron. The undulator light is focused by a cylindrical mirror and deviated directly onto to a plane grating by a plane mirror. The high stability of the electron beam passing through the undulator allows the monochromator to operate without the need for an entrance slit. The single plane grating monochromator is ruled at 1200 gpm, and as such a wide variety of odd harmonics, up to the $11^{\text{th}}$ are used to access the working range of photon energies, between 100 and 1200 eV. A translatable mirror directs the focused beam into one of three possible endstations. The I511-3 bulk station is equipped with a Gammadata XES, Nordgren type spectrometer. Originally this spectrometer housed an MCP detector, but instead now uses a phosphor screen – CCD combination to record spectral emission counts. XAS is recorded in TEY mode via drain current, and fluorescent yield may be recorded from a photodiode, and more recently an MCP.

Though not a very bright source by comparison to other soft X-ray emission beamlines, I511-3 has an advantage for polarisation dependent analysis, which is the basis of the investigation method of this volume of work. The emission spectrometer, together with the entire analysis chamber, including manipulator, sample and other accessories, can be rotated by 90° about the direction of the beam. This allows emission spectroscopy to be measured in the out-of-plane scattering geometry [25], where the measured scattering plane is orthogonal to the plane drawn out by the polarisation vector $\mathbf{E}$ and the propagation vector of the incident light.The optimum focused beam spot is $10 \times 30$ $\mu$m.

#### 2.4.3.4 X1B at the NSLS

The X1B beamline is in the National Synchrotron Light Source (NSLS), part of Brookhaven National Laboratory (BNL) on Long Island, New York. Specific parameters are summarised and quoted from Randall *et al.* [26] as well as the more up to date NSLS website. The beamline is named for its X1 undulator [27] which consists of 35 dipole periods. The minimum gap achieved surrounding the beam is 32 mm, achieving a maximum flux of $10^{18}$ photons per second. The range is 200 to 1600 eV. The monochromator system is based on the Dragon concept [28], allowing selection of four SGMs of 300, 600, 1200 and 1600 gpm, giving a maximum resolving power of 10,000. The monochromators used for the O $K$-edge and Ti $L$-edge XES experiments was the 600 grating. For high quality XAS the 1200 gpm grating was used to achieve sub 100 meV resolution.

The beamline is equipped with a Gammadata XES300 grazing incidence, spherical concave grating emission spectrometer with a selection of three gratings being accessible. Unlike the newer Gammadata XES350, it has a resistive anode encoder behind the microchannel plate, and does not have the extended range of motion of the detector on the XES350 allowing it to select up to $2^{\text{nd}}$ order for certain energies. Thus it is the same as Beamline 7.0.1 (BL7).

# 3 Rutile Structure

## 3.1 Introduction

Presented in this chapter is an overview of the physical and electronic details of the category of rutile-like transition metal compounds studied in this thesis, as well as an introduction to electronic structure calculations used to simulate the X-ray spectroscopic results of our measurements.

The rutile motif is a common polymorph of transition metal compounds with the binary stoichiometry $MA_2$. Here M represents the metal cation while A is the ligand anion, usually either oxygen or fluorine. This structural family is named after the transition metal(IV) oxide $TiO_2$ rutile crystal. The name comes from the Latin *rutilus*, meaning red, in reference to the deep red colour observed via transmitted light through some natural specimens of rutile mineral. This colour results from impurities, pure rutile $TiO_2$ is colourless. The rutile structure is one of the simplest and most common structural types adopted by metal oxides [29].

This chapter will begin with an overview of research performed on rutile and rutile-like compounds. After this the physical and electronic structure of both pure and distorted rutile compounds will be described, giving an outline of some general features in their bonding arrangements and states, especially focusing on the O $2p$ partial density of states (PDOS) and their relationship to both the emission and absorption spectroscopies, described in Chapter 3. A summary of the theory behind density functional theory (DFT) and hence the electronic structure calculations are detailed in Section 3.4. That section also describes how these PDOS calculations may or may not compare with experimental spectra and what is required to simulate such spectra.

The structure itself was first described by Vegard [30]. The properties of rutile-type compounds began to be measured as soon as techniques became available from the 1950s [31–33]. However real interest in transitions metal oxides, and thus the rutile structure, sprang to life in the early 1970s as the advent of computer technology allowed for theoretical calculations to be compared with experimental physical and electronic structure probes such as neutron and X-ray scattering. The theoretical and simulation work by Goodenough [34] into metallic oxides including $VO_2$ using molecular orbital bandstructure techniques [35] has proved long lasting and influential. Other pioneering experimental and simulation work on rutile-type compounds were performed by Baur [36], Mattheiss [37], Gupta [38], Caruthers [39]; and more recently by Burdett [40–42], and Bolzan [43]. A review by Sorantin *et al.* [44] outlines much of the work performed on rutile-type compounds.

## 3.2 Rutile Structure

The rutile structure is primarily adopted by the transition metal(IV) oxides and (II) fluorides which are shown in a periodic table form in Figure 3.1. Distorted rutile structures that form monoclinic unit cells are also listed in this figure but are highlighted by an asterisk. Their structure and relationship with pure rutile compounds will be discussed in Section 3.3. The transition metal rutile compounds display a wide variety of properties; from insulating to metallic and magnetic behaviour. Some, such as $VO_2$ and $NbO_2$, even undergo metal to insulator transitions at certain temperatures, accompanying a structural change from pure to distorted rutile. For these transition metal $MA_2$ compounds, the rutile type phase tends to be the most common [42]. For the Group-14 dioxides shown in Figure 3.1, it is a less common phase e.g. $SiO_2$. Though not discussed in this thesis, it is worth noting that there exist other rutile shaped compounds such as $FeSbO_4$ and $Ti_2N$. In the latter the positions of the cation and ligand anions are transposed, technically making it an anti-rutile. Compounds containing larger metal ions that have a different radius ratio (> 0.732) prefer to adopt the fluorite ($CaF_2$) structure [45].

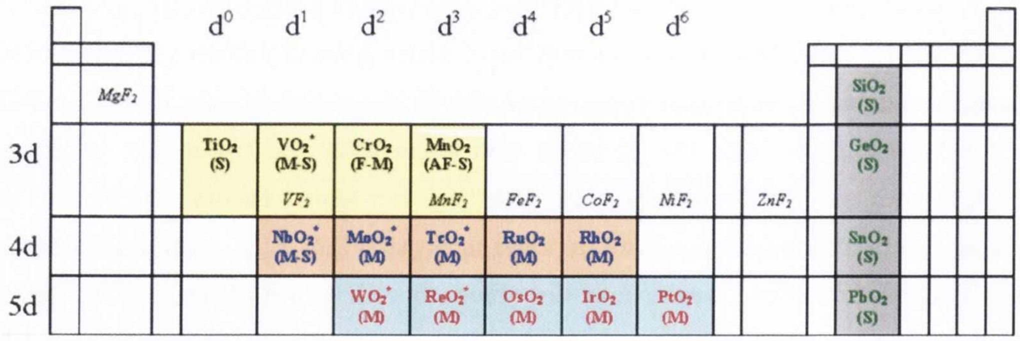

Figure 3.1: Periodic table of rutile and rutile-like oxides and fluorides. The oxides have added annotation in parentheses: where M is metallic, S is semiconductor, F is ferromagnetic and AF is an antiferromagnet. Starred compounds are compounds that are in a distorted rutile, or monoclinic phase at room temperature.

The rutile structure is described by two parameters: the axial ratio $c/a$ and the position parameter of the anion $\mu$. The lattice is tetragonal, as that of a cubic lattice stretched

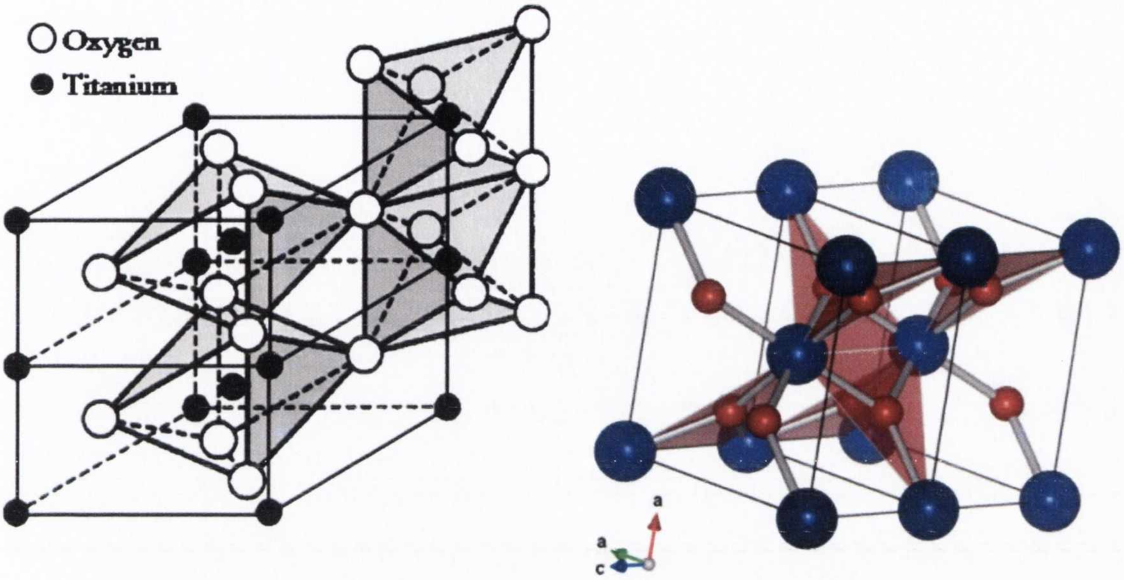

(a) Edge-sharing octahedra. (b) Trigonal planes.

Figure 3.2: (a)Adjacent edge-sharing octahedra in a typical rutile structure from Sorantin and Schwarz [44]. (b)Two unit cells of rutile $CrO_2$ contiguous along the $c$-axis. Alternating orientations of trigonal planes, all $\| c$, highlighted.

along one of its lattice vectors. Thus it possesses two equivalent $a$-axes and one inequivalent $c$-axis. Its unit cell contains two formula units and is described by the nonsymmorphic $P4_2/mnm$ space group, which is the simplest and most common type for $MA_2$ structures with octahedral coordination [42]. The atomic site positions for the cations and anions are $(0,0,0)(\frac{1}{2},\frac{1}{2},\frac{1}{2})$ and $(1 \pm u, 1 \pm u, 0)(\frac{1}{2} \pm u, \frac{1}{2} \pm u, \frac{1}{2})$ respectively with a value of 0.3 for the internal parameter $u$. Though the metal ions are octahedrally coordinated, they possess a tetragonal distortion resulting in the two apical M–A bond lengths being slightly different with respect to the four equatorial bonds. Among the heterocationic rutile structures studied in this work, the octahedral distortions primarily occur due to second order Jahn-Teller effects, where the apical bond lengths are slightly longer than the equatorial [46]. An exception being $RuO_2$ where the bond lengths are shorter [47]. It should also be noted that in general the octahedron has a rectangular cross-section at its equator due to tetragonal distortion and thus the site pointgroup symmetry of the metal cation is $D_{2h}$.

The octahedra share edges along the $c$-axis at their equator, forming alternating chains parallel to the principal rutile [001] axis or $c$-axis, where half of these chains are transformed with respect to the other half by a 90° rotation around the crystal $c$-axis, as seen in Figure 3.2a. It can also be seen from this figure that the two metal positions at the centre and corner of the unit cell are equivalent, once the surrounding octahedra are properly rotated.

The ligand anions are coordinated by three metal cations in a flat triangular or trigonal plane. Two of the triangle's angles are equivalent, while the third which is bisected by the apical bond mentioned above is different due to the tetragonal distortion, and thus a pointgroup symmetry of $C_{2v}$. These planes all lie parallel to the crystal *c*-axis, but as with the octahedra, half are transformed by a 90° rotation about the *c*-axis and a half a unit cell displacement in the [001] direction. This is shown for rutile $CrO_2$ in Figure 3.2b.

It is these $M_3A$ trigonal planes, rather than the $MA_6$ octahedra, that much of the discussion of this thesis will focus upon for a number of reasons: (i) it greatly simplifies the discussion of polarisation dependence and natural linear dichroism; (ii) the majority of the spectroscopic measurements presented in this thesis probe the PDOS of the valence and conduction bands of the ligand anions, so it is appropriate that the discussion relate from the perspective of the anion. The exception being in Chapter 8 where the metal *L*-edge PDOS is probed for two structural phases of $TiO_2$, rutile and anatase. This is not to say that the metal valence (*d*) orbitals and electronic structure will be ignored, on the contrary they hybridise significantly in bonding with the anion orbitals and are indispensable in any analysis or discussion.

### 3.2.1 Bonding

$MA_2$ compounds formed between elements of differing electronegative values, such as the dioxides and difluorides described in this thesis, as well as other dihalides and disulphides, can be described in the first instance by an ionic bonding model. This provides an approximate prediction of the resulting crystal structure, where the ligand anions form a regular octahedron around the metal cation, while the anions are surrounded by a triangle of metal cations forming a plane in which the anion also lies. The crystal structure of many transition metal dioxides are closely related to this rutile model structure. Previously, rutile being a common structure for dioxides and difluorides, led to this formation being treated purely by a simple ionic model [31], with some of the distortions of the structure being traditionally viewed using crystal field theory (CFT) [48]. This model however has come under scrutiny over the years as it does not adequately describe the physical parameters of the crystal. Developments over the past 40 years of solid state science and in particular molecular orbital (MO) theory have led to a much more accurate picture in the literature. Some degree of covalent bonding must be included to explain the observed real M–A bonding distances [41], and also the tetragonal distortion of the $MO_6$ octahedra [42]. That the bond lengths predicted by the ionic model were somewhat longer than the observed also indicates a degree of covalent bonding in the system.

Such a $M_3A$ planar geometry as described in the previous section, in (for example) oxygen or fluorine anions, calls for $sp^2$ hybridisation of the central anion. Before delving

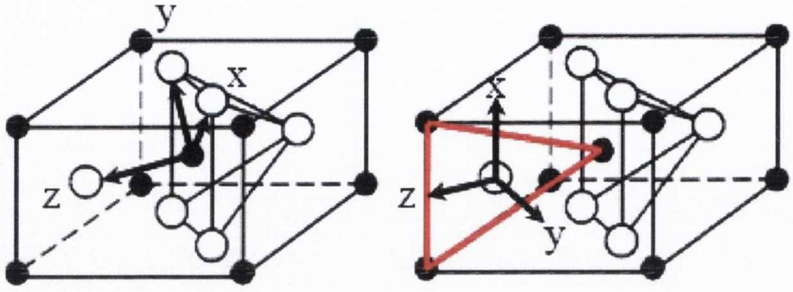

(a) Local cation coordination.

(b) Local anion coordination.

Figure 3.3: Defining the natural coordinate systems in a rutile geometry for (a) the cation and (b) the anion, adapted from Sorantin and Schwarz [44].

into the atomic and molecular orbitals involved and created respectively in bonding, it is necessary to describe the coordinate system of both anion and cation individually. The metal atoms in rutile structures form a body centred tetragonal lattice in the unit cell, thus it is convenient to follow Kunes *et al.* [49] when defining their local axis coordinate system. Figure 3.3a shows the local coordination of the metal cations, where the $z$-axis is along the apex of the octahedron while the local $x$ and $y$-axes point towards the equatorial anions. These assigned directions of the orthogonal $x$ and $y$ axes are only approximate due of the tetragonal distortion of the metal octahedra in rutile compounds, giving the equatorial base a rectangular shape. Figure 3.3b shows the local coordination of the anion. Here the local $z$-axis is collinear with the metal $z$-axis, pointing along the apex of the octahedron, while the anion $x$ and $y$-axes are effectively rotated by 45° with respect to their counterparts on the cation, the $x$-axis now being parallel to the crystal $c$-axis while the non-$sp^2$-hybridised $y$-axis orbital $p_y$ orbital lies perpendicular to the local $M_3A$ trigonal plane.

### 3.2.2 Electronic Structure

The $sp^2$ hybridisation occurs where the $2p_x$ and $2p_z$ orbitals hybridise with the $2s$ orbital creating three equivalent O $2sp^2$ orbitals in a plane, collectively denoted $p_{x,z}$. The $2p_y$ orbital lobes protrude perpendicular to this plane, and thus perpendicular to the $c$-axis. In a transition metal rutile compound, the cation orbitals primarily involved in bonding are the valence $d$-orbitals, of which there are 5. In an octahedral crystal field they are not all degenerate, rather two have lobes pointing towards the ligand anions and occupy a different energy level from the other three that straddle them. Conventional chemical nomenclature designates these the $e_g$ and $t_{2g}$ orbitals respectively as seen in Figure 3.4 with respect to the metal coordination axes. Figure 3.4 also shows the metal $d$ orbitals with respect to the

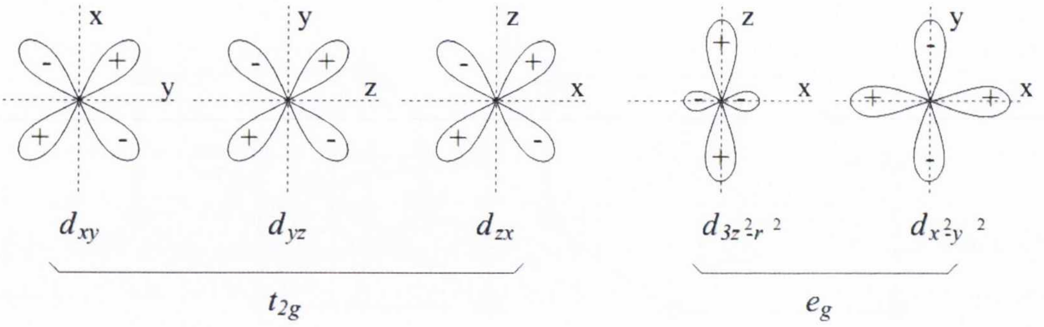

Figure 3.4: $d$ orbital shapes and orientation divided into two degenerate states by the octahedral crystal field: $t_{2g}$ and $e_g$.

cation coordinate system. In the metal octahedron, the $d_{z^2}$ lobes point along the apex, while the other $e_g$ orbital $d_{x^2-y^2}$, has lobes pointing to each of the equatorial ligand anions. The anion's $2p_z$ orbital thus overlaps with the metal $d_{z^2}$ creating a $\sigma$-type bonding arrangement, while the other two anion $2sp^2$ orbitals form $\sigma$ overlap the metal $d_{x^2-y^2}$ also with $\sigma$-type hybridisation. The metal $t_{2g}$ orbitals are not left out of the bonding arrangement. The lobes of the $d_{xz}$ and $d_{yz}$ orbitals straddle either side of an anion and will interact in a $\pi$-like fashion with the anion's $2p_y$ orbital. It is more convenient to recast these as two orthogonal orbitals $d_{z(y+x)}$ and $d_{z(y-x)}$, of which the latter is co-planer with the anion $2p_y$ orbital, as will be explained further on in this section.

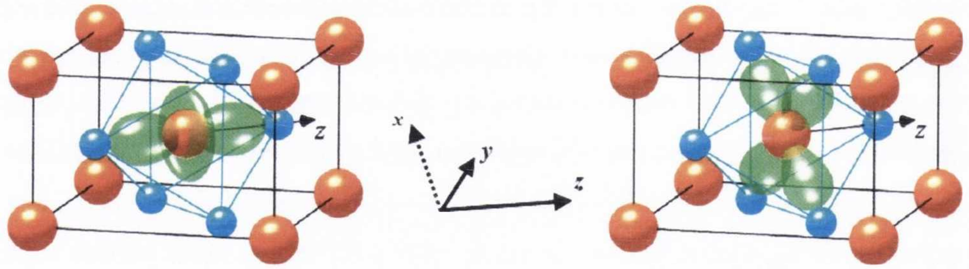

(a) $d_{z^2}$

(c) $d_{x^2-y^2}$

Figure 3.5: 3D visualisation of $e_g$ orbitals (a) $d_{z^2}$ and (c) $d_{x^2-y^2}$

Rutile and distorted rutile structures tend to be weak-field or high-spin complexes, where the ligand field splitting energy $\Delta_0$ between the nonbonding $t_{2g}$ and antibonding $e_g$ orbitals tends to be small. Due to the tetragonal distortion of the octahedron, metal valence orbitals do not strictly experience an octahedral ($O_h$) crystal field. Rather, using this local coordinate choice of orbitals, the degeneracy for the $t_{2g}$ orbitals is lifted. Thus the $d_{xy}$ states will differ in energy from the $d_{xz}$ and $d_{yz}$, which are isomeric within the unit cell. The $d_{xy}$ specifically is different as it has lobes parallel to the shorter rutile $c$-axis, characterised by

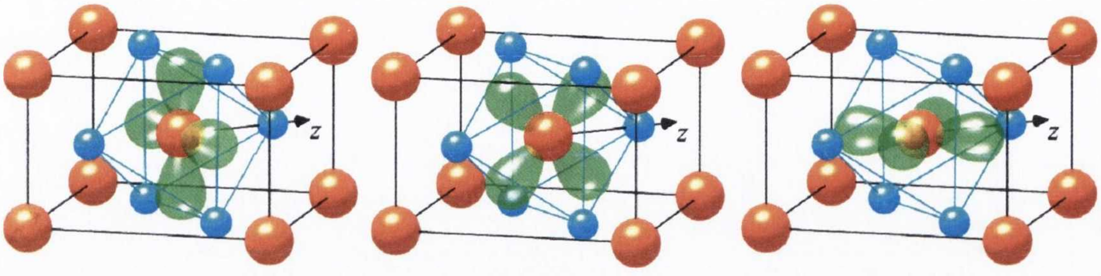

(d) $d_{xy}$ (e) $d_{z(y+x)}$ (f) $d_{z(y-x)}$

Figure 3.5: continuation of 3D visualisation, this time for $t_{2g}$ orbitals (d) $d_{z^2}$ and the alternatively designated remaining (e) $d_{z(y+x)}$ and (f) $d_{z(y-x)}$. Adapted from Eyert *et al.* [50]

the M–M distance along the octahedral chains, and the $d_{xy}$ orbital can play a role in metal-metal $\sigma$ MM$\sigma$ bonding along this axis. None of the rutile monoclinic compounds presented in this work can be described as purely octahedral $O_h$. Instead they possess $D_{4h}$ symmetry as a result of the tetragonal distortion; this reduction of symmetry and hence partial lifting of degeneracy in the orbitals technically means a more specific labelling is used. Table 3.1 shows the splitting of orbital degeneracies for $O_h$ versus $D_{4h}$ symmetry.

| $d$ | $O_h$ | $D_{4h}$ |
|---|---|---|
| $d_{xy}$ | $t_{2g}$ | $b_{2g}$ |
| $d_{xz}$ | | $e_g$ |
| $d_{yz}$ | | |
| $d_{z^2}$ | $e_g$ | $a_{1g}$ |
| $d_{x^2-y^2}$ | | $b_{1g}$ |

Table 3.1: Splitting of natural coordination $d$ orbital degeneracies in octahedral symmetry versus tetragonal-distorted octahedron.

In fact $D_{4h}$ is also approximate in some instances as the differing A–A distances along the equator of the octahedron further split the $d_{xz}$ and $d_{yz}$ orbitals, while mixing the $d_{z^2}$ and $d_{x^2-y^2}$ orbitals.

However the octahedral field splitting fits approximately for all the rutile and rutile-like compounds in this thesis. Thus except where necessary, the $t_{2g}$ and $e_g$ labels will be used to describe all metal $d$ coordination compounds with near octahedral symmetry. The interaction along the $c$-axis due in part to the $d_{xy}$ orbital can become important in the electronic properties of the compound. Sometimes strong MM$\sigma$ bonding can occur leading to a dimerisation of the metal atoms and the adoption of a monoclinic distorted rutile structure, as will be discussed later in this chapter. Further, the remaining $t_{2g}$ orbitals, lying in the local metal $xz$ and $yz$ planes respectively, are insufficiently differentiated in the $\pi$-hybridising component of the $t_{2g}$ orbitals with the anion $p_y$, and so an alternate designation for the remaining $t_{2g}$ orbitals can be more instructive. Eyert *et al.* [50–52] circumvented this issue by redefining the local metal coordination, rotating the axes 45° about the local $z$-axis. This rotated orthogonal basis changed the designation of most of the orbitals, transposing the $d_{xy}$ with the $d_{x^2-y^2}$ and thus the respective $t_{2g}$ and $e_g$ designations, although the disadvantage of this is that the "$t_{2g}$" orbital is then involved in $sp^2\sigma$ bonding with the anions, and the "$e_g$" orbital in MM$\sigma$ bonding along the $c$-axis. However an advantage was gained in that their $d_{xz}$ and $d_{yz}$ (in the rotated basis) were no longer degenerate, whereas in the natural coordinate frame defined in Figure 3.4 the $d_{xz}$ and $d_{yz}$ are mirror-isomers, and thus have an equal distribution of states. Another way to achieve the same effect as Eyert, yet maintain the naturally defined octahedral field metal cation coordination, is to redefine the $d_{xz}$ and $d_{yz}$ (in their natural basis) with a $y + x$ axis being parallel to $c$ and a $y - x$ axis being perpendicular, producing $d_{z(y+x)}$ and $d_{z(y-x)}$ $t_{2g}$ orbitals instead, as was shown by Sorantin *et al.* [44] This allows a more detailed explanation of bonding, and easier interpretation as to their hybridisation with the anion valence orbitals.

This same natural coordinate geometry, but with redefined $t_{2g}$ orbital positions, is shown in Figure 3.5, which is adapted and altered from Eyert *et al.* [50] As illustrated, $d_{z(y+x)}$ lies in the $\langle 001\rangle$ and $\langle 011\rangle$ directions, while the $d_{z(y-x)}$ is parallel to the $a$-$a$ or (001) basal plane which also contains the oxygen $p_y$ orbital axes, but with lobes in the $\langle 001\rangle$ directions.

## 3.3 Distorted Rutile Structure

As indicated earlier by Figure 3.1, some of the transition metal $MA_2$ compounds instead crystallise in a distorted rutile, or monoclinic motif. Some examples of compounds that form this distorted rutile structure are $WO_2$, $MoO_2$ and at room temperature: $NbO_2$ and $VO_2$. In the monoclinic structure the rutile crystal $c$-axis is redesignated as the $a$-axis, and will be referred to as such henceforth, except when it is referred to as the rutile $c$ equivalent, or $c_r$-axis for the sake of comparison. The formerly equivalent rutile $a$-axes now become the inequivalent monoclinic $b$ and $c$ axes.

These monoclinic distorted rutiles are very similar in structure to the undistorted structures. The distortion into monoclinic arises from metal-metal interactions along the $a$-axis ($c_r$-axis) which leads to a dimerisation of the metal atoms, with alternately shorter and longer metal–metal distances and a slight alternating displacement or kink from the $a$-axis. The metal cations are no longer equidistant along this axis, as they have effectively paired, the unit cell is doubled in size, becoming four formula units instead of two. The kink results from a skewing of the $c_r$-axis such that it's no longer at 90° with respect to one of the rutile $a$-axis. This $\beta$ angle tends to be very similar between the distorted rutiles; 120.95°

for $MoO_2$, 122.61° for room temperature $VO_2$, 120.47° for $WO_2$ etc. The space group for these structures is now designated $P2_1/c$.

Metal–metal bonds form along the monoclinic $a$-axis when the $d$–orbital occupation of the metal cation is $d^1$, $d^2$ or $d^3$ (but not $d^4$) [53]. Further, it should be noted that due to the dimerisation of the M atoms along the $a$-axis in distorted rutile compounds, two differing anion sites arise, which in the case of an oxide, are denoted O1 and O2. O1 is usually assigned as the oxygen site at the centre of a scalene triangular plane with the shorter of the M–M distances along the $a$-axis forming one side of the triangle. The O2 site is then at the centre of a triangle having the longer of the two M–M distances along the monoclinic $a$-axis as one of its sides. Examples of this phenomenon in the structure of $WO_2$ and $MoO_2$ highlighting the differing oxygen sites are illustrated in Chapter 6.[†]

### 3.3.1 Electronic Structure

A qualitative band model describing the interactions between the metal-metal bonds along the $c$-axis was introduced by Goodenough [34] and provided a simple explanation of the non-metallic behaviour found for the distorted variants of $VO_2$ and $NbO_2$, as well as the metallic behaviour of $MoO_2$ and $WO_2$. Even in a perfect undistorted rutile-like system, the $MA_6$ octahedra have local $D_{2h}$ rather than $O_h$ symmetry. In distorted rutile structures this symmetry is further reduced to $C_{2v}$. Consequently the nominal $t_{2g}$ orbitals are even further distinguished. As before, it is useful to distinguish the single orbital which lies in the plane described by the shared edges of the octahedral plane, denoted $d_{xy}$ in the natural coordinate geometry. Goodenough referred to this as $t_{\|}$ and in other literature it is often designated $d_{\|}$. The remaining two $t_{2g}$ orbitals are usually referred to collectively as $t_{\perp}$ or $d_{\perp}$. The metallic M–M bonding arises from a $\sigma$-like overlap of $d_{xy}$ ($d_{\|}$) orbitals along the monoclinic $a$-axis giving rise to bonding and antibonding M–M $d_{\|}(\sigma)$ and $d_{\|}(\sigma^*)$ states. The remaining $t_{2g}$ orbitals interact via weaker $\pi$-like and $\delta$-like overlap. In distorted $d^1$ systems such as room temperature $VO_2$ and $NbO_2$. The valence $t_{2g}$ $d_{xy}$ ($d_{\|}$) orbital contributing to M–M $\sigma$ bonding along the monoclinic $a$-axis is completely filled, while the remaining $t_{2g}$ bands remain empty. Thus these compounds do not exhibit metallic conductivity. However in the case of $d^2$ systems such as $MoO_2$ and $WO_2$ (see Chapter 6) the extra electron per cation partially fills the higher $t_{2g}$ bands and thus are metallically conducting with the Fermi level in these overlapping bands. It has been suggested recently that the structural distortion in these compounds may be regarded as a Peierls type instability [52,54].

---

[†] Figures 6.2 and 6.4 from page 119.

## 3.4 Electronic Structure Calculations

As our X-ray spectroscopic techniques, X-ray absorption spectroscopy (XAS) and X-ray emission spectroscopy (XES), especially at the anion $K$-edge, are probes of the anion $2p$ PDOS it is very useful to compare our experimental results with the results of electronic structure calculations. This section very briefly describes some of the methods used to obtain both the density of states (DOS) and PDOS of our rutile and rutile-like compounds and also the further steps necessary to simulate anion $K$-edge resonant X-ray emission spectroscopy (RXES) spectra. The focus is on DFT methods, principally the full-potential linearised augmented planewave (FP-LAPW) technique and specifically that implemented within the WIEN2K code.

### 3.4.1 Electronic Structure Methods

It is a straight forward matter to write the Hamiltonian of a crystal:

$$H\psi = (\frac{\hbar^2}{2m}\nabla^2 + V)\psi = E\psi \tag{3.1}$$

Here $\psi$ is the wavefunction for all particles and $V$ is the Coulomb potential between all the particles. To solve this equation however is not so straight forward, given that one molar unit of a crystal has $\sim 10^{24}$ particles. Thus it becomes essential to make approximations. The Born-Oppenheimer approximation takes some pioneering steps here by neglecting the nuclear kinetic energy such that the nuclei remain static at the lattice positions. This principally leaves only the Hamiltonian for the electrons. This method's success was due to the high ratio between nuclear and electronic masses and is valid in a large number of cases, however it's unsurprising that it fails when nuclear motion becomes important, for example in modes of vibrational coupling or when there are large distortions in a molecule. The Born-Oppenheimer approximation pre-dates DFT by approximately 40 years and was a foundation for other electronic structure calculations such as the Hartree-Fock method.

Modern band structure calculations are based upon DFT, which use the Hohenberg-Kohn theorems introduced in 1964, [55] and of which there are two. One states that the external potential is a unique function of the ground state electron density of a many-electron system that is in the presence of that external potential. The second states that the ground state energy is minimised by the ground state electron density, i.e. the density that minimises the total energy is the ground state density. These theorems were further improved by Kohn and Sham in 1965 [56]. All bandstructure and DOS calculations presented in this thesis were calculated using WIEN2K software package created by Peter Blaha *et al.* [57] This utilises the density functional theory, specifically the FP-LAPW method. The concept behind this will only briefly be covered here, a comprehensive introduction to this approach is given by Cottenier [58].

The FP-LAPW method, like most of DFT methods is a procedure for solving the Kohn-Sham equations for the ground state of compound, in this case a crystal with periodic boundary conditions. It does this by introducing a basis set which is specifically adapted for this problem. The adaptation divides the unit cell into two parts: atomic spheres that don't overlap and an interstitial region. In each of these a different basis set is used. Inside the atomic sphere a linear combination of radial functions times spherical harmonics is used, while in the interstitial region a plane wave expansion is utilised [57]. The bandstructure or DOS of the crystal is obtained from sampling the Brillouin zone by an appropriate mesh of $k$-points.

### 3.4.2 Simulating X-Ray Spectra, NXES and RXES

Local unoccupied PDOS calculated for the conduction band by the above method are often directly compared with XAS, particularly O $K$-edge XAS. It should not be forgotten that these calculations show the initial state of the system, while XAS is a direct measurement of a final state (or intermediate state of the RXES process). Thus proper account should be taken for the final state rule [59] and excitonic effects when comparing with experimental results. Nevertheless comparisons can be very instructive. As will be presented in later chapters, O $K$-edge XAS measured with linearly polarised light aligned along one axis can show excellent agreement with calculated O $2p$ PDOS projected along this same axis.[†] In practice a direct comparison between calculated and experimentally acquired conduction band (CB) PDOS is insufficient due to lifetime and instrumental broadening effects on the latter. A more meaningful spectral simulation can be achieved by taking into account the core-hole lifetime broadening Lorentzian, the excited state lifetime broadening, and the instrumental resolution by convoluting the calculation with a Gaussian. Excitonic effects are of greater importance where the core hole cannot be effectively screened, or the mobility of the excited conduction band electron is impaired and it is highly localised. Experimentally measured normal XES (NXES) and RXES are compared with the calculated occupied partial DOS projected across selected planes, after core-hole and instrumental broadening is applied to simulate these spectra. The exact projections used to simulate specific spectra are detailed in the chapters where they are compared, but a generalised overview will be given here.

First recall from Chapter 2 that in RXES the $k$-points selected in the unoccupied bandstructure during absorption determines the $k$-points directly below them that will contribute to emission (neglecting the momentum transfer of the photon). This being due to the crystal momentum selectivity, or $k$-selectivity of the resonant emission process. Thus for a given excitation energy a bandwidth is defined that, depending on the energy, will determine the parts of the Brillouin zone selected in the conduction band and thus determine the $k$-points of all bands in fluorescence. Additionally RXES displays polarisation and state selectivity. The projection of the linearly polarised light onto the real-space crystal axes effectively determines the level of absorption for unoccupied bands at that energy and whose component is parallel to the **E** vector. Thus the proportion of excitation at a particular energy-selected $k$-point can be determined. Subsequent emission from those $k$-points in the occupied bands is weighted by these factors.

---

[†] A particularly good example is presented in Figure 4.6 for $IrO_2$, page 56.

In normal XES this is no longer relevant as the emission recorded reflects equal contribution from the full range of crystal momentum in the valence band and is no-longer either polarisation-dependent or $k$-selective. More important in creating a simulated NXES spectrum is the orientation of the emission spectrometer with respect to the crystal axis. The transition from an excited state to the $1s$ core hole being filled by a valence electron results in dipole emission can propagate in only certain directions. The spectrometer selects only a small solid angle of this emission and for all experimental data shown here, is mounted at 90° to the incident X-ray propagation. Therefore the calculation must be a real space projection of the occupied $2p$ PDOS (for $K$-edge emission) in a plane perpendicular to the propagation vector of the emitted photons. In the resonant RXES case this orthogonal plane projection is applied in conjunction with the weightings assigned to the selected $k$-points, and these weighted PDOS are then used to simulate the RXES spectra with the appropriate transition matrix element between the core-hole and the valence electron.

Finally in a similar fashion to the more meaningful approach of broadening the unoccupied PDOS for direct comparison with XAS spectra, the simulated spectra are broadened by convolution with a Gaussian–Lorentzian combination (Voigt). The width is determined by the instrumental broadening, core-hole lifetime broadening, as well as the valence hole lifetime broadening.

## 3.5 Summary

The adoption of the rutile-like structure for $MA_2$ compounds strikes a balance between ionic and covalent bonding. The spatial arrangement $\sigma$ and $\pi$ hybridisation that occurs in this structure as a result of the latter gives rise to an orbital anisotropy. This anisotropic charge distribution around the anion gives rise to an expectation of natural linear dichroism at the anion $K$-edge. Combined with the selection rules of the X-ray absorption and emission techniques outlined in Chapter 2, this allows the weighted anion $2p$ PDOS projections along individual axes to be measured independently in a $k$-, state-, symmetry-, and geometry-selective manner.

The implementation of the FP-LAPW method of DFT, via WIEN2K, allows a realistic account of the electronic structure, providing projected PDOS from which experimental spectra can be simulated. Thus giving a strongly supported account of the observed features, most notably the polarisation dependent natural linear dichroism.

# 4 $IrO_2$ and $MnO_2$

## 4.1 Introduction

Manganese(IV) oxide and iridium(IV) oxide are both tetragonal structures that crystallise in a pure rutile motif. $IrO_2$ has a $d^5$ metal occupation while $MnO_2$ has $d^3$. Both have applications in industrial electrolysis [60].

The study outlined in the following chapter details the polarisation dependent X-ray spectroscopy of these similar compounds, with the end goal being to probe in detail their electronic structure by utilising the bulk crystals' inherent natural linear dichroism. This is the first reported account of the natural linear dichroism in the O $K$-edge XAS, and subsequent X-ray emission for both $MnO_2$ and $IrO_2$. Sections 4.2 and 4.3 discuss the physical and electronic structure of $IrO_2$ and $MnO_2$ respectively, giving a detailed review of earlier investigations where relevant. Section 4.4 describes the experimental set-up for the polarisation dependent X-ray absorption spectroscopy (XAS) and resonant X-ray emission spectroscopy (RXES) measurements. Section 4.5 presents and discusses in detail the results of the spectroscopic experiments, showing the occupation of specific states isolated by subtracting various resonant and non-resonant emission spectra from each other.

Iridium dioxide is a rare transition metal oxide and the only well characterised oxide of iridium. Like $MnO_2$ it belongs to a family of binary transition metal compounds with stoichiometry $MA_2$, where the anion A is usually either oxygen or fluorine, that possesses the $TiO_2$ rutile crystal structure, with two formula units contained in the unit cell. This structure has in the past elicited a lot of interest due to its electrical [61], magnetic [62] and electrochemical [63] properties. $IrO_2$, along with other rare oxides, has a number of modern applications including the coating of anode-electrodes in industrial electrolysis, and once elicited interest for data storage applications [64]. $IrO_2$ nanorods in particular have been found to be extremely good conductors [65], and more recently have exhibited useful photocatalytic activity [66]. A review of their synthesis and uses is given by Chen *et al.* [67]

While much applied research has been done on the electronic structure of bulk IrO2 crystals or films, surfaces, and interfaces [65,68–71] there has also been a variety of electronic structure calculations [37,72–74]. To date however, no experimental measurements have intensively probed the electronic structure in detail, at least not through the combination of both oxygen $K$-edge XAS and RXES as is presented here.

$MnO_2$ is of large technological importance, used widely in the production of dry-cell batteries. Within its wider family of manganese oxides, it has promising potential for chemical applications such as adsorbents, catalysts and sensors [75]. $MnO_2$ is also the only $d^3$ metal cation compound studied in this work and, as will be demonstrated, demonstrates unique results, namely the exchange splitting due to the spin orbit interaction. It has been studied by some semi-related X-ray methods: X-ray photoemission spectroscopy (XPS) [76], resonant photoemission spectroscopy [77], X-ray magnetic scattering and, in its natural crystal form, XAS [78,79]. The crystal compound possesses a screw type magnetic structure that has been at the core of much recent research activity into this crystal [80–84]. To date no X-ray emission spectroscopic studies have been published on bulk $\beta$-$MnO_2$. This is the first such account, and also the first account of the inherent natural linear dichroism possessed by this compound at the O $K$-edge.

## 4.2 Physical and Electronic Structure of $IrO_2$

In common with the other rutile transition metal oxides, $IrO_2$ adopts a tetragonal $P4_2/mnm$ spacegroup with $a = 4.5051$ Å, $c = 3.1586$ Å [43]. The structure contains edge-sharing octahedrally coordinated metal cations as well as trigonally coordinated oxygen anions. The shared edges of the $IrO_6$ octahedra form chains along the [001] direction that are cross linked by shared corners, so each chain is connected to four neighbouring chains. These octahedra do not exhibit equal Ir-O bond distances but as in other rutiles, display tetragonal distortion and as such are apically elongated [43]. For the purposes of the polarisation dependent study presented in this chapter, and indeed this wider project as a whole, it is far more instructive to view the structure from the perspective of the $Ir_3O$ trigonal planes as seen in Figure 4.1. The physical structure of rutile compounds, as well as the electron orbital coordinate frames used in this thesis are detailed in Chapter 3. To recapitulate briefly, such planar geometry calls for $sp^2$ hybridisation of the central anion, in this case oxygen, where the O $2p_x$ and O $2p_z$ orbitals hybridise with the O $2s$ orbital creating three equivalent O $2sp^2$ orbitals ideally lying 120° from each other in an isosceles plane. In this instance the triangular plane is scalene, forming Ir–O–Ir angles of 104.4° and 127.8° [43]. These oxygen $sp^2$ orbitals form $\sigma$ bonds with their occupied Ir $5d$ $e_g$ counterparts. In rutile compounds these $Ir_3O$ planes occupy two orthogonal orientations, [110] and [$1\bar{1}0$] (or collectively $\langle 110 \rangle$ and both sets of planes lie parallel to the $c$-axis. The remaining O $2p_y$ orbital lies perpendicular to each $Ir_3O$ plane, and thus is also perpendicular to the $c$-axis. Ir(IV) is a $5d^5$ metal cation and thus possesses an empty $t_{2g}$ orbital which mixes or hybridises with the O $2p_y$ orbital giving

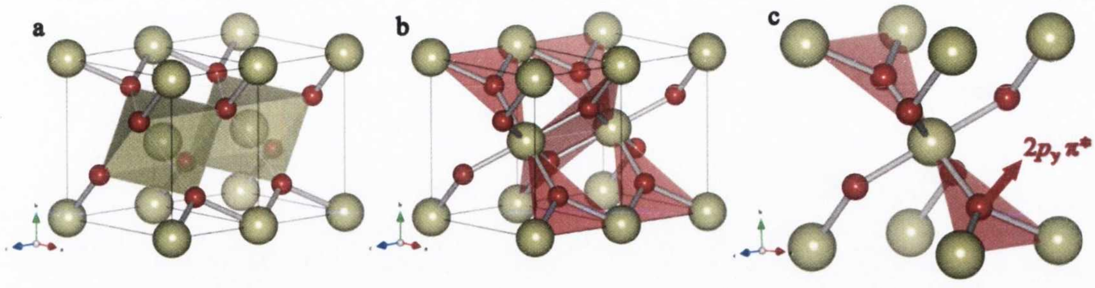

Figure 4.1: Rutile tetragonal $IrO_2$ crystal structure. Oxygen atoms in red, iridium in yellow. **a)** Two unit cells of $IrO_2$ showing the $c$-axis and the central metal cation in its octahedral coordination. **b)** Two unit cells of $IrO_2$, illustrating the alternating orthogonal arrangement of the $Ir_3O$ trigonal planes parallel to the $c$-axis. **c)** One unit-cell highlighting $2p_y$ orbital which hybridises in a $\pi$-like configuration with metal $t_{2g}$, shown perpendicular to the $Ir_3O$ $sp^2$ hybridised trigonal plane.

$\pi$-like molecular orbitals (MOs) which are partially occupied and gives rise to a metallic nature in $IrO_2$.

### 4.2.1 Electronic Structure Calculations

For comparison with the experimentally measured oxygen $K$-edge RXES and XAS spectra, the electronic structure of $IrO_2$ was calculated via density functional theory (DFT), specifically the full-potential linearised augmented planewave (FP-LAPW) method as implemented in the WIEN2K code [57]. This calculation follows the scheme described in the earlier calculation of the electronic structure of $IrO_2$ by de Almeida and Ahuja [73], The electronic structure was computed using the observed crystal structure (space group $P4_2/mnm$) with the experimentally determined lattice constants [43] of $a = 4.5051$ Å and $c = 3.1586$ Å used as initial inputs with the internal coordinate $u$ optimised in the calculation. The optimised internal coordinate $u$ was initially set to be $u = 0.3077$ in agreement with the observed $u$, a structural relaxation gives an internal coordinate of 0.30816, which is in close agreement with the observed value. The radius of the muffin tin spheres was 1.95, and 1.73 a.u. for Ir and O respectively. The standard settings of the code, except where noted, were employed and specifically the generalised gradient approximation (GGA) of Perdew *et al.* [85] was used. The calculation was iterated until the total energy difference of successive iterations converged to below $10^{-4}$ eV. The Brillouin zone was sampled with 3000 $\boldsymbol{k}$-points in order to obtain the density of states (DOS) and partial density of states (PDOS) results presented here which corresponded to a $12 \times 12 \times 18$ shifted $\boldsymbol{k}$-point grid generated according to the Monckhorst-Pack scheme.

Figure 4.1 presents a diagram of the crystal structure of $IrO_2$ emphasising the $IrO_6$ octahedra (Figure 4.1a) and the trigonal planar coordination of the O in $Ir_3O$ planes (Fig-

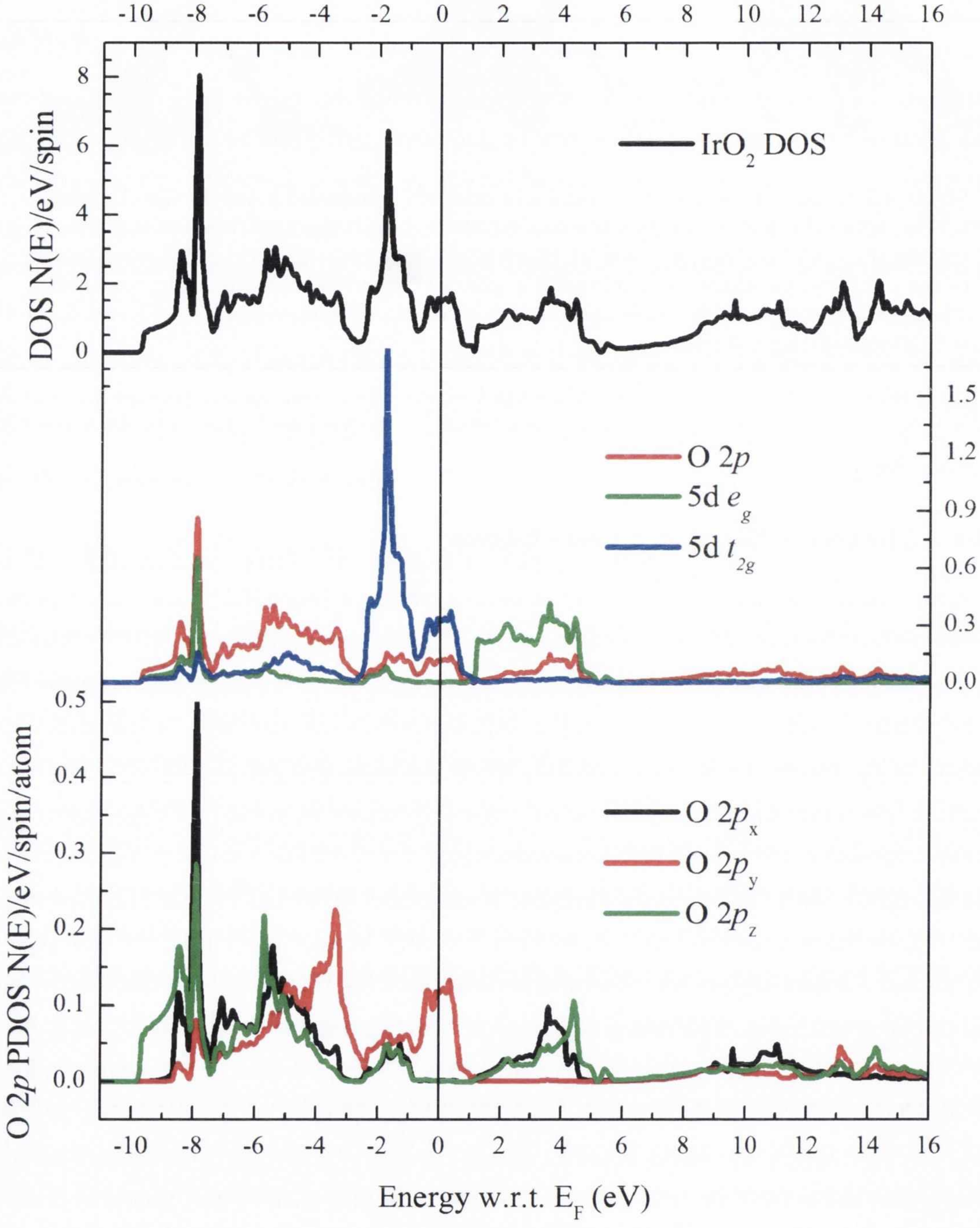

Figure 4.2: Electronic structure DFT DOS calculations for $IrO_2$ in the VB and CB, calculated by the FP-LAPW method. **a)** Total $IrO_2$ DOS. **b)** Component PDOS separated for O 2p, and the $t_{2g}$ and $e_g$ components of the Ir $5d$ states resulting from crystal field splitting. **c)** The orthogonal O$2p_x$, $2p_y$, $2p_z$ component PDOS for the natural coordination axes of the trigonally coordinated oxygen anion.

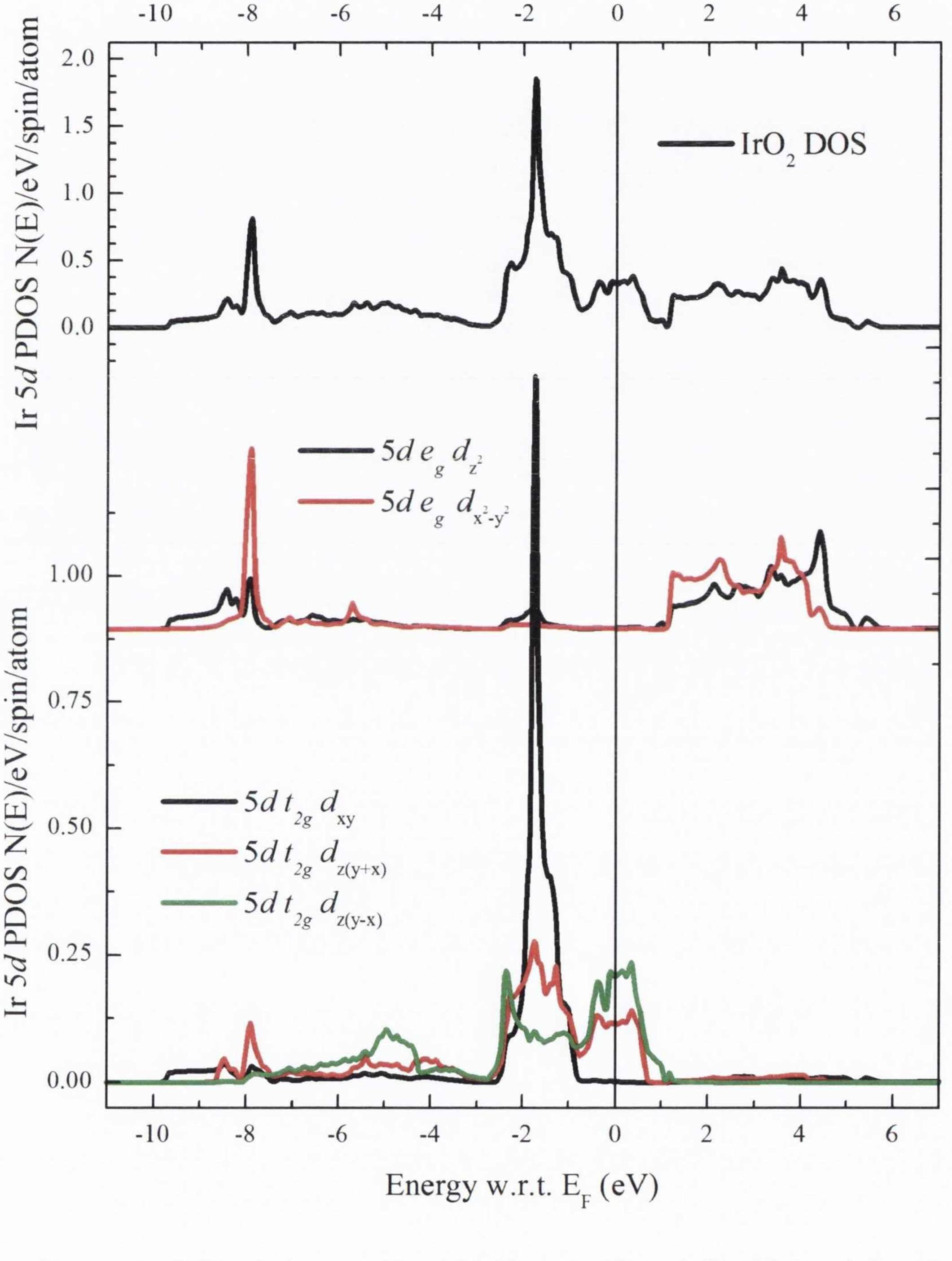

Figure 4.3: DFT calculations of Ir $5d$ PDOS in the VB and CB of $IrO_2$. **a)** Total Ir $5d$ PDOS. **b)** $e_g$ component states of Ir $5d$, $d_{z^2}$ and $d_{x^2-y^2}$. **c)** $t_{2g}$ component states of Ir $5d$, tetragonal distortion lifts degeneracy. $d_{z(y-x)}$ orbital in particular lies in the (001) plane, exhibiting significant $\pi$-like hybridisation with O $p_y$ (Figure 4.2c) in the region around $E_F$

ure4.1b). The local coordinate definitions on the O site and the Ir site is discussed in Chapter 3 but shall be outlined again here. In common with the discussion of Sorantin and Schwarz [44], the natural coordinate definition for the oxygen anion in the rutile tetragonal structure places the $z$-axis along the bond direction between the apical oxygen anion and the central Ir cation, with the $x$-axis being in the $Ir_3O$ plane, parallel to the [001] direction and the $y$-axis being perpendicular to the $Ir_3O$ plane, thus $p_y = p_\perp$.

The natural definition of axes for the metal cation share a common $z$-axis with the oxygen, but here the $x$ and $y$ axes are now defined in the waist plane of the octahedron, directed toward the neighbouring ligand oxygen anions [44,49]. Since every alternating oxygen (iridium) lattice site is at the centre of an $Ir_3O$ plane ($IrO_6$ octahedron) at 90° relative orientation to the other, and any spectroscopy records the response from all the lattice sites within the sampling volume, it is sensible when discussing the polarisation dependent oxygen $K$-edge XAS and RXES, to relate the orthogonal basis set to the crystal axes of the unit cell. As a result the projected oxygen $2p$ PDOS along the $c$-axis (O $2p_c$) is equivalent to the aforementioned O $2p_x$ while the projected oxygen $2p$ PDOS along the $a$-axis (O $2p_a$) is an equal mixture of the two O $2p_y$ and O $2p_z$ components. Figure 4.2(a) shows the total DOS of $IrO_2$, the O $2p$ PDOS is shown along side the Ir $5d$ $t_{2g}$ and $e_g$ PDOS in 4.2(b), and the angular momentum resolved components $2p_x$, $2p_y$, and $2p_z$ of the oxygen PDOS in the natural coordinate frame for the oxygen anion are given in the bottom, 4.2(c).

The tetragonal distortion of the $IrO_6$ octahedra lifts the degeneracy of the Ir $5d$ $t_{2g}$ orbital with that $t_{2g}$ $d_{xy}$ orbital located in the waist plane of the octahedron effectively lowest in energy; this orbital participates in Ir-Ir $\sigma$ M-M bonding along the $c$-axis. This gives a strong dispersionless band showing as a peak in the PDOS at $\sim$ 1.8 eV binding energy. The remaining two $t_{2g}$ orbitals, $d_{xz}$ and $d_{yz}$, are degenerate and have an equal distribution of their density of states; it is however more instructive to consider these as $d_{z(y+x)}$ and $d_{z(y-x)}$ [44] which are then $t_{2g}$ orbitals parallel to the O $xz$ plane and O $yz$ plane respectively.[†] The $d_{z(y-x)}$ $t_{2g}$ orbital participates in $\pi$-bonding with the O $p_y$ orbital, while the $d_{z(y+x)}$ also participates in M-O $\pi$ bonding, but with the equivalent O $p_y$ orbital on the four equatorial oxygen sites surrounding the Ir cation. It also participates in Ir-Ir $\pi$-bonding along the $c$-axis. Figure 4.3(a) shows the total Ir $5d$ PDOS, 4.3(b) gives the Ir $5d$ $e_g$ component PDOS $d_{z^2}$ and $d_{x^2-y^2}$; and the Ir $5d$ $t_{2g}$ component PDOS is in 4.3(c), decomposed as $d_{xy}$, $d_{z(y+x)}$ and $d_{z(y-x)}$. The M-O $\sigma$ bonding and hybridisation between the O $2p_z$ and Ir $5d$ $e_g$ $d_{z^2}$ forms the lowest occupied states of the valence band. The strong hybridisation between the O $2p_x$ (along the $c$-axis) and the Ir $5d$ $e_g$ $d_{x^2-y^2}$ shows the strong

---

[†] Bearing in mind the local oxygen orthogonal coordination axes are different to the metal, sharing only the $z$ direction.

M-O bonding giving rise to a dispersionless band at a binding energy of $\sim$ 8 eV. It is clearly seen that the $t_{2g}$ orbitals, $d_{z(y-x)}$ and $d_{z(y+x)}$, straddle the Fermi level giving $IrO_2$ its metallic character.

## 4.3 Physical and Electronic Structure of $MnO_2$

Several polymorphs of $MnO_2$ exist, but as with other members of the metal IV dioxides, $MnO_2$ crystallises in the tetragonal-rutile motif denoted $\beta$-$MnO_2$, also known as pyrolusite. Like $IrO_2$ it has the space group $P4_2/mnm$, but with $a$ = 4.3980 Å, $c$ = 2.8738 Å and $u$ = 0.3046 [43]. In the same fashion as $IrO_2$ it contains octahedrally coordinated metal cations and trigonally coordinated oxygen anions, the rutile structure is further elucidated in Chapter 3.

Like other rutile shaped transition metal dioxides, $MnO_2$ has a formal oxidation state of 4+, making the Mn a $d^3$ metal cation. According to Yoshimori [86], all the spins in $MnO_2$ are aligned parallel to the $c$-axis, but screw along the axis with a pitch of $\frac{7}{2}c$, rendering the magnetic unit-cell seven times larger along the $c$-axis than the chemical unit cell [87]. Rogers *et al.* and later Sato *et al.* demonstrated that the resistivity increases with decreasing temperature, becoming very large ($\approx 10^5\ \Omega\, cm$) at $T = 0$ K [32,80]. Zhuan and Halley [88] found the ground state of $MnO_2$ to be insulating, with a band-gap ranging between 0.1 and 1.0 eV; the size dependent on the parameters of their approach. Exchange splitting becomes an important factor in interpreting the absorption spectra for $d^3$ compounds, as ligand field splitting no longer accounts for all features observed. The effect of exchange splitting is to split the two energy levels, $t_{2g}$ and $e_g$, again into spin up and spin down. The spin up $t_{2g}$, occupying the lowest energy, is filled with the three electrons leaving the $e_g$ orbitals and spin down $t_{2g}$ empty. Figure 4.4 demonstrates that the exchange splitting (3.3 eV) is equivalent to the ligand-field splitting (3.0 eV). So instead of a 4 peak conduction-band structure as observed in other manganese oxides [89], rather a 3 peak structure is predicted.

A number of other electronic structure calculations are available for $\beta$-$MnO_2$m among them those by Franchini *et al.* [76], while valence band XPS spectra are also available. [77]

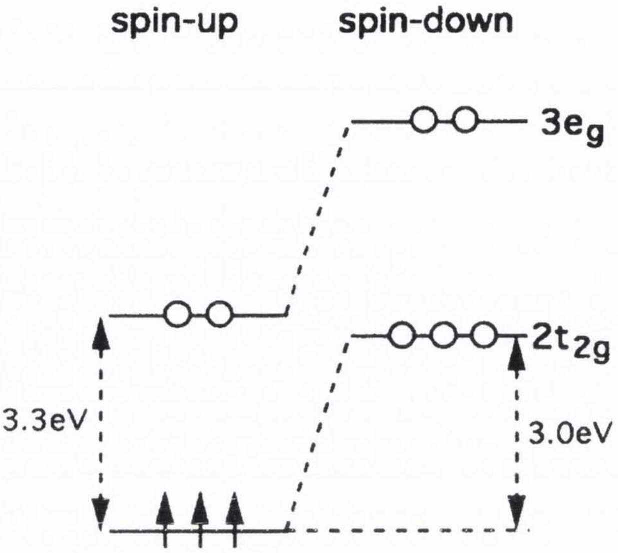

Figure 4.4: Partial molecular orbital diagram for manganese $d$ level splitting in $MnO_2$, note similar position of $t_{2g} \downarrow$ with $e_g \uparrow$ due to energetically similar crystal field and exchange splitting. Adapted from Kurata *et al.* [89]

## 4.4 Experimental Measurements

In this section the details of the samples, their growth, preparation, alignment, mounting and spectroscopy are set forth.

### 4.4.1 Sample Preparation

The bulk $IrO_2$ single crystal utilised for these experiments was a small platelet approximately 500 $\mu$m thick. It was provided by Y.S. Huang of the National Taiwan Institute of Technology in Taipei. It was grown using the open-flow chemical vapour transport technique, with flowing oxygen as a transport agent, with a pressure greater than one atmosphere in a quartz tube furnace. The starting materials were a mixture of polycrystalline $IrO_2$ and purified metal Ir powder. Further details of the crystal growth are described by Huang *et al.* [90] The $IrO_2$ platelet used had a (110) face, as confirmed by XRD, with the $c$-axis in the surface plane parallel to the long edge of the single crystal.

The $MnO_2$ crystal was supplied by Prof. Hirohiko Sato of Chuo University, Tokyo. It was prepared by the hydrothermal technique, similar to that reported by Rogers *et al.* [32] In this process $MnO_2$ powder was sealed in a gold capsule with a $H_2SO_4$ solution. This was then heated to 450°C under 1500 atm pressure. The rutile $\beta$-$MnO_2$ sample provided resembled a needle-like platelet measuring approximately $4 \times 1 \times 0.5$ mm, with a small, purportedly twinned L-shaped branch on one end. Part of this branch was removed and that end of the crystal was avoided during experiments so as not to compromise the polarisation dependent study. The surface plane was (110) with the *c*-axis parallel to the long edge of the crystal.

### 4.4.2 Sample Mounting for polarisation-dependent study

Since rutile structures, such as $IrO_2$ and $MnO_2$ are four fold symmetric (equivalent every 90°) about the *c*-axis, the orientation of the *a*-axes is immaterial once the *c*-axis is known. Elaborating on this: if the electric field vector of the linearly polarised light **E** is parallel to an *a*-axis, but perpendicular to both the *c*-axis and other *a*-axis, it is expected that a full component of absorption would occur in the orbitals lying along that *a*-axis, but no absorption would occur in the projection of the orbitals parallel to the other *a*-axis as it would be inaccessible. However, once the *c*-axis remains fixed perpendicular to the linearly polarised light, the cosine squared dependence of natural linear dichroism tells us that the component excitation into orbitals lying parallel to the plane made by the two *a*-axes will sum to an equivalent amount, irrespective of the rotational position of the *a*-axes about the *c*-axis. This applies in the same fashion for dichroism in the emission from a perfect rutile tetragonal solid, such as $IrO_2$ and $MnO_2$.

All "in-plane" measurements, obtained a 90° scattering geometry, refer to RXES measurements where the incoming linearly polarised light has its electric field vector within the plane of scattering. As a consequence the X-ray emission spectrometer views the rutile crystal along the same crystal axis (or direction) to which the electric field vector **E** is parallel. The term introduced by Harada *et al.* [91] to describe this geometrical setup is a "depolarized" configuration, though this term is most used in the context of metal *L*-edge resonant inelastic X-ray scattering (RIXS) measurements. By contrast, "out-of plane" measurements again obtained in a 90° scattering geometry, refer to RXES measurements where the incoming electric field vector is out of (or perpendicular to) the plane of scattering, Harada denotes this the "polarized" configuration. These two scattering geometries are illustrated in Figure 4.5 adapted from Harada *et al.* [91] For convenience we will refer these scattering geometries as either in-plane or out-of-plane.

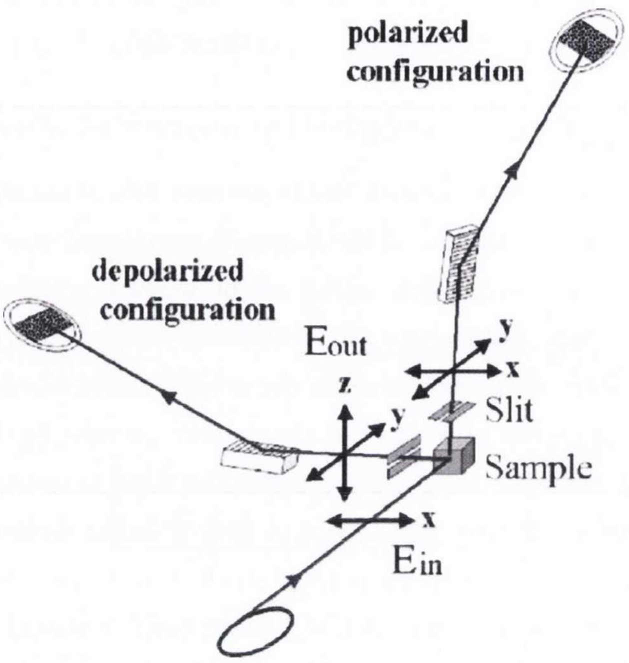

Figure 4.5: Schematic drawing of the "polarized" versus "depolarized" experimental configuration, or out-of-plane versus in-plane scattering respectively, for a normal planar undulator. Adapted from Harada *et al.* [91]

#### 4.4.2.1 $IrO_2$ Mounting

The in-plane measurements of $IrO_2$, where the optical axis of the spectrometer lies parallel to **E**, the electric polarisation vector of the incident light, were obtained at Beamline 8.0.1 (BL8) in the Advanced Light Source (ALS), Berkeley. The out-of-plane measurements, where **E** is perpendicular to the scattering plane and to the optical axis of the spectrometer, were taken at the I511-3 bulk beamline station in MAX-lab. See Chapter 2 for a more detailed description of these beamline endstations.

For the in-plane measurements the $IrO_2$ was cleaved in air into smaller platelets measuring approximately $2 \times 2$ mm. Two of these were mounted on the 4-axis manipulator at BL8, such that the platelets' (110) surfaces were parallel but with their $c$-axes perpendicular to each other, i.e. one with its $c$-axis horizontal, and the other with the $c$-axis vertical. These two crystal alignments were utilised in the measurements and are designated as $\mathbf{E}\|c$ and $\mathbf{E}\perp c$ for absorption measurements, and $\mathbf{E}\|c$;XES$\|c$ and $\mathbf{E}\perp c$;XES$\perp c$ for emission measurements; where XES$\|c$ and XES$\perp c$ refer to the direction of the spectrometer's optical axis with respect to the $c$-axis of the crystal. In the case of the $\mathbf{E}\|c$;XES$\|c$ RXES measurements, with the $c$-axis in the (110) plane of the surface of the sample a deviation from normal incidence of 12.5° was necessary to allow a grazing exit for the emitted photons from the illuminated beamspot on the sample to reach the emission spectrometer. Thus the **E**$\|c$;XES$\|c$ scattering geometry label is used as a close approximation to the alignment. The **E**$\perp c$;XES$\perp c$ geometry on the other hand is at 45° incidence with **E** perpendicular to the now vertical $c$-axis but parallel to one of the equivalent $a$-axes of the (110) face, the other $a$-axis was thus parallel to the propagation vector of the incident beam. The XAS measurements obtained from the $IrO_2$ crystals at BL8 were in identical geometries to those used for emission as they were performed contiguously.

For the measurements at I511-3 the set-up was much the same, but with the possibility of rotating the spectrometer about the incident direction of the incoming beam and thus access the out-of-plane scattering geometry. Here, weeks prior to measuring, one of the previously used platelets was sputtered by argon ions to remove surface contaminants that had aggregated over time. It was mounted flat on the six-axis manipulator, with its $c$-axis parallel to the surface of the sample holder, such that it could be aligned both horizontally and vertically with respect to **E** by adjusting the manipulator's azimuthal rotation. For XAS, the measurements were obtained at exactly normal incidence in two crystal geometries, **E**$\|c$ and **E**$\perp c$. The designations for the measurement geometries for out-of-plane scattering are **E**$\|c$;XES$\perp c$ and **E**$\perp c$;XES$\|c$. In the latter geometry a $\sim$ 15° deviation from normal incidence scattering was made to allow photons to enter the spectrometer, such that the $c$-axis was only approximately aligned parallel to the spectrometer.

#### 4.4.2.2 $MnO_2$ Mounting

For the in-plane (IP) measurements the single $MnO_2$ crystal was mounted flat on another six-axis manipulator, this time at Beamline 7.0.1 (BL7) at the ALS. For these measurements however the azimuthal rotation function of the manipulator was utilised to access the two geometries, similar to the ones used above for the $IrO_2$ at BL8. In a similar fashion to the orientation of the $IrO_2$ at BL8, the **E**$\|c$;XES$\|c$ geometry had the polarisation vector **E** approximately parallel to the horizontally oriented $c$-axis with near normal incidence with a 20° polar rotation offset of the sample plate from normal incidence. This was both to accommodate photons entering the spectrometer and to allow sufficient room for the manipulator housing near the spectrometer slits, such that the sample's position could be adjusted without risk of collision with the slits. In the **E**$\perp c$;XES$\perp c$, again in a similar manner to the $IrO_2$, the $c$-axis was aligned vertically, with the sample plate rotated to a 45° polar angle with respect to both the spectrometer, and the incident X-ray beam.

For the out-of-plane (OOP) measurements at I511-3 at MAX-lab a similar approach was taken, with the $MnO_2$ crystal mounted flat on the six-axis manipulator. This time however both the **E**$\|c$;XES$\perp c$ and **E**$\perp c$;XES$\|c$ measurements were recorded at a 45° incident and hence exit geometries. This meant that the designated $\mathbf{E}\perp c$;XES$\|c$ geometry had a large deviation from XES$\|c$ by 45°, a necessity due to time constraints and severely reduced counts when attempted at more normal incidences. These geometries were allowed for by the OOP set up at the I511-3 beamline, where the revolving of the chamber means the polar rotation of the manipulator effectively becomes tilt with respect to the beam.

### 4.4.3 Experimental details

For the $IrO_2$ sample, in-plane resonant soft X-ray emission spectroscopy (RXES) and X-ray absorption spectroscopy (XAS) were performed at the O $K$-edge of $IrO_2$ at BL8 of the Advanced Light Source in Berkeley. This beamline contains a U5.0 undulator together with a high throughput spherical grating monochromator with good resolution in the sub-keV photon energy range. For more information on the instrumental set-up at BL8 see Chapter 2.

BL7 of the ALS was where the $MnO_2$ XAS and IP RXES measurements were obtained. Similar to BL8, this beamline has a U5.0 undulator and spherical grating monochromator (SGM) with good resolution and brightness in the sub-keV soft X-ray range. This beamline is also detailed further in Chapter 2.

$IrO_2$ and $MnO_2$ XAS and OOP RXES were performed at the O $K$-edge at Beamline I511-3, which contains a U5.0 undulator together with a SX-700 monochromator with an energy range of $50 - 1500$ eV, a flux of $10^{11} - 10^{13}$ photons per second and a possible resolving power of 11,000 [24]. The endstation allows both electron and fluorescence yield to be acquired, the latter via a microchannel plate (MCP). It also possesses a Nordgren type X-ray spectrometer [18] which is at 90° to the incoming synchrotron beam but is rotatable about the axis of the beam to allow access to the out-of-plane scattering geometry [24]. Further details of the beamline and I511-3 bulk endstation can be found in Chapter 2.

Taking advantage of the fact that the monochromatised synchrotron light is linearly polarised, it was possible to probe the dichroic nature of those single crystal materials to observe the natural linear dichroism. XAS measurements were performed at the oxygen $K$-edge in total electron yield mode using the sample drain current method, while the total fluorescence yield (TFY) was measured via a channeltron.

At BL8 for $IrO_2$, the resolution of the monochromator during XAS measurements was 0.1 eV at the O $K$-edge. The resolution used for the O $K$-edge X-ray emission measurements, measured in 1st order emission, corresponded to a spectrometer resolution of 0.4 eV, equivalent to $\approx 10\mu$m entrance slit width.[†] During RXES measurements the incident monochromator resolution used was 0.6 eV.

---

[†] or 17 V on the piezo controller in June 2008.

At BL7 for $MnO_2$, the resolution of the monochromator during XAS measurements was approximately 0.2 eV at the O $K$-edge. The fluorescent spectrometer slit width was set to 10 $\mu$m equivalent to about 0.4 eV, while the monochromator resolution used for emission measurements was approximately 0.4 eV.

At MAX-lab for both samples, the beamline monochromator slits were set to 100 $\mu$m or 0.2 eV resolution for XAS. For emission the resolution of the incident light was set to 300 $\mu$m, equivalent to 0.65 eV resolution. The soft X-ray spectrometer slit was set to 14 $\mu$m allowing approximately 0.52 eV resolution for emission measurements.

All measurements were made at room temperature. The absolute photon energy scales were determined as follows: for the $IrO_2$ the O $K$-edge RXES spectra were calibrated using a combination of the $L_\alpha/L_\beta$ emission lines of Zn in the 2nd order of diffraction, and in addition the centres of the elastic peaks obtained in the $\mathbf{E}\perp c$ geometries. The O $K$-edge XAS spectra were calibrated by comparison with the O $K$ XAS of rutile $TiO_2$ [92,93]. The $MnO_2$ XAS spectra were calibrated in the same way while the $L_\alpha/L_\beta$ emission lines of Zn in 2nd order were used to calibrate the O $K$ RXES emission.

## 4.5 Results and Discussion

### 4.5.1 O $K$ Edge X-Ray Absorption Spectroscopy of $IrO_2$

Figure 4.6 shows the measured oxygen $K$-edge XAS spectra obtained at the MAX-lab I511-3 beamline, measured in TEY mode for two distinct orientations of the $IrO_2$ samples, with the rutile $c$-axis being either parallel or perpendicular to the electric field of the linearly polarised synchrotron radiation. These orientations for oxygen $K$-edge XAS are denoted $\mathbf{E}\|c$ and $\mathbf{E}\ \perp c$, respectively.

The lower part of Figure 4.6 shows the calculated unoccupied oxygen $2p$ PDOS projected either along the $c$-axis, and thus the O $2p_x$ component, or along an $a$-axis and therefore an equal mixture of O $2p_y$ and O $2p_z$ components. Neither PDOS are broadened by core-hole lifetime broadening nor by instrumental broadening.

It is useful to compare the axis-resolved unoccupied $2p$ PDOS, as measured by the oxygen $K$ XAS for $\mathbf{E}\|c$ and $\mathbf{E}\perp c$, with the results of the DFT calculation previously presented in Figure 4.2. These are now presented in the lower part of Figure 4.6 where O $2p_x$ PDOS can be compared to the $\mathbf{E}\|c$ XAS and the normalised sum of the O $2p_y$ and O $2p_z$ can be compared with the $\mathbf{E}\perp c$ XAS. The calculated O $2p$ PDOS is unbroadened whereas O $1s$ core-hole Lorentzian lifetime broadening and instrumental Gaussian broadening would contribute greatly to replicating the experimental spectrum even more closely. However, there is no need for that as the features of the oxygen $K$-edge XAS are very clearly explained

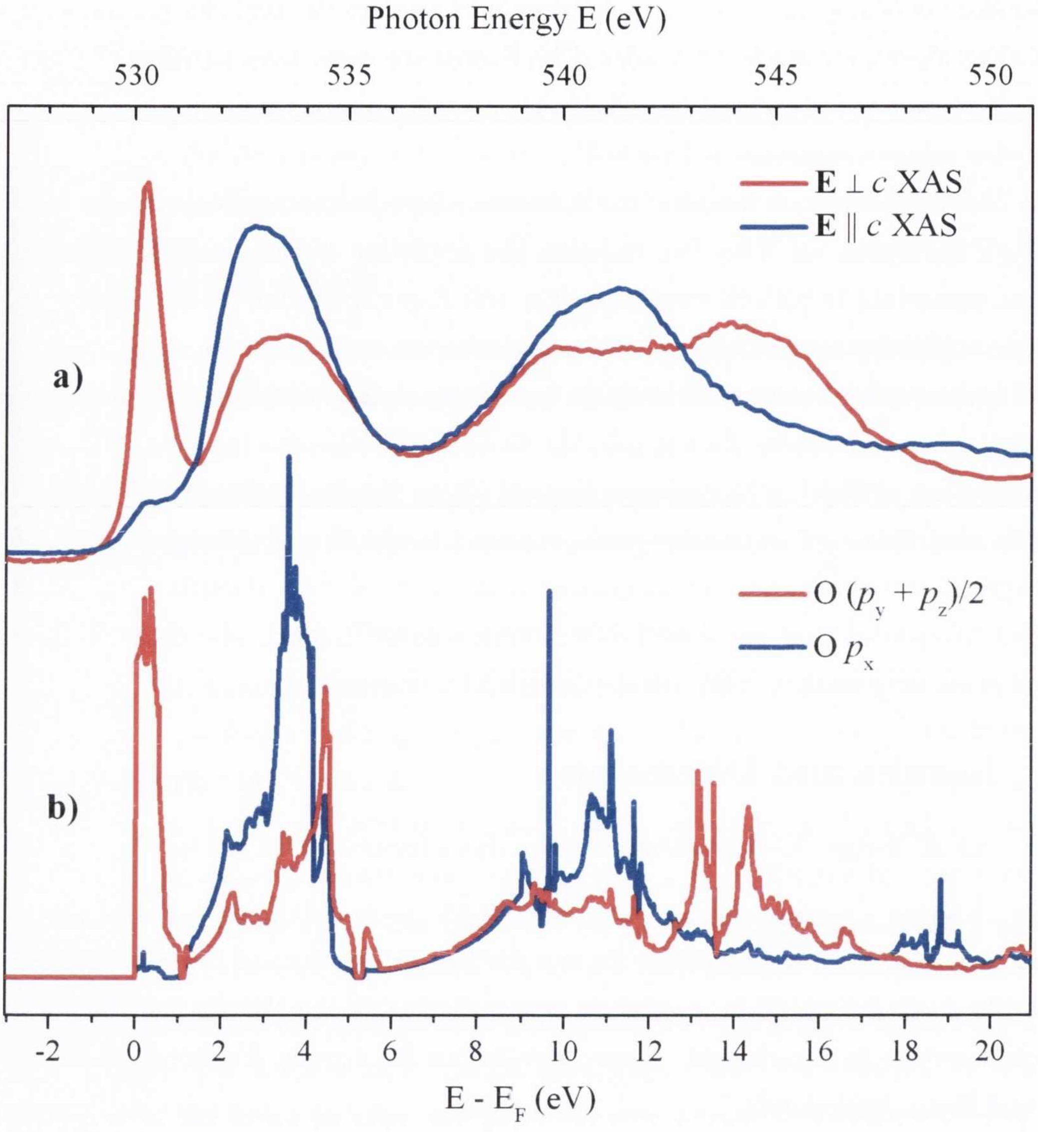

Figure 4.6: **a)**Polarisation dependent O *K*-edge XAS of $IrO_2$ for $\mathbf{E}\ \|c$ and $\mathbf{E}\ \perp c$ incidence geometries measured in TEY mode.**b)** DFT calculated partial DOS of oxygen $2p$ CB PDOS projected along the local $x$-axis (blue) and along the direction bisecting the local $x$ and $y$ axes (red).

by the presented PDOS. These are a $\pi^*$ derived peak at 530.3 eV observable only when $\mathbf{E}\perp c$; a strong $\sigma^*$ feature at 533 eV when $\mathbf{E}\ \|c$ mainly due to O $sp^2$ – Ir $5de_g\ d_{x^2-y^2}$; while the less strong $\sigma^*$ feature centred at 533.5 eV when $\mathbf{E}\perp c$ ($\|a$) is mainly due to O $sp^2$ – Ir $5de_g\ d_{z^2}$. The $\pi^*$ derived feature arises, as noted previously, from $\pi$-like interactions or chemical bonding between the O $2p_y$ orbital oriented ⊥ $Ir_3O$ plane and the Ir $5d\ t_{2g}\ d_{z(y-x)}$ orbital, and to a lesser extent the $d_{z(y+x)}$ .

The correlation of the theory predictions in 4.6b to the experimental XAS PDOS in 4.6a is excellent.

Excitation resonant with the oxygen $K$-edge XAS threshold, at approximately 530 eV, with the polarisation perpendicular to the $c$-axis or more specifically, perpendicular to 50% of the $Ir_3O$ planes, will preferentially excite into O $2p_y$ $\pi^*$ states as indicated from the components of the O $2p$ PDOS shown in Figure 4.2. The linear polarisation in the other 50% of $Ir_3O$ planes would be parallel to the O $2p_z$ orbital lying within the $Ir_3O$ plane but no excitation at threshold is possible as this has almost zero states available in the first electron volt above the Fermi level. Similarly, if the electric polarisation vector is parallel to the $c$-axis then excitation into only the oxygen $2p_x$ $\sigma^*$ states should occur whose density of unoccupied states is close to, but not equal to zero. The anisotropic charge distribution about the O atom caused by the respective O $sp^2$ – Ir $5d$ $e_g$ $\sigma$-like and O $p$ – Ir $5d$ $t_{2g}$ $\pi$-like chemical bonding gives rise to this observed natural linear dichroism which is readily apparent in the oxygen $K$-edge XAS spectra of $IrO_2$.

As an aside, previous XAS of $IrO_2$ nanorods by Tsai *et al.* [70] suggests (assuming the nanorods' $c$-axes are collinear) their spectrum was obtained somewhere approximately half-way between $\mathbf{E}\perp c$ and $\mathbf{E}\|c$.

The significant dichroism observed between the energies of 539–549 eV is likewise explained by O $p$ character chemical bonding with higher energy Ir $6s6p6d$ complexes. The peak at 541 eV in $\mathbf{E}\|c$ occurs where both the Ir $6s$ and Ir $6d$ $e_g$ components have their maxima, and is absent in the $\mathbf{E}\perp c$ spectrum at that energy. The O $2p_x$ component along the $c$-axis appears strongly hybridised with the Ir $6s$, this component decreases substantially from 541 eV upward. The $\mathbf{E}\perp c$ spectrum by contrast exhibits a broad peak near 544 eV arising from both O $2p_y$ hybridisation with Ir $t_{2g}$ orbital character and O $2p_z$ hybridisation with Ir $p$ and Ir $e_g$ orbital character. The oxygen $K$-edge XAS and the results obtained from the electronic structure calculations show excellent agreement in all respects. Such a correspondence should not necessarily be expected in a single particle approximation approach for the excited spectrum if, for example, there were strongly correlated electrons which needed to be taken into account [14]. A suitable explanation for the good correspondence is that the O $1s$ core-hole obtained in the absorption process may be strongly screened by low energy excitations of the occupied metallic Ir $5d$ $t_{2g}$ states across the Fermi level, as has been demonstrated by the strong screening observed in the O $1s$ XPS of $IrO_2$ [68]. Werthheim *et al.* observed a very asymmetric line-shape with a long tail and fitted it by inclusion of such an excitation spectrum, reflecting the high density of states at the Fermi level and the ease with which the Ir $5d$ $t_{2g}$ could be excited across the Fermi level [68].

### 4.5.2 O *K* Edge X-Ray Absorption Spectroscopy of $MnO_2$

The O $K$-edge XAS of $MnO_2$ is shown in Figure 4.7, obtained in both $\mathbf{E}\perp c$ and $\mathbf{E}\|c$ orientations at MAX-lab in TEY mode. In addition, included below in this figure is the electron energy loss spectroscopy (EELS) from Kurata *et al.* [89] as well as fluorescence yield (FY) mode XAS of an unoriented sample of $MnO_2$ from Figueiredo and Mirao [79]. The comparison between the measured TEY and the EELS is excellent, bearing in mind that Kurata used crushed poly-crystalline samples and thus their spectra should represent spherically averaged measurements, equating to $\frac{1}{3}\mathbf{E}\|c + \frac{2}{3}\mathbf{E}\perp c$ of the presented polarisation dependent XAS. Figueiredo used freshly fractured fragments of well crystallised mineral specimens, thus the orientations measured are arbitrary rather than spherically averaged as it would be in a powdered sample. The FY from Figueiredo, while resembling the measured TEY deviates somewhat in its spectral shape. To compare like with like, an additionally measured TFY spectrum of $\mathbf{E}\|c$ incident geometry is presented at the bottom of Figure 4.7 in cyan. This is far more consistent with the results from Kurata *et al.* A difference between fluorescent and electron yield can be a blunting of the intense features in the former, such as ($a_1$), which can be explained by decreased sample volume selected by the incident photons owing to the reduction in photon penetration depth, or higher photoabsorption cross-section at these peaks. For TEY the effect is rendered moot as only the volume very close to the sample surface contributes to the measurements, and is thus a more effective measure of the electronic structure.

Focusing on the polarisation dependent TEY, the $\mathbf{E}\perp c$ spectrum becomes somewhat noisy in the region of 535 eV; this is due to oxygen absorbing contaminants on the optics of the beamline reducing the brightness of the beam and causing a lower signal to noise ratio between 535 eV and 540 eV. In agreement with de Groot *et al.* [78] the first structure between 527–533 eV, or features ($a_1$) and ($a_2$) are nominally described as the $\pi^*$ and $\sigma^*$ resultant features, as with all O $K$-edge XAS presented in this thesis. The higher regions shown above 536 eV are attributed to the projected unoccupied $p$ states mixed with the manganese $4sp$ band [78].

While in $IrO_2$, dichroism aside, the splitting between the $\pi^*$ and $\sigma^*$ derived states is unequivocal, for $MnO_2$ however it appears far less striking. Rather the separation is in the form of an initially large peak followed by an shoulder, as if the near octahedral crystal field is not as robust in splitting the $d$-level degeneracy or the oxygen states are less hybridised with the $t_{2g}$ and $e_g$ for this crystal. Recall from section 4.3 however that Mn(IV) is nominally a $3d^3$ valence cation, thus in the ground state its $e_g$ state remains unoccupied, while the $t_{2g}$ states hold three degenerate $\uparrow$ electrons. It can be deduced from the MO diagram of Figure 4.4 (page 50), that the first peak ($a_1$) is assigned to a mixture of two separate transitions:

to O $2p$ states hybridised with the manganese $t_{2g} \downarrow$ as well as those hybridised with the $e_g$ $\uparrow$. This is accounted for by the very similar values of crystal field splitting (3.3 eV) with exchange splitting (3.0 eV) [78,89].

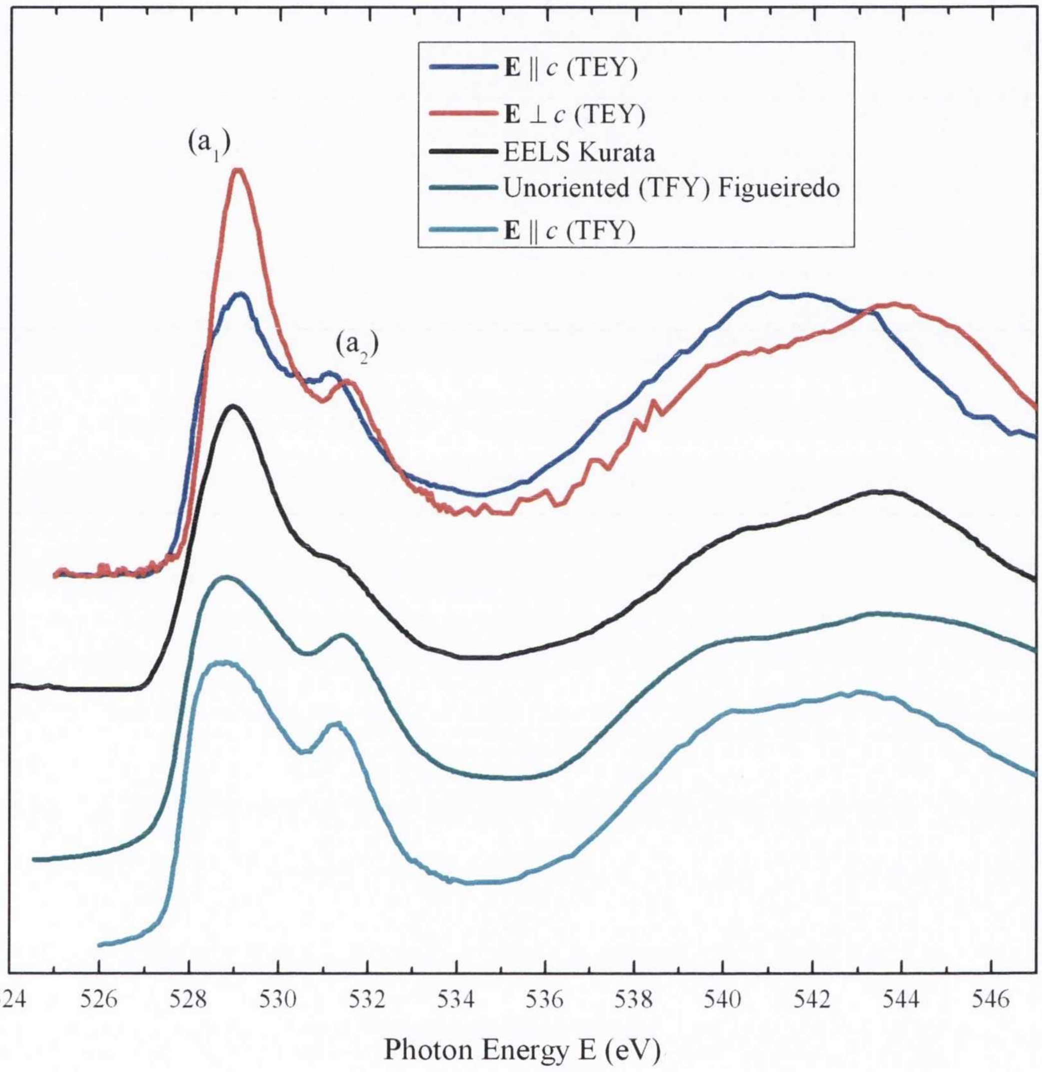

Figure 4.7: Polarisation dependent O $K$-edge XAS of MnO$_2$ measured in TEY mode (top) for the **E** $\parallel c$ and **E** $\perp c$ incidence geometries. Compared below with, respectively, EELS from Kurata *et al.* [89], O $K$-edge FY from Figueiredo *et al.* [79], and on the bottom XAS in the **E** $\parallel c$ geometry measured in TFY mode.

The shoulder (a$_2$) is attributed to transitions into the unoccupied $e_g \downarrow$ hybridised $\sigma^*$ states. Thus peak (a$_1$), while reduced in the **E**$\parallel c$ geometry, still exhibits considerable spectral weight and therefore cannot be designated solely as a $\pi^*$ feature, is not purely resultant from these states but rather a mixture of both $\pi^*$ and $\sigma^*$ states. The (a$_2$) on the other hand is attributed almost entirely to $\sigma^*$ states accessible in both orientations. The natural linear dichroism presented in the XAS can be explained in terms of the structure: in the $\mathbf{E}\perp c$ geometry, resonant excitation into $p_y$ orbitals perpendicular to the $Mn_3O$ planes is favoured, while in the $\mathbf{E}\|c$ geometry it is not. Thus the red $\mathbf{E}\perp c$ spectrum has a significantly larger ($a_1$) peak, due to the $\pi^*$ feature accessible in this geometry.

### 4.5.3 Polarisation Dependent XES of $IrO_2$

Now the O $K$-edge non-resonant and resonant X-ray emission spectroscopy (XES) spectra of $IrO_2$ will be discussed, together with their interpretation in the light of chemical bonding and electronic structure of $IrO_2$.

#### 4.5.3.1 Normal X-ray Emission

In normal XES (NXES) the core electron is excited well above threshold and into the ionisation continuum; as a result the NXES spectrum is independent of the incoming photon energy [10]. Unlike in RXES, when well above threshold, the intermediate excited state does not have a specific value of crystal momentum or $k$-vector (or $k$-vectors) as the outgoing photoelectron's momentum is no longer well correlated with the crystal momentum of the intermediate state. Thus all possible occupied $2p$ states contribute equally in the observed radiative decay of the $1s$ core hole, giving rise to a $k$-unselective spectrum spanning the Brillouin zone and reflecting the integrated oxygen $2p$ PDOS. Similarly, as the excitation energy lies above the observed region of dichroism in absorption, the electric polarisation vector $\mathbf{E}$ of the incident photon is unimportant. Rather it is the geometric position of the spectrometer with respect to the orientation of the crystal that becomes the all important factor for the distribution of spectral weight in the observed NXES spectrum, and thus resulting in the equivalent of a natural dichroism observed in the emission spectrum.

Figure 4.8 shows the non-resonant or NXES taken well above threshold for both in-plane (IP) and out-of-plane (OOP) scattering geometries. In each case the XES spectrometer views the crystal along either the $c$-axis or the $a$-axis. Also shown are the VB photoemission spectroscopy (PES) [69] and scanning photoelectron microscopy (SPEM) of $IrO_2$ nanorods [70]. The first thing to note from this figure is the difference in quality of the spectra between IP and OOP geometries. This is entirely related to the differences of experimental set-up at two different locations, which is discussed in section 4.4.3. Post-experimental 5-point adjacent averaging smoothing was applied to the OOP spectra for clarity. The OOP spectra are not strictly NXES but rather NXES-like RXES, as there are still some O $K$-edge unoccupied states evident in absorption at $\sim$ 543 eV, however it still serves as an instructive comparison as excitonic effects are minimal at this energy and a large range of crystal momentum is selected.

The SPEM and PES unlike O $K$-edge NXES measurements, do not select the O $2p$ states alone but rather the valence band as a whole. Thus at the VB maximum, from $0 \rightarrow -2$ eV, the narrow peak observed is due to the metal $d$ electrons. While the broader peak is attributed to the main O $2p$ bands. We know from Figures 4.2 and 4.3 that the Ir $5d$ states at the VB maximum can be attributed primarily to the $t_{2g}$ states, a large portion of which mix heavily with the O $2p_y$ in this region. Thus this feature is also observed in the NXES spectra of Figure 4.8, for example in the $\mathbf{E}\|c$;XES$\|c$ in-plane scattering geometry.

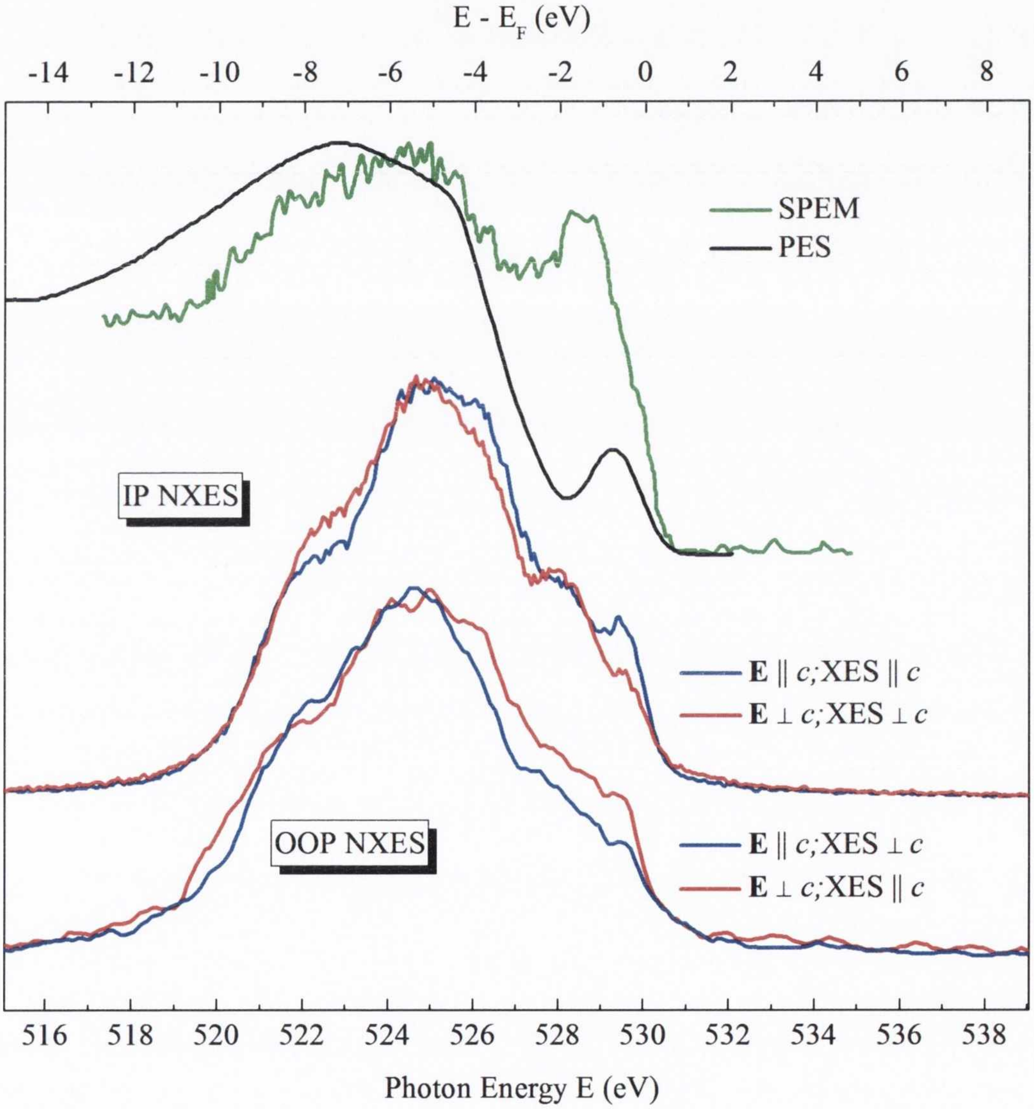

Figure 4.8: (Top) SPEM from (Tsai *et al.* [70]) and PES from (Daniels *et al.* [69]) compared with (middle) O $K$-edge IP polarisation dependent NXES of IrO$_2$ taken at 555 eV excitation energy at BL7, and (bottom) OOP NXES-like RXES of the same from I511-3.

With the above in mind, in examination of the IP NXES in the $\mathbf{E}\|c$;XES$\|c$ geometry only, the spectrometer is aligned approximately perpendicular (grazing exit) to the rutile basal ($a - a$) plane and thus also to the O $2p_y$ orbitals forming the Ir-O $\pi$ bonds. The stronger $\pi$ character is seen in the leading edge of this spectrum in Figure 4.8 illustrating the hybridisation between the O $2p_y$ and the occupied Ir $5d$ $t_{2g}$ $d_{z(y-x)}$ located just below the Fermi level. In addition, the main O $2p$ band has excess in spectral weight at $\sim$ 526 eV, which also reflects the O $2p_y$ projection if one considers the O $2p_y$ component in Figure 4.2 at a binding energy close to 4 eV. This $\mathbf{E}\|c$;XES$\|c$ NXES spectrum reflects a mixture of both Ir-O $\sigma$ ($p_z$) and Ir-O $\pi$ ($p_y$) contributions to the emission. For the second emission geometry the $\mathbf{E}\perp c$;XES$\perp c$ NXES in Figure 4.8, the emission reflects instead a contribution due to Ir-O $\sigma$ ($p_x$) occupied states and less predominantly features equal proportions of Ir-O $\sigma$ ($p_z$) and Ir-O $\pi$ ($p_y$) contributions as in the previous instance. Thus it should be clear that the O $p_x$ orbital only contributes to the $\mathbf{E}\perp c$;XES$\perp c$ NXES spectrum, whereas it is absent from the $\mathbf{E}\|c$;XES$\|c$ NXES spectrum. It is evident that the excess spectral weight between $\sim$521-522 eV in the $\mathbf{E}\perp c$;XES$\perp c$ spectrum coincides with the strong O $2p_x$ PDOS feature at $-8$ eV arising from hybridisation between the O $2p_z$ and the Ir $5d_{z^2}$ $e_g$ orbital.

A number of broadening factors that affect the resolution of these spectra should of course be noted. These are the combination of core hole lifetime broadening of $\sim$ 0.25 eV (Lorentzian), instrumental broadening of $\sim$ 0.4 eV (Gaussian-like), as well as valence hole lifetime broadening which contributes substantially to the Lorentzian-like broadening at these binding energies well into the depths of the valence band. Thus it is hardly surprising that the sharp peak at 8 eV binding energy is distributed widely across the emitted NXES.

The OOP NXES spectra in 4.8, as expected mimic the features of the in-plane NXES. Here they are reversed for the incident polarisation vector $\mathbf{E}$, showing further that NXES spectral features are not dependent upon $\mathbf{E}$ but rather the crystal orientation with respect to the spectrometer.

#### 4.5.3.2 Resonant X-ray Emission Spectra

Figure 4.9 presents the IP oxygen $K$-edge in-plane RXES spectra for $IrO_2$ at four selected resonant excitation energies labelled (a) to (d), as well as the non-resonant NXES spectra. In the IP scattering geometry the emission spectrometer is at 90° to the direction of the incident X-rays and the linear polarisation is in the plane of scattering and thus the optical axis of the spectrometer is always aligned parallel to $\mathbf{E}$, though at 90° to the incident propagation vector $\mathbf{k}$. The figure includes to the upper right both of the previous oxygen $K$-edge XAS spectra.

It should firstly be noted that elastically scattered peaks coincident with the excitation energy are not observed in the emission spectra (a) to (d) except for the $\mathbf{E}\perp c$;XES$\perp c$ spectra. In large part this is due to the geometrical arrangement of the $IrO_2$ (110) sample

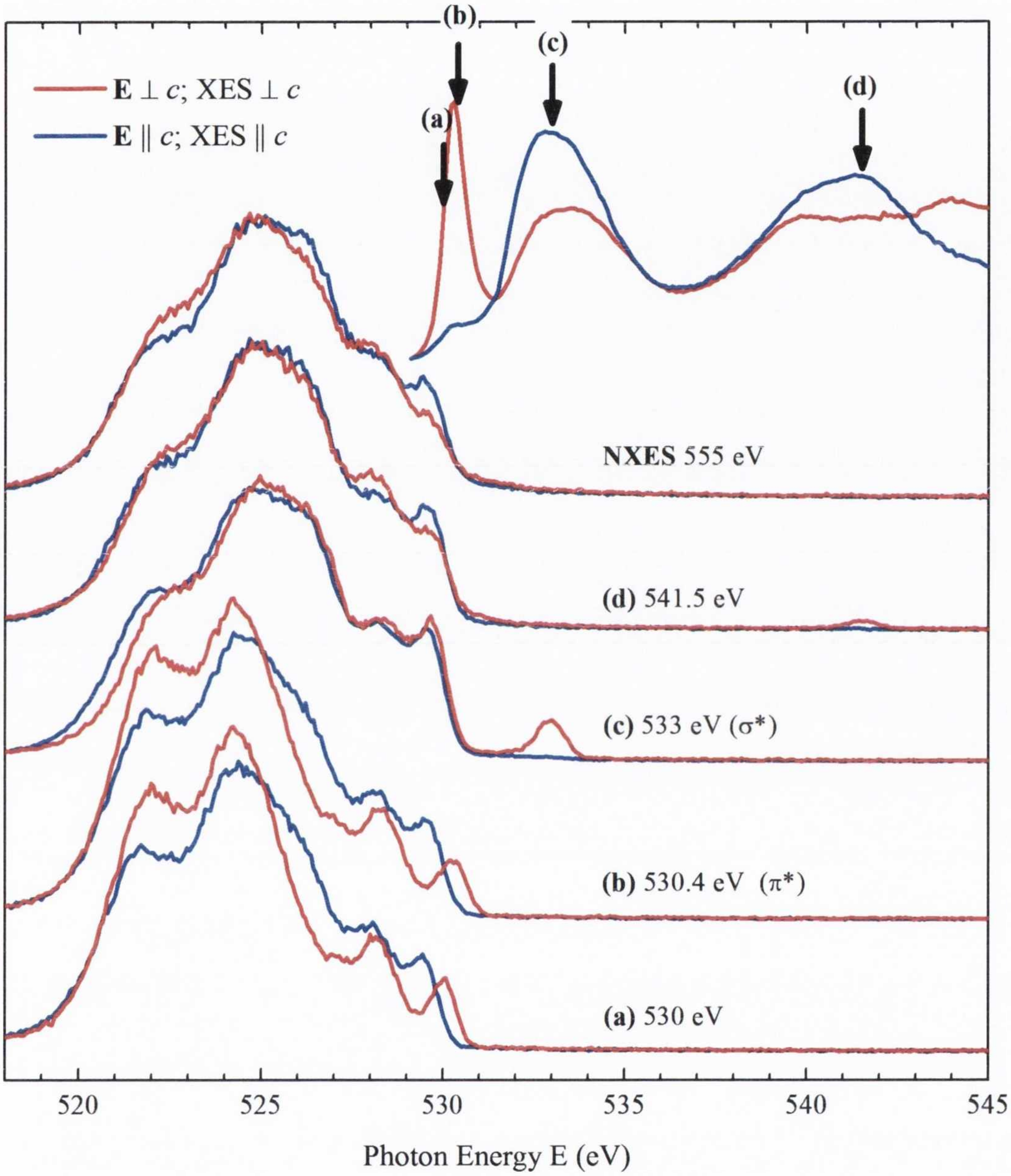

Figure 4.9: Polarisation dependent IP O $K$-edge RXES of IrO$_2$. **E**$\perp c$;XES$\perp c$ scattering geometry shown in red and the **E**$\parallel c$;XES$\parallel c$ in blue. Labelled arrows on formerly presented, and geometrically associated XAS spectra (top) indicate resonant excitation energies.

surface, with the [001] direction vertical with respect to the horizontal scattering plane, resulting in both a 45° angle of incidence onto the sample surface and a 45° angle of exit from the surface towards the spectrometer. This results in an enhancement of the elastically scattered peak due to resonant reflectivity. This elastic peak is most intense at threshold, and its intensity decreases slowly as we move away from threshold, though it can still be noted in spectrum (d). A similar geometrically enhanced elastic peak, albeit much more intense, is also seen in out-of-plane scattering spectra, heavily favoured in the $\mathbf{E}\|c$;XES$\perp c$ scattering geometry where again the incoming light is at a 45° incidence and exit angle with respect to the (110) surface. This is can be seen in the OOP RXES Figure 4.11, which will be discussed further on in this section.

In considering and discussing the detailed electronic structure revealed by the RXES spectra, it should be noted that there is a symmetry selectivity inherent in RXES. The intermediate state (XAS) is a probe of the spatial symmetry of the local molecular orbital, i.e. the $\sigma$ and $\pi$ bonding is probed on that site, where excitation to intermediate $\sigma^*$ states leads, in a 90° in-plane scattering geometry, to X-ray emission from occupied $\pi$ states in that scattering plane[†] (if they are mutually perpendicular). Excitation to intermediate $\pi^*$ states leads, in this scattering plane, to X-ray emission from the mutually perpendicular occupied $\sigma$ states [9]. In addition the occupied orbitals perpendicular to the scattering plane, whether $\sigma$-like or $\pi$-like, are also observed in the emission spectra in such a 90° scattering geometry.

Thus in the RXES spectra, the typical energy separation in the conduction band between $\sigma^*$ and $\pi^*$ derived states will influence greatly the observed spectral distribution of the RXES spectrum; the RXES is thus state-selective as well as symmetry-selective. Due to the aforementioned symmetry selectivity in a 90° scattering geometry, the states contributing to emission depend upon the symmetry or orbital projection of the intermediate state. Further, the orientation of the single crystal with respect to both the incoming linear polarisation and the direction of the outgoing observed scattering or emission also determines which of the orbital projections can contribute to the observed emission. Finally it should be explicitly stated that the RXES process is governed by the single-step Kramers-Heisenberg equation [10], where momentum is conserved and the crystal-momentum of the intermediate and final states only differ by the momentum of the scattered photon, and thus the observed RXES is also $k$-selective [17]. In the case of the oxygen $K$-edge RXES spectra obtained from $IrO_2$ here, the angle of scattering is 90°;-+ then the momentum transfer at the threshold RXES excitation energy of 530 eV corresponds to $\Delta\mathbf{k} \simeq 2\mathbf{k}\sin(\frac{\theta}{2})$ or $\sim 0.27\ \text{Å}^{-1}$ which is between 15-20% of the span of the Brillouin zone in $IrO_2$. Thus, as the $k$-selectivity is determined by the specific bands selected within the intermediate state by the excitation energy used, the portion of each band is selected by both the photon energy bandwidth, and the dispersion of that unoccupied band. In addition, the $k$-points in the valence band contributing to the emission will differ from those $k$-points selected in the intermediate state by the transferred crystal momentum $\Delta\mathbf{k}$.

---

[†] It will also lead to emission from any mutually perpendicular $\sigma$ states.

Considering the photon energy bandwidth used in these experiments is ~ 0.6 eV, in terms of the bandstructure of $IrO_2$ shown in Figure 4.10 and the transferred photon momentum, only relatively small changes in emission are observed with small changes in excitation energy. This is because, though the bands are dispersive, their number and weighting ensures that within the probed bandwidths, a very broad range of crystal momentum is selected. Take for example a threshold excitation from 0-1 eV above the Fermi level; this would be the region where the $k$-selective nature is potentially most discrete, yet examining Figure 4.10c it is clear that within that energy range O $2p_y$ states are distributed quite evenly across the Brillouin zone (assuming the O $2p_y$ orbital is geometrically favoured). As a result each subsequent excitation energy reflects an alternate, though similar selection of $k$-points in the Brillouin zone that contributes to the RXES spectrum.

This is the case unless gross changes in the weightings of the $k$-points occur due to the symmetry of the intermediate state being changed, e.g. where primarily $\sigma^*$ states are selected when $\pi^*$ states were dominant in the previous excitation. Therefore the selected $k$-points for a given RXES spectrum can be considered to give a representation in the RXES spectrum of the full character of the symmetry-selected PDOS. This is in contrast to the RXES spectra of graphite demonstrate by Carlisle *et al.* [17]†, which possesses comparatively few, but highly dispersed bands, and thus allows the selection of much smaller ranges of crystal momentum.

Focusing again on Figure 4.9, the threshold RXES spectra (a) at 530 eV, and at the peak of the $\pi^*$ resonance in spectra (b) 530.4 eV, differ little with the increase in excitation energy in their respective geometries. This is because they are both as a result of resonant excitation into the $\pi^*$ unoccupied peak and are not sufficiently energetic to access the $\sigma^*$ states. As a result of this state selectivity and resulting crystal momentum or $k$-selectivity, the $\pi$ emission at this energy will be suppressed and the resulting RXES spectra display strong $\sigma$ character. This is especially true for the $\mathbf{E}\perp c$;XES$\perp c$ threshold and $\pi^*$ spectra, where no evidence of the $p_y$ attributed feature at 529.5 eV is observed. Moreover, due to the geometric projection of the PDOS, the $\sigma$ emission in the $\mathbf{E}\| c$;XES$\| c$ geometry for the threshold and $\pi^*$ (a) and (b) excitations, is predominantly due to the O $2p_z$ VB states, while the emission in the $\mathbf{E}\perp c$;XES$\perp c$ geometry will predominantly be as a result of the O $2p_x$ VB states, and to a lesser extent O $2p_z$ (~ 50% to that from $p_x$), but no O $2p_y$.

The $\mathbf{E}\| c$;XES$\| c$ spectra (a) and (b) show contributions from both O $2p_y$, and hence the occupied $\pi$ feature at 529.5 eV, and the O $2p_z$, due to the geometric and symmetry selectivity. It should be noted that the intensity of this RXES spectrum is less in keeping with the XAS intensity. The relative amplitude of the $\mathbf{E}\|c$;XES$\|c$ and $\mathbf{E}\perp c$;XES$\perp c$ is somewhat arbitrary.

---

† Their figure is reproduced as Figure 2.5 on page 19.

As the excitation energy is increased and the $\sigma^*$ peak at 532 eV is reached, a marked change in the spectral weight of the RXES spectra is observed from that of the previous threshold spectra. The spectra in the two geometries are now extremely similar and more closely resemble their NXES counterparts, albeit with a greater definition of features. This change in character in the emission is qualitatively explained by the fact that at this energy, resonant with the $\sigma^*$ unoccupied states, the emission from occupied $\pi$ character states is now switched on in both $\mathbf{E}\|c$;XES$\|c$ and $\mathbf{E}\perp c$;XES$\perp c$. This accounts for the sudden shift of spectral weight for both orientations. That they are similar is due to the fact that unlike the $\sigma$ emission seen resulting from the threshold $\pi^*$ excitations, there is only one $p$ orbital, the $p_y$, that can contribute to oxygen $K$-edge $\pi$ emission. One feature in particular that is different in these spectra is the contrast in spectral weight at the bottom of the valence band emission between these two measurement geometries. In the $\mathbf{E}\|c$;XES$\|c$ geometry there is more spectral weight near the valence band minimum due to the $p_z$ states, which are also "switched on" at the $\sigma^*$ excitation for this geometry. This difference, resulting from the minor disparity between the occupied $p_x$ and $p_z$ VB states, is illustrated by the theoretical calculation in Figure 4.2. In the $\mathbf{E}\perp c$;XES$\perp c$ $\sigma^*$ excitation, the symmetry-selectivity prevents the O $2p_z$ VB states from contributing to this RXES spectrum, unlike the NXES spectrum in this measurement geometry, and thus the contributing states here are primarily $p_x$ and $p_y$, hence the notable dichroism at the bottom of the valence band.

Figure 4.11 gives the out of plane RXES for $IrO_2$ at the O $K$-edge. The significant anisotropic difference in the observed features for the in-plane spectra are not as easily defined in this figure due to the lower spectral resolution coupled with a far lower signal-to-noise ratio. This results from instrumental differences between BL8 compared with the present experimental configuration of I511-3, where these OOP spectra were recorded. However, a similarity in trends can be deduced. For example, excitation into the $\sigma^*$ peak (b) produces a shift in spectral weight towards the bottom of the valence band for the red $\mathbf{E}\perp c$;XES$\|c$ spectrum. The opposite is the case for the $\mathbf{E}\perp c$XES$\perp c$ IP spectra (c) in Figure 4.9. This is due to the OOP position of the spectrometer; the polarisation and energy select unoccupied states of $p_z$ ($\sigma$) character, whose subsequent measurement in the OOP scattering geometry is not forbidden, as is the case for in-plane emission.

Unlike the IP spectra, the features at the top of the valence band do not match exactly for the $\sigma^*$ excitation. For the IP the matching $\pi$ ($p_y$) contribution at this excitation energy can be explained as follows: in the case of $\mathbf{E}\|c$;XES$\|c$ the $p_y$ are resonantly selected by the excitation energy, but so too are the $p_z$. In the case of $\mathbf{E}\perp c$;XES$\perp c$ it is primarily unoccupied

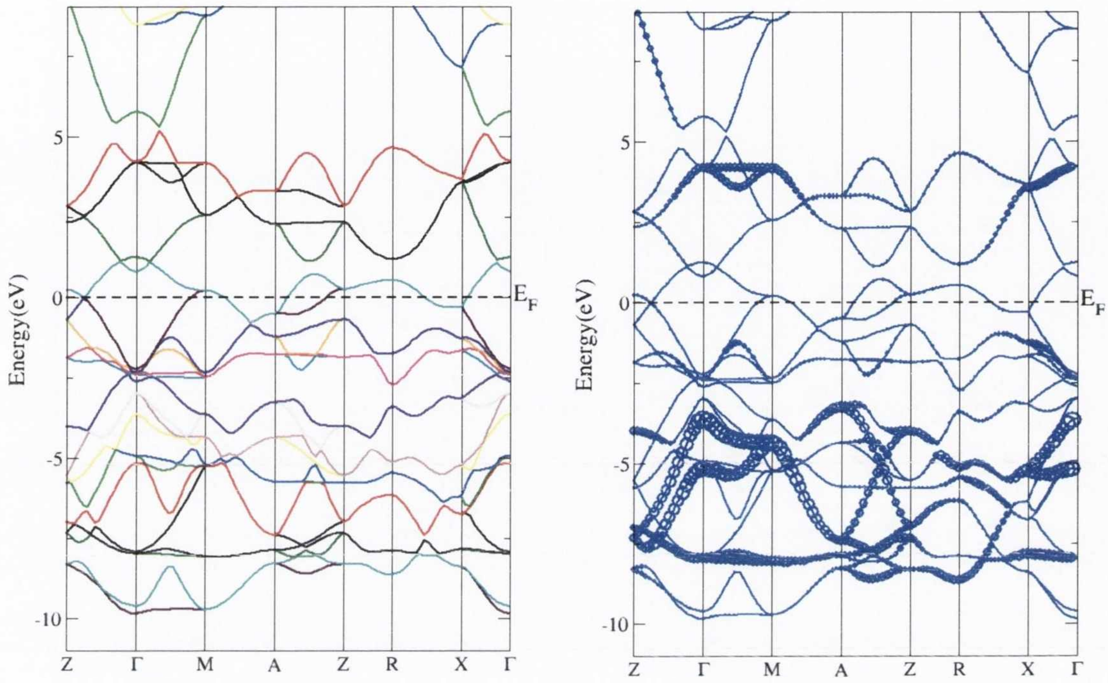

(a) IrO$_2$ Bandstructure (b) O $2p_x$

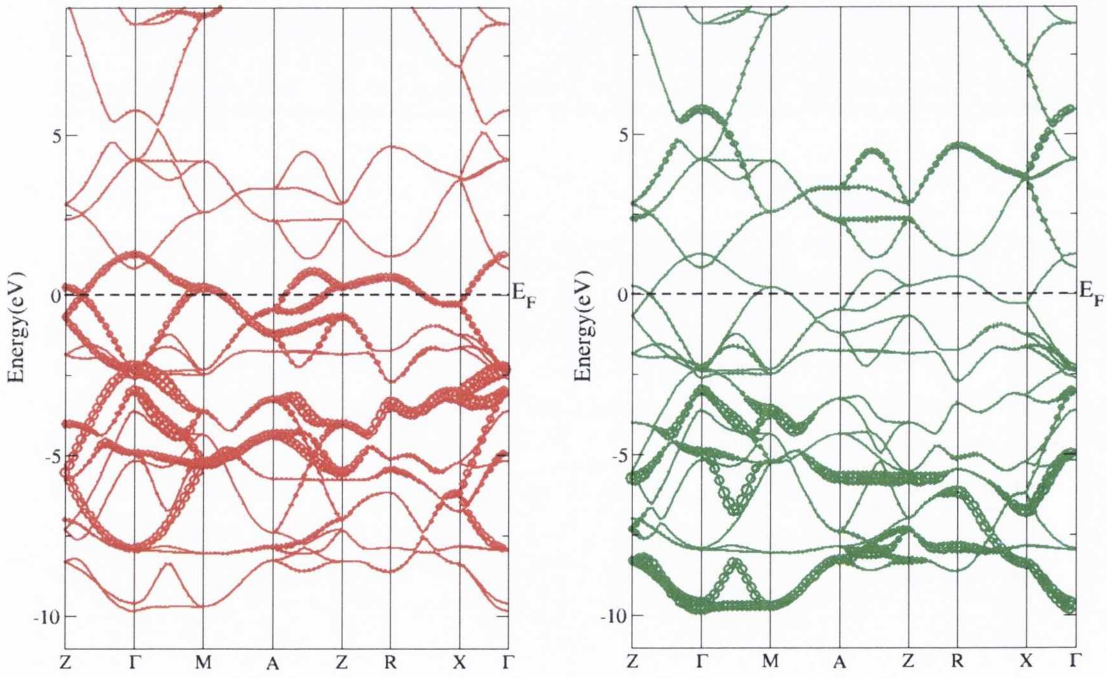

(c) O $2p_y$ (d) O $2p_z$

Figure 4.10: IrO2 bandstructures. **(a)** Presents the unweighted calculated bandstructure for rutile IrO$_2$. **(b)** IrO$_2$ bandstructure weighted for O $2p_x$ DOS. **(b)** IrO$_2$ bandstructure weighted for O $2p_y$ DOS. **(b)** IrO$_2$ bandstructure weighted for O $2p_z$ DOS.

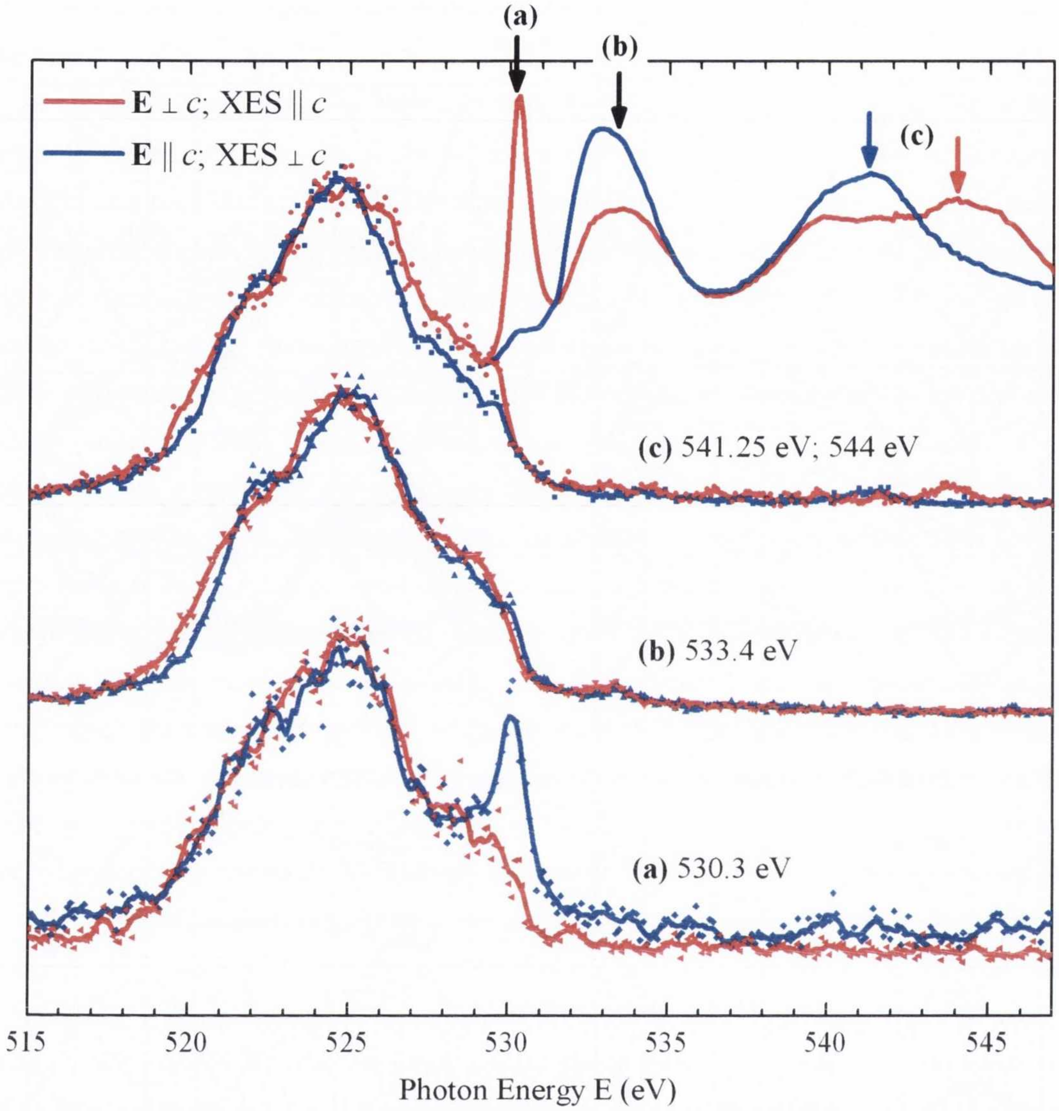

Figure 4.11: Polarisation dependent OOP O $K$-edge RXES of $IrO_2$. $\mathbf{E}\perp c$;XES$\|c$ scattering geometry shown in red and the $\mathbf{E}\|c$;XES$\perp c$ in blue. Labelled arrows on formerly presented, and geometrically associated XAS spectra (top) indicate resonant excitation energies. Due to relatively low signal to noise, a 5 point-adjacent averaging was applied to emission line spectra, while scatter points indicate raw recorded data.

$p_z$ states that are being selected. This results in a more-or-less equal distribution of $p_y$ and $p_x$ emission, just as the other geometry produced for $p_y$ and $p_x$ as evidenced by spectra (c) in Figure 4.9. For OOP the situation is slightly different, as resonantly selected orbitals in absorption now contribute to emission. Thus in the $\mathbf{E}\perp c$;XES$\|c$ (red) spectrum of Figure 4.11, $p_z$ states are selected, but only $p_y$ and $p_z$ contribute to emission. On the other hand in the $\mathbf{E}\|c$;XES$\perp c$ (blue), due to the geometry of the spectrometer, all three component orbitals are selected in emission with an emphasis on $p_x$. Thus the relative contribution from $p_y$ is lower.

Another thing to note in the OOP spectra, most noticeable at threshold for $\mathbf{E}\|c$;XES$\perp c$, is the significant elastic decay, or participator decay feature which is strongly allowed by the Kramers-Heisenberg equation in OOP (or sometimes referred to as "polarised") scattering geometry.

#### 4.5.3.3 Difference Spectra

In the first part of this section the attributed spectral weight of the $IrO_2$ NXES in section 4.5.3 will be taken further, focusing only on the IP NXES spectra. It is expected that the $\mathbf{E}\perp c$;XES$\perp c$ (red) NXES spectrum is a measure of the total PDOS from combination of the $\sigma$ states formed by the significant contribution of O $2p_x$, with a lesser but equal contribution from the $p_y$ and $p_z$. The $\mathbf{E}\|c$ geometry on the other hand would see contribution from significantly more $\pi$ states or O $2p_y$ orbital, as well as the $p_z$ $\sigma$ states, but ideally no $p_x$. Examining the calculated DOS in Figure 4.2, the approximation is made for the valence band $\sigma$ states that: $p_x \approx p_z \approx p_\sigma$. An approximation of the O $2p_y$ PDOS can therefore be extracted by subtraction of the NXES spectra presented in Figure 4.8. This is explained by the following set of equalities for these spectra:[†]

$$\begin{aligned} \mathrm{XES}\|c &= p_y + p_z \approx p_y + p_\sigma \\ \mathrm{XES}\perp c &= p_x + \frac{1}{2}(p_y + p_z) \approx \frac{1}{2}(p_y) + \frac{3}{2}(p_\sigma) \end{aligned}$$

Therefore the valence band $p_y$ PDOS can be extracted approximately from the NXES via equation 4.1, once appropriate normalisation has been applied.

$$\frac{3}{2}(\mathrm{XES}\|c) - (\mathrm{XES}\perp c) = p_y \tag{4.1}$$

Similarly in equation 4.2, and without the need of the approximation equating $p_x$ and $p_z$, the $p_x$ PDOS can be extracted from the NXES:

$$(\mathrm{XES}\perp c) - \frac{1}{2}(\mathrm{XES}\|c) = p_x \tag{4.2}$$

Equations 4.1 and 4.2 apply to both in and out of plane scattering geometries for NXES. Parts (a) and (b) of Figure 4.12 show these extracted difference spectra for the IP NXES. Plotted for comparison with each difference spectrum are the total VB component PDOS for the respective oxygen $2p_y$ and $2p_x$ projections. These were as shown before but broadened by convolution with a Lorentzian of 0.2 eV simulating the O $1s$ core-hole lifetime as well as a 0.5 eV Gaussian function to match the instrumental broadening of the spectrometer.

---

[†] Here as before, XES$\|$... and XES$\perp$... refer to the direction of the optical axis of the soft X-ray emission spectrometer.

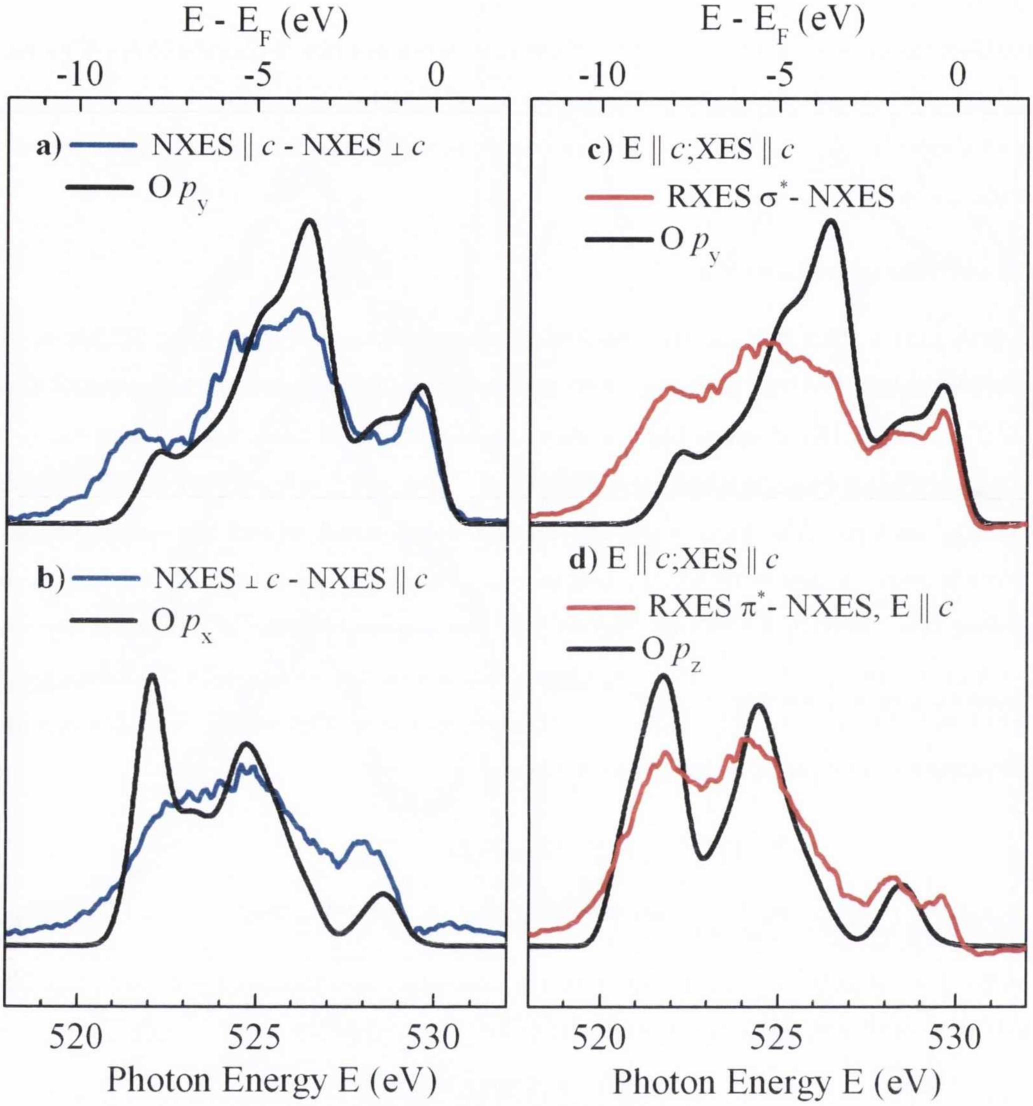

Figure 4.12: Difference spectra for IP $IrO_2$ using NXES and compared with broadened DFT component VB PDOS. **a)** XES$\|c$ - XES$\perp c$ NXES compared $p_y$. **b)** XES$\perp c$ - XES$\|c$ NXES compared $p_x$. **c) E**$\|c$;XES$\|c$ NXES subtracted from same geometry $\sigma^*$ resonant spectrum, compared with $p_y$ DFT. **d) E**$\|c$;XES$\|c$ NXES subtracted from same geometry $\pi^*$ resonant spectrum, compared with $p_z$ DFT.

However it was clear from the spectra that further broadening was required in order to sufficiently simulate the acquired spectra, the calculations possessing features that appear considerably sharper than is observed. This can be attributed to a combination of the contribution of valence hole lifetime as an additional observed broadening mechanism, and also the previously cited example of the metallic screening of the O 1$s$ core hole. Asymmetric broadening of the O 1$s$ core-level XPS spectrum has previously been observed and an agreement is obtained only when taking into account an excitation spectrum across the

Fermi level which considers the spectral distribution of the metallic occupied Ir $5d$ $t_{2g}$. To approximately account for this, the simulated spectra in this section were convoluted with a 1.5 eV Gaussian in lieu of the 0.5 eV Gaussian mentioned earlier, or for a full accounting of the valence-hole lifetime broadening. Once this larger broadening factor was applied, the agreement between the theoretical calculations and the difference spectra presented proved extremely good.

A similar recovery of the individual components of the O $2p$ PDOS can be obtained by subtracting NXES spectra from specific RXES within the same scattering geometry, specifically in this case $\mathbf{E}\|c$;XES$\|c$. The $\sigma^*$ RXES in this geometry, as discussed in section 4.5.3.2, while allowing emission from both $p_z$ and $p_y$ will resonantly favour orthogonal emission of $p_y$-character or $\pi$-character in contrast to NXES of the same geometry; thus subtracting a fraction of the same NXES from this spectrum should approximate the VB $p_y$ PDOS. The resulting difference spectrum is plotted with the calculated $p_y$ DOS in Figure 4.12c. The same method can be used to isolate the $p_z$ PDOS component by subtracting a fraction of the $\mathbf{E}\|c$;XES$\|c$ NXES from the $\pi^*$ RXES spectrum in this geometry, shown in Figure 4.12d. However part (d) of this figure is expected to be a more accurate representation of its labelled component than that of Figure 4.12a . This is indeed observed, and is a result of only $p_z$ $\sigma$ being recorded in this geometry; thus when the $\pi$ states are removed we are left with an experimental representation of the O $2p_z$ PDOS. Figure 4.12a on the other hand still shows considerable contribution from $p_z$ states, especially from the $k$-selected states near the bottom of the valence band.

Continuing with the principles outlined in this section, it stands to reason that if we approximate crystal momentum selection effects as negligible,[†] then RXES by itself can be utilised to isolate all three orthogonal components of the O $2p$ DOS for such rutile crystals. Figure 4.13 shows the experimentally derived difference spectra, as derived from RXES spectra alone, corresponding to each $p_x$, $p_y$ and $p_z$ compared to the broadened DFT calculated projections. Part a) of the figure simply compares the calculated O $2p_x$ component with the $\pi^*$ RXES spectrum in the $\mathbf{E}\perp c$;XES$\perp c$ measurement geometry, where emission is heavily biased for those states. The feature not predicted by calculations in this spectrum is attributed to elastic de-excitation of the core-hole excited electron.

As stated earlier the $\pi^*$ resonant spectra in the $\mathbf{E}\|c$;XES$\|c$ geometry will resonantly favour $\sigma$ emission, specifically that attributed to $p_z$. The $\sigma^*$ spectrum, exciting resonantly into unoccupied $p_x$ states in this geometry will favour emission of $\pi$ or $p_y$ character, but also orthogonal $\sigma$ emission from the $p_z$ states. With this in mind it can be deduced that by

---

[†] From Figure 4.9, the bands are observed to be relatively non dispersive for IrO$_2$ and thus for selected components, are a reasonable approximation to their $k$-unresolved DOS.

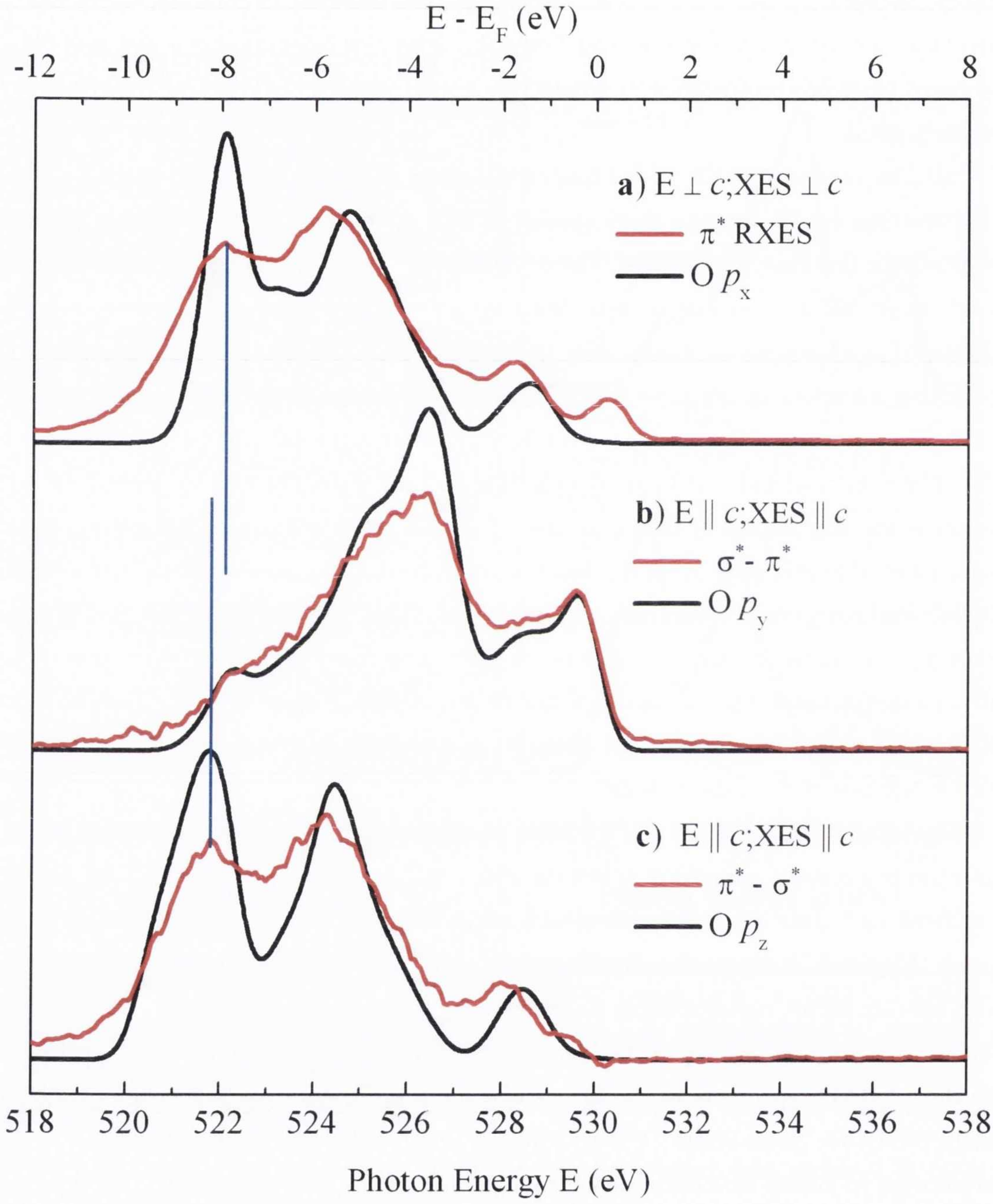

Figure 4.13: Experimentally isolated anisotropic orthogonal components of O $2p$ VB DOS using polarisation dependent IP RXES of $IrO_2$, compared with broadened DFT calculations of same. Blue lines indicate energy difference between O $2p_z$ and $p_x$ features. **a)** $\mathbf{E}\perp c$;XES$\perp c$ $\pi^*$ spectrum compared with $p_x$. **b)** $\mathbf{E}\| c$;XES$\| c$ $\sigma^*$ - $\pi^*$ difference spectrum compared with $p_y$. **c)** $\mathbf{E}\| c$;XES$\| c$ $\pi^*$ - $\sigma^*$ difference spectrum compared with $p_z$.

subtracting a fraction of the $\pi^*$ spectrum from the $\sigma^*$, a representation of the occupied $p_y$ states can be obtained. This is shown in Figure 4.13b compared to theory. The reverse is also true, subtracting a fraction of the $\sigma^*$ spectrum from the $\pi^*$ giving the $p_z$ component of the O 2$p$ occupied PDOS, given in Figure 4.13c.

The blue lines in the figure set out to illustrate the difference between the $p_z$ and $p_x$, which possess a very similar occupation density in the valence band. According to the calculations, the main area of difference between them is in the lower energy side of the VB; the blue lines show how this difference is echoed by the RXES and the RXES difference spectrum. The comparison between the derived experimental results and theory in Figure 4.13 is excellent.

### 4.5.4 Polarisation Dependent XES of MnO$_2$

Turning to MnO$_2$, the results of the XES measurements are presented in Figures 4.14 and 4.16. These present the polarisation dependent resonant X-ray emission spectra of MnO$_2$ at the O $K$-edge for in-plane and out-of-plane scattering geometries respectively. The IP spectra presented were recorded at BL7 of the ALS, while the OOP were taken at beamline I511-3 at MAX-lab. In each figure the XAS recorded for the measured polarisation geometries is also presented, the labelled arrows on each indicating the chosen excitation energy of emission.

The first thing of note is the difference in magnitude of dichroism of XAS between the two datasets, both of which were recorded in TEY mode via drain current. The lower degree of anisotropy in the ALS measurements is attributed to an experimental error, whereby the ideal crystal geometries with respect to the polarisation vector of the incident light was off by approximately 30° in both cases.[†] It was caused by an unintended azimuthal rotation of the sample plate during transfer into the analysis chamber of the BL7 endstation. This error went unnoticed as the sample plates are circular in shape and the small size of the crystal precluded visual confirmation of its orientation once mounted. While this setback acted to reduce the degree of fluorescent dichroism recorded, it should nevertheless be sufficient for it to be observed, should a VB anisotropy be present in this compound.

In both IP and OOP datasets, the main O 2$p$ emission band in all spectra appears to be characterised by three dominant features. These are denoted as a $\pi$ peak centred at 526.75 eV, a $\sigma$ peak at 524.5 eV and a $\sigma$ shoulder at the bottom of the VB in the region around 522 eV. Figure 4.15 shows that these three features are also evident in XPS [77], as well as in the calculated Heyd-Scuseria-Ernzerhof (HSE) valence DOS from Franchini *et*

---

[†] Determined by comparison of relative heights $\pi^*$ and $\sigma^*$ peak maxima from both datasets, acknowledging the cosine-squared dependence of linear dichroism.

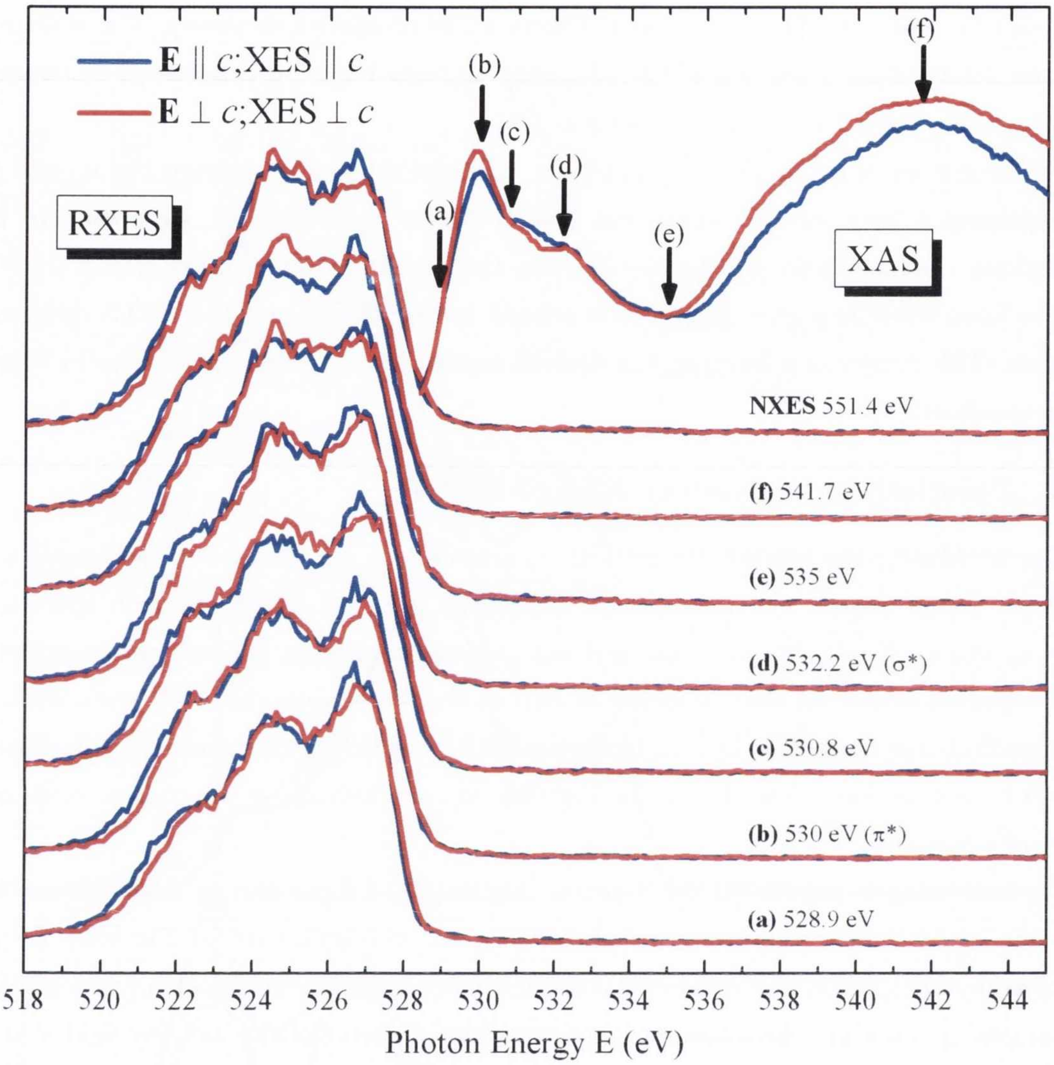

Figure 4.14: Polarisation dependent IP O $K$-edge RXES of MnO$_2$. $\mathbf{E}\perp c$;XES$\perp c$ scattering geometry shown in red and the $\mathbf{E}\|c$;XES$\|c$ in blue. Labelled arrows on formerly presented and geometrically associated XAS spectra (top) indicate resonant excitation energies.

*al.* [76], which are broadened by convolution with a Gaussian. Focusing on the $\pi$ attributed VB feature in Figure 4.14), it appears to remain the dominant feature throughout the IP emission in the $\mathbf{E}\|c$;XES$\|c$ geometry in blue, especially for the threshold excitation (a), and the excitation between the $\pi^*$ and $\sigma^*$ excitations (c).

Recall previously from sections 4.3 and 4.5.2, that the Mn $3d^3$ electron configuration of the Mn$^{2+}$ gives a ${t_{2g}}^3$ configuration, forming a magnetic ground state with an increased splitting between spin-up and spin-down. Calculations without a core-hole predict a three peak structure [94] in the first few eV from threshold. These are related to the $t_{2g}\downarrow$, $e_g\uparrow$ and the $e_g\downarrow$ states respectively. In these calculations by de Groot [94], the first two peaks

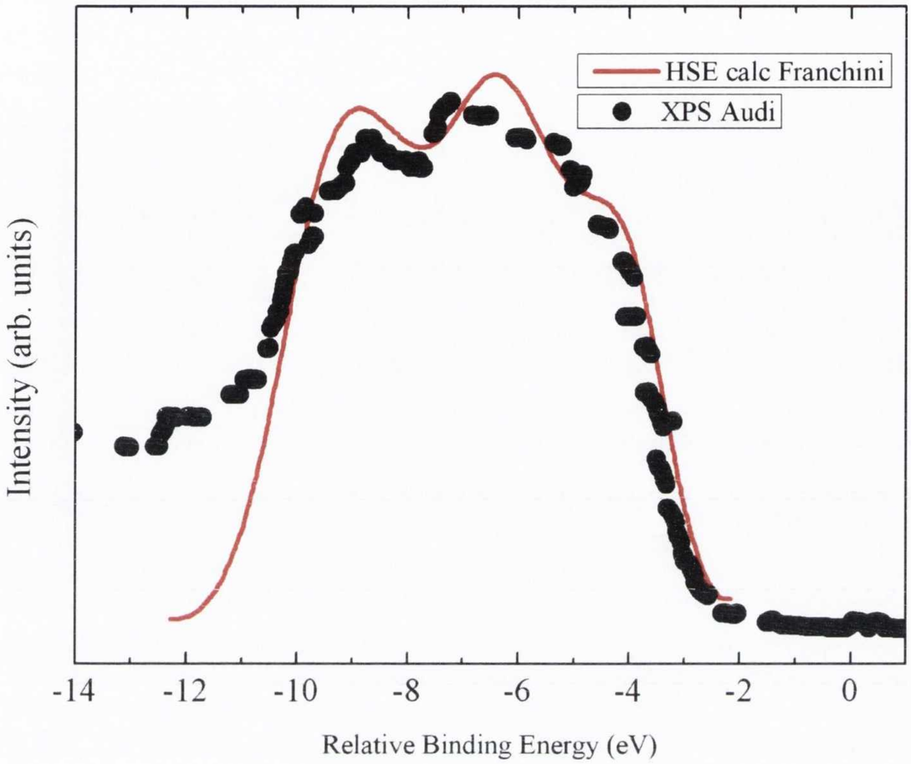

Figure 4.15: Figure adapted from Franchini *et al.* [76]. In black is an XPS spectrum of rutile $\beta$-MnO$_2$ obtained by Audi and Sherwood [77]. In comparison the red full line is the DFT calculated $d$-like DOS using the HSE method through VASP by Franchini *et al.* [76]. Three features can be observed.

are shown to heavily overlap. In experimental conduction band probing via XAS and EELS (see section 4.5.2) they are practically indistinguishable. Thus there is said to be a very large degree of overlap in the conduction band.

The presence of this $\pi$ peak in the near threshold emission is further testament to this, suggesting significant mixing of $p_x\sigma^*$ states especially at these excitation energies and thus a relative increase in $\pi$-character emission. This postulation is further supported by examining the $\pi$ peak in the OOP scattering geometry of Figure 4.16. For the $\mathbf{E}\|c$;XES$\perp c$ geometry in blue the $\pi$ peak remains strong for the first two excitations (a) and (b), again suggesting an abundance of unoccupied $p_x\sigma^*$ states these energies. As the excitation energy is increased into the $\sigma^*$ region in spectrum (c) for the same geometry, the spectral weight of the $\pi$ feature drops off sharply. This could be as a result of the crystal momentum of the bands in this energy region, favouring emission from occupied $p_z$ and especially $p_x$ $\sigma$ states, both of which are allowed in the $\mathbf{E}\|c$;XES$\perp c$ scattering geometry.

At this point it is relevant to ask whether the feature at 526.75 eV can really be attributed to emission of $\pi$ or $p_y$ character. As stated, in the in-plane $\mathbf{E}\|c$;XES$\|c$ spectra of

Figure 4.14, where both $p_z$ and $p_y$ emission are favoured while $p_x$ is precluded, the $\pi$ feature shows consistently higher spectral weight than that of the $\mathbf{E}\perp c$;XES$\perp c$ geometry. Secondly in the OOP $\mathbf{E}\perp c$;XES$\|c$ (red) spectra in Figure 4.16, where $p_z$ and $p_y$ are also favoured, it shows similar consistency. This is especially the case for the $\sigma^*$ excited spectrum (c) where a marked dichroism is observed. Here the core electron is expected to resonantly excite into $e_g\downarrow$ hybridised $p_z$ states, and favour emission of the $p_y$ much more than its orthogonal (also OOP) measurement geometry, as per the argument put forth for the OOP IrO$_2$ $\pi$ feature at the $\sigma^*$ excitation at the end of section 4.5.3.2.

This is not entirely conclusive, and it is difficult to make absolute assertions without higher resolution RXES or, as recommended here, further electronic structure calculations to support (or contra-indicate) these assumptions. However the energy position of the VB $\pi$ feature is the last piece of the puzzle that strongly suggests the $\pi$ peak's primary character conforms to its label. As a first approximation the near octahedral crystal field splits the metal $d$ states into $t_{2g}$ and $e_g$, the latter being more tightly bound. The oxygen $p_y$, in forming any hybridisation in the rutile structure will overwhelmingly favour the lesser bound $t_{2g}$ orbital in a $\pi$-type overlap, though some of it may also be non-bonding in nature. In either case, the $p_y$ states will tend to inhabit the energy region very close to the Fermi level, on both sides of it. Thus examination of both the XAS$^\dagger$ and RXES strongly support the case that the primary threshold ($\pi^*$) peak in absorption contains a considerable density of $\sigma^*$ attributed states.

The $\sigma$ denoted peak at 524.5 eV for the most part follows an opposing trend to the $\pi$ peak. For the IP spectra of Figure 4.5.2, it begins at the threshold excitations with a relatively lower weight than the $\pi$ peak, gradually increasing for higher excitation energies. To a certain extent the same can be said in the OOP spectra of Figure 4.16. This overall trend is likely due to the $k$-selectivity of RXES, where greater range of crystal momentum is selected in the CB, so too is the case for the valence band emission, suggesting that the occupied $\sigma$ bands of MnO$_2$ are largely present at different crystal momentum sites than the threshold unoccupied bands. Another trend of this feature for in-plane scattering is its favoured selection in the $\mathbf{E}\perp c$;XES$\perp c$ measurement geometry, implying it can be attributed primarily as being of $p_x$ character. This is supported by its consistent weight in the OOP $\mathbf{E}\|c$;XES$\perp c$ spectra.

The $\sigma$ shoulder at the bottom of the valence band appears to take on two distinctive and perhaps separable behaviours. The IP spectra shows an anisotropy in VB width, stretching to a lower occupied energy in the $\mathbf{E}\|c$;XES$\|c$ geometry for the threshold spectra, and most distinctively for the $\sigma^*$ excitation (d). For higher energies the dichroism in this feature

---

$^\dagger$As discussed previously in Section 4.5.2.

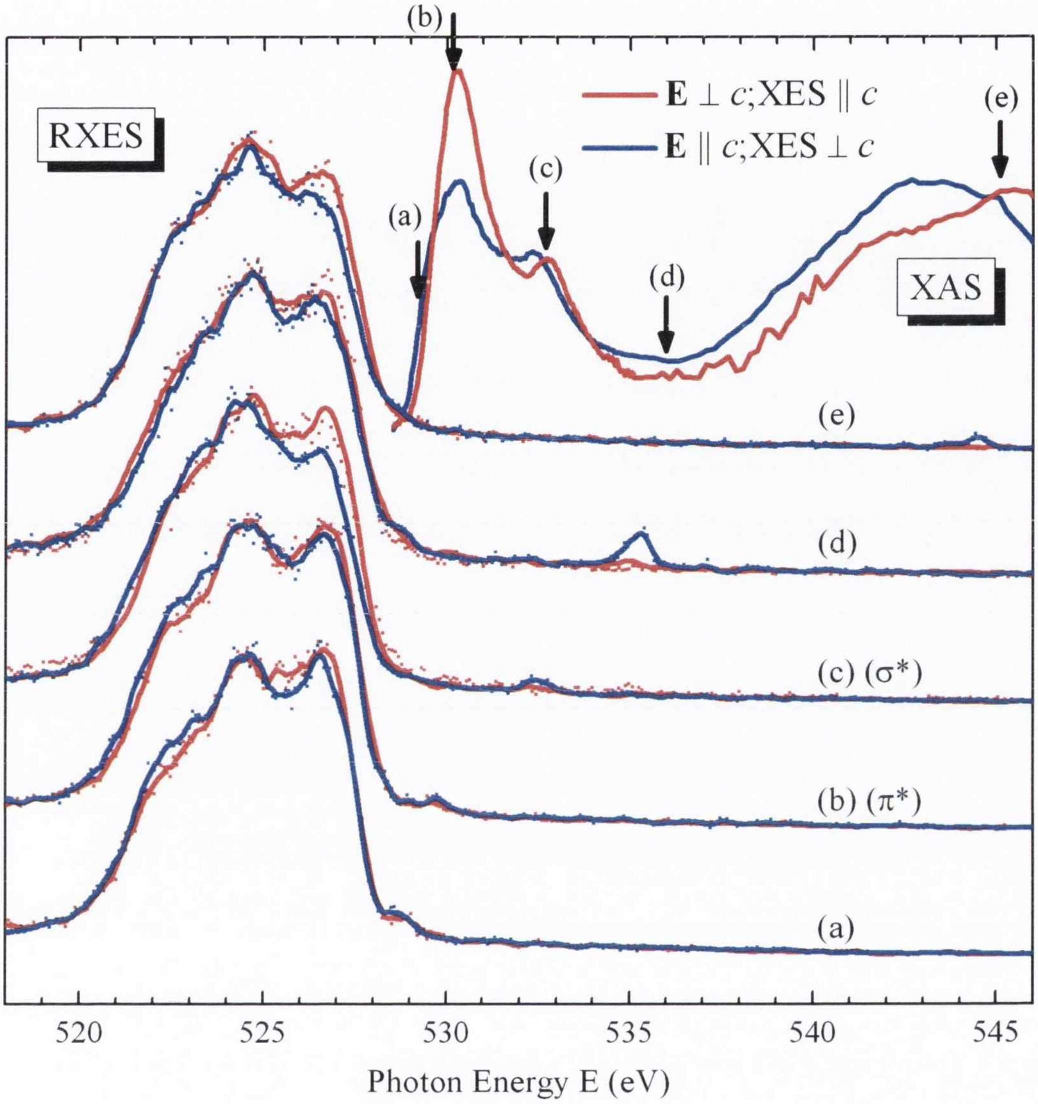

Figure 4.16: Polarisation dependent OOP O $K$-edge RXES of MnO$_2$. $\mathbf{E}\perp c$;XES$\|c$ scattering geometry shown in red and the $\mathbf{E}\|c$;XES$\perp c$ in blue. Labelled arrows on formerly presented and geometrically associated XAS spectra (top) indicate resonant excitation energies. Due to relatively low signal to noise, a 5 point-adjacent averaging was applied to emission line spectra, while scatter points indicate raw recorded data.

disappears or is reduced to an unobservable amount. Thus for this dataset it is attributed to $p_z$, as $p_x$ is not favoured in this scattering geometry.

In the OOP spectra of Figure 4.16, the shoulder feature behaves in a different manner. Instead of a dichroism in the VB width of the feature, the variance is in the spectral intensity or height at a slightly higher energy, possibly suggesting a different or additional origin to that of the IP $\sigma$ shoulder. Like the shoulder observed in the IP spectra, a dichroism is apparent only in the near-threshold excitations, in this case (a) to (c), disappearing for higher energy excitations. That it shows the same dependence on the polarisation vector **E** is surprising, as more often than not it is the spectrometer position that is the deciding factor. It is therefore most likely a feature related to the occupied $p_x$ states, referring specifically to the OOP $\mathbf{E}\|c$;XES$\perp c$, with comparable $k$-values to the shoulder feature observed in the IP RXES.

Broadly speaking for three degenerate $t_{2g}$ orbitals, if all occupied by the same spin, then a spherical charge distribution of the $t_{2g} \uparrow$ should result. Nevertheless, the anisotropy in bonding with the neighbouring O anion, and the various $sp^2$ M–O $\sigma$-like and $p$ M–O $\pi$-like orbitals, would give rise to a dichroism in the observed anion oxygen XES spectra regardless of such degeneracy. With the tetragonal distortion of the octahedron this degeneracy does not exist in $MnO_2$ in any case. The reasonably clear identification of $\sigma$-like features in the O $K$-edge RXES spectra suggest that at some level either the formal valence of Mn in $MnO_2$ as $Mn^{4+}$ or the distribution of the Mn $3d$ electrons as solely being $t_{2g}$ electrons is somewhat inaccurate.

To date electronic structure calculations have neglected to consider the distribution of Mn $3d$ PDOS in the valence band in part because of the difficulty in accurately modelling the bandgap and magnetic structure due to the exchange interaction. It may be the case that the M–O $\sigma$-like bands are almost exclusively of oxygen character.

Finally the insulating nature of $MnO_2$ and the size of the bandgap in particular cannot be accurately probed, bearing in mind the instrumental resolutions employed in XAS and XES, as well as the core-hole broadening. Nevertheless it is interesting to note that unlike $IrO_2$, there is no elastically scattered peak to be observed in the in-plane scattering, arising in part from the insulating nature of $MnO_2$.

## 4.6 Summary and Conclusions

The electronic structures of bulk $IrO_2$ and $MnO_2$ were investigated by a combination of O $K$-edge RXES, XES, XAS and in the case of $IrO_2$, DFT first principle calculations. The natural linear dichroism, resulting from the anisotropic charge distribution or anisotropic chemical bonding surrounding the oxygen anion, was observed in all experimental spectra. The measured O $2p$ PDOS in the conduction and valence band, projected along axes (XAS) or across planes (RXES) parallel and perpendicular to the $c$-axis, was obtained independently.

The basis for the polarisation dependent RXES measurements lies in the separation of states. When the excitation energy is resonantly tuned with $\pi^*$ and $\sigma^*$ states, $k$-selectivity and state-selectivity allowed the observation of specific states of strong $\sigma$ and $\pi$ character respectively.

For $IrO_2$, superior resolution and signal to noise, as well as an inherently distinct separation of the $\pi$ and $\sigma$, and $\pi^*$ and $\sigma^*$ states allowed a more thorough investigation, justifying the calculation of and comparison with the DFT projected PDOS. The unbroadened CB PDOS calculation is a strikingly strong match to recorded XAS. The $IrO_2$ NXES difference spectra showed the location in energy of the spectral weight due to the O $2p_y$ and $2p_z$ VB DOS, perpendicular to the $Ir_3O$ planes, and this was confirmed by comparison with their calculated VB PDOS. In $IrO_2$ there are numerous bands that disperse only slowly with energy, unlike graphite, and that in most instances a significant fraction of the Brillouin zone is selected, bearing in mind the monochromator bandwidth used for the emission measurements. Accepting this allowed us to take advantage of the symmetry selective nature of RXES, by using spectra either by themselves or in the form of difference spectra; it was possible to experimentally isolate all three orthogonal components of the O $2p$ VB PDOS and compare them to theoretical predictions, yielding excellent correspondence.

In $MnO_2$, significant mixing of states in the CB due to exchange splitting made it less achievable to entirely isolate specific O $2p$ components. Nevertheless natural linear dichroism was observed in XAS and also in the vast majority of XES spectra. The XAS dichroism was discussed in the context of previous assignment of the origin of these features, which was well matched by our experiment. This being the first fluorescent emission study of $MnO_2$, features observed were attributed to specific orbital states from a natural linear dichroism perspective using molecular orbital theory.

For the two compounds presented in this chapter, this is the first reported polarisation dependent study at the O $K$ edge. Further, for $IrO_2$ especially, RXES has been shown to be an exceptional probe of the occupied states arising from exploiting the resulting natural linear dichroism, and thus to gain a further experimental insight into the chemical bonding within this material.

# 5 $MgF_2$ and $MnF_2$

## 5.1 Introduction

In this chapter a polarisation dependent X-ray spectroscopic study of the electronic structure of bulk $MnF_2$ and $MgF_2$, using X-ray absorption spectroscopy (XAS) and resonant X-ray emission spectroscopy (RXES) at the fluorine $K$-edge, is presented. In both cases these are compared with original density functional theory partial density of states (PDOS) calculations. Together with comparisons to previously published work, these techniques are used to further explore the electronic structure of these materials with particular focus on the natural linear dichroism at the fluorine $K$-edge and hence electronic structure and anisotropic chemical bonding within these compounds.

A summary review of the literature will be covered in this section, followed in section 5.1.1 by an outline of how rutile fluorides compare to rutile oxides, which comprise the bulk of this body of work. The electronic and physical structures of the compounds will be described in section 5.2. The results section will present and discuss the polarisation dependent RXES, XAS and density functional theory (DFT) calculations, as well as the subsequent analysis, comparison with previous work and new findings.

$MnF_2$ and $MgF_2$ like their counterparts $VF_2$, $FeF_2$, $CoF_2$, $NiF_2$, and $ZnF_2$ are all large band gap insulators that possess a tetragonal rutile $TiO_2$ structural phase. $MnF_2$ is a well known, indeed the prototypical, antiferromagnetic compound, possesses relatively simple structure, and is optically anisotropic. It is thus used as a model system to study magnetic ordering [95,96]. It is transparent in the visual range and its optical properties such as absorption [97] have been documented in the literature for many years. Recently much focus has gone into the study of $MnF_2$ nanocrystals [98]. The electronic structure has been reported [99] calculated by the linear augmented planewave (LAPW) method, as well as experimentally by a host of experimental X-ray spectroscopies such as fluorine $K$-edge near edge X-ray absorption fine structure (NEXAFS) [100–102], non-resonant X-ray emission spectroscopy (XES) at the fluorine $K$-edge [103,104], a very recent publication on RXES at the fluorine $K$-edge [105] as well as resonant emission at the manganese edges [106,107].

$MgF_2$, having a wide band gap, also transmits optically and well into the vacuum ultraviolet (VUV) and infra-red (IR) ranges, and is thus used widely in optics research and instrumentation. In spite of its abundance and availability, studies concerning its electronic structure by X-ray spectroscopic means, or by ab initio calculations are not as prevalent as for other rutile compounds. The literature shows some near edge F $K$-edge XAS performed by Oizumi *et al.* [108] as well as non-resonant soft X-ray fluorescence (SXF) at the fluorine $K$-edge [109]. Ab initio PDOS calculations were performed by Catti *et al.* [110] using an all-electron self-consistent-field Hartree Fock method.

To the best of our knowledge this is the first published polarisation dependent study of the soft X-ray linear dichroism, at the F $K$-edge, in either $MgF_2$ or $MnF_2$. This electronic anisotropy was studied in both the conduction and valence bands through XAS, resonant and non resonant XES as well as ab-initio DFT calculations.

### 5.1.1 Transition Metal Fluorides

Fluorine is the lightest of the group 17 elements, or halogens, and is the most electronegative of the elements. It has an oxidation state of $-1$, as compared to oxygen's $-2$. Thus the metal cations in transition metal difluorides of $MF_2$ structure will possess an oxidation state of $+2$, whereas for $MO_2$ compounds it will be $+4$. While the physical structure may remain similar to analogous oxides, the electronic structure will not. For example manganese(II) fluoride ($MnF_2$) is a wide band gap and thus optically transmitting insulator, whereas manganese(IV) oxide ($MnO_2$[†]) is a narrow bandgap ($\sim$ 0.1 eV) semiconductor. The cation in $MnO_2$ has a $d^3$ occupation, while in $MnF_2$ it is $d^5$. Due to the strong electronegativity of fluorine, transition metal difluorides possess stronger ionic bonding than their oxide counterparts which in turn causes a comparative reduction in the covalency of the compounds.

## 5.2 Physical Structure

Both $MgF_2$ and $MnF_2$ are predominantly ionic compounds that crystallise in the tetragonal phase similar to that of rutile $TiO_2$. Since ionic bonding is electrostatic in nature, it is spherically symmetrical, and hence the most energetically favourable structure of the compound is the closest packed. The nature of this packing then depends on proportional size of the ions, and thus the primary predictor of structure in ionic compounds is the ratio of the atomic radii, $r_+$ and $r_-$. For $0.4 < (r_+/r_-) < 0.7$ a rutile tetragonal structure is predicted. $MgF_2$ and $MnF_2$ have $r_+/r_-$ values of 0.54 and 0.5 respectively. $CaF_2$ on the other hand, with its larger calcium cation, has an $r_+/r_- = 0.75$ and thus it favours a cubic crystal structure. The lattice parameters for MgF$_2$ are $a$ = 4.615 Å and $c$ = 3.043 and $u$ = 0.3030 Å [111]. For MnF$_2$ they are $a$ = 4.857 Å and $c$ = 3.309 Å [98] and $u$ = 0.305 [99].

---

[†] $MnO_2$ is presented in Chapter 4 page 43

## 5.3 Electronic Structure

MgF$_2$ is unique in this study since magnesium is not a transition metal element. It is in group 2 and possesses no occupied $d$ orbitals in its atomic configuration. The electronic structure from the point of view of the cation differs significantly from the other compounds presented in this thesis where the octahedral coordination involves primarily the metal $d$-orbitals. In its stead the metal $p$ and $s$ orbitals contribute to the chemical bonding. Given that difluorides are more ionic than their dioxide cousins, covalent interaction is minimal. In saying that there will still be some small hybridisation interaction of the empty Mg$^{2+}$ 3$s$ and 3$p$ atomic orbitals with the filled F$^-$ 2$p$ orbitals, giving rise to a valence band not wholly located on the F anion.

Unlike MgF$_2$, MnF$_2$ nominally possesses a $d^5$ metal cation. As with other rutile difluorides, the cation is surrounded by six ligand F$^-$ giving an octahedral crystal field, and are considered weak-field ligands. It is then expected that MnF$_2$ is a high-spin or weak-field complex, where the octahedral crystal field splitting parameter $\Delta_O$ (or 10Dq) is less than the spin pairing energy (p)$^\dagger$, and thus conforms with Hund's rule for $d$-orbitals. As a result, each $d$ orbital is populated with a single electron, three in the $t_{2g}$ and two in the $e_g$, giving a crystal field stabilisation energy (CSFE) of $3 \times \frac{2}{5}\Delta_0 - 2 \times \frac{3}{5}\Delta_0 = 0$. Though there is no CSFE, the compound is still stable because of the energetically favourable 3$d^5$ "half-filled" configuration. This is evident in the fact that Mn$^{2+}$ is the most stable and hence common oxidation state of manganese.

The electrons in the half-filled 3$d$ orbitals in MnF$_2$ show an antiferromagnet (AF) spin alignment below the Néel temperature of 67 K, thus doubling the size of its magnetic unit cell when compared to the structural unit-cell. In this AF structure there are two inequivalent alternating spin-up and spin-down Mn sites: Mn1 and Mn2 respectively. Figure 5.2 shows a schematic of the spin alignment on the Mn atoms in this doubled cell, which has new $a$- and $b$-axes directed along the [1,1,0] and [-1,1,0] directions of the original rutile cell. The $c$-axis remains the same. This leads to two inequivalent F sites, since in the MnF$_6$ octahedra the equatorial fluorine anions for Mn1($\uparrow$) (designated F1) will be the axial anions to Mn2($\downarrow$), and vice-versa. A simple diagram showing this arrangement of atomic site–spin relationship is given in Figure 5.1 adapted from Dufek *et al.* [99]. To elaborate on this,

---

$^\dagger$The energy required to pair two electrons in the same orbital.

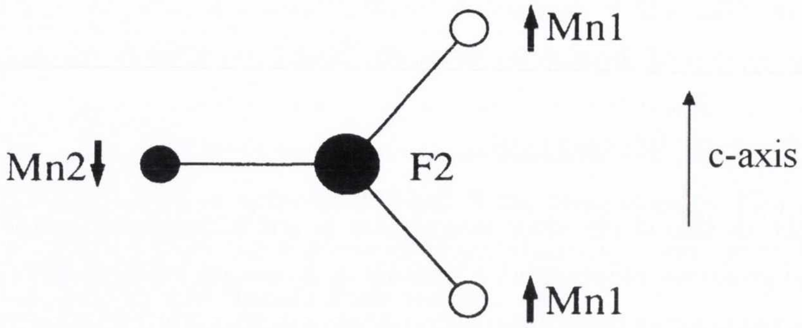

Figure 5.1: $Mn_3F$ plane, containing *c*-axis, showing the relationship between spin and site for manganese and fluorine in $MnF_2$, adapted from Dufek *et al.* [99]

the F1 and F2 sites only designate the relative position of the fluorine atoms with respect to their Mn counterparts, and do not indicate the direction of the spin for either site. As a consequence of the hybridisation with the Mn states, there is also a spin dependence to the F 2*p* density of states (DOS). A DFT calculation of the fluorine 2*p* PDOS (see proceeding section) should therefore produce one set of PDOS for each fluorine site, in each spin alignment. The situation is simplified however in that the F1↑ states are equivalent to the F2↓ states. For clarity the differing states will therefore be referred to as type A and type B F 2*p* PDOS, which are defined by the following equalities :

$$\text{Type A} = \text{F1}\uparrow + \text{F2}\downarrow \qquad\qquad \text{Type B} = \text{F1}\downarrow + \text{F2}\uparrow \tag{5.1}$$

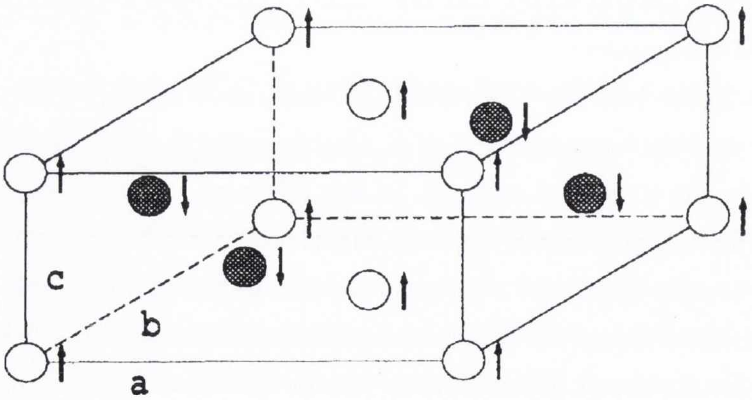

Figure 5.2: Doubled unit cell of $MnF_2$ showing spin alignment (spin↑ and spin↓) of the Mn atomic sites. Adapted from Dufek *et al.* [99]

For the purposes of this study it was deemed sufficient to present the average DOS calculations over the two manganese sites, as well as the F 2*p* states averaged over types A and B. For XAS on the F $K$-edge, this is the correct method of simulation as this technique is a direct probe of the available conduction band (CB) states. For non-resonant (or normal) XES this also applies since no F $1s$ core-hole spin excitation is favoured over another. For RXES however, if one spin is favoured over another at the selected CB energy, the spin will be conserved in the fluorescent process. Hämäläinen *et al.* [112] found this fluorescent spin conservation is maintained in MnF$_2$ at the hard X-ray Mn $K$-edge, and thus it is highly unlikely that spin-flipping occurs at the F $K$-edge. Therefore discussion of F $K$-edge RXES from this compound will require a further selection rule to be accounted for. This is discussed at length in Section 5.6.3 when comparing the calculations with experiment.

## 5.4 Electronic Structure Calculations

In order to make a complete comparison DFT calculations for the electronic structure of MgF$_2$ and MnF$_2$ were performed alongside experimental X-ray spectroscopic results. These calculations employed the full-potential linearised augmented planewave (FP-LAPW) method as implemented by the WIEN2K code. The electronic structure of these compounds was calculated using the observed crystal structure with experimentally determined lattice constants mentioned in Section 5.2.

### 5.4.1 MgF$_2$ Calculations

The electronic structure of MgF$_2$ was calculated using DFT and the FP-LAPW approach implemented in WIEN2K. The observed crystal structure (spacegroup $P4_2/mnm$) and experimental lattice constants were used, as was the experimental anion positional parameter $u$. No further structural relaxation was necessary as this positional parameter resulted in no unbalanced forces on the anion.

The radius of the muffin tin sphere for both Mg and F was set to 1.86 a.u. in each case. The standard settings of the code were employed with the generalised gradient approximation (GGA) of Perdew *et al.* [85] in use. The calculation proceeded until the energy difference of successive iterations converged to below $10^{-4}$ eV. The Brillouin zone was sampled with 3000 $k$-points in order to obtain the DOS and PDOS results presented here, which correspond to a $12 \times 12 \times 19$ shifted $k$-point grid generated according to the Monckhorst-Pack scheme.

The results of the MgF$_2$ calculation are presented in Figure 5.3, which shows the total DOS and the various Mg $s$, $p$ and F $2p$ PDOS components. The top panel shows the total DOS for the unit-cell contrasted with the total fluorine $2p$ PDOS per atom. The middle panel shows the fluorine $s$ component compared with the magnesium $s$ and $p$. The bottom panel shows the fluorine $2p$ PDOS further broken down into three components illustrating

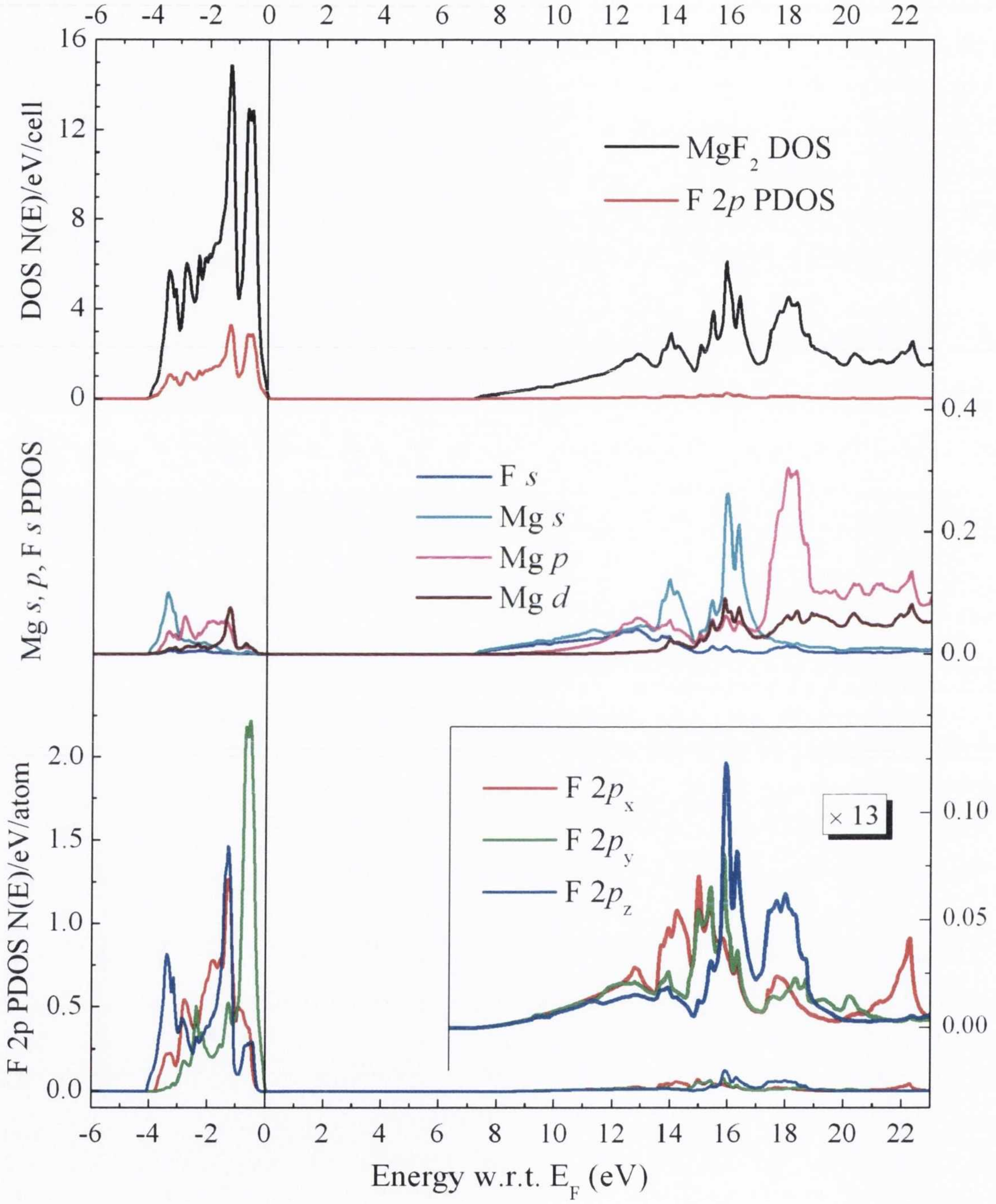

Figure 5.3: PDOS of $MgF_2$. Top: compares the total $MgF_2$ DOS with the total F $2p$ PDOS. Middle: comparing the fluorine $s$ states with the magnesium $s$, $p$ and $d$ states. Bottom: fluorine $2p$ PDOS broken down into its coordinate components $p_x$ $p_y$ and $p_z$, inset shows $\sim$ 13 times magnification of CB states.

its $p_x$, $p_y$ and $p_z$ character according to the natural coordinate frame, identical to that specified for oxygen in Chapter 3, for the Mg$_3$F trigonal plane. Here the local fluorine $z$-axis is projected parallel to the apical Mg–F bonds of the MgF$_6$ octahedron, the $x$-axis along the [001] direction and the $y$-axis protrudes perpendicular to the Mg$_3$F trigonal planes.

Comparing the middle panel in Figure 5.3 with the bottom, including the magnified inset, some of the chemical bonding and interaction can be deduced. While covalent interaction is low in this compound, some hybridisation can be seen in both the CB and valence band (VB) DOS between the F $p_z$ and the Mg $s$ DOS.

The M-F $\sigma$-like bonds which stabilise the structure are primarily bonding Mg $s$ – F $sp^2$ $\sigma$-type bonds, whether involving the Mg–F$_{(\text{apical})}$ $sp^2$ orbital, seen as part of the $p_z$ projection or the two Mg–F$_{(\text{equatorial})}$ $sp^2$ orbitals captured in both the $p_z$ and $p_x$ projections corresponding to the Mg $s$ and F $2p_z$ peaks at -3.5 eV. As previously noted unlike the other transition metal rutile oxides considered here, no $d$-orbitals on the metal cation are expected to participate in bonding. Instead the metal cation $3p$-orbitals participate in Mg $p$ – F $sp^2\sigma$ bonding, principally along the $c$-axis between Mg $p_x$ and F $p_x$ at -2.5 eV and -3.5 eV coincident with the Mg $s$ – F $sp^2\sigma$ peak as noted above.

Indeed the electronic structure of MgF$_2$ has its closest analogue in SnO$_2$ as described by Kennedy [5], where the filled $4d^{10}$ subshell is much lower than the O $2p$ valence band. However, unlike SnO$_2$, there is a $3d$-character ($5d$ in SnO$_2$) PDOS in the valence band which peaks strongly at -1.3 eV, a lower energy than the peak of the F $p_y$ component but is noted as strongly hybridised with the F $2p_x$ and $2p_z$ components giving $e_g - sp^2$ $\sigma$-like molecular orbitals (MOs). The fluorine states that have the least in common with the magnesium are the $p_y$ states. This fits very well with the current understanding, suggesting minimised interaction of $\pi$-character. Instead the $p_y$ orbital is effectively a lone pair, or non-bonding orbital similar to that observed in the prototypical rutile TiO$_2$ [44] or SnO$_2$ [5]. In both of these cases, calculations give a clear separation at the top of the VB where this non-bonding orbital is pinned. The CB minimum on the other hand is dominated by the Mg $3s$ and F $3s$ components.

### 5.4.2 MnF$_2$ Calculations

The electronic structure of MnF$_2$ was calculated using the DFT and FP-LAPW method implemented in WIEN2K. More specifically it replicated the calculations of Dufek, Schwarz and Blaha [99], whereby the antiferromagnetic unit cell, doubled with respect to the rutile unit cell, of spacegroup $C_{mmm}$ (or $D_{2h}^{19}$), was employed with two equivalent Mn sites and two inequivalent F sites, albeit with their spin polarised DOS inverted with respect to each other. Similarly to Dufek et al. [99] the most recent experimental lattice parameters were used to set up the cell with the Mn and F atoms having muffin-tin radii of 2.15 and 1.81 a.u. respectively. The GGA of Perdew et al. [85] was used, as were other parameters relating to the number of plane waves in the calculation as specified by Dufek et al. The Brillouin zone was sampled with 1000 $k$-points for the DOS and PDOS results presented here which correspond to an $8 \times 8 \times 12$ shifted $k$-point grid generated according to the Monckhorst-Pack scheme. The calculation proceeded on a spin polarised basis whereby the calculation was converged once the total energy difference between successive iterations was less than $10^{-4}$ eV.

All calculations resulted in spin dependent DOS. Since, as stated, the spin down of Mn1 is equivalent to the spin up of Mn2, a single spin was calculated for each. For the purposes of this comparative work, where spin is for the most part not preferentially selected, the average density was determined across both. The same was done for the fluorine sites F1 and F2 which, unlike the Mn sites, display only very minor differences. For a given Mn site, the spin is reversed on either side of the Fermi level. For example take the Mn1 site, then the occupied $3d$ $e_g$ and $t_{2g}$ orbitals are spin$\uparrow$ while the unoccupied are spin$\downarrow$; on an Mn2 site the reverse is the case. This is the crux of the antiferromagnetic $d^5$ state on each neighbouring Mn atom, as depicted in Figure 5.2.

Figure 5.4 shows in the top panel the calculated PDOS for the Mn $3s$, $3p$ and $3d$ components contrasted with the F $2p$. The bottom panel breaks the F $2p$ down further into its $p_x$, $p_y$ and $p_z$ components in the same manner as was done for the $MgF_2$. As expected the presence of the manganese $d$ orbitals show a significant contribution to the total DOS, though because this compound is significantly more ionic than its oxide counterpart $MnO_2$ (investigated in Chapter 4 page 43) the degree of hybridisation between the metal and ligand orbitals is less distinct. Some interaction is noted with the main fluorine $2p$ VB PDOS between $-8$ and $-4$ eV from the manganese $d$ PDOS, this being especially true of the $p_x$ and to a lesser extent $p_z$. The $p_y$, in a similar manner to the $MgF_2$, has little overlap with the metal valence states, showing a lack of $\pi$-character orbital overlap, and it too is effectively a lone pair or non-bonding orbital.

Moving to the conduction band, the main manganese $3d$ PDOS are strongly hybridised with the fluorine $2p$. On any given Mn site the unoccupied $3d$ states are of a different spin character to the occupied $3d$ states on that Mn. The first peak in the unoccupied $3d$ states at $\sim 3$ eV is of mostly $t_{2g}$ character and the second at $\sim 4$ eV is primarily $e_g$. Comparing the fluorine states at the same energy, it is clear the $p_y$ hybridises almost exclusively with the $t_{2g}$. Recall from Chapter 3 that the near octahedral ligand field can be approximated as splitting the metal $d$ orbitals into $t_{2g}$ and $e_g$, and only the $t_{2g}$ possesses lobes that have an effective net overlap with the anion's $p_y$ orbital. However because of the strong $2p_x$ and $2p_z$

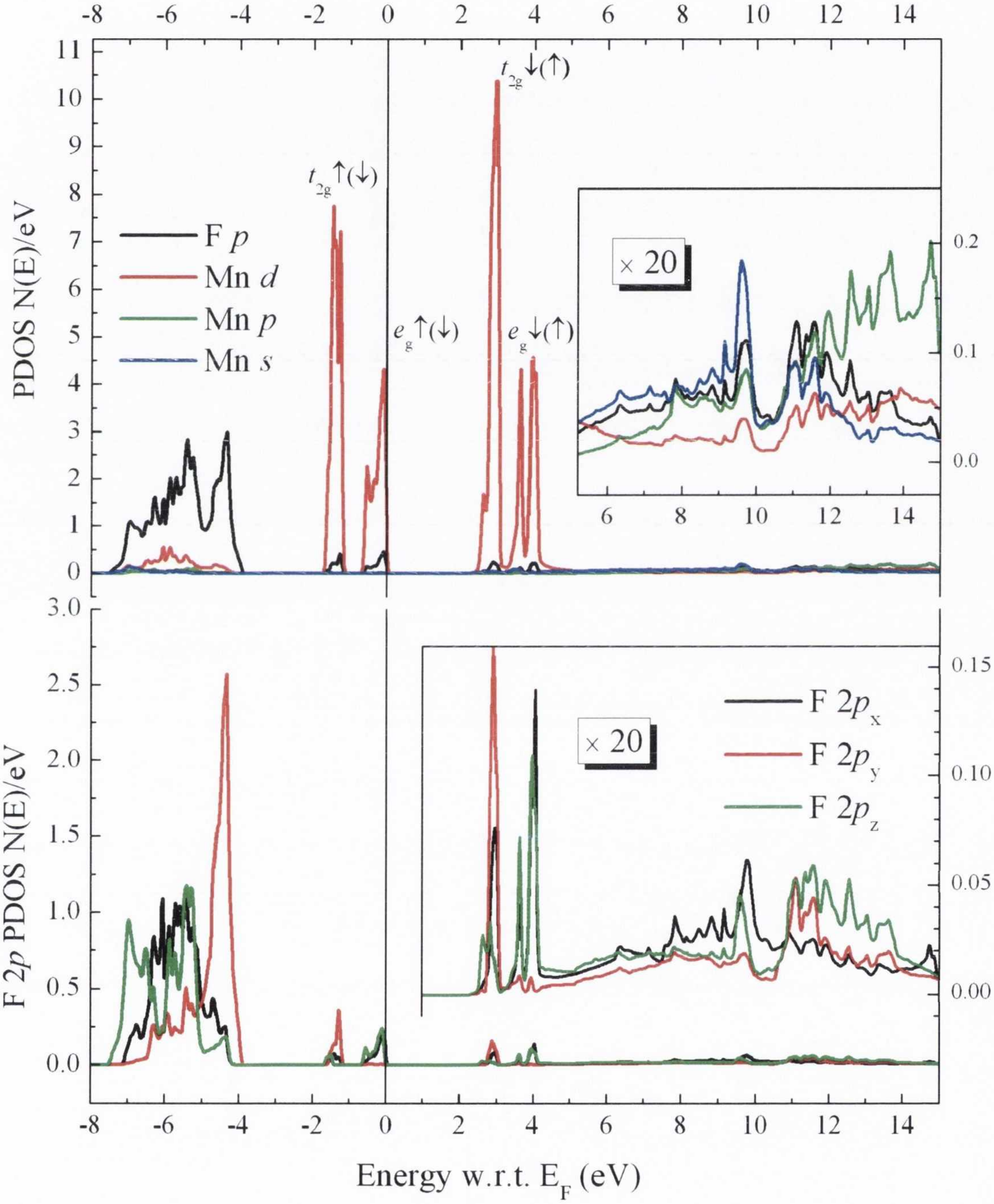

Figure 5.4: PDOS of MnF$_2$. Top part: total fluorine $2p$ states compared to total manganese $s$ $p$ and $d$ components. Bottom part: fluorine $2p_x$, $p_y$ and $p_z$, inset shows $\sim$ 20 times magnification of CB states.

components at $\sim 3$ eV, it is clear that this peak cannot solely be of $t_{2g}$ character. Focusing on the unoccupied fluorine $2p$, note should be made of the difference in states comparing the $p_x$ with the $p_y$ and especially $p_z$ between approximately 11 eV and 14 eV. This difference will discussed in greater detail in the experimental results section of this chapter.

## 5.5 Experimental Measurements

The $MgF_2$ bulk crystal was acquired commercially from CRYSTAL GmbH, measuring approximately 10 mm × 10 mm × 2 mm. One of the large surfaces was polished and corresponded to the (001) crystal plane.

The $MnF_2$ bulk crystal was acquired from Professor G. Frank Imbusch of the National University of Ireland, Galway [113]. It measures approximately 10 mm × 5 mm × 4 mm. Since rutile tetragonal difluorides tend to be optically transmitting, they polarise optical wavelengths about their axis of symmetry. Thus the crystal $c$-axis orientation was determined using cross polarisers, and was found to lie perpendicular to the largest surface. So, similar to the $MgF_2$, the main surface contained the (001) crystal plane.

Polarisation dependent RXES and XAS spectroscopy were performed on both samples at the fluorine $K$-edge. All measurements were performed at beamline I511-3 bulk station MAX-lab in Lund, Sweden.

### 5.5.1 Sample Preparation and Mounting

The $MgF_2$ was cleaved in air to create a more manageable sized sample. Its surface was prepared by light rubbing with isopropanol and then ethanol. Both crystals were mounted flat, with the crystals' respective (001) surface parallel to the surface of sample plate at beamline I511-3 at MAX-lab in Lund, Sweden. The $MnF_2$ was cleaned vigorously with isopropanol to remove surface contaminants, and glue from former mounting in non vacuum experimental set-ups. It was then sputtered briefly with argon ions in vacuum to prepare a clean surface and examined with X-ray photoemission spectroscopy (XPS) before being transported in atmosphere to MAX-lab.

### 5.5.2 Experimental Setup

Beamline I511-3 contains a U5.0 undulator together with a SX-700 monochromator with an energy range of $50 - 1500$ eV, a flux of $10^{11} - 10^{13}$ photons per second and a maximum resolving power of 11,000 [24]. The endstation allows both electron yield and fluorescence yield, via a microchannel plate (MCP), to be acquired. It also possesses a Nordgren type X-ray spectrometer [18] which is at 90° to the incoming synchrotron beam but is rotatable about the axis of the beam to allow access to the out-of-plane scattering geometry [24].

All fluorine $K$-edge emission spectra presented were acquired with the spectrometer in its standard position and thus with an in-plane scattering geometry. The beamline monochromator slits were set to 200 $\mu$m or 1 eV resolution, the spectrometer slits were 22 $\mu$m, equivalent to 0.7 eV resolution. For absorption scans the beamline monochromator slits were reduced to 30 $\mu$m or 0.15 eV resolution.

For measurements on both difluoride samples the two distinct in-plane crystal scattering geometries were utilised, designated $\mathbf{E}\|c$;XES$\|c$ and $\mathbf{E}\perp c$;XES$\perp c$. Given the (001) surface geometry of the crystals, the former geometry required the beam to be at grazing incidence to the sample surface, with its $c$-axis approximately parallel to the optical axis of the spectrometer, and hence also approximately parallel to the polarisation vector $\mathbf{E}$ of the horizontal linearly polarised beam. A 10° deviation from grazing incidence was required to allow the beam to be easily positioned on the samples. The XAS scans in this geometry were acquired with the same deviation in polar angle. For the second geometry, $\mathbf{E}\perp c$;XES$\perp c$, fluorescent spectra were taken at a near normal incidence of the beam, with a 15° deviation to allow a sufficient flux to enter the spectrometer slits via a grazing exit of the emitted photons towards the emission spectrometer. The XAS scans for this geometry however were taken at exactly normal incidence. Due to the high resistivity and physical thickness of the samples, total electron yield (TEY) measurements of absorption were not practical. Thus all experimental XAS spectra presented were recorded by total fluorescence yield (TFY). TFY absorption measurement has a number of advantages over TEY; fluorescence is more bulk sensitive due to its significantly reduced attenuation when compared to secondary electrons. It also known to be low background and is insensitive to applied electric or magnetic fields. However, due to self-absorption and resonant effects it is not considered completely representative of true absorption [114]. In the present case of wide band gap insulators where the valence and conduction band states are localised, core-level excitonic states may cause screening, lowering the energy of valence band emission. The latter should have little effect on a TFY measurement, and self-absorption is usually insignificant at the $K$-edge of light elements due to the lack of adjacent emission lines. However, the strongest effect on TFY is the changing illuminated volume of the sample, which contributes to the non-linear saturation of the TFY for strongly absorbing in the XAS due to increased photon absorption cross-section and decreased photon penetration depth.

## 5.6 Results and Discussion

### 5.6.1 F *K*-Edge X-Ray Absorption Spectroscopy

Figure 5.5 and 5.6 show the experimental and simulated polarisation dependent X-ray absorption spectra of $MgF_2$ and $MnF_2$ respectively at the fluorine $K$-edge. The monochromator energy for the experimental spectra was calibrated by comparing to the known nearby Fe $L_3$ $2p_{3/2}$ absorption peak of metallic Fe. The two measurement geometries, as discussed in the previous section, correspond to $\mathbf{E}\|c$ in blue and the orthogonal $\mathbf{E}\perp c$ in red. The x-axis alignment of the calculated PDOS to the experimental spectra is approximate, with an estimated VB maximum energy of 679 eV and 685.15 eV for $MgF_2$ and $MnF_2$ respectively.

The experimental spectra are compared to previously published F $K$-edge XAS spectra of $MnF_2$ by transmission through thin-films by Nakai *et al.* [101], powdered $MnF_2$ by Vinogradov *et al.* [102] and that of Jiménez-Mier *et al.* [103], the latter two were measured via TEY. None of these methods suffered from the saturation observed in our TFY data, but neither do they take into account the polarisation dependence or the natural linear dichroism to be expected in those compounds.

The simulated spectra correspond to the fluorine $2p$ conduction band PDOS. In the $\mathbf{E}\|c$ experimental geometry, the absorption accesses and therefore represents the projected F $2p_x$ densities of states along the $c$-axis. Due to the dipole selection rules these are limited to the F $2p$, specifically excitation into $p_x$ states as a result of the geometric selectivity of natural linear dichroism [8]. Similarly the $\mathbf{E}\perp c$ absorption geometry gives an equal and averaged projected DOS of the F $2p_y$ and $2p_z$. This is understood from the rutile structure, where two orthogonal sets $Mg_3F$ trigonal planes lie parallel to the rutile $c$-axis, in which the local $x$ coordinate also lies parallel. These calculated PDOS components were convolved with a combined Gaussian of 0.2 eV and Lorentzian of 1.2 eV. The full-width half-maximum (FWHM) were chosen to account for the instrumental broadening, and the fluorine $1s$ core-hole lifetime broadening respectively. The significance of the latter width accounts for a further contribution from the vibrational envelope associated with excitation on a fluorine site. There is a very large variation of F $1s$ core-level line widths associated with simple fluorine molecules, ranging from 1.2 eV for $F_2$ to 2.63 eV for $XeF_6$ [115]. The value used here is at the lower end of the scale, nevertheless a very satisfactory agreement between theory and experiment is reached.

#### 5.6.1.1 XAS of $MgF_2$

Overall the comparison between the calculation and experimental dichroism for the fluorine $2p$ conduction band PDOS in the upper panel of Figure 5.5 is good. Most of the features,

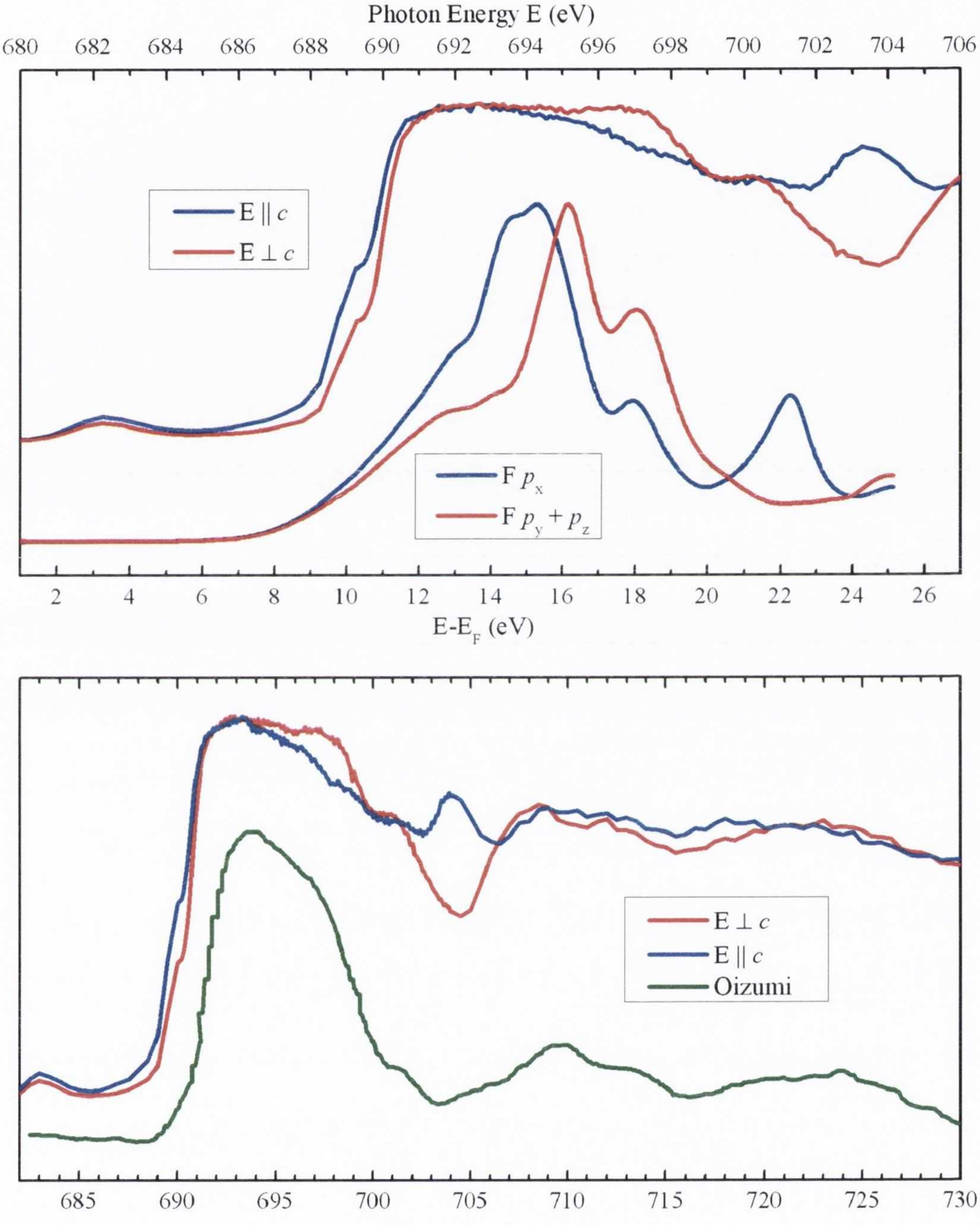

Figure 5.5: Top panel shows XAS of MgF$_2$ at the fluorine $K$-edge for two measurement geometries $\mathbf{E}\perp c$ and $\mathbf{E}\|c$ measured in TFY compared with the simulated XAS for the two geometries, created from the $p_x$ and average $p_y + p_z$ calculated CB DOS respectively. These were then broadened by convolution with a Gaussian and Lorentzian concurrent with the instrumental and core-hole lifetime broadening. Bottom panel gives the raw FY XAS counts for the same measurements but graphed over a broader energy range. This is then contrasted with previous transmission XAS measurements obtained by Oizumi *et al.* [108].

especially those that differ between the two excitation geometries and thus pertain to the anisotropic chemical bonding of the material and natural linear dichroism, are replicated very well by the component PDOS calculations. Both geometries show an inflection point, or shoulder, on the threshold slope of the F $K$-edge onset. Their relative intensities, and to some degree their positions, differ between the geometries. The simulated spectra predicts this well, though they are not as pronounced in the experimental spectra. Similarly the relative shift of spectral weight in the $\mathbf{E}\perp c$ geometry at approximately 697 eV is also predicted. This results almost completely from the F $p_z$ states, which upon examination of the DOS calculations in Figure 5.3, interacts relatively strongly with both the magnesium $3s$ and $3p$ states at this energy. The last dichroism related feature is the peak in the blue $\mathbf{E}\perp c$ absorption scan at about 703 eV, which in the other geometry displays a notable drop. This anisotropic feature duplicated in the calculations, though predicted at a lower energy, and thus is attributed purely to the fluorine $p_x$. Again looking back at Figure 5.3, this has some overlap with the Mg $3p$, but not $3s$ at this energy.

Apart from an excellent prediction of the details of dichroism, the simulated spectra fail when comparing to the overall shape of the spectra. For an absence of dichroism in, say an XAS scan of an unoriented (powder) $MgF_2$ sample, this might suggest a poor match. Most notable in the difference is the relatively featureless plateau between 690 and 698 eV, where the intensity is not predicted to be so high near threshold. This plateau also appears to shift the predicted features to a higher energy. This is similarly the case for $SnO_2$ [5,116–118], and it may be that an local density approximation (LDA)+$U^{SIC}$ calculation involving a self-interaction correction will adequately account for the unoccupied density of states and the underestimated separation between features in the spectrum. This may be only part of the solution however. The disagreement in the shape of the calculations and experiment, but agreement of features and behaviour is very similar to that found for the Mn $K$-edge of MnO by Soldatov *et al.* [119] who attributed the disagreement partially to failings in the small cluster model they utilised. The use of a relaxed potential instead of a more realistic model that includes a core hole effect may explain the underestimation of the threshold features' intensity.

The lower panel of Figure 5.5 gives a broader energy range of the measured XAS FY[†] and compares it to the transmission XAS measurements obtained by Oizumi *et al.* [108]. Overall the features are seen to correspond very well. The difference between the spectra arises from the natural linear dichroism and the apparent blunting of high-absorption features inherent in FY measurements, as discussed previously in Section 4.5.2 for $MnO_2$. The net effect is that the FY (or TFY) represent something similar to an inverse logarithm of absorption intensity, which explains why the same drop in intensity seen in the the spectrum obtained by Oizumi *et al.* after the initial threshold strong features is not mimicked to the same degree in the presented measurements.

---

[†] Not normalised to flux, but raw counts.

In transition metal compounds, the metal valence orbitals will often have an abundance of states near the Fermi energy, for example the Mn states of MnF$_2$ in Figure 5.4. These states, especially those (usually $t_{2g}$) nearest the Fermi energy, contribute strongly to core hole screening in the excited state [14]. The lack of $d$-orbitals and hence electrons near the Fermi level in MgF$_2$ implies a stronger core-hole effect, and is thus attributed to the threshold intensity disagreement between theory and experiment in the conduction band.

### 5.6.1.2 XAS of MnF$_2$

Similarly for MnF$_2$, the two possible geometric orientations of the electric field vector with respect to the $c$-axis, $\mathbf{E}\perp c$ and $\mathbf{E}\| c$, were employed in obtaining F $K$-edge XAS spectra. Figure 5.6 compares these two F $K$-edge XAS spectra of MnF$_2$ with the simulated spectra from the fluorine $2p$ PDOS components, similar to that of MgF$_2$ in the previous section. A clear dichroism is observed in the XAS, mirrored very well in the calculated PDOS. The first two peaks at 688 and 689.5 eV display an expected natural linear dichroism and result from fluorine $p$ hybridisation with the metal $d$ bands.

The first peak at 688 eV in the $\mathbf{E}\perp c$ geometry is dominated by transitions to the F $2p_y$ unoccupied orbital which forms a $\pi^*$ MO with the Mn two $d_{z(y-x)}$ as well as partly with the Mn $t_{2g}$ $d_{z(y+x)}$, though in the latter case the hybridisation is weak. When in the $\mathbf{E}\| c$ geometry, this same feature at 688 eV is dominated by transitions to the F $2p_x$ unoccupied orbital which, of the three nearly degenerate $t_{2g}$ orbitals located at this position of $\sim 2.8$ eV in the CB, appears to be hybridised most strongly with the Mn $d_{z(y+x)}$. Jiménez-Mier *et al.* commented on this [103] when comparing Mn $L$-edge XAS multiplet spectra with F $K$-edge XAS spectra by visual aligning of the features.[†]

The second peak is much more clearly designated the $e_g$-$\sigma^*$ derived feature, comprised almost equally between $d_{z^2}$ and $d_{x^2-y^2}$ as seen in the unbroadened PDOS at $\sim 4$ eV above the VB maximum in Figure 5.7. By comparing with the earlier Figures 5.4 and 5.7 of the calculated MnF$_2$ PDOS, it can be seen that the unoccupied fluorine $p_y$ states hybridise significantly with this $t_{2g}$ bands but are almost zero for the $e_g$. The $p_z$ states are almost the opposite, showing a significant overlap with the $e_g$ at this energy, while the fluorine $p_x$ hybridise to some extent with both. Further, while the $\mathbf{E}\perp c$ will pick out the F $2p_z$ component and its hybridisation with the $d_{z^2}$, and to a lesser extent the $d_{x^2-y^2}$ component, the $\mathbf{E}\| c$ geometry will pick out the F $2p_x$ component which strongly hybridises with the

---

[†] Figure 3 of [103].

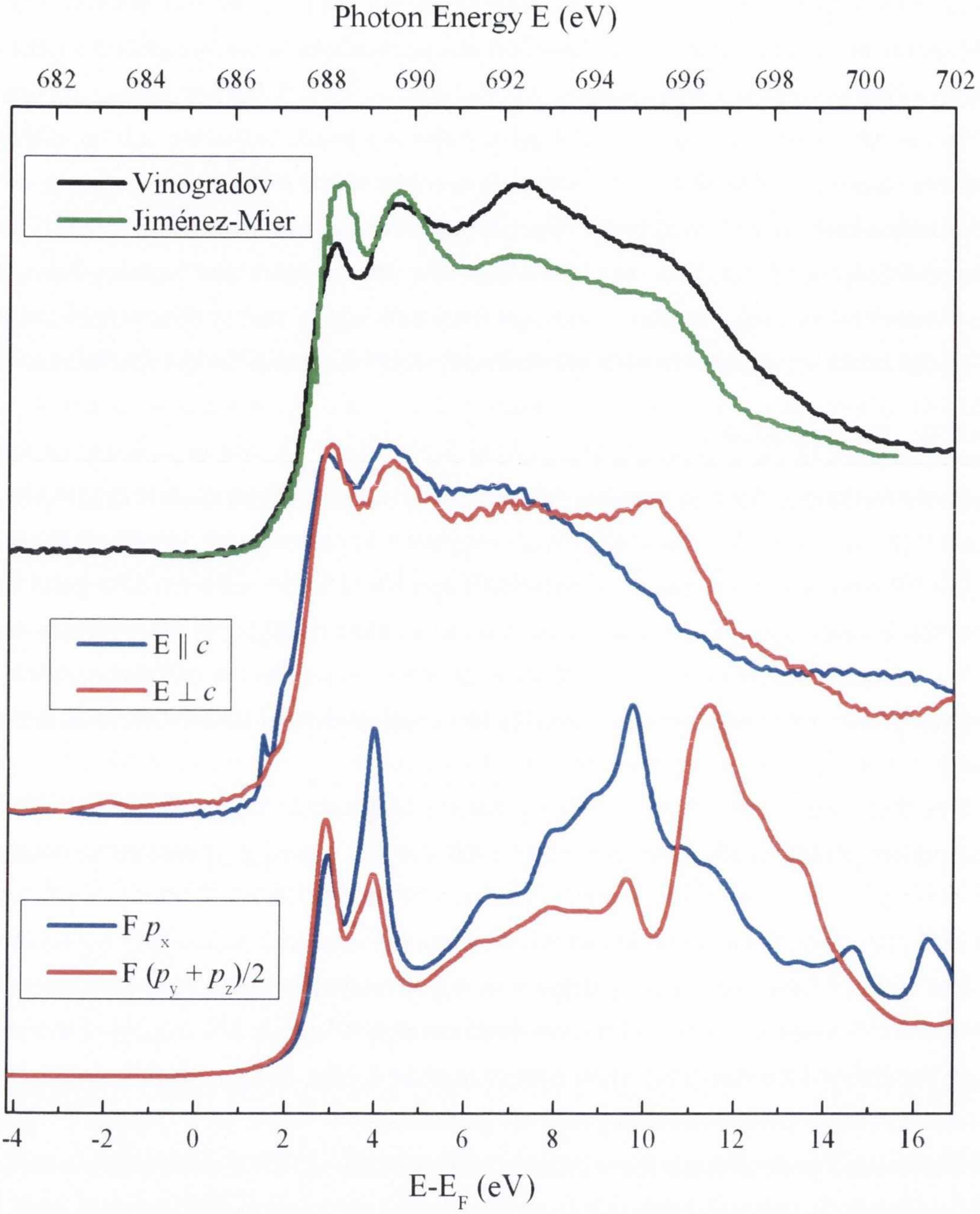

Figure 5.6: XAS of $MnF_2$ compared to calculations and previous measurements from the literature. Top reproduces XAS measurements from Jiménez-Mier *et al.* [103] and Vinogradov *et al.* [102]. Middle shows XAS of $MnF_2$ at the fluorine $K$-edge for two measurement geometries $\mathbf{E}\perp c$ and $\mathbf{E}\|c$ measured in TFY mode. Bottom are the simulated XAS for the two geometries, created from the fluorine $p_x$ and average $p_y + p_z$ calculated CB DOS respectively. These were then broadened by convolution with a Gaussian and Lorentzian concurrent with the instrumental and core-hole lifetime broadening.

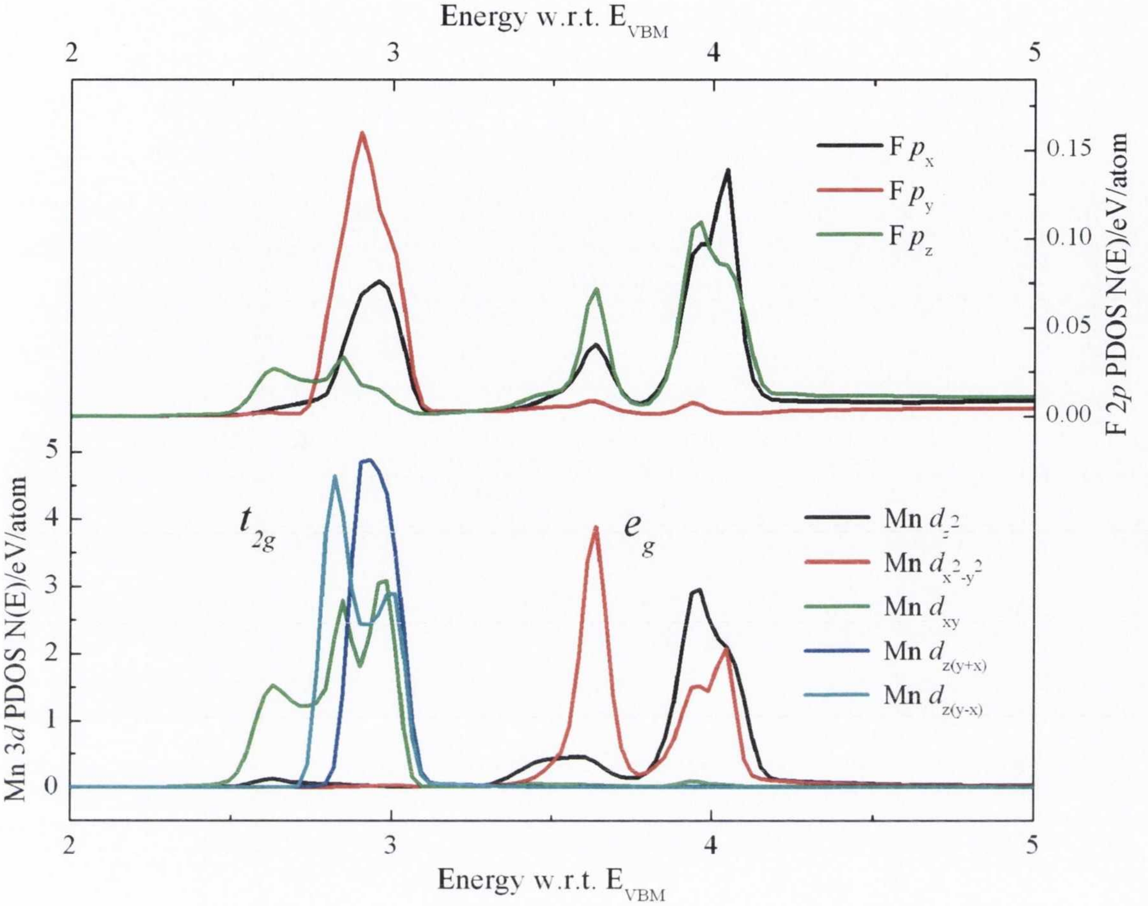

Figure 5.7: Conduction band calculated PDOS for MnF$_2$ illustrating the detailed hybridisation or correspondence between the unoccupied F 2$p$ and Mn 3$d$ orbitals

upper portion of the $d_{x^2-y^2}$ band at ~ 4 eV. Though not clearly distinguishable as a peak, the low valley close to 688.8 eV between these two peaks (in Figure 5.6) is dominated by the less intense F $2p_x$ and $2p_z$ components hybridised with the lower part of the $d^{x^2-y^2}$ $e_g$ component at ~ 3.6 eV above the VB maximum, forming the lower Mn–F $e_g - sp^2$ $\sigma*$ feature.

Since the red $\mathbf{E}\perp c$ XAS spectrum is a mixture of both the $p_y$ and $p_z$, a reasonable intensity balance between the two peaks in either geometry is expected. Though as the simulated spectra in Figure 5.6 show, some dichroism is still expected. This is observed in the experimental spectra in the relative heights of the two peaks in both geometries. Higher in energy a large difference in spectral weight is observed in the spectra, the red $\mathbf{E}\perp c$ intensity increasing well above the $\mathbf{E}\|c$ at approximately 695 eV and then below it again at 700 eV. The simulated spectra emulate these features imperfectly, but nevertheless with a good correspondence.

Unlike the MgF$_2$ simulated spectra, the shape of the F $K$-edge is considerably better, and the energy position of the features is predicted with a greater accuracy. If anything the projected F $2p$ PDOS appears slightly stretched along the energy axis with respect to the experimental measurement, which is the opposite of the $MgF_2$ where the simulated PDOS features are noticeably compressed. The improved shape agreement between theory and experiment of the $MnF_2$ in Figure 5.6 over the $MgF_2$, as well as the difference in behaviour[†] could come down to the core hole screening effects of the occupied Mn $3d$ $t_{2g}$ hybridised states, not present in $MgF_2$.

Lastly, focusing on the previous XAS measurements obtained by Jiménez-Mier *et al.* [103] and Vinogradov *et al.* [102] replicated in the upper part of Figure 5.6, the features are consistent with the presented measurements, saving for the dichroism. This is especially the case for the more recent measurements from Jiménez-Mier which strongly resembles a spherically symmetric[‡] hybrid of our bulk polarisation-dependent measurements. Both reproduced spectra were performed on commercially acquired powdered samples of nominal purity, and were measured in TEY mode. The disparity in relative peak intensity of the Vinogradov XAS could be attributed to mild impurity of the sample.

### 5.6.2 Polarisation Dependent NXES and RXES of $MgF_2$

For the purpose of simulating experimental-like spectra, occupied F $2p$ PDOS calculations were broadened with a combined Lorentzian of 0.25 eV and Gaussian of 0.5 eV, to account for the core-hole lifetime and instrumental width respectively. Though these overestimate the expected resolution, correspondence with experimental spectra was nevertheless satisfactory.

The valence band fluorine $2p$ PDOS for $MgF_2$, like its conduction band counterpart, can be broken down into its $2p$ $x$, $y$ and $z$ components. This is illustrated, along with the total fluorine $2p$ PDOS in Figure 5.8b broadened DFT calculations. As with the other rutile and rutile-like compounds in this doctoral thesis, the PDOS may be categorised into two types, $\sigma$ and $\pi$ like states. Though the rutile fluorides are primarily ionic in nature, it is still instructive to associate orbital components with their expected M–F hybridised molecular orbitals. The $\sigma$ component comprise the addition of the fluorine $2p_x$ and $2p_z$ which lie in the $sp^2$ hybridised $Mg_3F$ trigonal plane which contains the orbital lobes that form a $\sigma$-type overlap with the magnesium $3d$ $e_g$ valence orbitals. The $\pi$ component is comprised purely of the fluorine $p_y$, that lies perpendicular to this trigonal plane and shows characteristics of being mostly a non-bonding orbital, but may interact still in a $\pi$-like fashion. The calculated VB PDOS are presented in terms of this division of states in Figure 5.8a. Also shown are

---

[†] $MnF_2$ calculations spread features across a broader energy range, whereas the $MgF_2$ calculations compresses them.

[‡] Equal contributions from F $2p_x$, $2p_y$ and $2p_z$.

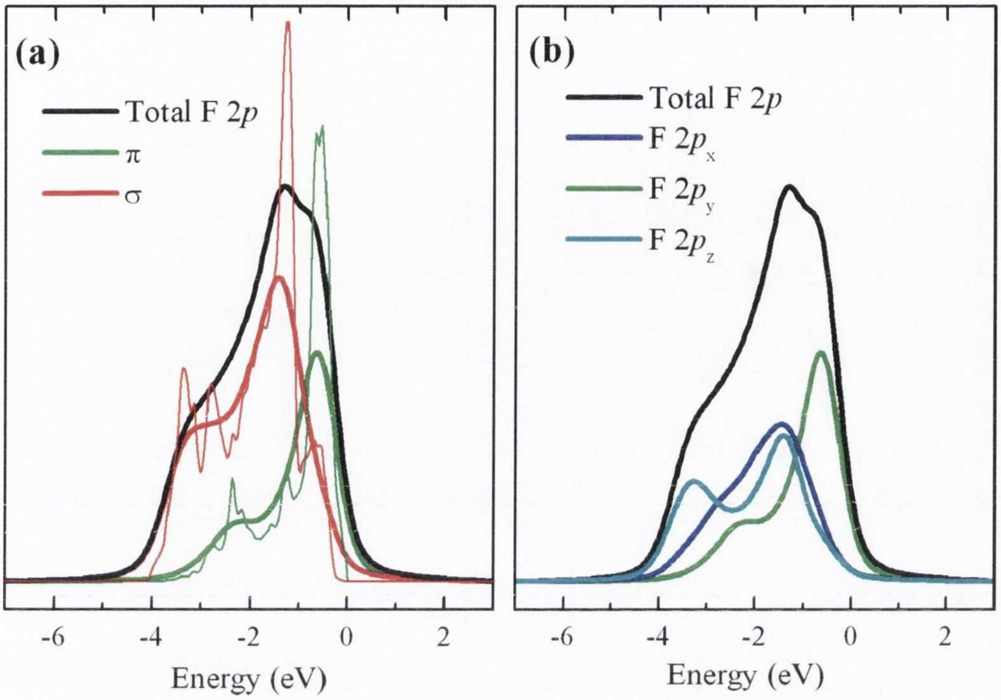

Figure 5.8: Part **(a)** shows the total fluorine $2p$ VB DOS for MgF$_2$ broadened to simulate core-hole and instrumental broadening of XES, this is then shown split into its component $\pi$ and $\sigma$ states, the unbroadened calculation of each overlaid. Part **(b)** breaks this down further showing the simulated fluorine VB $p_x$, $p_y$ and $p_z$ components of the PDOS which should correspond to the emission.

the unbroadened raw PDOS of these two components. The familiar shift of spectral weight of the $\pi$ component toward the valence band maximum is clearly present, as with the rutile oxides, particularly both TiO$_2$ and SnO$_2$ [5,44].

Both resonant and non-resonant XES spectra were acquired for the two orthogonal scattering geometries. The upper part of Figure 5.9a shows the F $K$-edge NXES spectra of MgF$_2$ acquired at 708.25 eV, approximately 22 eV above the F $K$-edge XAS threshold in these geometries. A clear dichroism can be observed between the two spectra.

In creating simulated NXES spectra, it is important to note that the excitation is above the ionisation threshold, so the intermediate excited state does not have a specific value of crystal momentum or $k$-value because the outgoing photoelectron's momentum is no longer well correlated with the crystal momentum of the intermediate state. Thus in NXES, all possible occupied $2p$ states contribute equally in the observed radiative decay of the $1s$ core hole, giving rise to a $k$-unselective spectrum spanning the Brillouin zone and reflecting the integrated oxygen $2p$ PDOS. Similarly, as the excitation energy lies above the observed region of dichroism in absorption, the electric polarisation vector $\mathbf{E}$ of the incident photon is

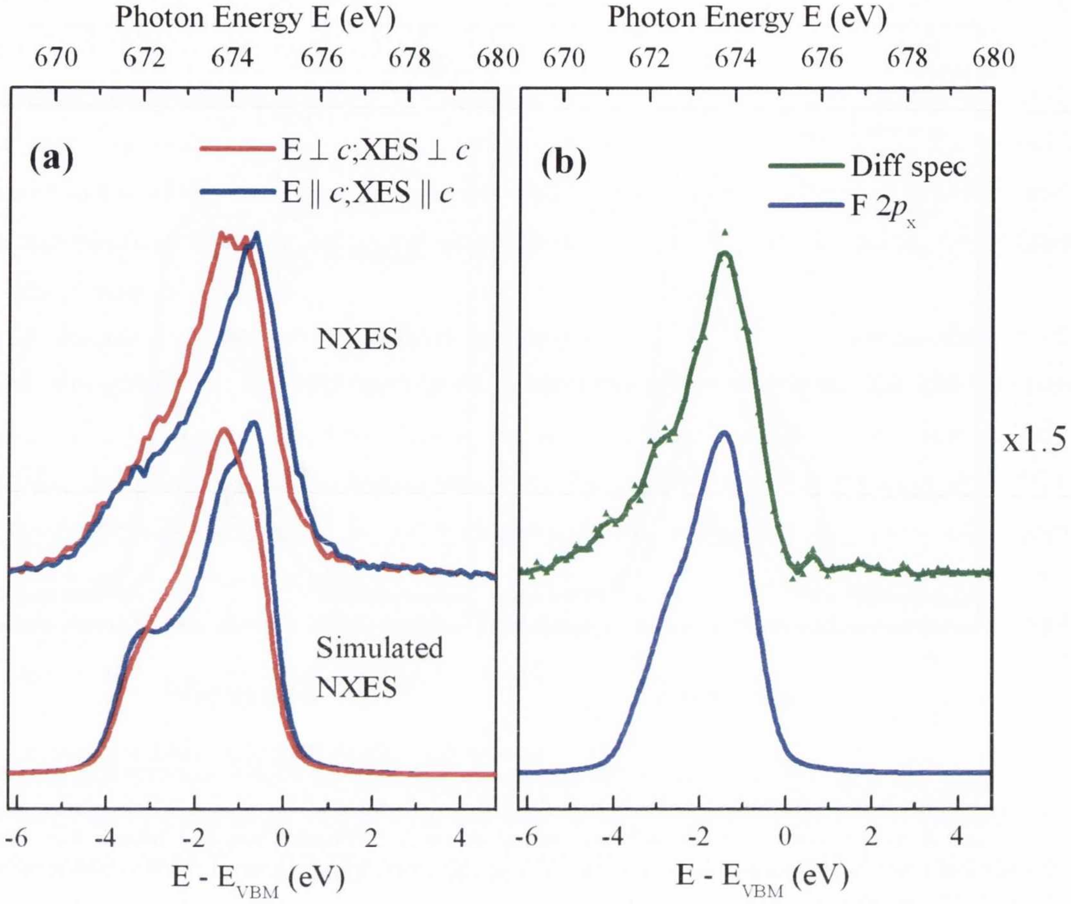

Figure 5.9: $MgF_2$ NXES and difference spectrum compared with theory. **(a)** compares the measured NXES on top in both measurement geometries, with the simulated NXES spectra below. The simulated spectra are a broadened addition of the $p_y + p_z$ for the XES$\|c$, and $p_x + (p_y + p_z)/2$ for the XES$\perp c$ measurement geometry. The upper portion of part **(b)** shows the 3-point adjacent-average smoothed difference spectrum (line) and raw difference spectrum (triangles) created by the subtraction: XES$\perp c-$XES$\|c\times 0.6$. Below is the comparison with the simulated $p_x$ component of emission.

unimportant, and the spectrometer position with respect to the crystal geometry becomes the contributing factor of the observed emission dichroism.

In the NXES, the emission observed is from the total F $2p$ projected densities of states in the plane perpendicular to the optical axis of the spectrometer. In the case of the $\mathbf{E}\|c$;XES$\|c$ (or just XES$\|c$ for NXES) spectrum this comprises the $a-a$ plane and contains only $2p_y$ and $2p_z$ components. The XES$\perp c$ scattering geometry gives the projected DOS from the $c-a$ plane, and thus will produce varying contributions from all three fluorine coordinated $p$-orbitals. The exact breakdown in creating the XES$\|c$ simulated spectrum was $p_y + p_z$, while for the XES$\perp c$ simulated normal emission spectrum was created by adding $p_x + (p_y + p_z)/2$ broadened components. The result of these simulated NXES is shown in the lower part of

Figure 5.9a, and the match between the theory and experiment is excellent.

Taking the formula for creating the simulated NXES spectra, it is consistent that by subtracting a fraction of the XES$\|c$ from the XES$\perp c$ NXES spectrum, it is possible to experimentally isolate the $p_x$ component of the fluorine emission. The upper part of Figure 5.9b shows the result of this difference spectra and below it for comparison is the broadened F $2p_x$ VB DOS. The difference spectrum and its simulated analogue were not normalised or scaled by any means after subtraction, rather the y-axis of the Figure 5.9b graph is magnified by a factor of 1.5 with respect to 5.9a. The comparison is extremely good.

Figure 5.10a shows a waterfall graph of the resonant X-ray emission spectra of MgF$_2$ at the fluorine $K$-edge in the two selected geometries: $\mathbf{E}\perp c$;XES$\perp c$ in red and $\mathbf{E}\|c$;XES$\|c$ in blue. The selected excitation energies are illustrated by the arrows in 5.10b, with the final NXES spectra being acquired at approximately 708 eV.

Unlike, for example, oxygen or carbon $K$-edge RXES spectra, only minor and gradual changes are observed in the spectral shape and weight between consecutive energy steps. In a similar fashion to the significantly broadened absorption, this may result from the vibrational envelope associated with excitation on a fluorine site, or to the combination of the slowly dispersing bands in MgF$_2$ and the relatively large excitation bandwidth selected by the monochromator, though the excitation energy bandwidth is quite likely to be more important in the range of intermediate states selected. As mentioned earlier in this chapter in section 5.6.1, there is a very large variation of F $1s$ core-level line widths associated with fluorine molecules. This may not significantly broaden the emission spectrum itself, but effectively broaden the selecting range of the incident light, and thus produce a wider range of intermediate states. So while crystal momentum would be conserved in resonant spectra, the range of crystal momenta selected would not be sharp. Alternatively there is considerable overlap between the differing fluorine $2p$ conduction band component states, as shown in Figure 5.10b. Thus it could simply be that the lack of variety between consecutive energy steps in the respective RXES spectra results from many overlapping slowly dispersing bands, either in the CB or VB.

Focusing on Figure 5.10a, a clear and consistent dichroism is observed between the two geometries in all presented spectra. As with the NXES, the resonant $\mathbf{E}\|c$;XES$\|c$ blue spectra show a relative shift of spectral weight favouring the $p_y$ or $\pi$-like states in the valence band in comparison to the $\mathbf{E}\perp c$;XES$\perp c$ spectra at each excitation energy. The $\mathbf{E}\perp c$;XES$\perp c$ red spectra on the other hand display more contribution from the $\sigma$-like states i.e. the F $2p_x$ and $2p_z$ projections. Of note, especially in the blue $\mathbf{E}\|c$;XES$\|c$ spectra, is the evolution of the spectral weight at the bottom of the valence band between 670 and 673 eV. In spectrum (1) the increase in intensity with increasing energy is smooth and quadratic until

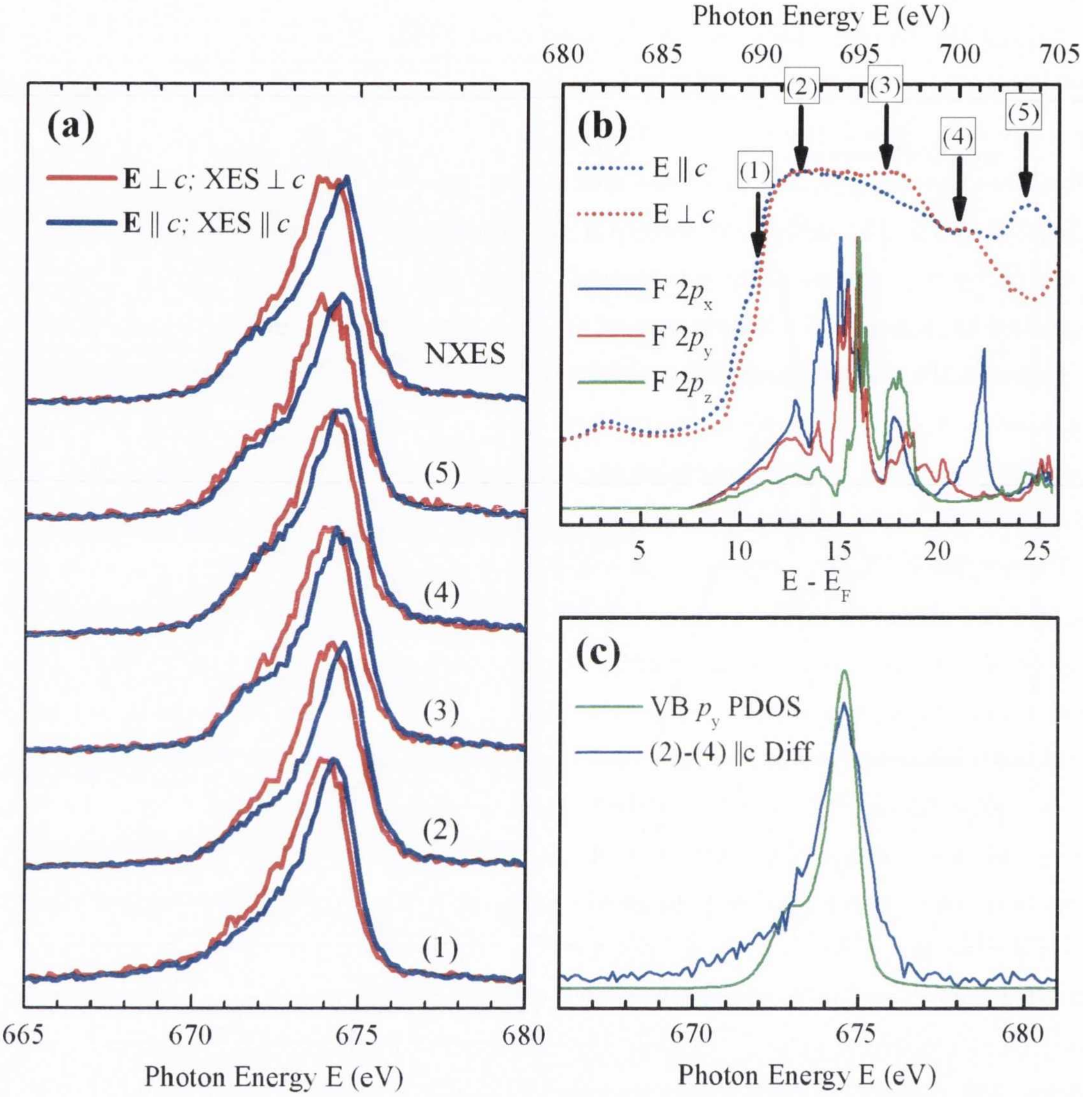

Figure 5.10: Part **(a)** shows the stepwise RXES measured in both in-plane geometries: **E**⊥$c$;XES⊥$c$ and **E**∥$c$;XES∥$c$ for $MgF_2$ at the fluorine $K$-edge. Part **(b)** is the XAS for the same crystal, numbered black arrows indicate the energies where emission was recorded. This is compared with the unbroadened calculated fluorine $p_x$, $p_y$ and $p_z$ CB components. Part **(c)** is a second difference spectrum created by subtracting 0.5× spectrum (4) from spectrum (1), both in the **E**∥$c$;XES∥$c$ measurement geometry. This was then normalised and directly overlaid with the fluorine VB $p_y$ simulated component of emission.

the maximum. In spectrum (2) this is interrupted by the faint emergence of a new feature which grows further in spectrum (3) and beyond. This feature is attributed to the $2p_z$ $\sigma$ states. Examining the component CB PDOS in 5.10b, it is clear that the main unoccupied $p_z$ states are not accessed at threshold energies, unlike the $p_y$ and $p_z$, but this is not the explanation. The XES∥$c$ measurement geometry favours emission from the $p_z$ and $p_y$ states thus explaining this feature's presence in the blue spectra (3) and above. By contrast this

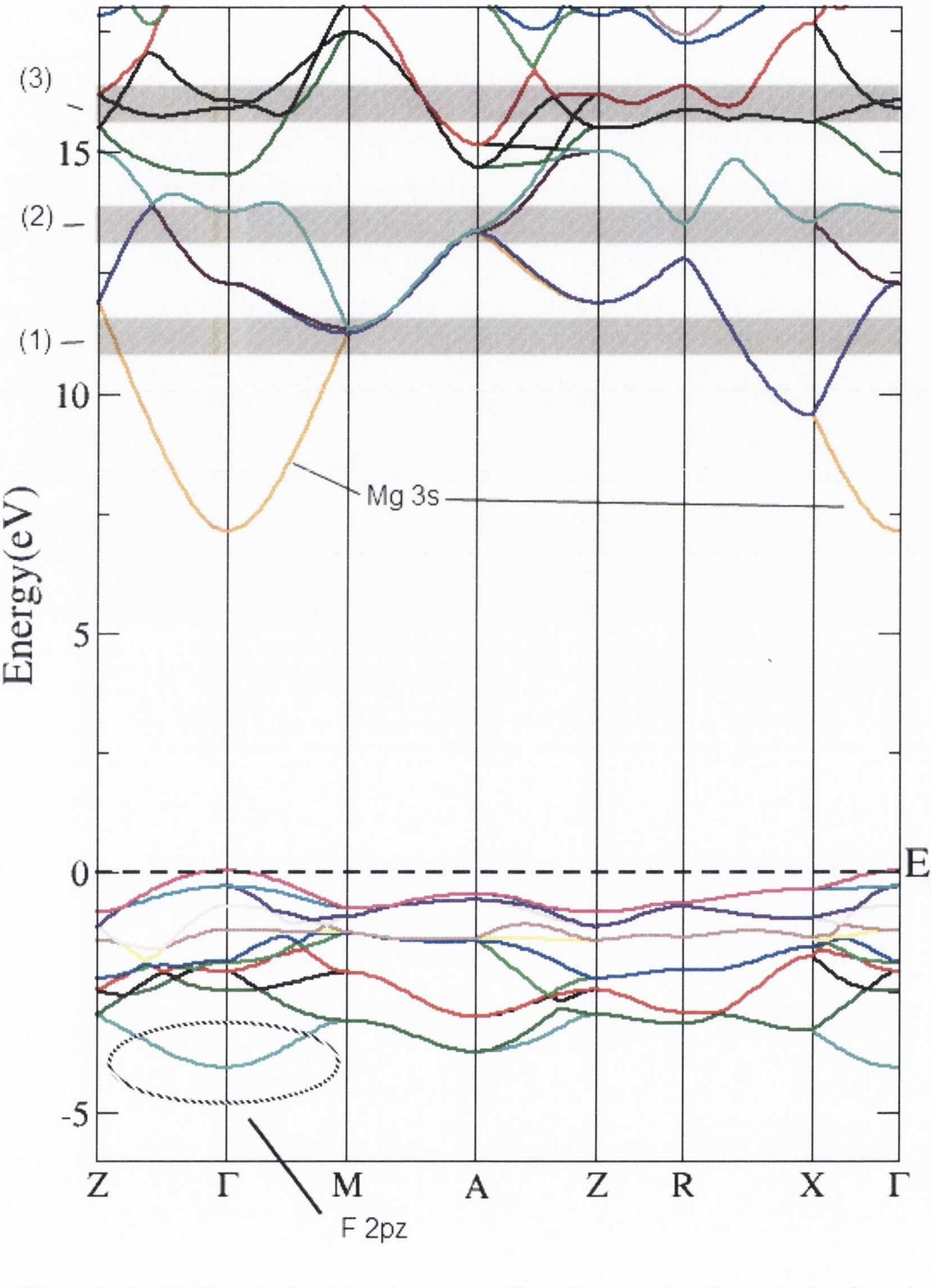

Figure 5.11: MgF$_2$ calculated bandstructure. Greyed rectangles illustrate the first three RXES excitation bandwidths. Note yellow bands at the bottom of the CB are attributed to Mg 3$s$.

does not explain the $p_z$ component's absence in the first two threshold blue spectra (1) and (2), which may be explained by the $k$-selective nature of the RXES process.

If we consider the bandstructure of $MgF_2$ in Figure 5.11, then for excitations (1) and (2) the $k$-points selected in the intermediate state within the conduction band are in a ~0.6 eV wide band centred around 11 and 13 eV above the VB maximum respectively. However for excitation (3), centred ~ 16 eV above the VB maximum, $k$-points close to the Brillouin zone centre $\Gamma$ are essentially selected for the first time. Now considering the lowest band in the occupied states, this reaches a minimum in energy only at $\Gamma$, and is almost exclusively a F $2p_z$ projected component.

From the above paragraph it follows that the $\mathbf{E}\|c$;XES$\|c$ spectrum (2) tends to consist more of $p_y$ states, while its spectrum (4) tends more toward the $p_z$. A subtraction of a factor, say 0.5, of spectrum (4) from spectrum (2) should give an adequate representation of the isolated VB $p_y$ states. This difference spectrum, along with the simulated VB $p_y$ PDOS is shown in 5.10c.

The difference spectra by themselves may appear at first to simply mimic the asymmetric peak structure of the fluoride emission, their correlation easily overlooked. When contrasted directly however, as in Figure 5.12, the differentiation become very clear. In the lower half of Figure 5.12, the calculated fluorine $2p_x$ and $2p_y$ PDOS exhibit excellent correlation with the experimentally derived difference spectra corresponding to these orbital projections.

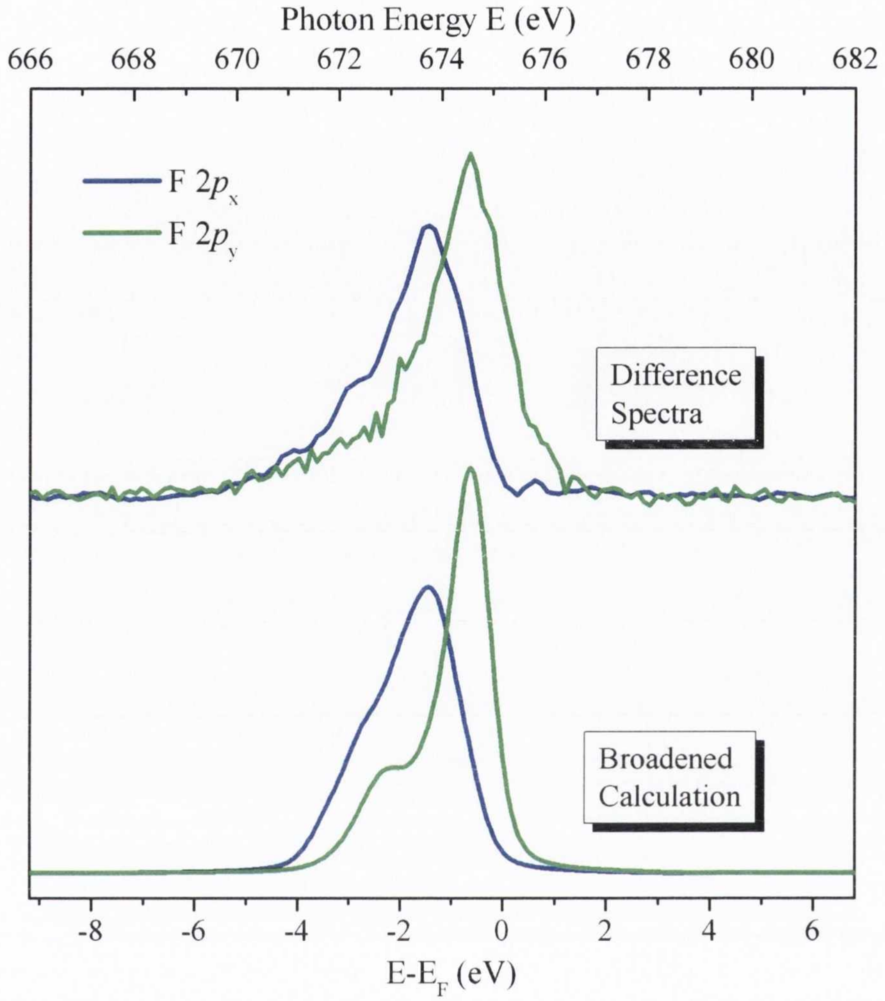

Figure 5.12: MgF$_2$ difference spectra from previous Figures 5.9b and 5.10c compared directly, and contrasted below with the simulated $p_x$ and $p_y$ components of the F VB respectively. The Fermi energy is rigidly shifted to 675.2 eV.

### 5.6.3 Polarisation Dependent RXES and NXES of MnF$_2$

In similar treatment to the MgF$_2$, the calculated VB fluorine $K$-edge PDOS for MnF$_2$ is broken down into its component $2p$ $x$, $y$ and $z$ local fluorine coordinate PDOS in Figure 5.13b, compared with the total fluorine $2p$ PDOS, broadened as noted before to match experimental resolution. Figure 5.13a presents the VB PDOS categorised into its $\sigma$ and $\pi$ components, both broadened and unbroadened. Comparing to the similarly produced Figure 5.8 for MgF$_2$, the main fluorine $2p$ bands are largely similar. The $\sigma$ and $\pi$ states appear to have a greater separation in MnF$_2$, no doubt due to the comparatively stronger covalent bonding with the now extant metal $3d$ $e_g$ orbitals in the near-octahedral crystal field. The predominant difference in the valence band lies in the pre Fermi-edge features in MnF$_2$ between $-2$ and 0 eV, which result from hybridisation with the occupied manganese

$t_{2g}$ and $e_g$ orbitals for neighbouring spin↑ Mn sites (Mn1). Figure 5.13 demonstrates that the higher energy feature at $\sim -0.25$ eV possesses no F $2p$ $\pi$ component, and can therefore be easily identified as the $e_g$ derived hybridisation feature, making the lower energy ($\sim -1.5$ eV) the $t_{2g}$ derived.

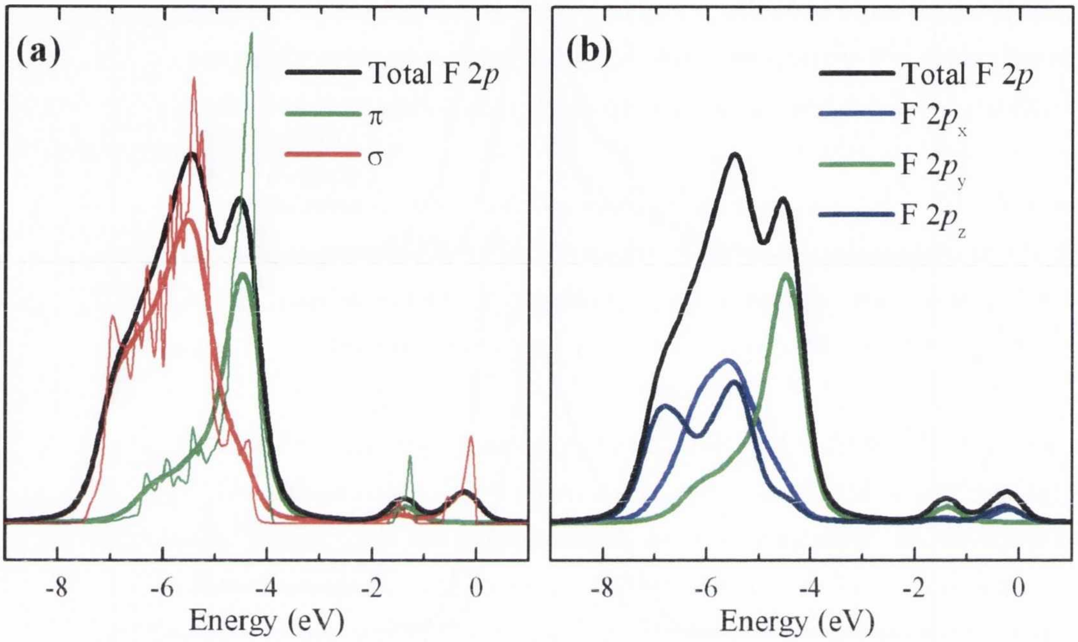

Figure 5.13: Part **(a)** shows the total fluorine $2p$ VB DOS for $MnF_2$ broadened to simulate core-hole and instrumental resolution of XES, this is then shown split into its component $\pi$ and $\sigma$ character states, the unbroadened calculation of each is overlaid. Part **(b)** breaks this down further showing the simulated fluorine VB $p_x$, $p_y$ and $p_z$ components of emission.

Figure 5.14a is a waterfall graph of the RXES and NXES results for $MnF_2$ at the fluorine $K$-edge in the two selected geometries: $\mathbf{E}\perp c$;XES$\perp c$ in red and $\mathbf{E}\| c$;XES$\| c$ in blue. The excitation energies for the presented RXES spectra are indicated by the arrows on the XAS spectra in part (b) of the figure. The evolution of the emission spectra going from resonant to non-resonant is explicit and very similar to that of $MgF_2$. The main fluorine peak broadens as a larger range of crystal momentum is selected. This is particularly the case toward the bottom of the valence band as more occupied $p_z$ states contribute to emission. Similarly to the case in $MgF_2$ the bottom of the valence band is dominated by the F $2p_z$ component close to the Brillouin zone centre Γ. Only by spectrum (4) in Figure 5.14, apart from perhaps the threshold excitation in spectrum (1), do $k$-points in the CB (intermediate states) get selected close to the zone centre Γ.

In all spectra the pre-edge states below from Mn $3d$ hybridisation are visible as a higher-than-background feature between 675 to 680 eV, though it is not well enough resolved to distinguish the two predicted two peaks. There are two sets of spectra labelled "NXES", with more obvious difference in spectral weight at this metal hybridised feature. This feature, prominent in the NXES2 set of spectra, is a $KL - L^2$ satellite peak observed for higher energy excitations of ionic fluorine compounds due to double core hole ionisation involving F $1s$ and F $2s$ holes, though its intensity is chemically sensitive, being inversely proportional to the covalency of the compound [120], and in some cases the peak even displays anomalous behaviour.† Rubensson *et al.* estimates that the $1s2p$ transfer for fluorine, such that a second core-hole is created, is 715 eV [122] CaF$_2$. The NXES2 set of emission spectra were recorded with an excitation energy of 717 eV. Thus the extra feature present here is attributed to the $KL - L^2$ double satellite. [105]

As introduced in section 5.3, spin is conserved in resonant fluorescence, as according to the Kramers-Heisenberg equation it can be explained as a single quantum process with two photons [10].

Recall our earlier discussion of the spin-dependent F $2p$ PDOS on F1 and F2 sites. A spin$\uparrow$ $1s$ core electron may be excited into empty spin$\uparrow$ $2p$ states on the F1 site. Any subsequent emission must then be from the occupied spin$\uparrow$ F $2p$ states on that same F1 site, as no spin-flips are allowed (spin is conserved).

The spin$\downarrow$ F $2p$ states on the F2 site are exactly equivalent to the spin$\uparrow$ F $2p$ states on the F1 site. Their states are designated as type "A" F $2p$ PDOS. Conversely on the F1 site, the spin$\downarrow$ unoccupied states must differ from the spin$\uparrow$, as it neighbours two Mn2 $d^5$ $\downarrow$ sites and one Mn1 $d^5$ $\uparrow$ site. The F1 spin$\downarrow$ is equivalent to the F2 spin$\uparrow$ and is designated as type "B" F $2p$ PDOS.

Thus type A absorption will result in type A emission and vice versa. Figure 5.15 presents the simulated spin-selective valence and conduction band states for the F $K$-edge of MnF$_2$. Figure 5.15b replicates the CB states for the two projections that match the experimental measurement geometries of the XAS in Figure 5.6. Here however they are staggered and further divided into type A and B. Recall from the equality formulae 5.1, type A represents the additions of the equivalent F1 $\uparrow$ and F2 $\downarrow$ states. Figure 5.15a presents the normal emission simulated spectra, showing its $\sigma$ and $\pi$ components much in the same way as 5.13a, but this time staggered to demonstrate the contributions from type A in the upper part, and type B in the lower. A difference, though not significant, is noted in the spectra weight, especially near the lower more tightly bound region of the main $2p$ DOS.

Briefly touched upon in section 5.3 was the importance of this spin-type separation in simulating spectra. It is correct to take the average for XAS, which is a measure of the

---

† See 1986 PRL paper by Benka *et al.* [121] qualitatively interpreting the anomalous behaviour of this satellite peak in KF as "resonant transfer".

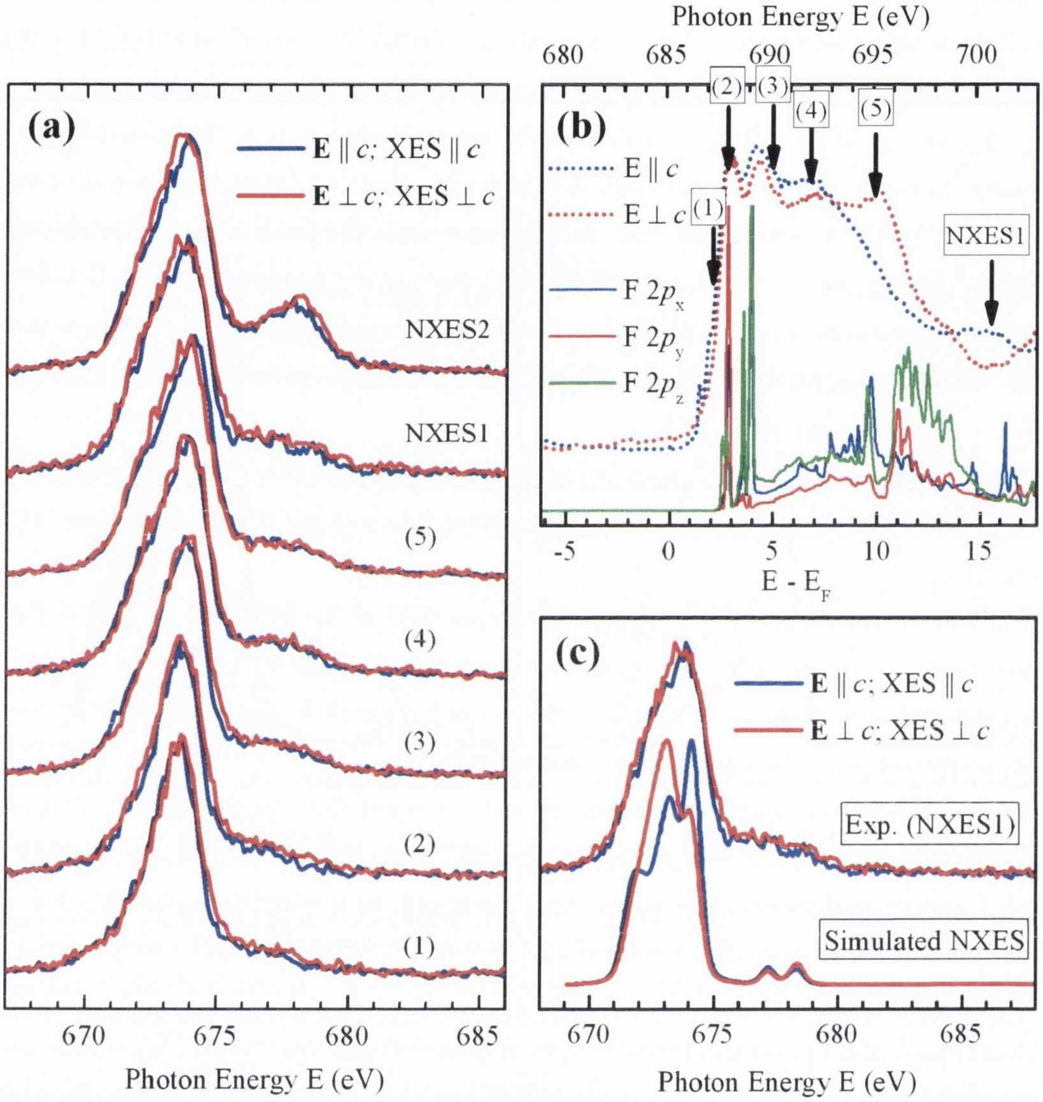

Figure 5.14: Part **(a)** shows the RXES in the two in-plane measurement geometries: **E**⊥$c$;XES⊥$c$ and **E**∥$c$;XES∥$c$ for MnF$_2$ at the fluorine $K$-edge. Part **(b)** is the XAS for the same crystal, numbered black arrows indicating the energies where emission was recorded. This is compared with the unbroadened calculated fluorine $p_x$, $p_y$ and $p_z$ CB components. Part **(c)** contrasts NXES on top in both measurement geometries, with the simulated NXES spectra below. The simulated spectra are a broadened addition of the $p_y + p_z$ projected states for XES∥$c$, and $p_x + (p_y + p_z)/2$ for the XES⊥$c$ measurement geometry. The predicted dichroism is not observed in this crystal.

unoccupied states, the same is true for NXES where no one core-hole spin is favoured. For RXES however, the probability of the core hole vacancy spin being a one type is proportional to the number of available states of that type at the energy- and geometry-selected region of the CB. Thus looking at Figure 5.15b, an excitation into the region approximately 4 eV above the Fermi energy in the **E**∥$c$ geometry, will significantly favour emission of type A.

While nothing conclusive can be drawn in this regard from the RXES spectra in figure 5.14a, it is noted from Figure 5.15b that threshold excitations in both measurement geometries will select on average more states of type A, while in higher energy RXES neither are significantly preferred. This could further contribute to the shape difference near the bottom of the valence band RXES between the threshold excitations and those of higher energy; there the threshold resembles type A much more in shape than type B simulated spectra in Figure 5.15a.

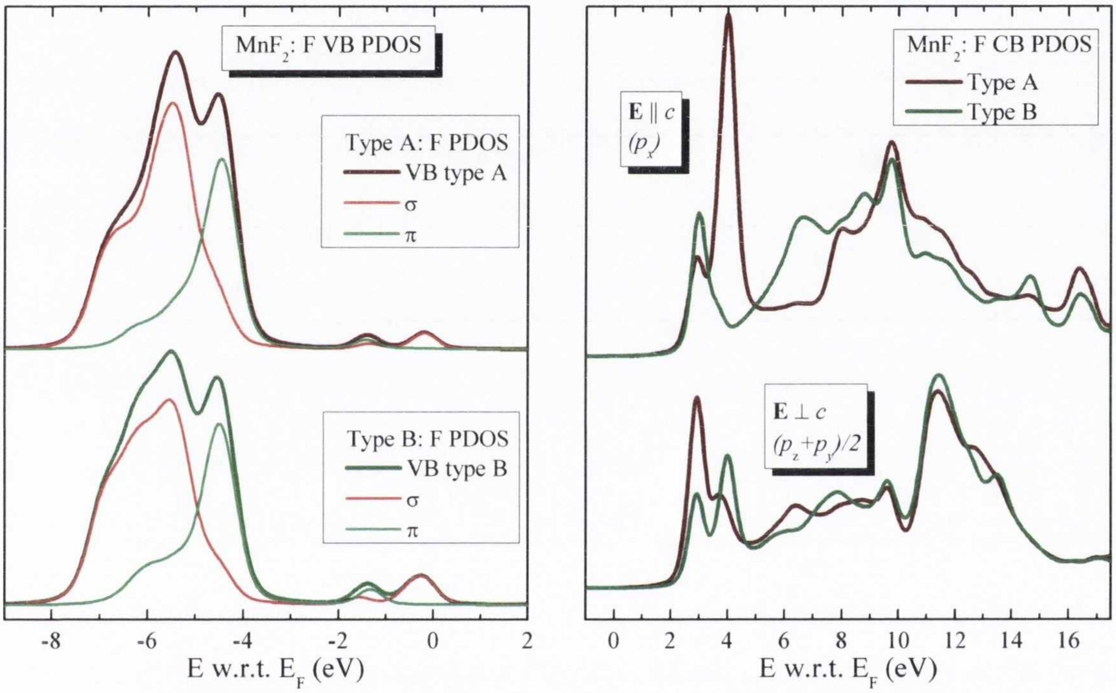

(a) VB spin selection.

(b) CB spin selection.

Figure 5.15: (a) The F $K$-edge calculated projected total densities for type A and type B "spin states" in the VB, divided further for $\sigma$ and $\pi$ character. Broadened to simulate experimental emission. (b): The F $K$-edge calculated densities for type A and type B states projected along $p_x$ (top) and half-way between the $p_z$ and $p_y$ (bottom) in the CB. Broadened to simulate experimental absorption parameters during RXES.

Unfortunately, unlike most of the other rutile compounds presented in this theses, and indeed the similarly structured MgF$_2$, MnF$_2$ shows almost no significant dichroism in either resonant or normal emission at the F $K$-edge. This is contrary to the calculated NXES spectra shown in Figure 5.14c, projected along the planes probed by the emission, that suggest a distinct dichroism in the main fluorine $2p$ VB region.

The lack of observed anisotropy in the valence band could be for a number of reasons. Perhaps the calculations inadequately describe the anisotropy of the system and any dichroism present in the VB is simply too subtle to be observed within the resolution confines of the instruments used and the RXES technique itself. Another possibility could be an error in determining the alignment of the crystal using cross-polarisers, though this is unlikely since the dichroism in absorption, which was taken contiguously with the emission measurements, appears to match reasonably with the theoretical predictions. It could be related to an unanticipated electronic property resulting from the spin properties of the crystal, or it could be that the spherical symmetry of the $d^5$ occupied manganese cation reduces the chemical anisotropy of this mostly ionic system at the F $K$-edge.

Finally in Figure 5.16, we compare both the experimentally measured and DFT calculated F $2p$ VB PDOS for $MnF_2$ with a very recent example from Jiménez-Mier *et al.* [103], as well as to the calculated PDOS from Dufek *et al.* [99] The top panel compares the NXES1 spectra shown above taken on a bulk crystalline sample in the two measurement geometries, and contrasts it with the $MnF_2$ fluorine $K$-edge XES spectrum from the Jiménez-Mier paper, measured on an unoriented powder sample. All were taken at approximately the same excitation energy ($\sim$ 700 eV).
In the bottom panel of 5.16 the DFT PDOS calculations are compared, both raw and broadened to mimic the spectra. The energy for both panels is aligned to the Fermi energy, as determined by Jiménez-Mier. In the case of the emission, this is taken as the point where the spectral weight drops to background levels. The calculations adapted from Dufek *et al.* were calculated in the same manner as the calculations performed for this thesis, and subsequently broadened here making them essentially the same. It should be noted that the Dufek calculations are for the F1 site spin-up states only (type A), and while it would be similar to the averaged states presented here, some minor differences are expected. All calculations were performed using the FP-LAPW method. The more recent LDA+U$^{\text{SIC}}$ calculations performed by Jiménez-Mier *et al.* were done through the WIEN2K software package, of whom one of the creators Peter Blaha, is a co-author on the Dufek paper.

For the experimental comparison, in spite of the differences in the sample, an unoriented powder compared to two geometries of a nominally anisotropic bulk single crystal, the XES measurements are for all intents and purposes identical. In terms of the DFT calculations, our calculations are identical to the earlier calculations performed by Dufek *et al.* They also compare very favourably in terms of spectral shape and energy scaling with the experimental measurements. However, there is some spectral weight evident in the 675 to 677 eV region of the RXES spectra, between the main fluorine $2p$ states and those hybridised with the manganese spin$\downarrow$ $d$ states, which is not mimicked in the analogous -4 to -2 eV region of the simulated spectra.

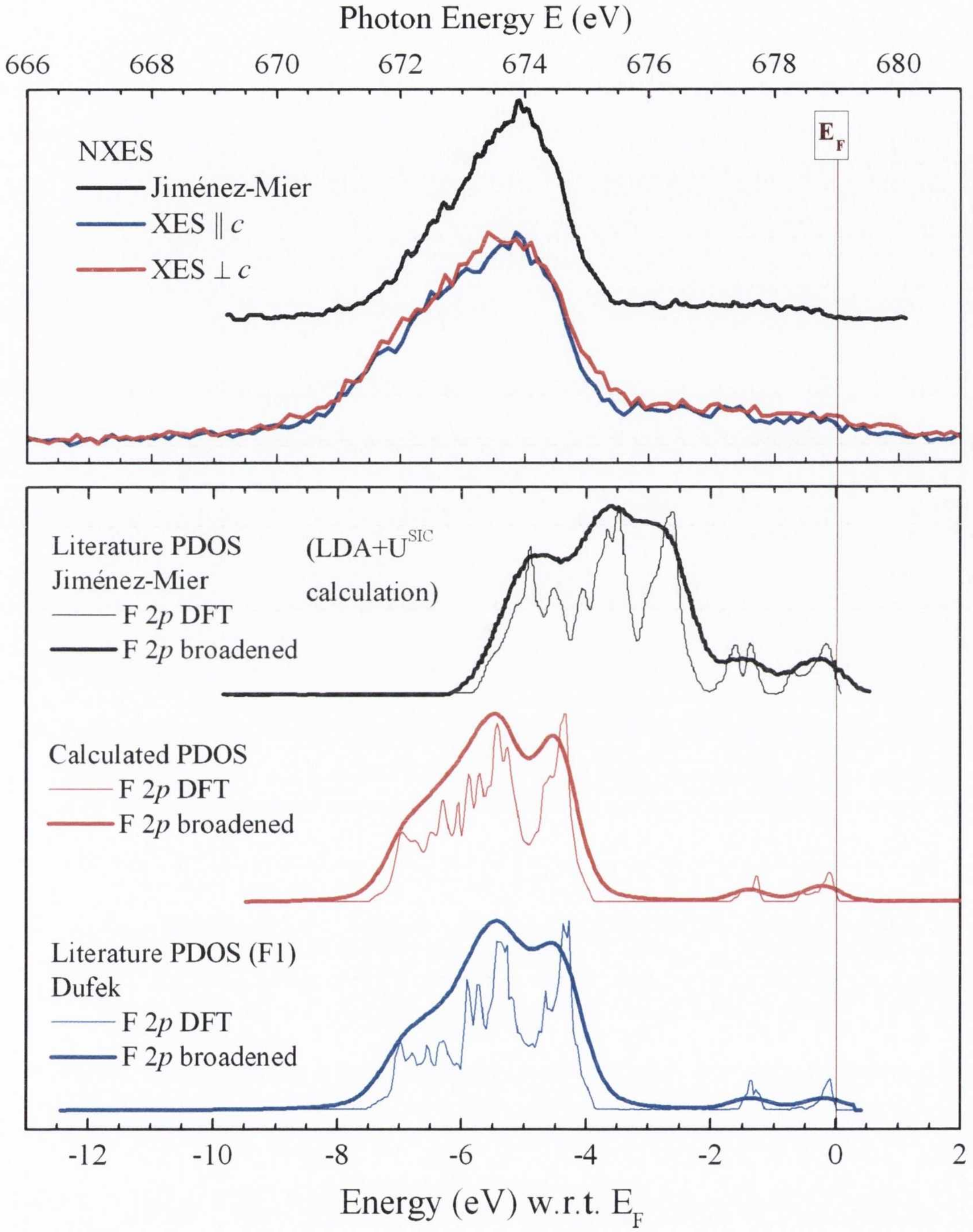

Figure 5.16: Top panel: MnF$_2$ NXES1 spectra from Figure 5.14 for the two measurement geometries compared with XES from Jiménez-Mier *et al.* [103] on an unoriented powder sample at approximately the same excitation energy of 700 eV. Bottom panel: Three sets of DFT calculations for the total fluorine 2$p$ VB DOS. Top calculation from Jiménez-Mier *et al.* [103] middle is presented here, while the bottom is adapted from Dufek *et al.* [99] and is for type A (F1 ↑) states only, while the other two are averaged. All were calculated using the FP-LAPW method. The placement of E$_F$, and hence alignment of the emission spectra with the calculations was adopted from the method used by Jiménez-Mier *et al.*

## 5.7 Summary and Conclusions

The natural linear dichroism of rutile structured $MnF_2$ and $MgF_2$ was investigated at the fluorine $K$-edge using XAS, RXES, NXES and *ab initio* DFT PDOS calculations. To the best knowledge of the author, this is the first reported account of polarisation-dependent XAS, NXES or RXES of $MgF_2$ and $MnF_2$ at the F $K$-edge.

Dichroism was observed for $MgF_2$ both in the conduction and valence bands, and correlated definitively with the predicted observations from the PDOS calculations and subsequent simulated spectra. For $MnF_2$, only the XAS conveyed clear evidence of anisotropy in the spatial projections that correlated with the predicted calculations. The emission displayed a distinct lack of discernible difference between the measurement geometries, though the calculations predicted otherwise. The reason for this lack of observed anisotropy in the projected densities of states in the VB is unclear, and further investigation into the modelling of this compound may be required. Overall, however, the calculations did a reasonable job of predicting the general shape and energy position of the fluorine $2p$ emission.

Although $MgF_2$ is predominantly an ionic compound, the existence of $\sigma$ and $\pi$ component $2p$ valence states were nevertheless shown experimentally. Further, it was possible to experimentally isolate specific spatial component orbital states by subtraction of NXES spectra as well as by taking the difference of symmetry- and $k$-selective RXES. This was then confirmed by comparison with calculated projected DOS for these components and an excellent correspondence was observed.

In both compounds, and indeed with other polarisation dependent rutile-fluoride results acquired by the author (not presented in this thesis), the FWHM of the main F $2p$ DOS was observed to change significantly with excitation energy. Beginning narrow at threshold, widening significantly at the first XAS peak and then more gradually for increasing excitation energy after that. This trend was mostly attributed here to the $k$-selectivity of RXES, where a larger range of crystal momentum and thus greater number of bands are selected at higher excitation energy. This F $K$-edge resonant XES behaviour has been observed before in $MnF_2$ [105] as well as in cubic $CaF_2$ by Rubensson *et al.* [122]. It was even shown for LiF by Kikas *et al.* [123] who attributed it to core excitonic effects. Rubensson, while making note that the width of the $2p$ main band results from the $k$- and state-selectivity of resonant emission, also apparently attributes the behaviour of the FWHM to screening. From the results presented in this chapter, in particular the polarisation dependence observed in $MgF_2$ and its correlation with the calculated states, it cannot be ignored that a significant contributing factor to this behaviour is the $k$- and state-selective nature of the resonant emission process, whereby a greater range of selected $k$-values in the CB leads to a greater range of $k$-values possible for emission. Further, as particular unoccupied $\pi^*$ or $\sigma^*$ states are selected in the CB, this leads to state-selective emission.

The $\sigma^*$ states appear to be dominant at the bottom of the CB. This is a feature unique to fluorides in this thesis, which is perhaps due to them being wide-bandgap insulators, as most of the anion-edge investigations presented here are metallic. Further, similar CB characteristics are observed for $SnO_2$ [5].

# 6 $WO_2$ and $MoO_2$

## 6.1 Introduction

Presented in this chapter is an X-ray spectroscopic study of the electronic structure of $WO_2$ and $MoO_2$, using both X-ray absorption spectroscopy (XAS) and resonant X-ray emission spectroscopy (RXES). In the case of $WO_2$, these are compared with original electronic structure calculations. Together with comparisons to previous works, these techniques are used to further explore the electronic structure of these rutile-like materials.

From the rutile periodic table presented in Figure 3.1 (page 30) $WO_2$ and $MoO_2$ are noted to have the same valence $d$-level electronic configuration. Previously, $WO_2$ has been studied by ultra-violet photoelectron spectroscopy (UPS) [124,125], core level photoemission, electron energy loss spectroscopy (EELS) [126] as well as tungsten $L_{2,3}$ XAS and oxygen $K$-edge non-resonant X-ray emission [127]. Similarly $MoO_2$ has also been studied by UPS [124,128], core level photoemission [128,129] as well as Mo $L$-edge non-resonant X-ray emission [129], angle-resolved photoemission [130], and polarisation dependent O $K$-edge XAS [131]. Theoretical band-structure and density of state calculations for $MoO_2$ have also been published [52,129,130]. As yet, however, no study has exploited the expected dichroism at the O $K$-edge for $WO_2$, nor has any O $K$-edge soft X-ray emission study of $MoO_2$ been published to date.

This work presents the first such polarisation dependent and symmetry selective XES and RXES measurements of both $WO_2$ and $MoO_2$ at the oxygen $K$-edge, and the current polarisation-dependent XAS supplements the previous experimental oxygen $K$-edge XAS measurements [130].

$WO_2$ in its pure state does not currently possess many direct applications. Much of the scientific interest in it, like with $MoO_2$, is motivated by its similarity to other transition metal compounds that share the same electronic interactions and structure, of which the often quoted $VO_2$ is but one example. It is hoped that a better understanding of compounds such as $WO_2$ may serve as a basis for greater understanding of this class of compounds as a whole, including some unusual properties like metal to insulator transitions, which $MoO_2$ and $WO_2$ do not share; the explanation for these transitions is still somewhat controversial.

Unlike $WO_2$, $MoO_2$ has a variety of technologically important applications by itself. For example it is used as a catalysing agent in the dehydrogenation of alcohols [132], as well as the reformation of hydrocarbons [133]. It has also been used as a precursor of catalysts in the processes of hydrocracking and desulfurisation [134] and in the manufacture of synthetic fibres, mainly in the production of the monomer anhydride [135]. It is used as an electrochromic and photochromic material for solar cell technologies [136]. Finally, molybdenum nano-wires have been produced by reducing $MoO_2$ deposited on graphite [137].

## 6.2 Physical and Electronic Structure

$MoO_2$ and $WO_2$ belong to a family of binary transition metal compounds with stoichiometry $MA_2$, where the anion A is either oxygen or fluorine. These compounds are either isomorphous with rutile $TiO_2$ or adopt a distorted variant of this structure, as is found for $MoO_2$, $WO_2$ and the room-temperature insulating phases of $VO_2$ and $NbO_2$. The distortion arises from metal-metal interactions along the $a$-axis (corresponding to the $c$-axis in the undistorted rutile structure) which leads to a dimerisation of the metal atoms, with alternately shorter and longer metal–metal distances and a slight alternating displacement or kink along that axis. This distortion arises from the Peierls instability of a one dimensional chain of atoms with 1 electron per atom. The electronic structure of $WO_2$, $MoO_2$ and of similar distorted rutile-like oxides such as $NbO_2$ and $VO_2$, are of fundamental interest due to the variety of metal-metal interactions, and in the latter cases, metal to insulator transitions that these materials exhibit. [34,50–52]

Metal–metal bonds strong enough to result in a distortion of the tetragonal structure along the rutile-like $c$-axis can occur when the $d-$orbital occupation of the metal cation is $d^1$, $d^2$ or $d^3$ (but not $d^4$) [53]. A qualitative band model describing these interactions was introduced by Goodenough [34] and provided a simple explanation of the non-metallic behaviour found for the distorted variants of $VO_2$ and $NbO_2$, as well as the metallic behaviour of $MoO_2$ and $WO_2$. Like their rutile $MA_2$ counterparts, the cation valence $d$ orbitals undergo octahedral field splitting into $t_{2g}$ and $e_g$ states. However, even in a perfect undistorted rutile-like system, the $MO_6$ octahedra have local $D_{2h}$ rather than $O_h$ symmetry. The distorted $WO_6$ (and $MoO_6$) octahedra have this symmetry further reduced to $C_{2v}$ [125]. Consequently the $t_{2g}$ orbitals are no longer equivalent. It is useful to distinguish between the single metal valence $d_{xy}$ orbital that lies in the plane described by the shared edges of the octahedron (often denoted $d_{\|}$ or $t_{\|}$, the former will be the case here) and the remaining two $t_{2g}$ $d_{\perp}$ orbitals perpendicular to the shared edges (denoted $t_{\perp}$ in Goodenough *et al.* [34]). At this point it is instructive to note Figure 6.1, where there are two sets of labelled axes. These represent the local anion (oxygen) coordinate axes as well as the local metal coordinate axes for the three left-most tungsten atomic sites displayed in the figure. The increased metal-metal bonding, and hence dimerisation due to the Peierls instability, arises from a $\sigma$-like overlap of the $d_{xy}$ ($d_{||}$) orbitals along the monoclinic $a$-axis as shown in Figure 6.1. This gives rise to a splitting of the $d$ bands into bonding and antibonding $d_{||}(\sigma)$ and $d_{||}(\sigma^*)$ states. The remaining $t_{2g}$ orbitals interact via weaker $\pi$-like and $\delta$-like overlap. Although the $\sigma$ interactions are strong enough to split apart the $d_{||}(\sigma)$ and $d_{||}(\sigma^*)$ bands, this is not case for the bands derived from the other $t_{2g}$ orbitals, which will be designated by $d_{\perp}$. Thus distorted $d^1$ systems like NbO$_2$ and VO$_2$ are non metallic with one filled $d_{||}(\sigma)$ band per formula unit, whereas the $d^2$ systems discussed in this chapter, WO$_2$ and MoO$_2$, are metallic with a Fermi level in the overlapping bands derived from partial occupation of the remaining $t_{2g}$ levels.

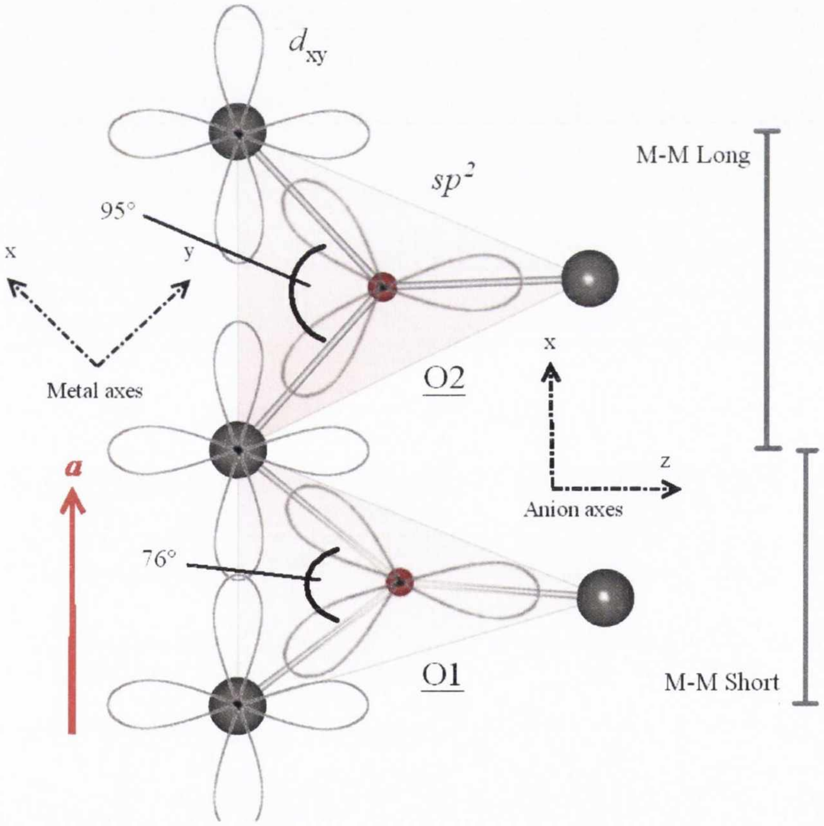

Figure 6.1: Corner sharing parallel W$_3$O trigonal planes along the crystal $a$-axis, shown in the $xy$ plane for the metal coordination, equivalent to the $xz$ plane of the oxygen. Differing bond angles and bond lengths exhibited for O1 (bottom) and O2 (top) sites. Oxygen $sp^2$ hybridised orbitals lobes are shown with respect to the metal $d_{xy}$. Metal–metal dimerisation is also illustrated along the $a$-axis by overlap of $d_{xy}$ orbitals in the O1 trigonal plane. A similar structural relationship, with the separation of oxygen into two distinct sites, is seen in MoO$_2$.

| **M-O Bond direction** | **O1** | **O2** |
|---|---|---|
| $\|\|M_x$ | 2.0195 Å | 2.061 Å |
| $\|\|M_y$ | 1.969 Å | 2.107 Å |
| $\|\|A_z$ | 1.9868 Å | 1.98872 Å |

Table 6.1: Table of M–O bond distances for the two anion sites of $WO_2$ with respect to the local metal and anion axes illustrated in Figure 6.1.

In rutile and rutile-like structures the oxygen anions are trigonally coordinated, undergoing $sp^2$ hybridisation within the $M_3O$ planes. In $WO_2$ and $MoO_2$ the $a$-axis is the monoclinic equivalent of the rutile $c$-axis, i.e. in projecting the crystal structure along this axis all trigonal planes are observed edge-on. Thus, even in a distorted rutile-like compound there is an expectation of natural linear dichroism in connection with the rutile-like $c_r$-axis, or $a$-axis in this case. Further, it should be noted that due to the dimerisation of the metal atoms along the $a$-axis in these compounds, two inequivalent oxygen sites arise denoted O1 and O2. These differing sites are illustrated as part of the corner sharing distorted trigonal planes in Figure 6.1. The oxygen site O1 is at the centre of a scalene triangular plane with the shorter of the metal–metal distances along the $a$-axis, forming one side of the triangle. The O2 site is then at the centre of a triangle having the longer of the two metal–metal distances along the monoclinic $a$-axis as one of its sides. Taking the example of $WO_2$ the average W–O1 bond-length is 1.9876 Å whereas the average W–O2 bond length is 2.0525 Å.

### 6.2.1 $WO_2$

The physical structure of $WO_2$ is shown in Figure 6.2. The net result of the distortion is that the crystal structure of $WO_2$ is monoclinic with space group $P2_1/c$ ($C^5_{2h}$) and lattice parameters $a$ =5.563 Å, $b$ =4.896 Å, $c$ =5.663 Å and an angle $\beta$ =120.47° as determined by neutron and X-ray diffraction [138]. As with $MoO_2$, there are four formula units per cell, as compared with two in undistorted rutile. Figure 6.2 shows also that while there are two inequivalent oxygen sites there is only one tungsten site. The bond lengths were previously given for $WO_2$ in Table 6.1.

The trigonal planar coordination of the oxygen atoms in $W_3O$ planes accompanies the $sp^2$ hybridisation on the oxygen site and an octahedral ($WO_6$) coordination of the W atoms by the surrounding six oxygen atoms. This structure is depicted in Figure 6.2, where the differing oxygen sites, octahedra and trigonal planes are noted and are discussed as follows. The $WO_6$ octahedra, as with the structurally similar rutile $TiO_2$, form edge sharing chains that also share a corner with an adjacent column of $WO_6$ octahedra, but whose axes are rotated by 90° from one chain to the next. This is distinct from $TiO_2$ which has regular

$TiO_6$ octahedra and only 2 distinct Ti-O distances, relating to either the apical O or the equatorial O around the waist of the octahedron. In $WO_2$ there are 6 distinct W–O distances (listed in in Table 6.1) leading to an irregular $WO_6$ octahedron. It was previously noted that this distortion arises due to the dimerisation of the W atoms along the monoclinic *a*-axis with small displacements away from this axis. As a result there are now two distinct inequivalent oxygen sites, each in the centre of a different $W_3O$ triangular plane which nevertheless remains essentially edge on to the monoclinic *a*-axis (rutile *c*-axis) with each oxygen site alternating along the [100] direction as seen in Figure 6.2(a) and 6.2(b).

The distorted rutile (monoclinic) structure is discussed in greater detail in the structure chapter, section 3.3 of this thesis.

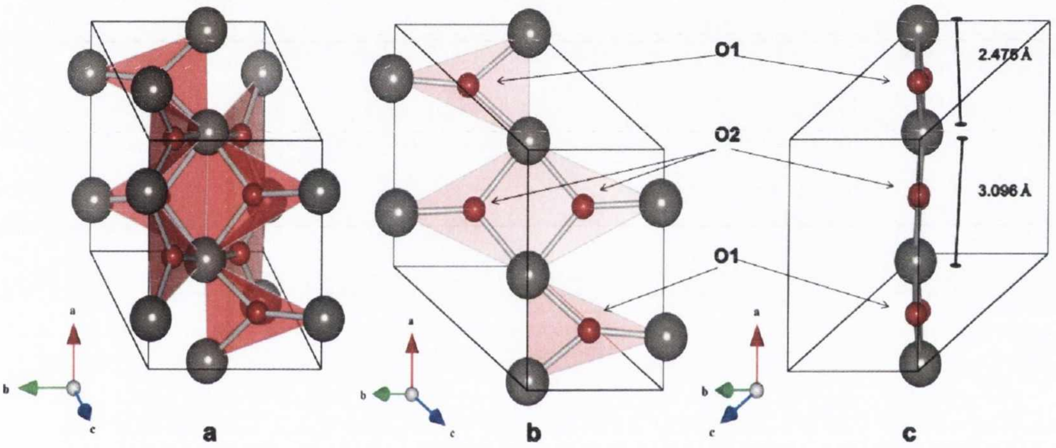

Figure 6.2: **a)** Unit cell of monoclinic $WO_2$. Oxygen atoms shown in red, tungsten in grey. **b)** cropped and rotated slightly to emphasise one orientation of $W_3O$ trigonal planes, note average bond length is larger for O2. **c)** Cropped further and rotated 90° from b) to emphasise the W–W bonds along the *a*-axis, note the kink-like distortion and alternating bond length.

### 6.2.2 Electronic Structure Calculations of $WO_2$

Electronic structure calculations were performed in order to examine the bandstructure, density of states (DOS) and partial density of states (PDOS), and to compare with the measured oxygen *K*-edge XAS and RXES spectra which effectively probe the unoccupied and occupied oxygen 2*p* partial densities of states (PDOS) respectively. The density functional theory (DFT) calculations presented here employ the full-potential linearised augmented planewave (FP-LAPW) method as implemented in the WIEN2K code [57], and were modelled after those performed by Jiang *et al.* [126] The FP-LAPW method is a density-functional based electronic structure method obtaining iteratively the ground-state electronic structure by solving the Kohn-Sham equations. In this instance the form of the exchange correlation functional used was the generalised gradient approximation (GGA) of Perdew and Wang [85]. The input to the calculation consisted of the experimentally determined lattice parameters of Palmer *et al.* [138] while the radius of the muffin tin spheres for W were 2.0 a.u. and 1.7 a.u. for both oxygen sites. The cut-off value used was $R_{MT}{}^{*}K_{max}$ of 7.0 while the charge densities and potentials were expanded up to $l$ =10, which gives about 6800 plane waves to describe valence and semi-core states. For the sampling of the Brillouin zone a selection of 2000 $k$-points was made, from which a 12 × 12 × 12 shifted $k$-point grid was generated according to the Monkhorst-Pack scheme, allowing for densities of states to be calculated via this tetrahedral mesh. The total energy in the calculation was converged to the level of $10^{-4}$ eV with the charge on an atomic site converged to $10^{-3}$ e between successive iterations. No structural relaxation was performed.

The complete results of the current electronic structure calculation of $WO_2$ are shown in Figure 6.3. The top panel displays the $WO_2$ total density of states, the decomposition into the W $5d$ PDOS including the $t_{2g}$ and $e_g$ components, while the lower two panels show the respective O1 and O2 total $2p$ PDOS. The oxygen $2p$ PDOS are further decomposed in the lower panels within Figure 6.3 into their orthogonal components within their respective $W_3O$ trigonal planes, using the natural coordinate system for the anions, as discussed earlier and shown in Figure 6.1. The overall influence of the W $5d$ orbitals and their hybridisation with the main band of the O $2p$ orbitals from 3 eV to 10 eV is exhibited most clearly in the case of the O1 site PDOS. As the average W–O distance for the O1 site is smaller, there is much more hybridisation with the W $5d$ orbitals than for O2. In particular the O1 $2p_x$ $sp^2$ $\sigma$-like component projected along the $a$-axis appears as the most tightly bound occupied oxygen band. This is hybridised very strongly in O1 with the W $5d_{x^2-y^2}$ $e_g$ orbital at binding energies close to -9 eV and -6 eV, and also with the $5d_z^2$ at -9 eV. These are presented together as the $5d$ $e_g$ component in Figure 6.3. Recall that the W–O1 distance for one of the equatorial bonds in the distorted $WO_6$ octahedron is the shortest, and the lobes of the W $5d_{x^2-y^2}$ overlap with the O $2p$ $sp^2$ orbitals forming the $\sigma$ molecular orbitals (MOs).

The appropriate orthogonal axes used to describe the W $5d$ orbital basis is the natural coordinate system described for rutile and distorted rutile structures in Chapter 3, also described in Sorantin and Schwarz [44] as well as illustrated in Figure 6.1. The metal $z$-axis lies approximately parallel to the bond directions between the W and the apical oxygens, perpendicular to the $a$-axis, and equivalent to the $z$ direction previously defined for the oxygen $2p$ bases. The metal coordinate $x - y$ plane lies in the waist of the $WO_6$ octahedra, parallel to the direction of the edge sharing octahedral-chains along the monoclinic $a$-axis. Thus the lobes of the $d_{x^2-y^2}$ $e_g$ orbital point toward the waist oxygens while the lobes of the $d_{xy}$ $t_{2g}$ orbital lie along the $a$-axis; this latter orbital is clearly $d_{\|}$ in Goodenough's

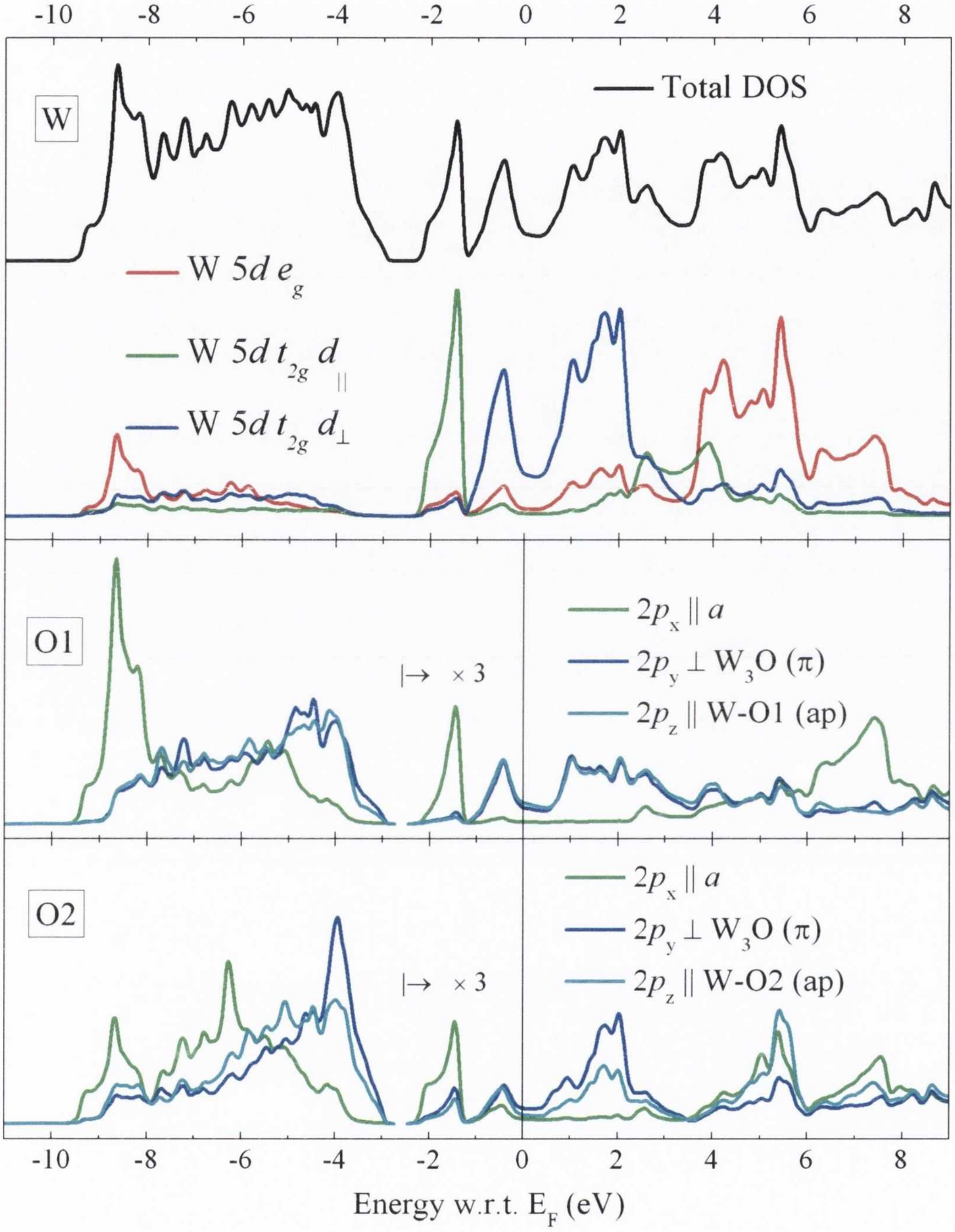

Figure 6.3: The WO$_2$ total DOS and W 5$d$, O1 2$p$ and O2 2$p$ PDOS are shown in the upper panel as well as the W 5$d$ $t_{2g}$ ($d_\perp$ and $d_\parallel$) and $e_g$ components In the two lower panels, the O 2$p$ PDOS is decomposed into the projections $\parallel$ $a$-axis, $\perp$ W$_3$O plane and the $a$-axis, and within the W$_3$O plane and parallel to the W-apical oxygen bond direction.

designation. As previously mentioned the remaining two $t_{2g}$ orbitals are the $d_\perp$ components $d_{xz}$ and $d_{yz}$†. The O1 and O2 2$p_z$ $sp^2$ $\sigma$ components, whose projections are within the W$_3$O plane but perpendicular to the $a$-axis, show much less but equal hybridisation with the W $5d$ $e_g$ component than do the $2p_x$ components, according to the calculation; note the near-equal W–O bond distances along the anion's $z$-axis. Finally, the O1 $2p_y$ component $\perp$ $W_3O$ plane appears largely similar to the remaining in-plane $2p_z$ $sp^2\sigma$ component and is indicative of a relatively strong $\pi$ –bonded W–O1 orbital, where hybridisation is seen with the W $5d$ the $d_\perp$ components. An alternative viewpoint might be the transfer of electronic charge and spectral weight from the O1 $2p_y$ orbital to the O1 $2p_z$ orbital, reflecting the very short $sp^2$ $p_x$–$d_{x^2-y^2}$ $e_g$ $\sigma$-like bonds extant for the O1. This is in sharp contrast to the equivalent $2p_y$ component for O2 which is effectively a non-bonding orbital, although potentially of $\pi$ symmetry, similar to that observed in $TiO_2$ [44].

---

† or $d_{z(y+x)}$ and $d_{z(y-x)}$ depending on how they're defined.

### 6.2.3 $MoO_2$

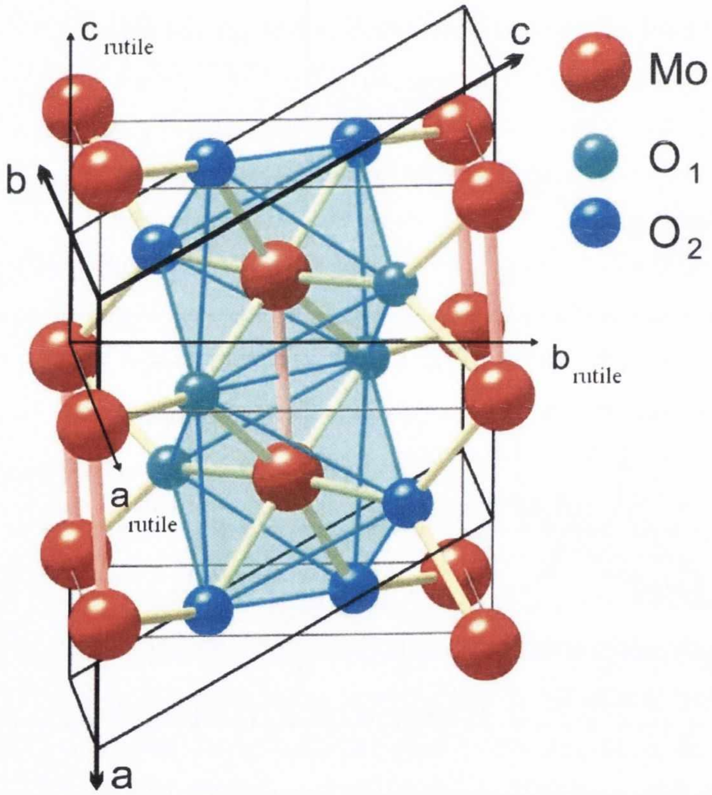

Figure 6.4: Monoclinic structure of $MoO_2$. Differing O1 and O2 sights shown. Dimerised metal pairs highlighted with thicker bonds. The *abc*-axes for a hypothetical pure rutile $MoO_2$ structure is superimposed for clarity. Figure is adapted from Moosburger-Will *et al.* [130]

Molybdenum(IV) dioxide crystallises in a monoclinic structure which deviates only slightly from the rutile structure as illustrated in Figure 6.4. Here, apart from atomic displacements, the atoms can be seen to form two stacked rutile cells as indicated by the thin solid lines. The corners of the monoclinic and tetragonal cells are shifted by half the hypothetical rutile unit-cell along the rutile $c_r$-axis (a quarter of a monoclinic unit cell along the $a$-axis). The lattice constants and the monoclinic angle amount to $a = 0.56109$ nm, $b = 0.48562$ nm, $c = 0.56285$ nm, and $\beta = 120.95°$ [139]. Like $WO_2$, it is metallically conducting, and is in a distorted rutile phase where the $d^2$ metal cation nominally forms an octahedral coordination with the surrounding oxygen ligand with the space group $P2_1/c$ $(C^5_{2h})$ [44,139].

In a similar manner to that discussed for $WO_2$, in particular what is shown in Figure 6.2, Mo atoms in $MoO_2$ dimerise along the monoclinic $a$-axis, displaying a kink-like distortion and alternating Mo–Mo bond lengths in this direction. And it is worth nothing that although there are two inequivalent oxygen atomic sites, there is only one molybdenum site with two Mo–Mo bond lengths along the $a$-axis. This leads to three separate Mo–O bond lengths within the trigonal plane for each oxygen site. Figure 6.2 adapted from Scanlon *et al.* [140] gives the bond lengths for each of these bond lengths. In this Figure O(a) and O(b) represent the O2 and O1 sites respectively for the notation used in this thesis.

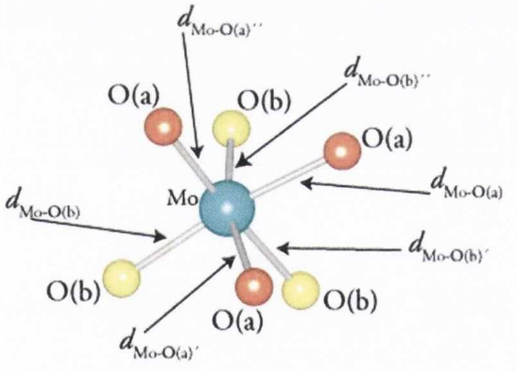

(a)

| **Bond** | Distance (Å) |
|---|---|
| $d_{\text{Mo-O(a)}}$ | 2.065 |
| $d_{\text{Mo-O(a)'}}$ | 2.073 |
| $d_{\text{Mo-O(a)''}}$ | 1.977 |
| $d_{\text{Mo-O(b)}}$ | 1.995 |
| $d_{\text{Mo-O(b)'}}$ | 1.972 |
| $d_{\text{Mo-O(b)''}}$ | 1.984 |
| $d_{\text{Mo-Mo(short)}}$ | 2.510 |
| $d_{\text{Mo-Mo(long)}}$ | 3.020 |

(b)

Table 6.2: Bond lengths in $MoO_2$. O(a) and O(b) represent the O2 and O1 sites respectively. $d_{\text{Mo-O(a)''}}$ and $d_{\text{Mo-O(b)'}}$ represent the apical bonds of the approximate octahedron. Figure adapted from Scanlon *et al.* [140] Experimentally obtained bond lengths in table originally from Brandt and Skapski [139].

Part of the interest in this compound stems from its structural similarity to the low-temperature phase of its neighbouring compound $VO_2$, in an effort to understand the factors that govern the stability of the latter compound's monoclinic phase [52,130]. It has been suggested recently in the literature that the monoclinic structure of $MoO_2$ results from a so-called embedded Peierls-type instability [52]. For more detail on the monoclinic distorted-rutile structure see Chapter 3.

### 6.2.4 Electronic Structure Calculations of $MoO_2$

The $MoO_2$ electronic structure calculations reproduced further on in Section 6.4, from Moosburger-Will *et al.* [130], were based on DFT and the local density approximation (LDA). They were performed using the scaler-relativistic implementation of the augmented spherical wave (ASW). Similar electronic structure calculations of $MoO_2$ were performed by Scanlon *et al.* [140], who employed DFT code through VASP. This software uses a plane wave basis set to describe valence electronic states.

## 6.3 Experimental Measurements

For the $WO_2$ presented here, all measurements were carried out on a single crystal provided by Prof. R. Egdell of Oxford. It was grown by a vapour transport method [141] from commercially available $WO_2$ powder. The $WO_2$ crystal was characterised by UPS, low energy electron diffraction (LEED) and scanning tunnelling microscopy (STM) [124,125]. The crystal measures approximately 4mm × 5mm × 2.5mm and has a single flat smooth face, suspected to be of (012) orientation [125], which was suitable for spectroscopy. It was discovered by comparing XAS scans to those published in the literature, that long-term exposure to atmosphere had produced a relatively thick oxidised $WO_3$ layer on this surface, resulting in the necessity of the disregarding of a significant volume of acquired data prior to this discovery. Since tungsten is appreciably heavier than oxygen, the desired $WO_2$ surface stoichiometry was again achieved by considerable argon ion sputtering while monitored, in part, by X-ray photoemission spectroscopy (XPS).

For the $MoO_2$, all measurements were similarly carried out on a select few bulk single crystals provided by Dr. Matthias Klemm of the Universitt Augsburg, Germany. The single bulk crystal was grown by the chemical transport method, using $TeCl_4$ as transport agent [142]. The crystal measures approximately 2mm × 2mm × 0.5mm. Its surface was shown to have a (100) face identified by Laue X-ray backscattering. The orthogonal monoclinic $b$ and $c$-axes thus lie in the plane of the surface, while the $a$-axis is aligned out of the surface at an angle of 120.95° with respect to the $c$-axis.

X-ray spectroscopic measurements presented here were carried out at the undulator beamline I511-3 of the MAX-lab facility in Lund, Sweden [24]. The beamline is equipped with a Nordgren type X-ray spectrometer [18] situated in the plane of the orbit of the synchrotron at 90° to the incoming synchrotron beam, which is also the plane that contains the polarisation vector of the linearly polarised light. Though the spectrometer is rotatable about the axis of the beam to an out-of-plane scattering geometry [24], only in-plane scattering measurements were recorded for this sample. The I511-3 endstation at MAX-lab is described in greater detail in Chapter 2

The O $K$-edge XAS measurements presented here were obtained with a beamline monochromator resolution nominally set to $\sim$ 0.1 eV. The resolution used for the O $K$-edge X-ray emission measurements, measured in $1^{st}$ order, corresponded to a spectrometer entrance slit width of $\sim$12 $\mu$m and a spectrometer slit resolution of 0.6 eV. The monochromator resolution used during emission measurements was 0.5 eV. The emission spectra were calibrated with the $L_\alpha/L_\beta$ emission lines of Zn in the $2^{nd}$ order of diffraction, while the absorption photon energy scales were calibrated by comparison with the X-ray absorption of rutile $TiO_2$ [92,93].

### 6.3.1 $WO_2$ Measurements

The $WO_2$ crystal was cleaned ultrasonically in ethanol to remove adsorbed surface contamination and mounted as is with the suitable flat surface approximately parallel to the surface of the sample plate. O $K$-edge XAS by total electron yield (TEY) revealed high degree of acquired surface oxidation, differing significantly from the more bulk sensitive TFY. The sample surface was sputtered for considerable length until the two absorption methods were in reasonable agreement. Further angle-dependent XAS revealed the surface was not (012), and thus did not contain the monoclinic $a$-axis. Repeated angle-dependent absorption measurements at the O $K$-edge, varying first polar and then azimuthal angle showed the threshold $\pi^*$ peak to go through a point of maximum relative intensity, and in an orthogonal geometry it went through a point of minimum intensity. This allowed the determination of the direction of the monoclinic $a$-axis; which deviated $\sim$ 30° from normal to the primary smooth surface of the crystal. This strongly suggested that the $b$ and $c$-axes were contained within the plane of this surface making it a (100) face, similar to that of the $MoO_2$ crystals used. The $b$-axis, being orthogonal to the $a$-axis was therefore parallel to the long straight edge of the crystal.

The four-axis manipulator used during these emission measurements only allowed for polar rotation and thus the crystal had to be remounted for each measurement geometry. The first of these in-plane geometries was $\mathbf{E}\perp a$;XES$\perp a$. Here the crystal was oriented such that the $a$ and $c$-axes lay in the horizontal scattering plane, with the $b$-axis vertical. The incidence angle of the incoming X-rays was 30° deviated from normal incidence such that $a$-axis was aligned parallel with the incident x-ray propagation vector $\mathbf{k}$, the $b$-axis was perpendicular to both the optical axis of the spectrometer and $\mathbf{k}$, and the $c$-axis was approximately parallel to $\mathbf{k}$ and the spectrometer, with 30° offset. Thus the full description of this measurement geometry would be $\mathbf{E}\perp a, \perp b, \sim \| c$;XES$\perp a, \perp b, \sim \| c$, but will be abbreviated $\mathbf{E}\perp a$;XES$\perp a$ from here on out.

For the second geometry, $\mathbf{E}\| a$;XES$\| a$, the sample was azimuthally rotated 180° such that, as with the first geometry, the $a$ and $c$-axes lay in the horizontal scattering plane and $b$ vertical. Here the polar angle was set such that there was a 60° angle of incidence onto the (100) surface, aligning the $a$-axis parallel to $\mathbf{E}$ and the optical axis of the spectrometer, with $c$ approximately 30° offset from parallel with $\mathbf{k}$. Unabbreviated, this geometry can be written: $\mathbf{E}\| a, \perp b, \sim \perp c$;XES$\| a, \perp b, \sim \perp c$.

### 6.3.2 $MoO_2$ Measurements

Since the primary measurable surfaces of the supplied $MoO_2$ crystals were (100), similar to the surface face identified on $WO_2$, the very same two in-plane measurement geometries were used. Thus two samples were mounted flat on the sample holder, the surface of which was parallel to the (100) crystal faces. Both were aligned with their $b$-axes vertical, and their $a$ and $c$-axes within the crystal plane, but azimuthally rotated 180° with respect to each other. So for the $\mathbf{E}\perp a$;XES$\perp a$, the incident angle was 30° on one sample, while for $\mathbf{E}\| a$;XES$\| a$ a 60° angle of incidence was used on the other sample. This is exactly the same as described for the $WO_2$.

## 6.4 Results and Discussion

Taking advantage of the fact that the monochromatised synchrotron light is linearly polarised, it was possible to probe the dichroic nature of a single crystal material using XAS and RXES at the O $K$-edge. Two in-plane crystal alignments were utilised in the measurements, as detailed in Section 6.3. These comprise the bulk of the comparative work.

### 6.4.1 Polarisation Dependent XAS of $MoO_2$

It is pertinent to note at this juncture that similar to the isostructural $WO_2$ covered in the proceeding section, there is no evidence from high resolution O $1s$ XPS studies that there can be anything other than a common O 1s binding energy assigned to the O1 or O2 sites [140]. This eliminates the possibility of there being a chemical site specific cause of the rapidly changing near threshold RXES spectra, where O $1s$ core holes are being created on one oxygen site in preference to the other due to different thresholds. Instead, the O $1s$ XPS, not shown here, exhibits an O $1s$ main line with a binding energy of 530.05 and a satellite line at 531.17 eV which has $\sim 63\%$ of the area of the main line and can be ascribed to a plasmon loss peak where the energy difference between the components to this plasmon loss peak is $1.0 \pm 0.2$ eV. There can still be an imbalance in the rate of creation of O $1s$

core holes on the two sites, but this can only be due to the relative transition intensities to the unoccupied bands that arise according to their relative O $2p$ PDOS and XAS intensities at a given excitation energy and orientation.

MoO$_2$ exhibits very distinct natural linear dichroism in the O $K$-edge XAS. This is illustrated in Figure 6.5 which shows the contrast for the two orientations explained in the experimental details section of this chapter: $\mathbf{E}\|a$ and $\mathbf{E}\perp a$. The top set of spectra is MoO$_2$ O $K$-edge XAS for both orientations recorded in total fluorescence yield (TFY) mode. The middle pair of spectra were recorded simultaneously as the above and measured via TEY. The bottom set of three spectra in Figure 6.5 were taken from Eyert *et al.* [52] and include a spectrum from an unoriented, presumably powdered sample, in black[†]. Spherically unoriented XAS for a perfect rutile crystal structure would be made up of $\frac{1}{3}\mathbf{E}\perp a + \frac{2}{3}\mathbf{E}\|a$, which would approximately be the case for a distorted rutile. There is excellent agreement with the Eyert results, especially for the TFY. There is some discrepancy comparing the TEY with the TFY, but only for the $\mathbf{E}\perp a$ red spectra. The second peak at ~534 eV in the $\mathbf{E}\perp a$ TFY shifts to ~533 eV in TEY. This can be explained by mild surface contamination, most likely surface oxidation resulting in a very small layer of MoO$_3$.

As mentioned in Section 6.3.2, two samples were used, one for each measurement geometry. The sample utilised for the $\mathbf{E}\|a$ orientation (blue in Figure 6.5) underwent surface preparation by argon ion sputtering, the sample used for the $\mathbf{E}\perp a$ orientation (red) did not have its surface sputtered. Electron yield is significantly more surface sensitive than fluorescence, due to reduced electron escape depth, thus it can be concluded that the TFY results in this case are a more accurate measure of the polarisation selected unoccupied PDOS, especially for the $\mathbf{E}\perp a$ orientation. Thus in the following discussion of MoO$_2$ XAS features, the TFY will be what is referenced. However, even the TEY overwhelmingly resembled MoO$_2$ and not MoO$_3$ [20,143]. RXES and TFY are inherently bulk sensitive techniques and thus very minor surface effects such as these can be effectively ignored.

The lettered arrows in Figure 6.5 indicate at what energies resonant emission spectra were recorded for both orientations, but serve a second purpose in highlighting features. As with other rutile and rutile-like materials in this body of work, the first peak at feature (c) is identified as the $\pi^*$ peak, resulting from the $\pi$-like overlap of the O $2p_y$ bonding hybridisation with the Mo $4d$ $t_{2g}$. More specifically in this case however it is the $d_\perp$ orbitals which have lobes that straddle the apical oxygen anion. This feature is significantly suppressed in the $\mathbf{E}\|a$ geometry. The Mo$_3$O planes lie almost entirely parallel to this monoclinic $a$-axis and hence the O $2p_y$ orbitals that lie perpendicular to these planes are not accessed by the

---

[†] In Eyert [52] it states the XAS data is originally from the PhD thesis by Müller [131], which was not accessible. Eyert does not state whether the unoriented sample was powdered, nor does he state some experimental details of the measurements; whether TEY or TFY was used etc.

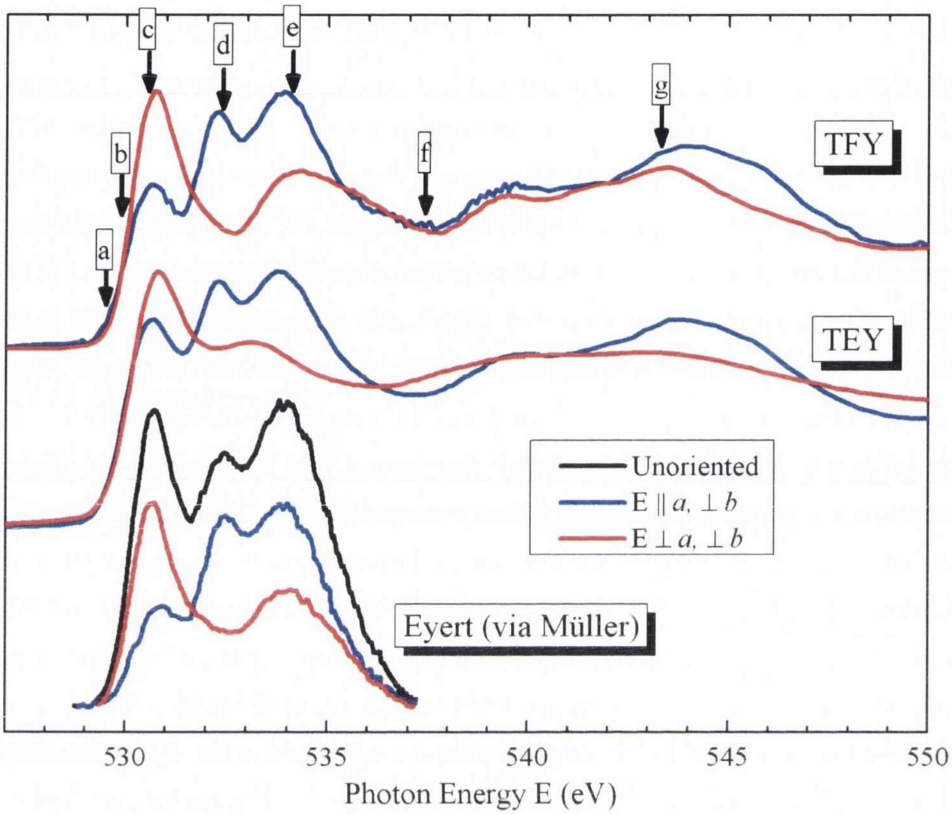

Figure 6.5: XAS of $MoO_2$ at the O $K$-edge at two orthogonal measurement geometries, $\mathbf{E}\|a$ and $\mathbf{E}\perp a$. Simultaneously recorded TEY and TFY are shown to highlight difference between bulk and surface sensitivity. These are compared with previous results acquired from Eyert *et al.* [52], though were originally published in a PhD thesis by Müller [131]. Here the black is for unoriented $MoO_2$.

excited core electron in this geometry. This is in contrast with the $\mathbf{E}\perp a$ orientation where preferential excitation into these states occurs.

Mo–O hybridisation allows an indirect probe of the bonding metal valence orbitals at the O $K$-edge. It is therefore instructive to study the calculated Mo partial DOS of monoclinic $MoO_2$ in Figure 6.6, adapted from Moosburger-Will *et al.* [130] These calculations were based on DFT and the LDA, specifically using the ASW method [144]. Part **a)** of this figure contrasts the calculated DOS of the Mo $4d$ $t_{2g}$ (red), $4d$ $e_g$ (green) and O $2p$ (blue). Note the sudden shift in weight from the $t_{2g}$ to $e_g$ states in the conduction band at ~3 eV above the Fermi energy due to the antibonding $e_g$ derived $\sigma^*$ states occurring at a higher energy.

The Mo $4d$ $e_g$ states, i.e. the $d_{x^2-y^2}$ and $d_{z^2}$, form a $\sigma$-type bonding arrangement with the O $sp^2$ hybridised orbitals which includes the $2p_x$ and $2p_z$, similar to other rutile-type structure compounds. The unoccupied states derived from these molecular orbitals can be

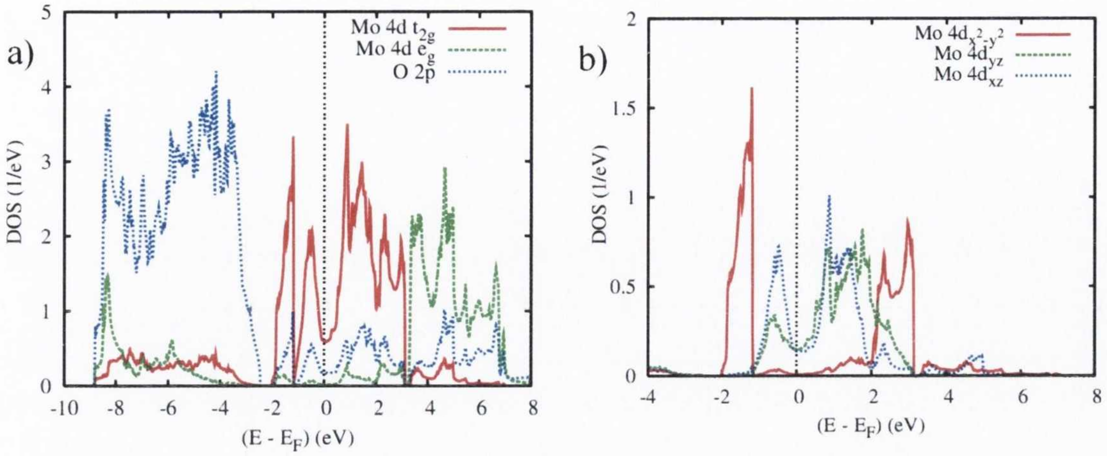

Figure 6.6: Adapted from Moosburger-Will *et al.* [130] **a)** Partial calculated DOS of MoO$_2$ for Mo $4d$ $t_{2g}$ (red), $4d$ $e_g$ (green) and O $2p$ (blue). **b)** Partial DOS of Mo $4d$ $t_{2g}$ individual orbitals, where local coordinate frame of Mo cation is rotated by ~45° about the $z$-axis with respect to the natural coordinate frame used in this thesis. Thus $d_{x^2-y^2}$ in the rotated frame, as described by Moosburger-Will, is transformed into our $d_{xy}$ in the natural coordinate frame. Similarly their $d_{xz}$ and $d_{yz}$ are transformed into our $d_{z(x+y)}$ and $d_{z(x-y)}$ respectively.

observed in the O $K$-edge XAS in Figure 6.5 at approximately ~534 eV, highlighted by (e) for both the $\mathbf{E}\|a$ and $\mathbf{E}\perp a$. This feature, resulting from metal $e_g$ orbitals $\sigma$-bonding with the $sp^2$ hybridised oxygen $p_x$ or $p_z$, is designated the $\sigma^*$ peak. The oxygen orbitals hybridised with the Mo $d_{x^2-y^2}$ molecular orbital will be accessed in either orientation, but the chemical bond or MO formed by the Mo $4d_{z^2}$ and the O $2p_z$ states is only accessed in the $\mathbf{E}\perp a$ geometry. Bearing in mind this is O $K$-edge XAS, and simplifying by briefly picturing it as a pure rutile structure in the first approximation; the $\mathbf{E}\perp a$ absorption should give a projection of O $\frac{1}{2}(2p_z + 2p_y)$ unoccupied states while the $\mathbf{E}\|a$ would give the O $2p_x$ projected unoccupied PDOS. This justifies why feature (e) is apparent in both orientations, and why it is comparatively larger in the $\mathbf{E}\|a$ geometry ($p_x > \frac{1}{2}(p_z)$).

It is worth noting that while comparable in energy, the $p_z$ and $p_x$ represent primarily differing $\sigma$ bonds which explains the slight shift and difference in shape between them. However, the $p_z$ projection will "sample" components from all three $sp^2 - e_g$ MO in the M$_3$O plane, and thus the $\mathbf{E}\perp a$ measurement geometry will contain some character from the $sp^2$–$d_{x^2-y^2}$ MO. As mentioned earlier, and similar to the XAS of other structures studied in this work, feature (c) or the $\pi^*$ peak, is heavily suppressed in the $\mathbf{E}\|a$ geometry since all O $p_y$ orbitals lie orthogonal to the monoclinic $a$-axis and thus are not accessible in this excitation geometry.

Feature (d) in Figure 6.5 at an energy of ~ 532.2 eV, is possibly the most interesting feature given its apparently total suppression in $\mathbf{E}\perp a$, and also the fact it is does not appear to have an analogue in pure undistorted rutile compounds. It can be attributed to the bonding-antibonding splitting of the Mo $4d_{xy}$ $t_{2g}$ states, whose separation is greater than $d_{xz}$ or $d_{yz}$ due to the tetragonal distortion of the octahedron in a rutile compound. In distorted-rutile, monoclinic compounds this distortion is exacerbated and the separation amplified. The distortion, and hence exacerbated splitting, is due to a Peierls type instability in the $d_{xy}$ states [52] which mediates the metal-metal overlap along the dimerised chains of Mo atoms parallel to the monoclinic $a$-axis forming metal-metal $\sigma$-type bonds, as mentioned in Section 6.2.

$d_{xy}$ in these systems are often referred to as the $d_{\|}$ states and thus feature (d) is designated the $d_{\|}(\sigma^*)$ peak, previously postulated as arising from O $2p_x$ hybridisation with the Mo $4d_{xy}$ [52]. The splitting is shown in Figure 6.6b in red (labelled $d_{x^2-y^2}$ in Eyert's basis[†]). This orbital clearly does not contribute to the metallic conductivity of the material, and its splitting contributes to a significant dip in the $t_{2g}$ states around the Fermi energy. It results in the $d_{xy}$ bonding states being at a lower energy than the other $t_{2g}$ orbitals. In turn the antibonding states, visible as the $d_{\|}(\sigma^*)$ peak, are at a higher energy than the $d_{\perp}$ $t_{2g}$ states that hybridise to form the $\pi^*$ peak (feature (c)).

While Eyert postulated this feature (c) being $sp^2$–$d_{xy}$ derived, it is difficult to believe that this is its primary origin. In pure rutile oxides the $d_{xy}$ orbital is the only $t_{2g}$ orbital that is simply not involved in bonding with the anion $p$ orbitals at all, due to its primary $\sigma$-type overlapping of metal-metal atomic sites along the rutile $c$-axis. Further, in the O2 site of $MoO_2$, any net bonding of the $d_{xy}$ orbital with the equatorial O2 $sp^2$ lobes would be highly doubtful in the 90° Mo–O–Mo (in the trigonal plane) due to cancelling phases of the wavefunction. In O1 however the bond angle is reduced significantly, as illustrated in Figure 6.1 on page 117 for isostructural $WO_2$, meaning there would no longer be such a net cancellation. Additionally, the significant difference between equatorial Mo–O1 and Mo–O2 bond lengths (Table 6.2b) strongly predicts an energy difference between O1 and O2 derived $sp^2$–$d_{x^2-y^2}$ MOs. The double peak feature in the $e_g$ PDOS calculations from Moosburger-Will in Figure 6.6 supports this. The same would not be the case for the apical oxygen sites as their bond-lengths and hence overlap are nearly identical.

Therefore it is proposed here that feature (c) of Figure 6.5 is primarily a combination of O2 derived $p_x$ hybridisation with $d_{x^2-y^2}$ states, with some contribution from O1 derived $p_x$ hybridisation with $d_{xy}$.

Lastly it is noted that in the $\mathbf{E}\|a$, while the $\pi^*$ peak is significantly reduced, it does not disappear entirely, or to the same degree as it does in, for example, rutile $IrO_2$ (Chapter 4). From PDOS calculations presented in Eyert *et al.* [52][‡] it can be deduced that there is an O

---

[†] It should be noted that this figure uses a rotated metal coordinate frame as described in Eyert *et al.* [52], where the $d_{x^2-y^2}$ orbital is transformed with the $d_{xy}$ orbital in the natural coordinate frame used here.

[‡] Figure 14 of this paper.

$p_x$ component in the threshold energy region, possibly from less tightly bound hybridisation of the equatorial O2 with $d_{x^2-y^2}$ as well as partial net overlapping of $p_x$ with the $t_{2g}$ orbitals for both oxygen sites arising from the monoclinic distortion.

### 6.4.2 Polarisation Dependent XAS of $WO_2$

Figure 6.7 shows the measured O $K$-edge XAS spectra for $WO_2$, measured in TFY mode for two distinct orientations, with the monoclinic $a$-axis being either parallel or perpendicular to the electric field of the linearly polarised synchrotron radiation. These orientations are detailed in Section 6.3.1 and are denoted $\mathbf{E}\|a$ and $\mathbf{E}\perp a$ respectively. The present XAS measurements are compared with calculated conduction band (CB) oxygen $2p$ PDOS, averaged over the equally weighted O1 and O2, projected along the $a$-axis ($p_x$) and orthogonal to it ($p_y + p_z$). These have been broadened from their original form by a 0.2 eV Gaussian and 0.25 eV Lorentzian to simulate the instrumental broadening and the O $1s$ lifetime broadening, respectively. The Fermi level of the calculated PDOS was rigidly shifted to 530.2 eV, matching the corresponding slope-determined threshold of states in the absorption, in agreement with the O $1s$ binding energy as measured by XPS.

There are three orthogonal subcomponents of the oxygen $2p$ PDOS for each site: first is the component projected along the monoclinic $a$-axis which lies within the $W_3O$ planes ($p_x$). Second is the component perpendicular to the $a$-axis which for each site also lies within the respective $W_3O$ plane (O1 or O2) ($p_z$). These two orthogonal components within the $W_3O$ planes can together describe the densities of states arising from the three oxygen $sp^2$ derived orbitals, which may bond with W $5d$ $e_g$ $d_{z^2}$ and $d_{x^2-y^2}$ orbitals to form $\sigma$-like W–O orbitals. Finally, the third orthogonal component is the lone $2p$ orbital lying perpendicular to each $W_3O$ plane ($p_y$) and which can form $\pi$-like W–O orbitals where bonding with W $5d$ $t_{2g}$ $d_{z(y-x)}$ and $d_{z(y+x)}$ orbitals occurs. This O $2p_y$ $\pi$-like component of the W–O orbitals is, for both oxygen sites, perpendicular to the monoclinic $a$-axis. Thus in the $\mathbf{E}\|a$ measurement geometry, excitations to the unoccupied $\pi^*$-like $2p$ PDOS of the W–O orbitals cannot occur, whereas in the $\mathbf{E}\perp a$ geometry they are favoured. The O $K$-edge XAS in Figure 6.7 can be thus compared with the O $p_x$, $p_y$ and $p_z$ components derived from the electronic structure calculation. It should be remarked that the calculation, in contrast with the experiment, indicates that the unoccupied $2p_x$ PDOS component of both O1 and O2, i.e. their projected PDOS along the monoclinic $a$-axis, is almost zero for the first two electron volts above the Fermi level. The O $K$-edge XAS threshold absorption in the $\mathbf{E}\|a$ geometry on the other hand, though significantly suppressed by comparison, is not reduced to the same degree. Part of the reason may be the error inherent in the aligning of the crystal axes for the desired measurement geometry. This would only be a small factor however due to the $\cos^2$

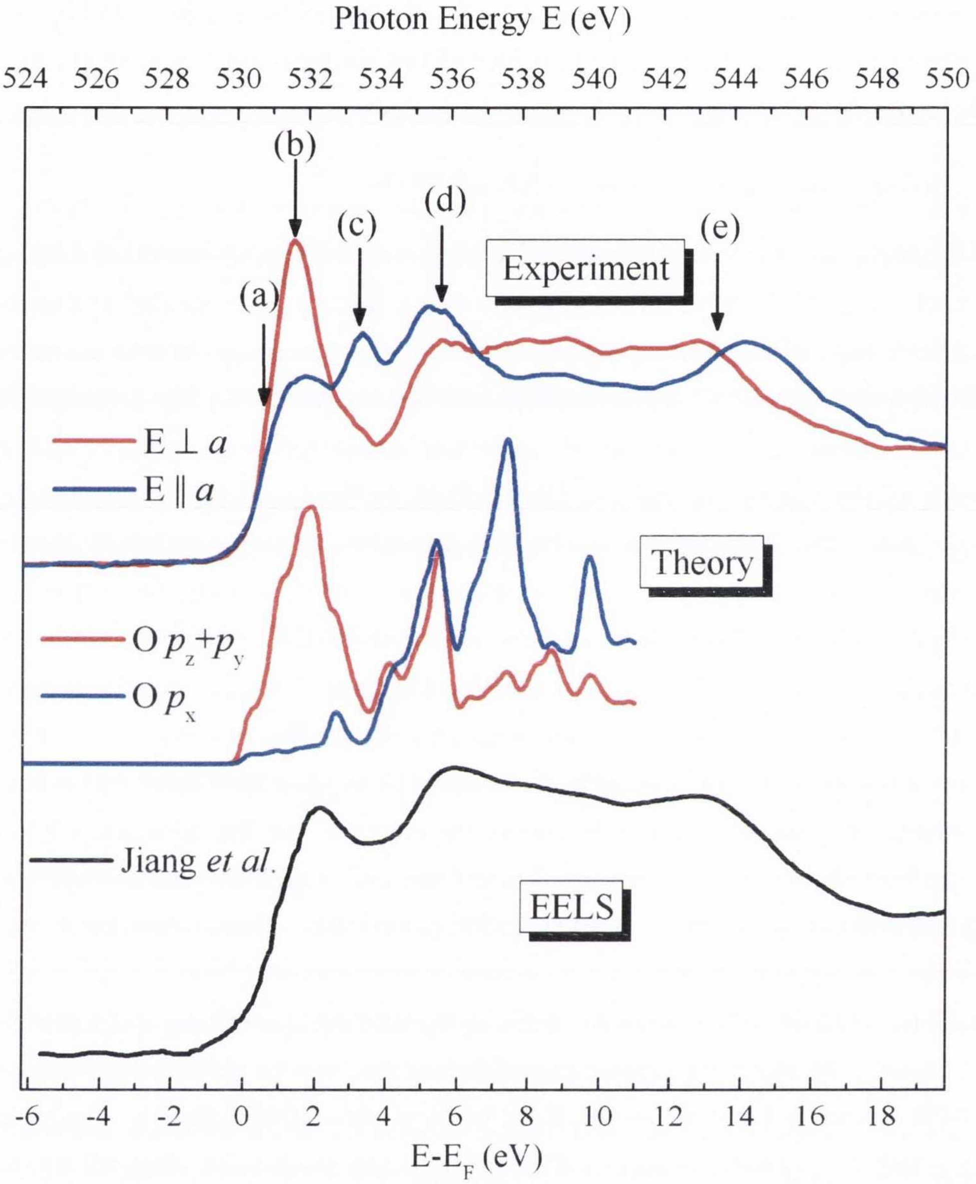

Figure 6.7: XAS of $WO_2$ at the O $K$-edge at two orthogonal measurement geometries, $\mathbf{E}\|a$ and $\mathbf{E}\perp a$. Compared below these are the simulated XAS constructed from the calculated oxygen $2p$ CB PDOS for the $p_x$ and $(p_y + p_z)/2$ respectively. These were averaged between the O1 and O2 sites and broadened with a 0.2 eV Gaussian and 0.25 eV Lorentzian to simulate experimental resolution.

dependence in natural linear dichroism. It may be that a full structural relaxation in the calculation will improve this correspondence but that is not attempted here, nor is the effect of a core hole exciton included in this simple comparison. Thus the correspondence between the O $2p$ PDOS and the O $K$-edge XAS should not be expected to be exact, as the former is obtained from a ground state calculation and the final state rule should apply to the XAS;

thus a calculation of the O $K$-edge XAS involving a core hole would be required to model this correctly. It is apparent however that states of O $p_x$ character occupy this threshold energy region of the CB more than predicted.

Overall however there is good agreement between the experimental absorption and calculations. This is most notably the case for the $\mathbf{E}\perp a$ geometry, where the correlation is especially close. The shifting of spectral weight between the two orientations very much conforms to the trend predicted by the dichroism in calculated state density. Moreover it is highly comparable to the XAS seen for isostructural MoO$_2$ (Figure 6.5). In the $\mathbf{E}\|a$ geometry the appearance of a new feature (c) at 533.5 eV compares closely to that observed in MoO$_2$, and thus it is similarly attributed here to primarily apical O2 derived $p_x$–$d_{x^2-y^2}$ as well as O1 derived $p_x$–$d_{xy}$ $t_{2g}$ hybridisation due to the monoclinic distortion.

Unlike MoO$_2$, calculations have been performed for this thesis. Unfortunately no clear account for this feature (c) has been demonstrated in the literature. It is suspected that feature (c), nominally called the $d_{\|}(\sigma)^*$ feature due to its shared energetic position with W 5$d_{xy}$ ($d_{\|}$) states, results from a combination of O 2$p_x$ with both the $d_{xy}$ and $d_{x^2-y^2}$.

This natural linear dichroism arises from both the $sp^2$ hybridisation and the rutile-like structure of the material. The significant dichroism in the absorption, or natural linear dichroism observed in these absorption measurements at the oxygen $K$-edge, while matching closely with its isostructural $d^2$ neighbour MoO$_2$, is also similar to that observed for rutile oxides such as IrO$_2$ (Chapter 4) by Cockburn *et al.* [145] and for rutile CrO$_2$ by Stagarescu *et al.* [146]. In common with WO$_2$ and MoO$_2$, the Cr metal ion formally has a $d^2$ metal $d$ orbital occupancy, but crystallises in a tetragonal rutile as opposed to distorted rutile (monoclinic) structure, although in CrO$_2$ there is also a large exchange splitting separating spin↑ and spin↓ components resulting in a half-metal [44].

### 6.4.3 Polarisation Dependent RXES of MoO$_2$

The left panel in Figure 6.8 shows the polarisation dependent RXES spectra for the first four energies indicated by the black arrows in the XAS Figure 6.5. The right panel shows the resonant emission from incident excitation energies (e)-(g) as well as the normal XES (NXES) comparison taken at $\sim$ 560 eV. These NXES spectra display a very strong natural linear dichroism in X-ray emission.

This significant shift between the NXES spectra is a non-resonant effect attributed to the crystal orientation with respect to the spectrometer. This natural linear dichroism in emission is discussed in more detail in the linear dichroism section of Chapter 2 on page 18. Briefly, it results from the anisotropy of the orbitals or charge distribution as viewed from the perspective of the spectrometer. When the spectrometer optical axis is aligned such that XES$\|a$, as it is in the blue NXES spectrum, the spectral weight is biased toward emission from the O $p_y$ and O $p_z$ of each oxygen site. Respectively these correspond to the $\pi$ Mo–O, and the $2p$ projection of the $sp^2$ $\sigma$ orbitals along the Mo–O apical direction. In the contrasting emission scattering geometry where XES$\perp a$ the O $2p_x$ projection of the $sp^2$–$\sigma$ hybridisation becomes the dominant contribution, as it lies parallel to the $a$-axis. The occupied O $2p$ $\pi$-character states are less tightly bound than the O $2p$ $\sigma$ states, and thus the XES$\|a$ (blue) NXES spectrum is shifted to a higher photon energy with respect to the red.

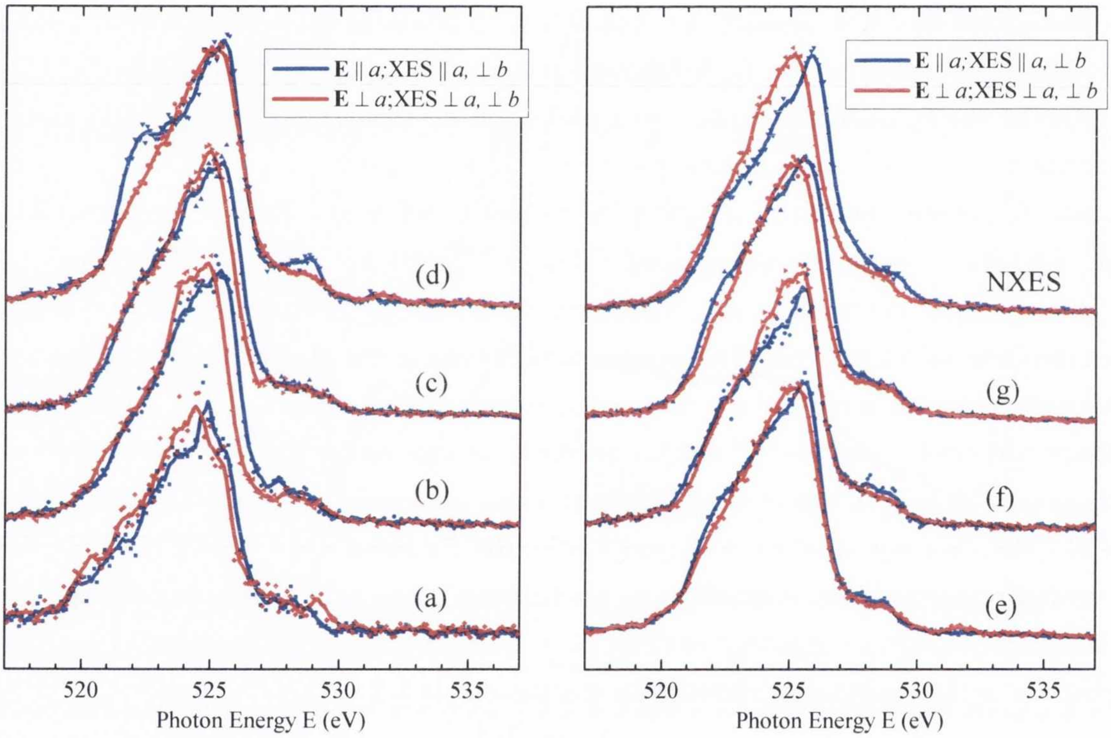

Figure 6.8: Waterfall graphs of $MoO_2$ emission spectra at the O $K$-edge in the two measurement geometries indicated: $\mathbf{E}\perp a$;XES$\perp a$ and $\mathbf{E}\|a$;XES$\|a$. Left panel shows the first four chosen RXES excitation energies labelled (a) through (d) as indicated by the correlating labels on the XAS in Figure 6.5. Right panel shows the next three resonant excitation energies as well as the normal emission on top. Scatter points represent recorded data while solid lines are after 5-point adjacent averaging.

The spectra obtained nearer to threshold in Figure 6.8 also display a clear dichroism. It is worth noting the leading edge of the main O $2p$ band at $\sim$ 526.5 eV is noticeably shifted down in energy in the $\mathbf{E}\perp a$ (red) spectra, by comparison to its counterpart, for the near threshold excitations (a), (b) and (c). At spectra (d), when the intermediate absorption state is resonant with the $d_{\|}(\sigma^*)$ unoccupied band however the valence band edges of the emission appear to converge.

It is useful for interpretation of resonant features to examine the calculated bandstructure diagram, presented for MoO$_2$ in Figure 6.9 and adapted from Scanlon *et al.* [140]. It is difficult to draw concrete conclusions from this, since the bandstructure diagram is unweighted. However it is possible that the unoccupied $p_y$ and $p_z$ component states preferentially selected in the $\mathbf{E}\|a$;XES$\|a$ threshold region experience a minimum around the $\Gamma$ point. The unoccupied $p_x$ states in the CB, excited when $\mathbf{E}\perp a$, might then experience a maximum at this high symmetry $k$-point in the 0-2 eV range above the Fermi energy. Examining now the occupied bandstructure in the region of $\Gamma$, the main O $2p$ bands, especially in the region of $-2$ to $-7$ eV, exhibit a prominent upward shift in energy. Thus by $\mathbf{k}$-conservation rules, the occupied states in the region of $\Gamma$ would be selected for emission in the $\mathbf{E}\|a$;XES$\|a$ measurement geometry, whereas the $\mathbf{E}\perp a$;XES$\perp a$ geometry selects across a broader range of crystal momentum, where the bands are significantly less dispersed. This would account, at least in part, for the natural linear dichroism observed in spectra (a)-(c). It would also account for convergence of the peaks at spectrum (d) whose excitation is $\sim 2$ eV above the Fermi energy, as it can be seen there is an absence of states, $p_x$ or otherwise at the $\Gamma$ point in this energy region.

Another plausible factor that would partially explain this divergence in mean spectral weight between the two measurement geometries for the near threshold is simple natural linear dichroism, similar to that seen for the NXES of MoO$_2$. The $\mathbf{E}\|a$;XES$\|a$ favours emission from $p_y$ and occupied states, since they are both orthogonal to the optical axis of the spectrometer. Further, assuming similarity with isostructural WO$_2$, they are on average less tightly bound than their occupied $p_x$ component counterpart, leading to a shift in spectral features toward a higher energy.

We focus now on the states at the top of the valence band (VB), just below the Fermi level. This low spectral-weight feature, ranging from 527 eV to 529 eV is visible in all presented emission spectra and results specifically from O $2p$ hybridisation with Mo $4d$ $t_{2g}$ orbitals. This is clear when comparing with the calculated DOS in Figure 6.6. In that figure it is evident that it is actually two distinct features washed together in the RXES experimental spectra presented, as a result of insufficient resolution and coupled with inadequate signal to noise ratio, for these low density features. However, Gulino *et al.* reports O $K$-edge VB UPS spectra for WO$_2$ and MoO$_2$ where the features are observed individually in both compounds [124]. The UPS from Gulino showing these low binding energy features is illustrated in Figure 6.10, and is contrasted with the RXES spectra (c) as well as VB O $2p$ PDOS calculations made by both Scanlon *et al.* [140] and another set by Moosburger-Will *et al.* [130] The lower energy hybridised $d_{\|}(\sigma)$ peaks is attributed to the occupied bonding states of the splitting of the $d$ band, specifically the Mo $4d$ $d_{xy}$ (or $d_{\|}$) orbital which facilitates

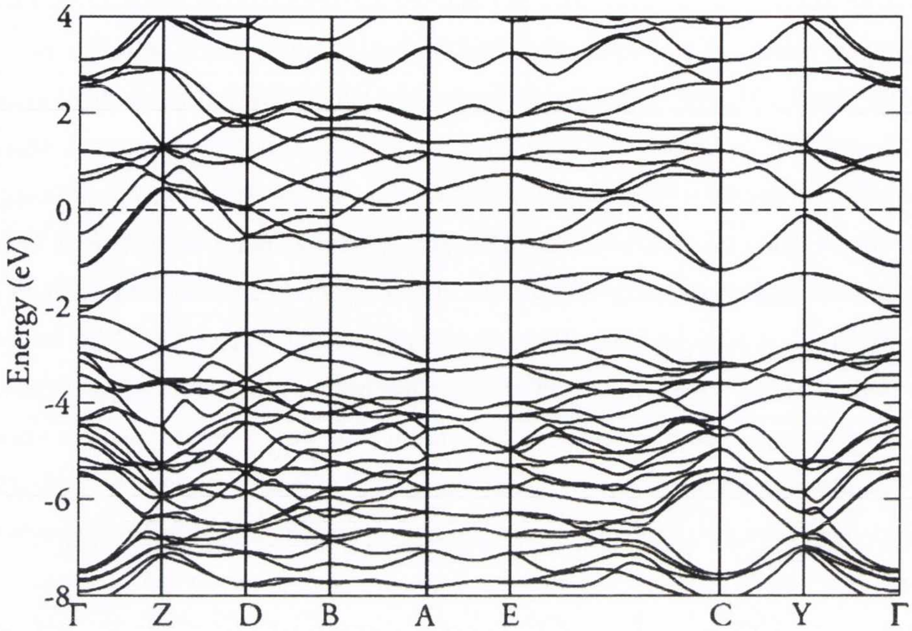

Figure 6.9: Electronic band structure along the high-symmetry points for $MoO_2$. The dashed line denotes the Fermi energy. From Scanlon *et al.* [140]

Mo–Mo bonding along the monoclinic $a$-axis. Thus it is referred to as the $d_{\|}(\sigma)$ feature and lies at approximately 1.4 eV below the Fermi energy [124]. The higher energy peak at the VB maximum is attributed to the hybridisation of the remaining $t_{2g}$ ($d_{xz}$,$d_{yz}$) orbitals with the O $p_y$ and $p_z$, especially the O1 site.

The $\mathbf{E}\|a$;XES$\|a$ (blue) RXES spectrum at energy (d) in 6.8 displays a significant shift of spectral weight towards both the top and bottom (though not the very bottom) of the VB. Examining again Figure 6.9, the bandstructure of $MoO_2$, the bandwidth of spectrum (d) falls around the 3 eV region. The crystal momentum of the CB states here is concentrated in the region of the Y-Γ-Z high symmetry $k$-points. As will be seen for the $WO_2$ in the proceeding section, and assuming a similar weighting of the $MoO_2$, this region may also show the heaviest weighting of the O $p_z$ in the bottom of the VB; $p_z$ and $p_y$ being the favoured component emission for the $\mathbf{E}\|a$;XES$\|a$ geometry.

The shift of spectral weight toward the very front of the VB of spectrum (d) in this same geometry is again attributed to O1 $p_z$ and $p_y$ emission, their emission being favoured in this geometry. The VB maximum bands are selected in excitation (d) due to site and symmetry selectivity. Again assuming similarity with isostructural $WO_2$ discussed in the proceeding subsection, $\mathbf{E}\|a$ at excitation (d) is strongly biased toward the O1 site, where strong hybridisation occurs for the Mo VB $t_{2g}$ $d_{\perp}$ with the O1 $p_y$ and $p_z$ occupied states. Further, a $k$-selective element may be present due to this feature's amplification only at

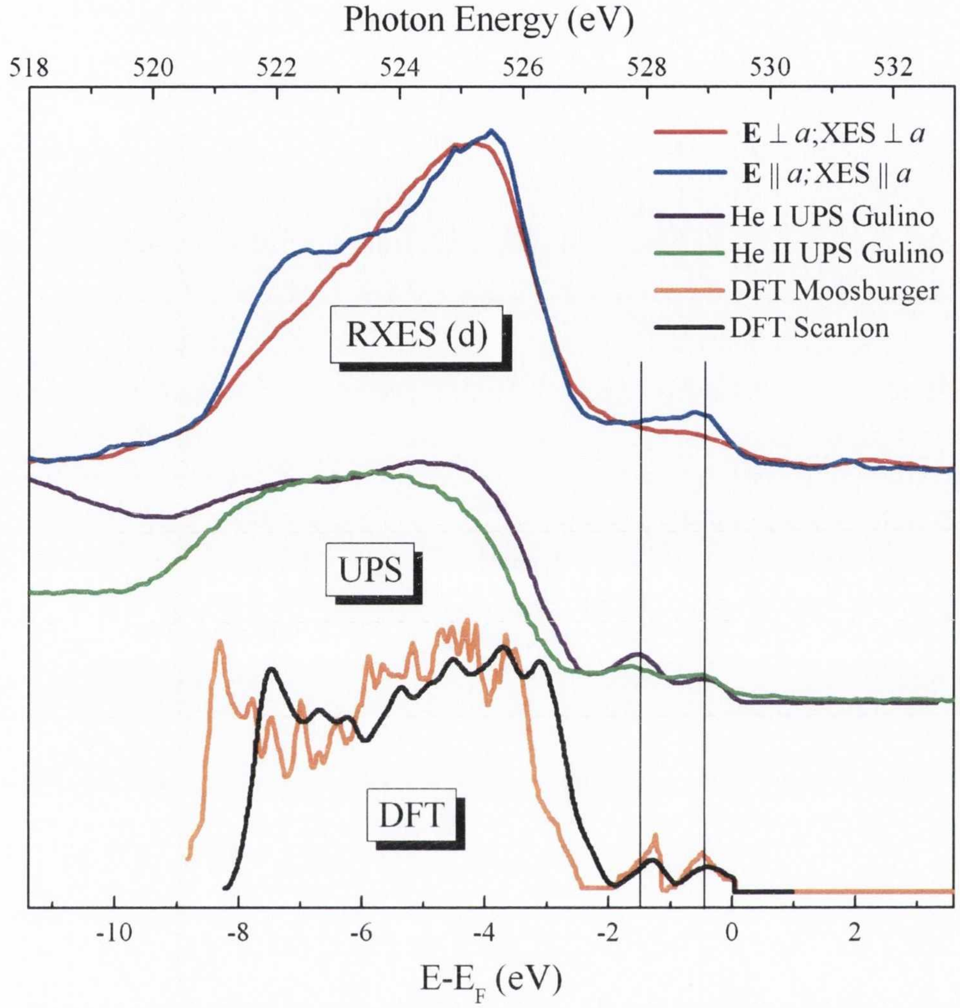

Figure 6.10: Comparison of polarisation dependent O $K$-edge RXES of MoO$_2$ at excitation (d) (top) with O $2p$ VB He I and He II UPS from Gulino *et al.* [124] (middle), and two sets of O $2p$ VB DFT calculations from Scanlon *et al.* [140] as well as Moosburger-Will *et al.* [130] Lines on this figure show the position of the $d_{\|}(\sigma)$ and $d_{\perp}(\pi)$ features at approximately -1.5 eV and -0.5 eV respectively, with respect to the Fermi energy.

excitation energy (d). The bandstructure in Figure 6.9 in the region of the Y-Γ-Z high symmetry points just below the Fermi energy shows that the "$d_{\perp}$" band goes through a maximum at Y and crosses the Fermi level between Γ and Z. This RXES $k$-selectivity is the primary reason proposed here for the significant dichroism observed at excitation (d) in the O $K$-edge of MoO$_2$.

The extra spectral weight towards the bottom of the main O $2p$ valence band states in this same spectrum is attributed to the tightly bound oxygen $p_z$, bonded with the Mo $4d_{z^2}$ to form $\sigma$ states. In this $\mathbf{E}\|a$;XES$\|a$ geometry, emission is preferred from the plane perpendicular to a $a$-axis made up equally of $p_y$ and $p_z$ states but not $p_x$, and resonant excitation into the $t_{2g}$ derived $d_{\|}$ hybridised unoccupied states results in preferential in-plane emission from the $e_g$ derived $d_{z^2}$ hybridised occupied states. This is a form of resonant symmetry selective dichroism discussed in greater depth in Chapter 2.

As the excitation energy increases as in (e), (g), (f) and NXES, beyond the main $\sigma^*$ peak observed in the O $K$-edge, excitation to both O1 and O2 sites returns to equality, and also the majority of $k$-points within the zone will now contribute to the emission. The bandstructure (not shown) makes it clear that the selected bands and excitation bandwidth essentially span the Brillouin zone. Though the excitation geometry and the projected oxygen character of the excited band still influence the emission spectra, preserving the dichroism even until the non-resonant X-ray emission spectroscopy (XES) spectra, the features in the emission are seen to become less well defined as now the whole zone and the whole of each occupied band participates in the emission.

### 6.4.4 Polarisation Dependent RXES of $WO_2$

Figure 6.11 also shows the results of the RXES and NXES measurements of $WO_2$ at the oxygen $K$-edge in the two in-plane scattering geometries. The resonant excitation energies are labelled (a) through (e) and indicated by arrows on the XAS in Figure 6.7. For clarity of features, noise was reduced by 5-point adjacent averaging for the solid lines. The original recorded spectra are represented by the scatter points.

The spectra possess an overall likeness, both in shape and in resonant evolution, to the $MoO_2$ shown in Figure 6.8, which is not surprising given the shared structure and valence $d^2$ orbital occupancy. Most striking are spectra (c), analogous to spectra (d) of the $MoO_2$ Figure 6.8, where resonant excitation into the $d_{\parallel}(\sigma^*)$ feature is only apparent in the $\mathbf{E}\|a$ absorption geometry. Here, in a behaviour practically identical to that of the $MoO_2$, a strong dichroism is observed at both the very top and the very bottom of the valence band spectral weight. This reflects a preferential core hole excitation on O1 sites, resulting in an emission spectrum that largely reflects the O1 $2p$ PDOS of the $p_x$ and $p_z$ components.

The O $K$-edge XES spectra, selecting only the O $2p$ component of the occupied DOS is nevertheless sensitive to the hybridisation that occurs between the O $2p$ orbital and the occupied W $5d$ orbitals which are observed most clearly as the two prominent features near the Fermi edge in the UPS spectra. This is observed in Figure 6.12, which reproduces spectra at energy (c) and the NXES in both geometries, comparing them above with helium (I) valence band UPS data adapted from Jones *et al.* [125] Below are the DFT calculations for the O $2p$ PDOS, divided into the expected observed states in NXES, as will be discussed further on in this section. Two lines show the matching of these features between all VB representations. Making direct comparisons between calculated O $2p$ PDOS and the RXES/NXES spectra, it is worthwhile bearing in mind that the experimental spectra are

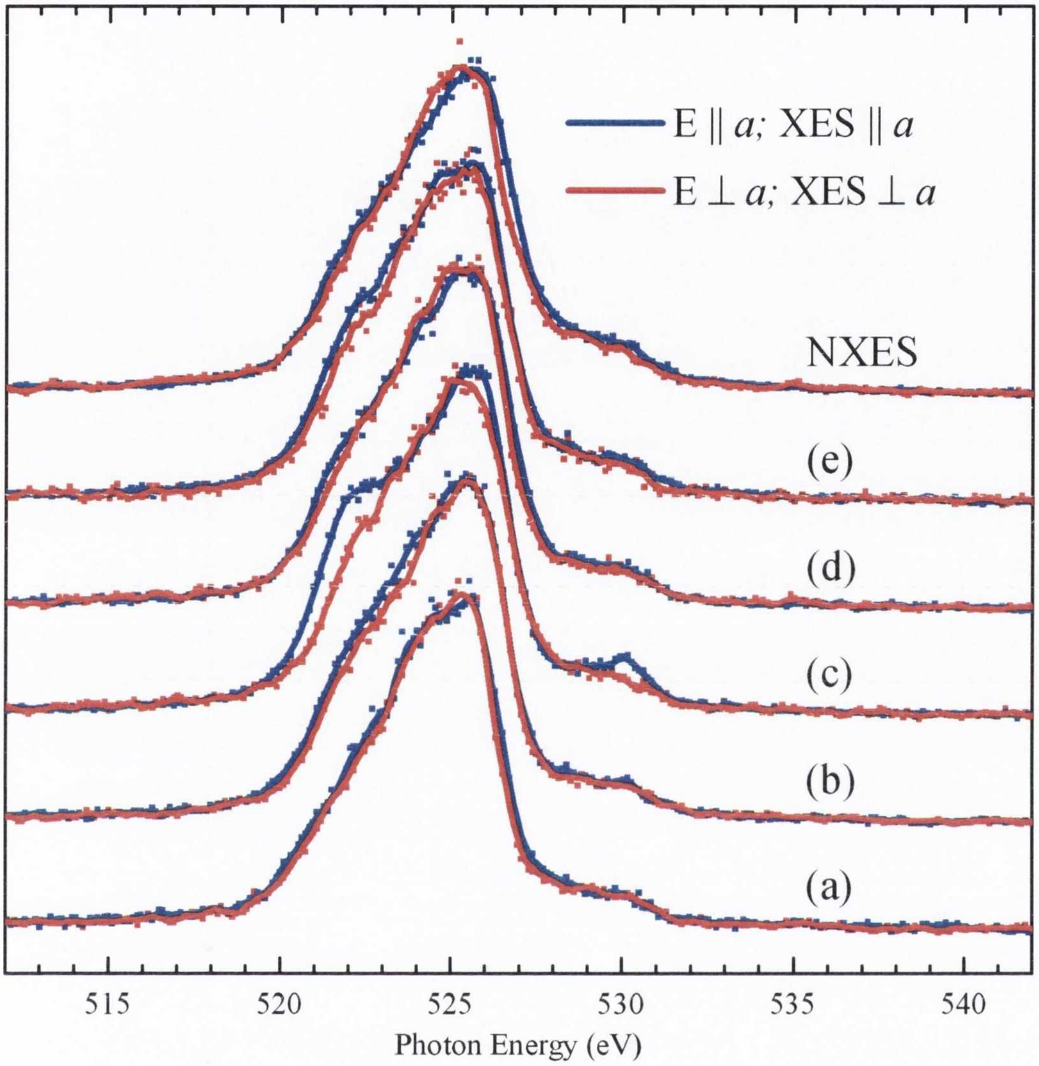

Figure 6.11: Waterfall graphs of WO$_2$ emission spectra at the O $K$-edge in the two measurement geometries indicated: $\mathbf{E}\perp a$;XES$\perp a$ and $\mathbf{E}\|a$;XES$\|a$. Labels (a)-(e) are the RXES excitation energies as indicated by the correlating labels on the XAS in Figure 6.7. Top spectra are polarisation dependent NXES. Scatter points represent recorded data while solid lines are after 5-point adjacent averaging.

both instrumentally broadened, core-hole lifetime broadened, and as we reach the bottom of the valence band, are also subject to valence hole lifetime broadening. Hence the absence of sharp features near the bottom of the observed valence band emission.

While O $K$-edge XAS is considered an effective measure of the unoccupied O 2$p$ PDOS within a metal oxide, O $K$-edge non-resonant XES spectra are a direct measure of the occupied O 2$p$ PDOS sampled across the entire Brillouin zone. Non-resonant XES from WO$_2$ has been reported before but from an unoriented sample and with poor resolution [127].

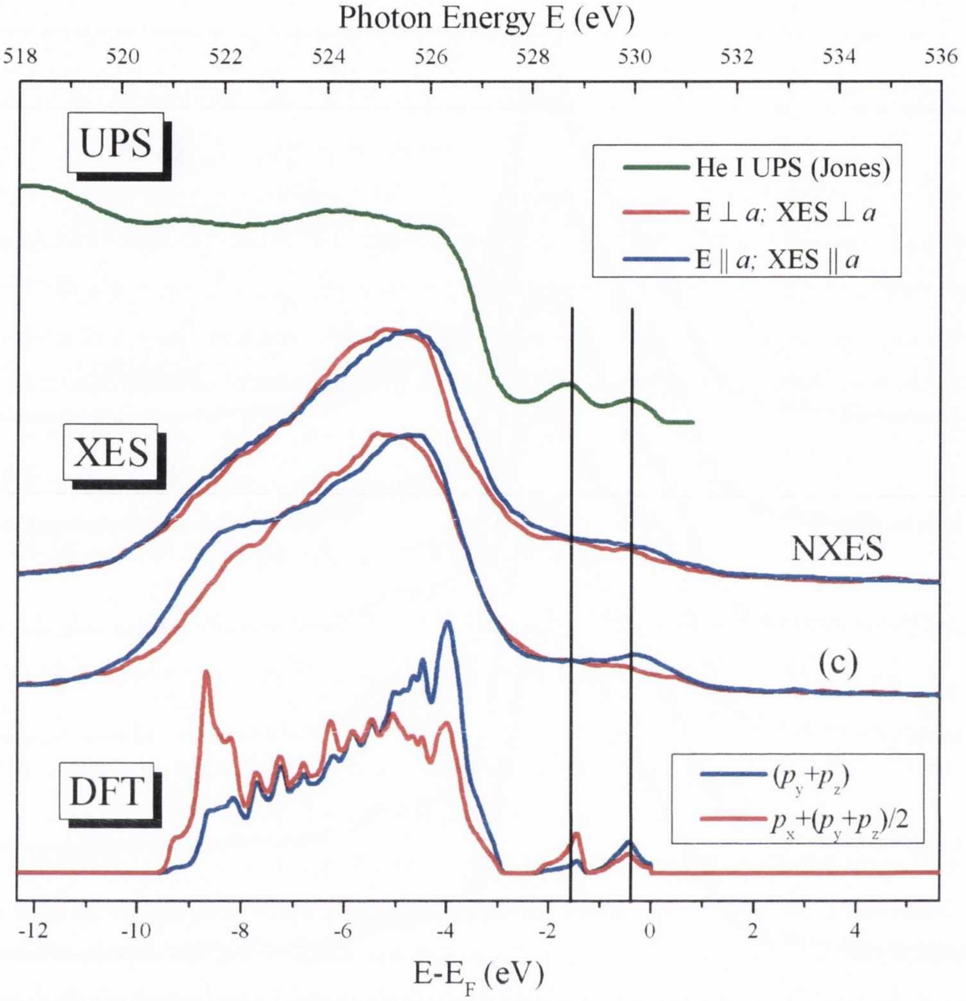

Figure 6.12: Comparison of polarisation dependent O $K$-edge XES of $WO_2$ at excitation (c) as well as NXES (middle) with O $2p$ VB He I UPS from Jones *et al.* [125] (top), and VB DFT calculations presented in this thesis for the projection PDOS in the plane parallel and perpendicular to the monoclinic $a$-axis. Lines on this figure show the position of the $d_{\|}(\sigma)$ and $d_{\perp}(\pi)$ features at approximately -1.5 eV and -0.5 eV respectively, with respect to the Fermi energy.

The $MoO_2$ emission results presented in section 6.4.3 showed a distinct divergence in their threshold spectra, and a strong linear dichroism in its NXES spectra. The same magnitude of contrast is not observed for the $WO_2$ NXES. Nevertheless, some dichroism is observed in the $WO_2$ NXES. While the average spectral weight changes only a small amount, there is a shift in the peak maxima by approximately 0.4 eV. This is explained in terms of **k**-independent (in that the entire Brillouin zone is selected) and $\Omega^{\dagger}$-independent natural linear dichroism resulting from the measurement geometry of the crystal with respect to the spectrometer, as described for an electronic transition in Chapter 2. Assuming all $k$-

---

[†] Incident photon energy.

values are equally selected, emission should be proportional to the O $2p$ total PDOS. The orbitals in this crystal structure possess an anisotropy in their charge densities and thus depending upon the crystal orientation, will favour emission from particular orbitals. Thus in the XES$\|a$ blue NXES spectrum, the spectral weight is biased toward the higher energy, valence band maximum, indicating preferential emission from the O $p_y$, but also from O $p_z$. Respectively these correspond to the O $2p$ $\pi$-like non-bonding, or $\pi$ W–O, and the $2p$ projection of the $sp^2$ $\sigma$ W–O orbitals along the apical W–O direction, where the PDOS is sampled over both the O1 and O2 atomic sites. Since both of these are approximately orthogonal to the $a$-axis. In the contrasting emission scattering geometry where XES$\perp a$ the third orthogonal O $2p_x$ projection, the O $2p$ component of the $sp^2$ $\sigma$ W–O orbital projected parallel to the monoclinic $a$-axis, becomes the dominant contribution. Emission is still geometrically allowed from the $p_z$ and $p_y$ orbitals as half the $W_3O$ planes are perpendicular to the remaining half within the crystal structure (see Figure 6.2 (a)). In this XES$\perp a$ geometry, the $p_x$ component contributes 50% and the other two components contribute equally in the remaining 50%. According to the calculations the occupied $\pi$-character $p_y$ states exhibit lower binding (higher fluorescent) energies than the $\sigma$-type $p_x$ or $p_z$. This is especially true of the O2 occupied $p_y$ states (see Figure 6.3) which are effectively non-bonding. Thus the blue NXES spectrum shows at 527 eV more spectral weight with respect to the red, reflecting the higher proportion of O2 $2p_y$.

Focusing on spectra (c) from Figure 6.11 and reproduced Figure 6.12, there is a shift in spectral weight of the tungsten hybridised states at the very top of the valence band for the $\mathbf{E}\|a$;XES$\|a$ spectrum in blue. As stated previously, this excitation favours the O1 site, an assertion supported by Figure 6.13b; though not completely comparable to XAS, it nevertheless proposes that in the excitation bandwidth for (c), O1 atomic sites are selected by a factor of $> 2$ over O2. Thus by comparing the O1 and O2 PDOS for $p_x$ and $p_z$ in Figure 6.3 (page 121) it is clear that there is much greater density of states for these components at the VB maximum for O1. The anisotropic nature of this is partially due to the reduced presence of these states in the $\mathbf{E}\perp a$;XES$\perp a$ geometry in favour of $p_x$. Further, there must also be a $k$-selective element since this shift is seen only at excitation (c). This excitation energy spans a bandwidth between $\sim 3 \rightarrow 3.5$ eV above the Fermi energy. Examining the weighted O1 $2p_x$ presented in Appendix A.5[†] on page 211, it can be seen that the majority of the bands in this bandwidth lie around the Y-Γ-Z $k$-points, with some further states around B. Following these high symmetry points down to the energy region just below the Fermi level it is noted that they correlate strongly with occupied O1 $p_x$ and $p_z$ bands (Figures

---

[†] Appendices A.5–A.8 present the weighted bandstructures for $WO_2$ for each valence O1 and O2 $2p$, and W $5d$ $t_{2g}$ and $e_g$ component orbitals.

A.5b and A.5c) either at the top of the VB maximum (Y-Γ, Z) or crossing the Fermi Level (Γ-Z, and around B).

Taking the $\mathbf{E}\|a$;XES$\|a$ spectrum (c) again and comparing with the calculations in Figure 6.12, it is somewhat surprising that there is a shift of spectral intensity towards the bottom of the main O $2p$ valence band, given that the (primarily) O1 $p_x$ states that form the maximum observed at the bottom of the VB in the calculations are forbidden in this XES$\|a$ measurement geometry. It perhaps pertinent to note here that the calculations for $WO_2$ predict what is essentially a swapping of the spectral weight between $2p_z$ and $2p_x$ components in $WO_2$ when compared to pure rutile oxides, at least for O1. The W–W dimerisation in the monoclinic structure has the effect of making the W–O $d_{x^2-y^2}$–$sp^2$ $\sigma$ orbital more tightly bound than the W–O $d_{z^2}$–$sp^2$ $\sigma$ orbital, especially in the case of O1. This ordering is the opposite for other undistorted rutile oxides such as IrO2, MnO2 (Chapter 4), RuO2 and TiO2 [5]. This ordering is noted in Figure 6.3. Thus the surprising shift in spectral weight at the bottom of the VB of spectrum (c) must be explained by $p_z$ and $p_y$ components in terms of site selectivity and $k$-selectivity. A partial explanation may be deduced by examining the difference between $p_z + p_y$ (result of $\mathbf{E}\|a$;XES$\|a$) for O1 and O2 in Figure 6.13a. The atomic site selectivity of excitation (c) will favour O1 in this measurement geometry, leading to a relative shift of spectral weight observed towards the bottom of the main O $2p$ bands. The further amplification of this feature in spectrum (c) may be accounted for by $k$-selectivity. As stated, this excitation preferentially selects bands around the Y-Γ-Z and B high symmetry $k$-points, which, when examining the O1 weighted bandstructure for $p_y$ and $p_z$ in Figures A.5b and A.5c respectively, correlate to regions of high density of these components in the bottom of the valence band. This is especially true for Y-Γ.

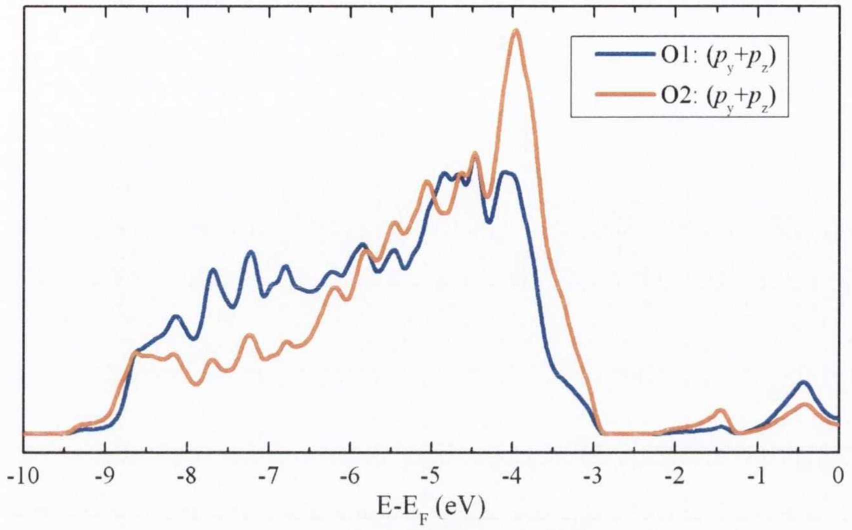

(a) Simulated VB XES$\|a$

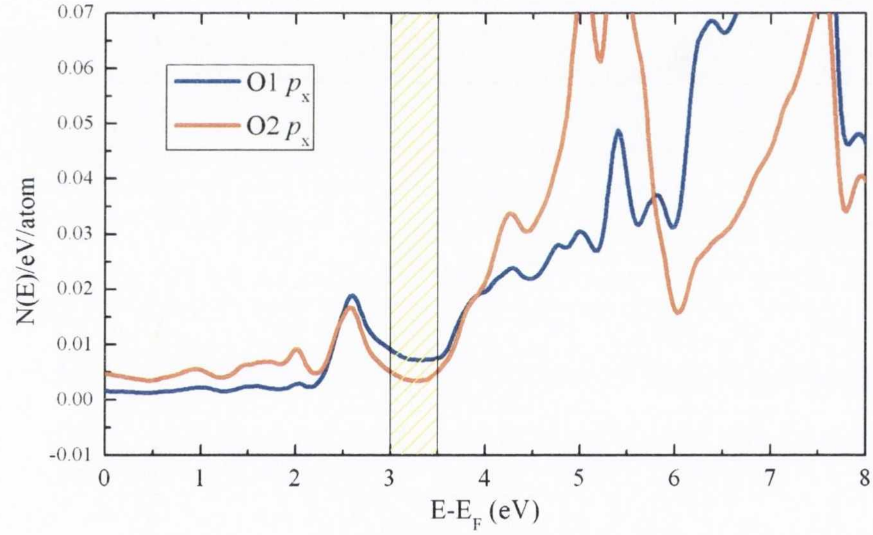

(b) Simulated CB $\mathbf{E}\|a$

Figure 6.13: **(a)** Comparison of WO$_2$ VB $2p_z + 2p_y$ component calculated PDOS between O1 and O2. Components correspond to those probed in the XES$\|a$ emission measurement geometry. **(b)** Comparison of WO$_2$ CB $2p_x$ component calculated PDOS between O1 and O2, corresponding to $\mathbf{E}\|a$ excitation. Yellow area highlights bandwidth selected by excitation energy (c).

## 6.5 Summary and Conclusions

Bulk single crystals of monoclinic WO$_2$ and MoO$_2$ were investigated and strong linear dichroism was observed for both at the oxygen $K$-edge using XAS, NXES and RXES. While the electronic structure of WO$_2$ and especially MoO$_2$ has been probed before by experimental and theoretical means, this is the first report of polarisation dependent XES and RXES at the O $K$-edge for these compounds, and the first report of polarisation dependent XAS in $WO_2$.

The trends in charge distribution, natural linear dichroism and $k$-selectivity between the two compounds was acutely similar, unsurprising as they are not only isostructural, but nominally share the same valence $d$-level occupation. Especially of interest was a feature unique to these compounds in this body of work, the splitting of the metal $t_{2g}$ $d$-bands into $d_{||}$ and $d_{\perp}$ states, and the observed oxygen $2p$ hybridisation with these states. The unoccupied $d_{||}$ states contribute in part to a feature in the O $K$-edge XAS only apparent in the $\mathbf{E}||a$ measurement geometry, and unseen in similar measurements of the tetragonal-rutile compounds presented in this thesis. Energy selective RXES at the energy corresponding to this feature produced striking dichroism in the emission spectra for both compounds. NXES also showed an inherent natural linear dichroism in $MoO_2$, similar NXES dichroism was observed in $WO_2$ though its magnitude was not as great. Density functional PDOS and bandstructure calculations supporting the anisotropic projection of states were presented in this for $WO_2$. These allowed a more thorough analysis of the experimental results and a proposed explanation of the anisotropic and resonant features present in $WO_2$, and by proxy, the same features in $MoO_2$.

The spectral features were not as straight forward to explain as those in pure rutile tetragonal compounds such as $IrO_2$ in Chapter 4, or $TiO_2$ [5]. Nevertheless, utilising the electronic structure calculations, they were discussed in detail and attributed here to a delineated combination of site-, polarisation- and especially $k$-selectivity of the RXES technique. Further insight was thus gained into the electronic structure, bonding and hybridisation of these explored materials. This serves as a testament to this powerful combination of the polarisation dependent RXES technique with electronic structure calculations, an approach that can be extended to the analysis of not only other distorted rutile oxides, but a host of transition metal compounds.

# 7 $VO_2$

## 7.1 Introduction

This chapter presents the polarisation dependent emission, and absorption spectra of $VO_2$ at the O $K$-edge for both its rutile tetragonal and monoclinic phases. First a brief and general literature review will be given in this introduction. This will be followed by an overview of the compound's most widely studied feature, its transition from a rutile conductor to a monoclinic semiconductor as the temperature goes below 340 K in a metal-to-insulator transition (MIT). The physical and electronic structure of the compound as a bulk crystal will be elaborated on in later sections, as will the details of the experiment carried out, before the presentation and discussion of results.

Vanadium dioxide $VO_2$ has been at the forefront of scientific investigation for the last half century [34,147], especially in the realm of X-ray spectroscopic techniques. Much of the focus of that research tends towards its MIT from a paramagnetic metal to a non-magnetic semiconductor, with a sudden drop in conductivity of several orders of magnitude. Accompanying this is a structural phase change from rutile tetragonal to monoclinic [148–150], both of which occur at approximately T = 340 K for pure bulk $VO_2$. A splitting of the $d$ bands makes this low temperature monoclinic phase similar in electronic structure with its isostructural $MoO_2$ and $WO_2$, both of which are investigated in Chapter 6. It also resembles the only other undoped binary transition metal dioxide that undergoes a known MIT, $NbO_2$. $NbO_2$, (not studied in this thesis) shares the nominal $d^1$ valence occupancy of $VO_2$ and its MIT occurs at approximately 1080 K.

The breadth and depth of published literature surrounding investigations of $VO_2$ and other vanadium oxides is too large for a comprehensive review here, instead a brief overview of the most recent and relevant contributions will be given, while the interested reader should look at the review by Eyert *et al.* [50]. Recent publications documenting spectroscopic techniques to probe the electronic structure of $VO_2$ include **1)** an X-ray total scattering study of the real space structural changes of rutile $VO_2$ at the MIT temperature investigated by Corr *et al.* [151]. **2)** Yao et al. has studied the nature of the kinetic process in the MIT through in-situ temperature dependent X-ray absorption spectroscopy (XAS) measurements and density functional theory (DFT) calculations [152]. **3)** And Booth and Casey have used X-ray absorption fine structure (XAFS) at the vanadium $K$-edge on tungsten doped $VO_2$ in order to investigate the anisotropic structure deformation across the phase transition [153]. Of particular relevance to this study is the resonant inelastic X-ray scattering (RIXS) observed by Braicovich *et al.* at the V $L_{3,2}$-edge [154].

### 7.1.1 Metal-Insulator Transition

Though explanations remain controversial to this day, the mechanism of the MIT has been consistently associated with the observed crystallographic distortion. In attempting to understand the origin of this transition several models have been proposed, ranging from Peierls transitions to Mott-Hubbard type scenarios, both as far back as 50 years ago [35,155]. Despite strong motivation and significant research investment the picture is still not complete. Even recently the debate continues with Wentzovitch *et al.* attempting to deal directly with the issue and stressing electron-phonon interaction (Peierls-transition) [156] as the driving force for the splitting of the $d$-bands and opening of the band gap. More recently Eguchi *et al.* [157] shows photoemission evidence for Mott-Hubbard type transition, while Haverkort *et al.* [158], by examining vanadium $L$-edge XAS and theoretical calculations suggests a description of the phase transition as an "orbital assisted Peierls-Mott" combined scenario. Perhaps the most comprehensive published study on $VO_2$ in recent years, focusing on the MIT, was the review paper by Eyert [50], which took a band theoretical approach.

Direct comment on this debate is out of the scope of this thesis. Here the anion O $K$-edge is investigated in both the rutile conducting and monoclinic insulating phases using resonant X-ray absorption and emission techniques to ascertain the level of natural linear dichroism that exists in this material. While published studies have investigated the polarisation dependence of $VO_2$ at the O $K$-edge using XAS [159–161], to my knowledge this is the first reported polarisation dependent resonant X-ray emission spectroscopy (RXES) study of $VO_2$, as well as the first O $K$-edge RXES study spanning both sides of the MIT. It should be noted that Braicovich *et al.* studied the polarisation dependence of the V $L_{3,2}$-edge RIXS [154]. Polarisation dependence aside, the electronic structure of $VO_2$ has been studied via O $K$- and V $L_{3,2}$-edge XAS [159,162,163] as well as by RXES of both edges. [154,164–167]

## 7.2 Physical and Electronic Structure

As previously stated there are two structural and electronic phases of $VO_2$, rutile and monoclinic, which will be addressed separately to some degree. To avoid confusion, a subscript "R" will be used when designating crystal axes of the rutile phase, while subscript "M" will be used for the monoclinic phase. It is worth noting that across the transition, the $c_R$-axis is equivalent to the $a_M$-axis, while the $a_R$-axes become the $b_M$ and $c_M$ axes in the monoclinic phase. The term "$c_R$" is used here interchangeably to describe both the rutile $c$ and monoclinic $a$ axes.

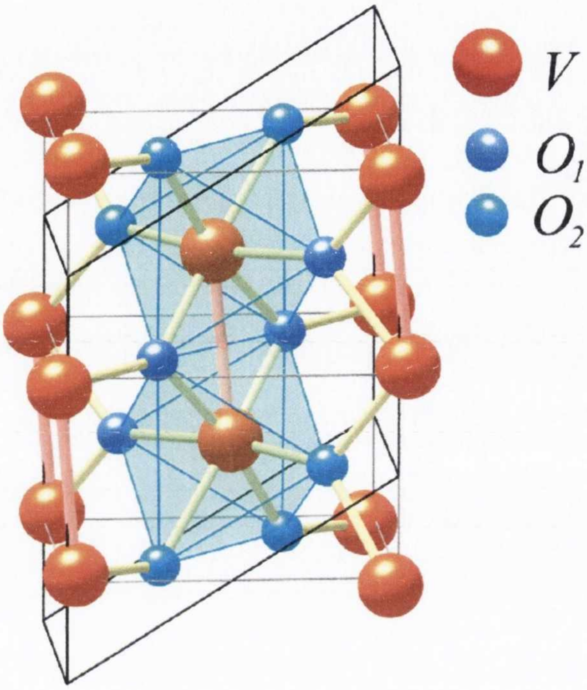

Figure 7.1: One unit cell of VO$_2$ structure in the monoclinic phase showing the two oxygen sites, and with the rutile unit cells overlayed. From Eyert [50].

Above 340 K VO$_2$ is metallically conducting and possesses a rutile tetragonal P4$_2/mnm$ structure as described in Chapter 3. According to McWhan *et al.* [148] the lattice constants are $a_R$ = 4.5546 Åand $c_R$ = 2.8514 Å, while the internal oxygen anion parameter is $u$ = 0.3001. As outlined in Chapter 3 the same natural local coordinate systems are applied for both the metal cation and ligand in our descriptions. For the near octahedral crystal field the metal $d$ orbitals are approximated into $t_{2g}$ and $e_g$ states, the first comprising the $d_{xy}$, $d_{xz}$ and $d_{yz}$ states, while the $e_g$ comprise the orbitals with lobes pointing toward the ligands: $d_{3z^2-r^2}$ (or more commonly just $d_{z^2}$) and $d_{x^2-y^2}$. As a result of the tetragonal distortion of the octahedron, it is not strictly correct to suggest $t_{2g}$ orbitals are degenerate, as described in section 3.2.2 of the Rutile Structure chapter (page 33). Also as detailed in that section it is instructive to describe the $t_{2g}$ orbitals as $d_{xy}$, $d_{z(x+y)}$, and $d_{z(x-y)}$ in the local vanadium cation coordinate system. The latter two are effectively a 45° rotation from the projection of the degenerate $d_{xz}$ and $d_{yz}$ orbitals about the local $z$-axis. In the rotated basis of $d_{z(y-x)}$ and $d_{z(y+x)}$, one lies $\perp c_R$ and the other lies $\| c_R$ (respectively) and thus they are no longer degenerate. In this rutile and distorted-rutile structure the $d_{xy}$ orbital lobes point toward the edges of the rectangular cross-section, or waist of the octahedron, two sides of which lie parallel to the rutile $c_R$-axis; the $d_{z(y+x)}$ and $d_{z(y-x)}$ lobes are directed toward the eight faces of the octahedron. The $d_{z(y-x)}$ orbital lobes in particular point in the $\langle 110 \rangle$ directions. As a result of this the $d_{xy}$ and $d_{z(x+y)}$ orbitals mediate the vanadium-vanadium $\sigma$ and $\pi$ overlap along the vertical chains of octahedra, parallel to the $c_R$-axis. On the other hand the $d_{z(y-x)}$ orbital contributes to a smaller $\sigma$ overlap between metal sites in adjacent unit cells when translated by vectors $\langle 1,0,0 \rangle$ [50]. The $d_{xy}$ orbital, which experience a strong metal-metal overlap parallel to the $c_R$-axis is often referred to as the $d_{\|}$ band.

The local oxygen coordination is identical to that described in Chapter 3 and in other chapters dealing with pure rutile structures. Two orthogonal sets of trigonal $V_3O$ $sp^2$-hybridised planes lie parallel to the rutile $c_R$-axis. The local $x$-axis for oxygen is also parallel to the $c_R$-axis, the local $z$ direction is along what is the apical V–O bond of the octahedron, while the $y$-axis is normal to the trigonal plane. Thus the O $2p_y$ orbital is not involved in the $sp^2$ hybridisation and instead contributes to V–O interaction of $\pi$ character with the metal $t_{2g}$ orbitals. Specifically this will tend to occur with the metal $d_{z(y-x)}$, since it is the only orbital described that possesses lobes in the (001) plane that straddle the adjacent anion O $2p_y$ orbitals. Expanding on the vanadium–oxygen bonding in the high temperature rutile phase, the metal $e_g$ orbitals form a direct overlap with the $sp^2$ hybridised orbitals in the trigonal plane, resulting in a covalent bonding arrangement of $\sigma$ character with the O $p_z$ and $p_x$ respectively with the $d_{z^2}$ and $d_{x^2-y^2}$. These $\sigma$ and $\pi$-type overlaps give rise to states of $\sigma$ and $\sigma^*$ character, as well as of $\pi$ and $\pi^*$ character.

The low temperature ($< 340$ K) monoclinic phase of $VO_2$ is structurally very similar to the other monoclinic transition metal dioxides studied in this work, $MoO_2$ and $WO_2$ (Chapter 6). It too is characterised by a simple monoclinic lattice with $C_{2h}$ symmetry, and has a space group of $P2_1/c$ [168,169]. The lattice constants of the monoclinic phase are $a_M = 5.7517$ Å $b_M = 4.5378$ Å and $c_M = 5.3825$ Å, while the monoclinic angle is $\beta_M = 122.646°$ according to Longo and Kierkegaard [169]. As with the other monoclinic oxides mentioned, the unit cell is effectively doubled compared to the rutile counterpart due to a dimerisation of the metal atoms along the $a_M$-axis (equivalent to the rutile $c_R$-axis), as well as an in-plane shift parallel to the local $z$-axis ($\langle 110 \rangle$ direction) causing a zigzag-like alternating distortion. As a result of this there are two separate oxygen sites, making two apical V–O bond lengths of 1.77 Å for V–O2 and 2.01 Å for V–O1. It should be noted that there is a much more significant V displacement away from $a_M$ than is the case in either $MoO_2$ or $WO_2$. These features are presented in Figure 7.1, a structure diagram of the monoclinic phase of $VO_2$. While the structure of monoclinic $VO_2$ is very similar to that of other distorted rutile (monoclinic) oxides, some distinct differences are apparent.

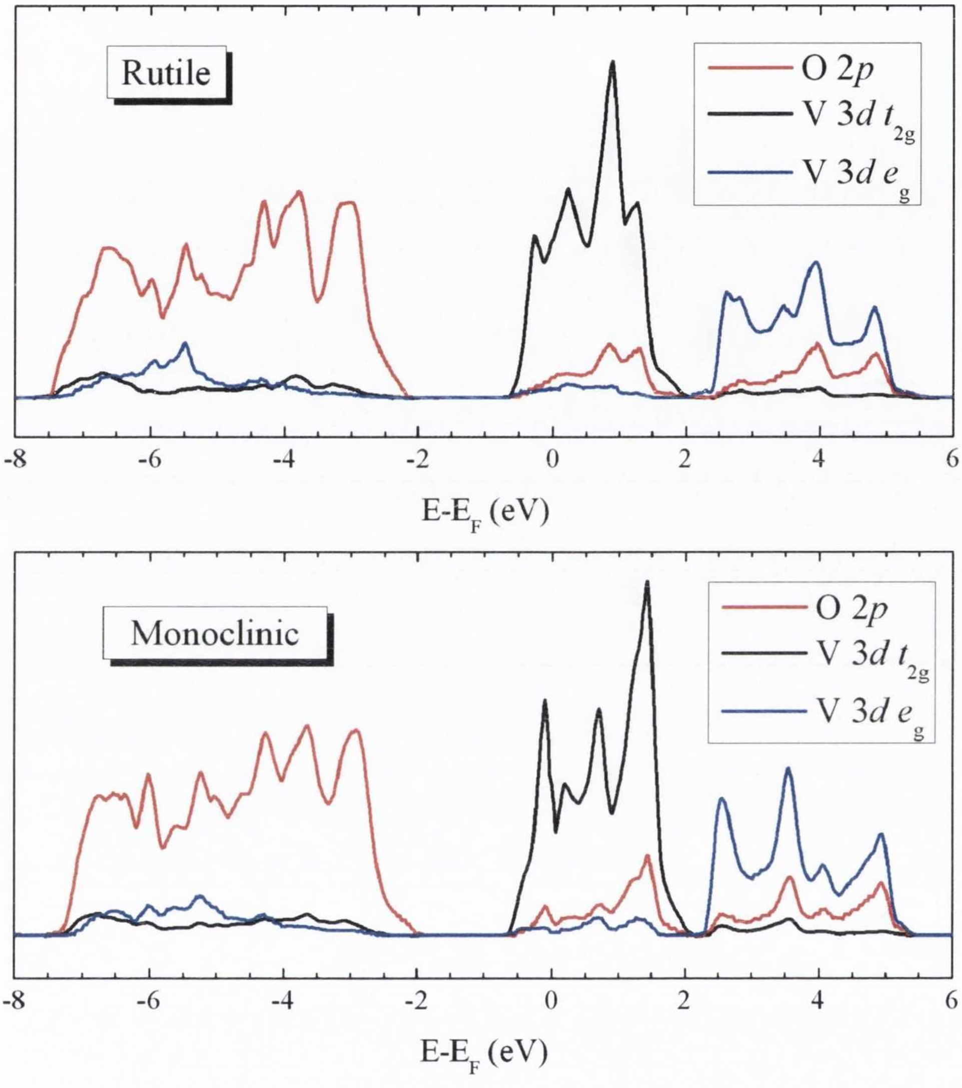

Figure 7.2: Calculated DFT PDOS of both rutile and monoclinic $VO_2$ showing the oxygen $2p$ total DOS in red, and the $t_{2g}$ and $e_g$ components of the vanadium $3d$ in black and blue respectively. Adapted from Eyert [50], Figures 11 and 23.

Unlike $MoO_2$ for example, the oxygen atoms do not follow the metal cation in-plane shifts, staying almost in their original positions [50]. Thus the shifting of the vanadium atoms is relative to a fixed oxygen atom, whereas in $MoO_2$ the effect of the molybdenum shifting is compensated considerably by the simultaneous displacement of the oxygen atoms from its hypothetically rutile structure. The in-plane shifting of the vanadium ions themselves is unique in that it is almost parallel to the local $z$-axis with a deviation of 3°, whereas the molybdenum atoms deviate from the $z$-axis by an angle of 18°, as well as the shift along the $c_R$-axis.

Figures 7.2 and 7.3 are DFT PDOS calculations for $VO_2$ in both the monoclinic and rutile phases. They are adapted from Eyert [50] who employed the augmented spherical wave (ASW) method based on the local density approximation (LDA). In Figure 7.2 it can be seen that the valence band states are made up mainly of the O $2p$, while the next two groups of bands ranging from $-0.6$ eV to $+5.5$ eV originate mainly from the V $3d$, though as a result of the $p-d$ hybridisation mentioned earlier, the near $E_F$ portion of the valence band (VB) and the conduction band (CB) show contributions from the O $2p$ in the same energy range. The two groups of bands higher than $-0.6$ eV demonstrate the usefulness of approximating to an octahedral crystal field, as a clear splitting is noted between the majority of nominal $t_{2g}$ and $e_g$ states in the CB and is replicated to a degree by the hybridised oxygen $2p$. However in discussing the O $K$-edge XAS these groups will be referred to as the V–O $\pi^*$ and V–O $\sigma^*$ states respectively.

Figure 7.3 breaks down the metal $t_{2g}$ and $e_g$ orbitals in the $-1$ to $+5.5$ eV range. Clearly observed is the splitting of $d_{xy}$ ($d_{\|}$) states in the monoclinic phase, which now consists of filled bonding (V–V$\sigma$) and empty antibonding (V–V$\sigma^*$) states. The empty antibonding orbital above the Fermi level is usually designated $d_{\|}{}^*$ in the monoclinic phase, while the part below is given the $d_{\|}$ denomination. The remaining $t_{2g}$ orbitals shift higher in energy due to the lateral antiferromagnetic distortion of the $VO_6$ octahedra [34], leaving them almost unoccupied and increasing the $p$–$d$ covalent bonding. Consequently there is a lowering of the density of states at the Fermi energy in the monoclinic phases, visually resembling the expected DOS of a semiconductor, though comparison with experiment suggests a larger band gap [50,156,161]. The failure of the calculations to predict a bandgap, observed for example through optical measurements by Qazilbash *et al.* [170], is attributed by the authors to the shortcomings of the local density approximation (LDA), which underestimates the band gap by about 50%, and in some small band gap semiconductors like germanium, predicts no gap [144]. On the other hand the rutile phase DOS correctly predicts a metallic conductor. Due to the complexities inherent in a calculation of the electronic structure of $VO_2$, no attempt was made to do so in this work. With the proviso that there is a gap of 1 eV [170] in the monoclinic phase, which effectively moves the $d_{z(x+y)}$ and $d_{z(x-y)}$ components by $\sim 1.25$ eV and increases the splitting between $d_{\|}$ and $d_{\|}{}^*$, then the description by Eyert can be usefully compared and applied to our experimental data.

In terms of orbital hybridisation between the vanadium and oxygen ions in the monoclinic phase, much of the explanation remains the same as it did for the rutile phase. The most prominent change of states across the MIT is the splitting of the V $3d_{xy}$ ($d_{\|}$). The oxygen $2p$ orbital most closely hybridised with this is the $p_x$, and experimental evidence of this splitting has been previously observed for these states [159–161] via XAS.

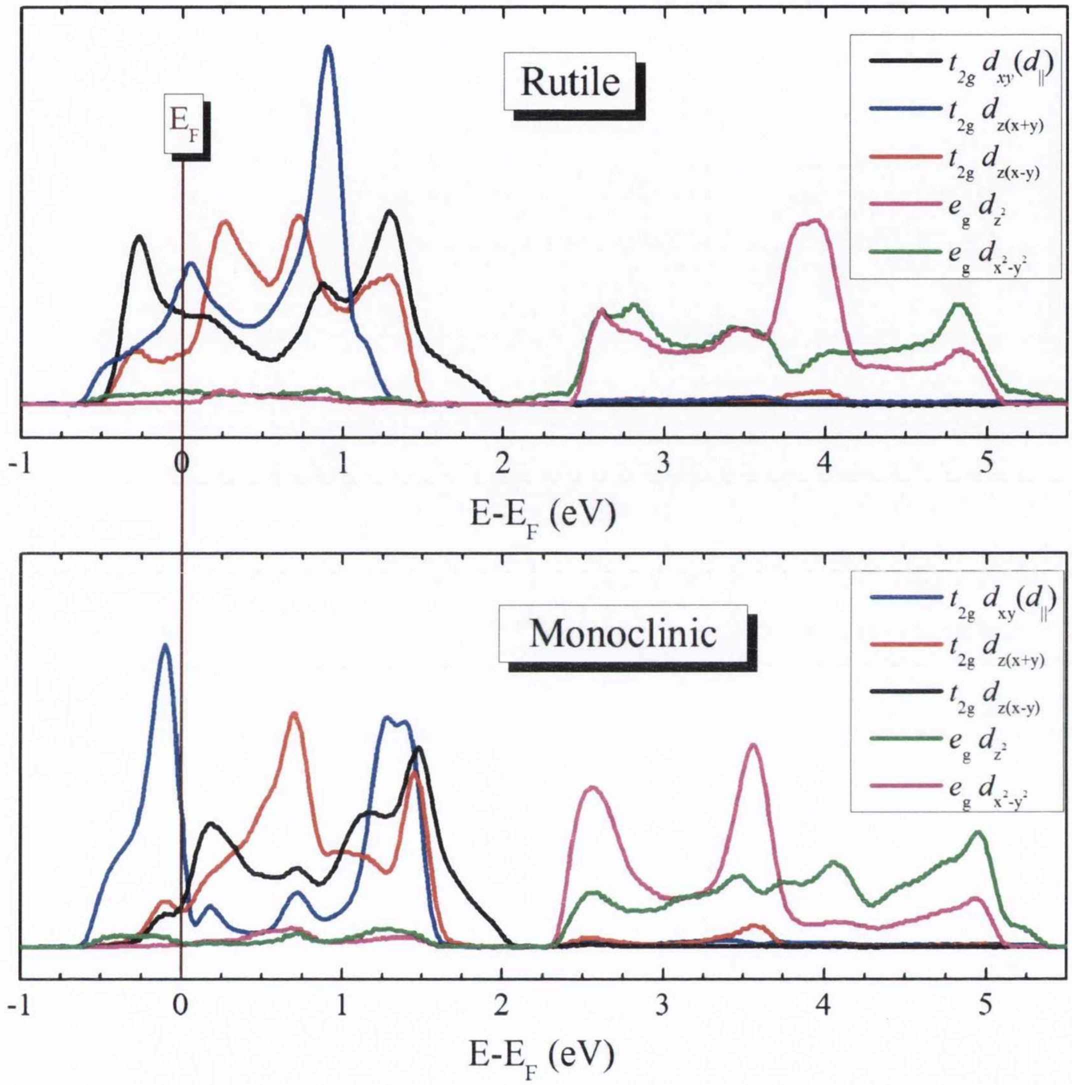

Figure 7.3: Calculated DFT PDOS of the vanadium $e_g$ and $t_{2g}$ components for both rutile and monoclinic VO$_2$, focusing primarily on the CB and region around the Fermi energy. The are divided into their component orbitals based on the local metal coordination detailed in Chapter 3. Adapted from Eyert [50], Figures 12 and 24.

## 7.3 Experimental Measurements

Two bulk VO$_2$ samples were provided by R.G. Egdell of the Dept. of Chemistry in Oxford; both were relatively cuboid in shape measuring approximately 3 × 3 × 6 mm. Prior to receiving they had been cycled through their MIT numerous times for previous experiments. The repeated structural phase changes left them brittle and cracked, shedding many individual shards. These shards were needle-like in appearance and were suspected to contain the $c_R$-axis parallel to their length, this was confirmed by XAS. Some of these shards were large enough to be used for measurements, though later some were shown to have a reduced stoichiometry, their XAS closely resembling that of $V_2O_3$.

Attempts were made to grow $VO_2$ thin films on sapphire and $TiO_2$ (001) substrates by pulsed laser deposition (PLD) using a $V_2O_5$ target in a partial oxygen atmosphere, following the procedure outlined by Bowman *et al.* [171], but were unfruitful. This was likely due to the narrow margin of error required to obtain stoichiometric $VO_2$. The differences in growth apparatus would have required much further experimentation with growth parameters. This coupled with questions over the resulting epitaxy (on sapphire substrates) and usefulness of a thin film in bulk measurements halted any repeated attempts. Although Piper *et al.* successfully produced a 100 nm thin film of epitaxial $VO_2$ on a $TiO_2$ (011) substrate via reactive bias target ion-beam deposition [172].

### 7.3.1 Sample Preparation and Mounting

In the first set of measurements at Beamline 8.0.1 (BL8), one large shard suitable for measurement was mounted vertically on the sample plate for the $\mathbf{E}\perp c_R$;XES$\perp c_R$ measurements. In the case of the other measurement geometry, $\mathbf{E}\|c_R$;XES$\|c_R$, a number of thinner needle-like shards were mounted horizontal, side-by-side and parallel to each other making a near contiguous surface. In subsequent measurements the two bulk crystals were prepared by careful scratching off the surface layer, and mounting in a similar fashion, one with the $c_R$-axis vertical, and one horizontal. In the final set of measurements a single crystal was cleaved into two equally sized parts in air prior to mounting. The new surfaces of each were utilised for measurements, mounting in the same geometries as before. The sample plate in each case was equipped with a thermocouple and allowed sustained resistive heating to a chosen temperature; 373 K was chosen for all the rutile phase measurements.

### 7.3.2 Experimental Setup

All presented spectroscopic measurements of $VO_2$ were recorded in the in-plane scattering geometry at the Advanced Light Source (ALS), Berkeley on Beamline 8.0.1. For the $\mathbf{E}\|c_R$;XES$\|c_R$ scattering geometry, the polar angle of the manipulator was 10°-15° from normal incidence to allow fluorescent photons to enter the spectrometer. For the $\mathbf{E}\perp c_R$;XES$\perp c_R$ geometry the polar angle was increased to 45° to maximise spectrometer counts. The resolution of the monochromator during XAS measurements was nominally 0.2 eV at the O $K$-edge when using the medium energy grating (MEG) and $< 0.1$ eV for the high energy grating (HEG). The resolution used for the O $K$-edge X-ray emission measurements, measured in $1^{\text{st}}$ order emission, corresponded to a spectrometer resolution of 0.4 eV, equivalent to $\approx 10\mu$m entrance slit width. During X-ray emission measurements the incident monochromator resolution used was 0.6 eV. The monoclinic phase was measured at room temperature, approximately 300 K, while the rutile phase was measured with a thermocouple and temperature controller set to 373 K.

The O $K$-edge absorption spectra were calibrated by comparison with the X-ray absorption of rutile $TiO_2$ [92,93], while the O $K$-edge emission spectra were calibrated using the $L_\alpha/L_\beta$ emission lines of Zn in the $2^{nd}$ order of diffraction.

## 7.4 Results and Discussion

### 7.4.1 XAS of $VO_2$

Figure 7.4 shows the O $K$-edge XAS for $VO_2$ taken for both the rutile and monoclinic phases in the two measurement geometries; $\mathbf{E}\|c_R$ in blue and $\mathbf{E}\perp c_R$ in red. Part (a) of the figure was taken with the medium energy grating at BL8, while part (c) with the high energy grating, allowing greater resolution. Both were measured on bulk crystal samples and recorded in total electron yield (TEY) mode. Part (b) of the figure shows similar data adapted from Müller *et al.* [161].

A clear dichroism between the two measurement geometries is observed between the relative heights of the $\pi^*$ peak at 530 eV and $\sigma^*$ peak at 532 eV. The $\mathbf{E}\perp c_R$ geometry favours absorption into the oxygen $p_z$ and $p_y$ orbitals, while the $\mathbf{E}\|c_R$ favours the $p_x$. Though the two peaks share states from all three orbitals, the $p_x$ are most notably hybridised with the $e_g$ (specifically the $d_{x^2-y^2}$ states in a $\sigma$-type overlap, while the $p_y$ orbital hybridises most closely in a $\pi$ like fashion with the $t_{2g}$ ($d_{z(x-y)}$) states). The anisotropic contrast appears to be greater, for both the MEG and the HEG higher resolution spectra, in the rutile phase. This could indicate the splitting of the $d_\|$ states contributing to greater mixing between the $t_{2g}$ and $e_g$ states in the $\pi^*$ and $\sigma^*$ features for the monoclinic phase.

However, the feature at approximately 531 eV in the monoclinic $\mathbf{E}\|c_R$ geometry as seen by Müller and others [159,160], attributed to an up-shift of the unoccupied $d_{xy}$ ($d_\|{}^*$) states [159], was not observed in our spectra. Further, while the dichroism is unambiguous in the presented measured spectra, the degree of dichroism is not as conspicuous as that observed in the literature. This could contribute to the explanation as to the lack of a visible $d_\|{}^*$ split peak at 531 eV. Several possible explanations exist: the alignment of the crystal may have been slightly misjudged, the surface may have been partially oxidised or reduced which would affect the surface sensitive TEY especially, or perhaps the overall surface quality of the crystal having gone through its numerous MIT cycling may have contributed. The quality of the surface argument is lent credence in Figure 7.5(a), which

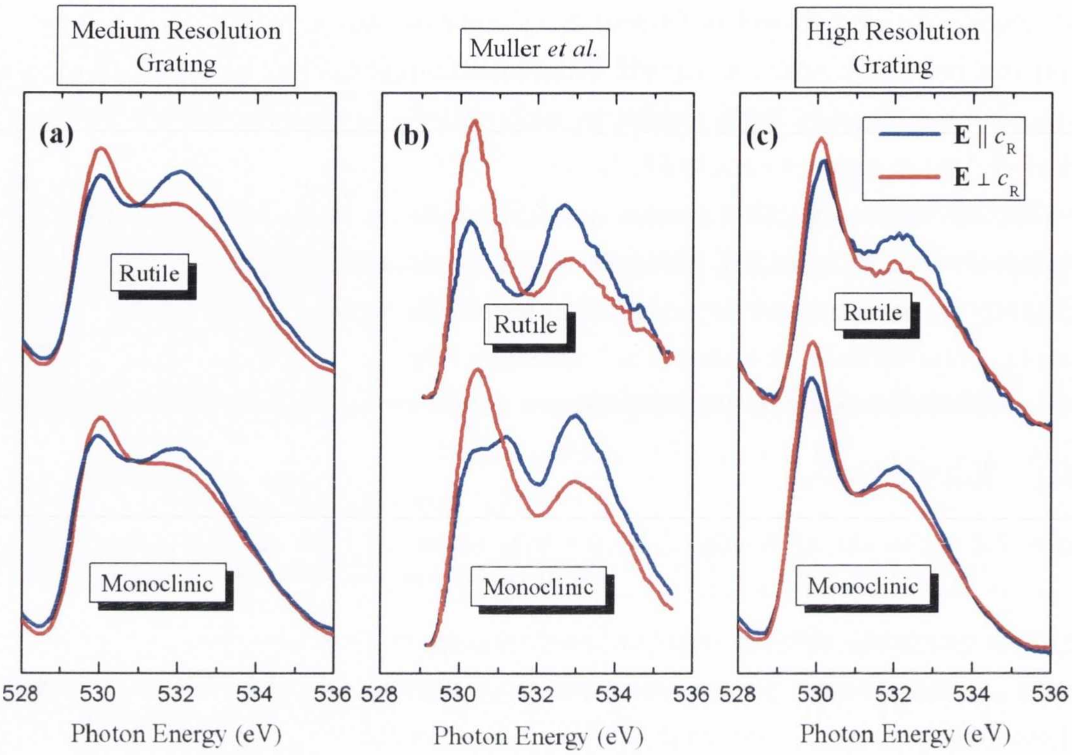

Figure 7.4: Polarisation dependent XAS at the O $K$-edge of VO$_2$ in the rutile and monoclinic phases. **(a)** TEY measured using the MEG at beamline 8.0.1 with a resolution of approximately 0.2 eV. **(b)** Similar results from the literature, adapted from Muller *et al.* [161]. **(c)** TEY taken using the HEG at beamline 8.0.1 with a nominal resolution of approximately 0.1 eV.

shows the TFY recorded simultaneously as the TEY in Figure 7.4(a) for the monoclinic phase, using the MEG. The TFY gives a ratio of peak height difference between the two geometries of more than three times greater than that of the TEY. The splitting of the $\pi^*$ peak is still not observed however.

The vanadium $L_{2,3}$-edges are located at approximately 512 eV and 520 eV, conveniently only a few eV lower than the oxygen $K$-edge. Thus it is possible to perform XAS on the two edges as one. This is presented in Figure 7.5(b), showing the XAS of the oxygen and vanadium edges using the HEG monochromator, recorded in TEY mode for both measurement geometries in both structural phases. In comparing the two sets of spectra in this figure, a dramatic switching of orbital occupation across the MIT is observed. As the intention was to measure the polarisation dependence O $K$-edge, a by product is that the vanadium edges are similarly probed. There is a clear polarisation dependence of the V $L$-edges in the monoclinic phase, particularly the lower energy $L_3$-edge, with a strong shift in spectral weight as well as a significant redistribution of shoulder-like features on the threshold side of the peak. In contrast the rutile phase shows only very weak dichroism at the V $L$-edge

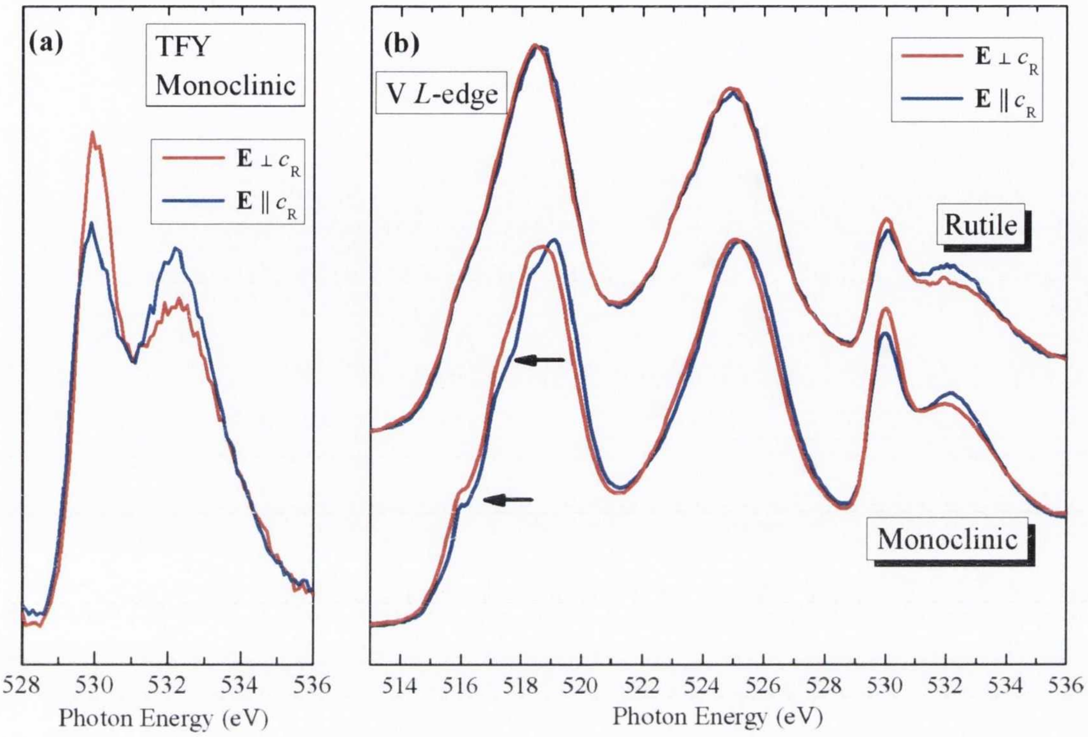

Figure 7.5: **(a)** Polarisation dependent TFY on monoclinic VO$_2$ at the O $K$-edge recorded simultaneously with the TEY in Figure 7.4(a). **(b)** High resolution TEY taken at both the V $L$- and O $K$-edges using the HEG at beamline 8.0.1. Arrows indicate areas dichroism in the vanadium edge of the monoclinic phase.

XAS. This polarisation dependence at the vanadium edges, specifically in the monoclinic phase, has implications into the understanding of the MIT; it was previously observed and studied in detail by Haverkort *et al.* [158].

### 7.4.2 Polarisation Dependent RXES of VO$_2$

Resonant emission at the oxygen $K$-edge in the two orthogonal in-plane scattering geometries was recorded for both the rutile and monoclinic phases of VO$_2$, for a large range of excitation energies. Due to a number of experimental problems detailed in sections 7.3 and 7.5, only three of these excitation energies possessed complete sets of complementary spectra viable for inclusion, i.e. showing variation with temperature and the variation with polarisation and crystal axis selection. These spectra are presented in Figure 7.6. The XAS part of the figure iterates the absorption spectra from Figure 7.4(c), with the addition of arrows to indicate the three excitation energies. These are, in order of increasing energy, 7.6(a): half way up the V–O $\pi^*$ peak at 529.3 eV, 7.6(b): resonant with the V–O $\pi^*$ peak at 530.1 eV, and 7.6(c): resonant with the V–O $\sigma^*$ peak at 532 eV.

Unseen in the RXES graphs are the vanadium $L_\alpha$ and $L_\beta$ VB emission peaks lying at approximately 510 eV and 515 eV respectively, directly preceding the bottom of the O $K$-edge valence band in photon energy. Since all presented emission spectra result from excitation at least 10 eV above the V $L$-edge threshold, it can be considered non-resonant. Thus the relative intensities of the vanadium emission peaks will have negligible dependence on the excitation energy[†] and their intensity should remain proportionately constant for these small increases in excitation energy, and changes in crystal orientation. Thus all presented RXES spectra are normalised to the vanadium $L$ emission peaks, relative within each contained graph.[‡] Their fortuitous presence allows for a far more instructive insight into the relative intensities of features than is usually possible through other methods of normalisation.[§]

As the excitation energy is increased through (a), (b) and (c), a striking evolution of the resonant spectra is observed. Specifically the feature at approximately 524.8 eV begins small at threshold, reaches a maximum on excitation into the $\pi^*$ peak, and is no longer evident upon higher excitation. This transformation can be seen in greater detail in Figure 7.7, which shows a single scattering geometry in both the structural phases above and below the MIT. This figure shows a greater range of excitation energies illustrated by the lettered arrows on the XAS spectra in the top panel. As noted in spectra A through F, the feature at 524.8 eV rather than suddenly disappearing, gradually decreases as the excitation energy moves off resonance with the $\pi^*$ peak. This energy dependence of the O $K$-edge resonant spectra was noted by Schmitt *et al.* [167], who recorded V $L$- and O $K$-edge XAS and RXES on monoclinic $VO_2$. It was attributed to "RIXS features and excitation of different O $2p$ sites", however specific features were difficult to pinpoint due to comparatively low resolution and signal to noise ratio. Listing the features observed in the main O $2p$ band part of the O $K$-edge X-ray emission spectroscopy (XES) we see in 7.6(a) features (i) at 523.4 eV, (ii) at 524.75 eV and (iii) at 525.8 eV. These are replicated in 7.6(b), while in 7.6(c) the peak of emission at (iv) now lies at 526.2 eV while (ii) is absent.

In examining Figure 7.7, the 524.8 eV feature is more apparent in the monoclinic spectra than the rutile. In both cases its peak position appears to also be energy dependent, shifting to a higher energy as excitation energy is increased. Since the shifts are small, and do not correspond to an energy loss feature, this is attributed to $k$-selectivity or band dispersion, like that reported earlier for $MoO_2$ and $WO_2$ in Chapter 6. As greater ranges of crystal momentum are selected by increasing excitation energy, resonant peaks follow the dispersion of the bands away from high symmetry points, as photons are emitted from a larger span or subset of $k$-values in the Brillouin zone contributing to the O $2p$ PDOS and VB XES.

---

[†] For a more detailed explanation, see the discussion around the Kramers-Heisenberg equation Chapter 2 page 11.

[‡] i.e. the $y$-scale (arbitrary intensity) for Figure 7.6(a) should not, for example, be directly compared to that of 7.6(c).

[§] For the traditional method of max-min normalisation, there is a version of Figure 7.6 in the appendix which may allow the reader a more direct contrast of the spectral features. Please see Figure A.3 on page 209.

While the O $K$-edge XES data in Figure 7.6 are normalised to the V $L_{3,2}$ XES (not shown), it is often more useful to compare the spectral shape of the O $K$ XES in the two alternative geometries by normalising the height of the emission spectrum in each geometry to be equal at a specific emission energy, often the peak of the emission intensity. An alternative form of Figure 7.6, where the spectra are normalised to the peak height is included in Appendix A.3.

With respect to the most threshold excitation of the presented emission in Figure 7.6(a), some differences are observed between the rutile and monoclinic spectra. In monoclinic $VO_2$ a gap opens of $\sim 0.6$ eV [170]$^\dagger$ and the states just above $E_F$ are dominated by $\pi^*$ features. Thus absorption and creation of O $1s$ holes is maximised for $\mathbf{E} \| c_R$, while the rate of creation of V $L_{3,2}$ holes is not so strong a function of photon energy or orientation. If the spectra are normalised to their O $2p$ peak maxima (see Figure A.3a), then the monoclinic $VO_2$ RXES at this energy shows, in contrast to the rutile $VO_2$, a broadening in the width of the O $2p$ band in the $\mathbf{E} \| c_R$ spectrum. As well, the monoclinic spectrum exhibits a matching of spectral weight between the two measurement geometries in the region of the VB maximum, where the O $2p$ is strongly hybridised with the V $t_{2g}$ orbitals, especially $d_{xy}$ ($d_\|$). The elastic peak structure, which overlies $E_F$, and the peak for the V $t_{2g}$ $d_{xy}$, is similar in both orientations.

As to why the elastic feature is maximised in the $\mathbf{E} \| c_R$ spectrum in the rutile $VO_2$: the feature is asymmetric, and it may reflect a greater propensity for inelastic losses of the type $d_\|$–$d_\|{}^*$ across the Fermi edge, due to the continuous density of states at $E_F$; in particular the $d_{xy}$ ($d_\|$) orbital allows for a continuous spectrum of low energy excitations starting from 0 eV.

For a slightly higher excitation energy of 530.1 eV, as shown in Figure 7.6(b), the contrast in the behaviour of the elastic feature in rutile $VO_2$ is striking. Again in the $\mathbf{E} \| c_R$ spectrum, the elastic feature is very identifiable and again dominated by a continuous spectrum of very low energy inelastic losses arising from the $d_{xy}$ ($d_\|$) and other $t_{2g}$ bands crossing the Fermi level. Similar behaviour is observed in the metallic $IrO_2$, studied in Chapter 4. Now the $\mathbf{E} \perp c_R$ RXES spectrum of rutile $VO_2$ reflects the hybridisation of the O $2p$ states with the V $3d$ $t_{2g}$ states close to $E_F$ but without any noticeable contribution of a genuine elastic peak, although the RXES spectrum may instead only show the inelastic losses. If these contrasting rutile $VO_2$ are normalised to peak height (Appendix A.3) then, as for the 529.3

---

[†] As suggested by Qazilbash *et al.* [170] from optical conductivity measurements.

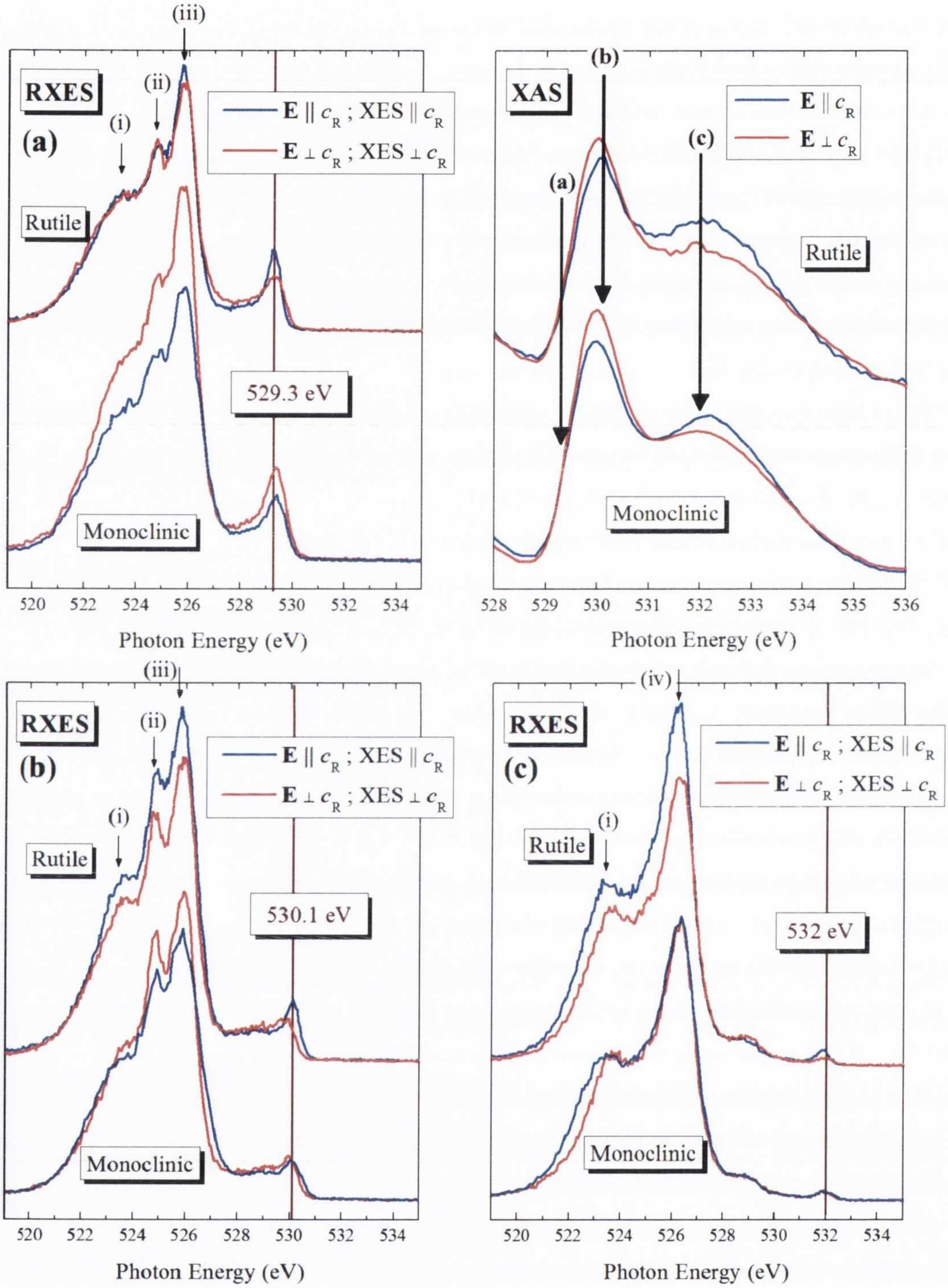

Figure 7.6: RXES spectra taken at the O $K$-edge threshold (a), the $\pi^*$ peak (b), and the $\sigma^*$ peak, as indicated by arrows on the XAS spectra in the upper right panel. Emission was recorded for the two labelled scattering geometries in both the rutile and monoclinic phases. The XES spectra are comparable in form with those observed for monoclinic $VO_2$ by Schmitt *et al.* as E7, E8 and E11 in their Figure 5 [167].

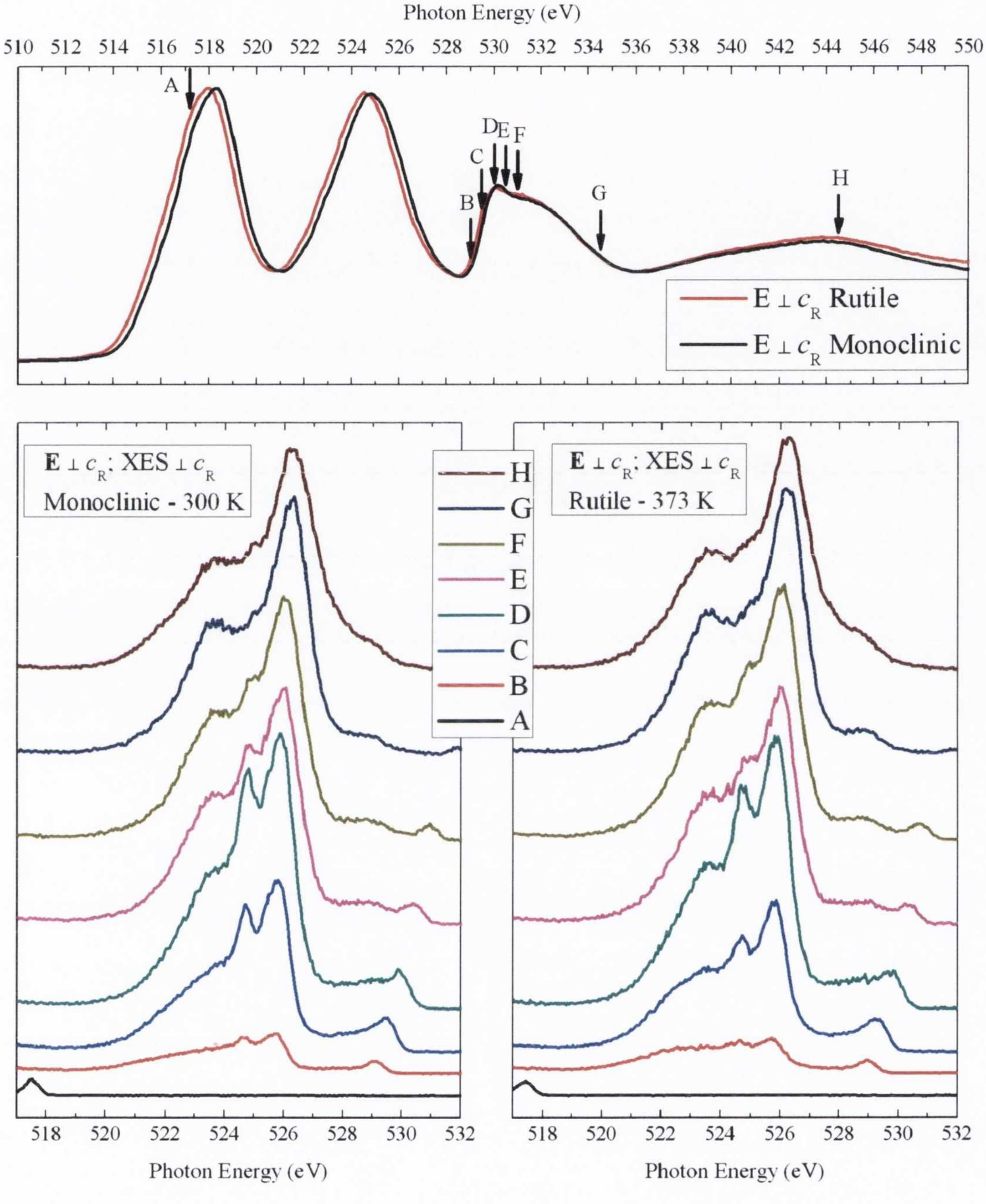

Figure 7.7: Waterfall RIXS (RXES) Figures for the $\mathbf{E}\perp c_R$;XES$\perp c_R$ scattering geometry only, for the O $K$-edge of VO$_2$ in both the rutile and monoclinic phases. XAS panel (top) shows arrows indicating excitation energies.

eV spectrum (a), the relative spectral weight of the region from 527 to 529.5 eV is more prominent in the $\mathbf{E}\perp c_R$ spectrum. From consideration of the possible O $2p$ PDOS that can contribute in each orientation, it must be that the O $2p_x$ dominates the V–O hybridisation here, reflecting in part the strong V–V $\sigma$ bonding derived from the V $d_{xy}$ ($d_{\|}$) $t_{2g}$ orbital.

For the monoclinic $VO_2$ spectra in 530.1 eV (b), the situation is again similar to that for (a) at 529.3 eV, whereby the width of the valence O $2p$ band is greater in the $\mathbf{E}\|c_R$ spectrum. In these monoclinic spectra, both orientations show an (almost) equivalent elastic peak. Much more prominent at this excitation energy is feature (ii) of the O $2p$ band located at 524.8 eV, not only in the monoclinic phase, but also in the $\mathbf{E}\perp c_R$;XES$\perp c_R$ scattering geometry of both structural phases, where excitation is geometrically favoured by molecular orbitals (MOs) or non-bonding orbitals of $\pi$ character between the O $p_y$ and V $t_{2g}$ $d_{z(x-y)}$ orbitals. That and the fact that it is significantly diminished once away from resonance with the $\pi^*$ XAS peak suggests it is a $\sigma$ feature, and more than likely representative of the O $2p_x$ states projected along the $c_R$-axis, which are dominant with the XES$\perp c_R$ spectrometer alignment. There the O $2p_x$ is primarily concerned with V–O $d_{x^2-y^2}$–$sp^2$ $\sigma$ bonds, but should be invisible when XES$\|c_R$. However O $2p_z$ must also have a projection of the V–O $d_{x^2-y^2}$–$sp^2$ $\sigma$ bonding, hence the lessened contribution in the $\mathbf{E}\perp c_R$;XES$\perp c_R$ spectra. This is due to the space and symmetry selective nature of resonant XES of an in-plane 90° measurement geometry, where $k$-selectivity should play a part. The relative intensities of the O $K$ emission, as normalised to the vanadium $L$ emission peaks, follows a similar pattern in both structural phases, with the $\mathbf{E}\perp c_R$;XES$\perp c_R$ (red) spectra decreasing in intensity with respect to the $\mathbf{E}\|c_R$;XES$\|c_R$ (blue) spectra on increasing excitation energy, properly corresponding with the trend in relative absorption intensity.

As stated, when the peaks are normalised to the O $K$-edge peak maxima as in Appendix A.3, a relative broadening of the main O $2p$ bands is observed in the room temperature monoclinic XES spectra (a) and (b) for the $\mathbf{E}\|c_R$;XES$\|c_R$ scattering geometry. This may be explained in terms of the shifting of the $d_{\|}$ states (and their hybridised O $p_x$ states) with respect to the other $p_y$ hybridised $t_{2g}$ states in the monoclinic phase, as shown in Figure 7.2. So while in the rutile structure, both $p_x$ and $p_y$ unoccupied states are more or less equivalent for threshold and $\pi^*$ absorption, their separation in the monoclinic phase allows a greater degree of state selectivity. This leads the monoclinic (red) $\perp c_R$ spectrum to exhibit more $p_x$ character near the middle of the main O $2p$ band, while the (blue) $\|c_R$ resonantly favours the (non-bonding) $p_y$, and $p_z$ (V–O $\sigma$ bonding) near the top and bottom of this band respectively.

Taking these spectra recorded at 530.1 eV excitation energy, it is instructive to plot them alongside valence band photoemission. This is shown in Figure 7.8a, where the RXES spectra are now grouped to contrast the structural phase in the two geometries. The VB photoemission spectroscopy (PES) is adapted from Koethe *et al.* and was measured using 700 eV photons [160]. It is important to note that the rutile (metallic high-temperature phase) and monoclinic (semiconducting low temperature phase) possess different O 1$s$ binding energies. O 1$s$ core level hard X-ray photoemission spectroscopy (HAXPES) for the two structural phases of a 10 nm thick film $VO_2$ sample[†] was recorded by Eguchi *et al.* [157] and is presented in an adapted form in Figure 7.8b. It can also be seen from this figure that the O 1$s$ core level undergoes a shape change between structural phases, going from a symmetric peak in the insulating phase to an asymmetric Doniach-Šunjić line shape in the metallic phase. The difference in binding energies between the two phases means that to make a true comparison with the VB PES in Figure 7.8a, the RXES spectra were subtracted by their associated binding energy. The monoclinic RXES spectra, possessing the higher O 1$s$ binding energy were thus shifted downward relative to the rutile RXES. The spectra in this figure were then all normalised to peak height and plotted on a negative binding energy scale.

Overall there is reasonable correlation between the PES and the RXES. That the RXES possesses spectral weight above the Fermi energy is attributed mostly to the presence of the elastic feature. The features (i) and (ii) (as described in Figure 7.6) appear to be replicated in the PES with good correspondence in energetic position. Further the trend of their peak maxima between the two phases of $VO_2$ is replicated well also, as does the leading edge of the main O 2$p$ band between -3.5 and -2.5 eV, these features being more tightly bound in the monoclinic spectra. The metal $d$ states at the top of the valence band in the PES, though of course not directly replicated by the O $K$-edge RXES, nevertheless show some similarity, likely from the O 2$p$ – V 3$d$ hybridisation. The main O 2$p_y$ band or feature (iii), which occupies the region between -4 to -3 eV in this plot, are not nearly as prominent in the VB PES, though it is clear that there is O 2$p$ derived spectral weight there.

The overall shape of the spectrum changes dramatically on going to 532 eV excitation energy, shown in Figure 7.6(c). Absent is feature (ii), which was prominent at an energy of 524.8 eV, now that the intermediate state corresponds to V–O $e_g$ derived $\sigma^*$ states, which in particular have a significant O–V $2p_z$–$d_{z^2}$ character at this energy [50]. The main peak of the emission has moved to a slightly higher energy marked by (iv) in Figure 7.6(c). This arises due to the greatly increasing contribution of the non-bonding O 2$p_y$ part of the O 2$p$ main valence band which now contributes much more to the emission at these energies. This is not just due to the geometric and state selectivity, vis-a-vis $\sigma^* \rightarrow \pi$ emission, but in large part also due to the bandstructure, where this non-bonding component of the O 2$p_y$ is maximised at the zone centre, or Γ in the Brillouin zone. Inspection of the $VO_2$ rutile bandstructure presented in Figure 7.9a as calculated by Eyert [50], clearly shows this, and further it shows that this intermediate state selects for Γ via the $k$-selectivity. Lower

---

[†] Noting that thin film $VO_2$ samples, depending on their thickness, have a lowered MIT temperature.

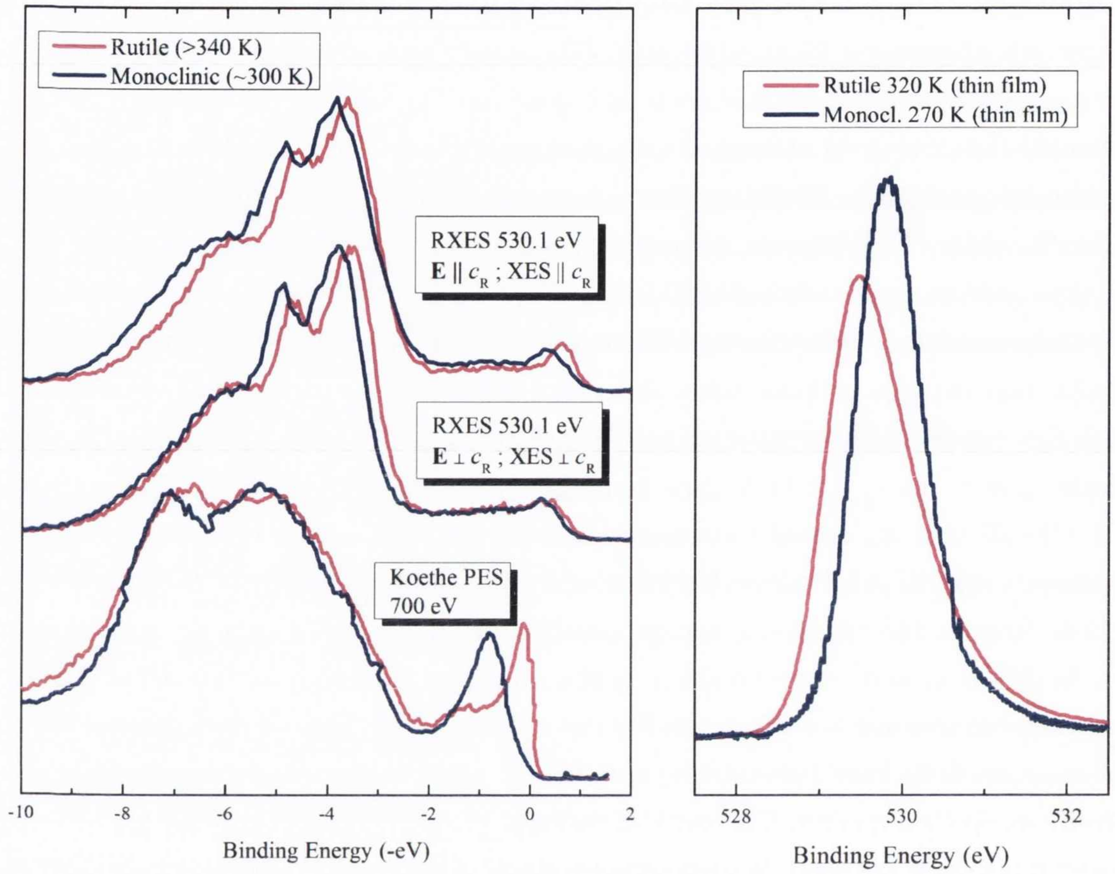

(a) Comparison of PES with RXES

(b) O 1$s$ binding energy.

Figure 7.8: **(a)** Binding energy subtracted RXES at 530.1 eV excitation energy of monoclinic and rutile $VO_2$ compared with VB PES in the same structural phases. The PES is adapted from Koethe *et al.* **(b)** O 1$s$ core-level hard X-ray photoemission comparison of a 10 nm $VO_2$ thin film in its monoclinic and rutile phases, adapted from Eguchi *et al.* [157]

excitation energies on the other hand very clearly do not select for $\Gamma$, except at the very threshold above $E_F$, but with little weighting in proportion to the dominant $t_{2g}$ derived empty states. Again, as in for excitation energies 529.3 and 530.1 eV in Figures 7.6(a) and 7.6(b) respectively, the rutile $VO_2$ $\mathbf{E}\perp c_R$ shows greater spectral weight in the near $E_F$ region than the $\mathbf{E}\| c_R$ spectrum. Also of interest in the rutile spectra (c) is the shoulder from 523 to 524 eV, more prominent in the $\mathbf{E}\perp c_R$ geometry. If we previously ascribed feature (ii) from (a) and (b) as partially due to the O $p_x$ orbital, being more pronounced in this geometry, then the same reasoning should apply here.

For the monoclinic case in Figure 7.6(c), the spectra are almost identical for both geometries in the higher energy region, though show a strong anisotropy at the bottom of the VB, feature (i) between 521 and 523.5 eV. We know that $\sigma^*$ states are selected with bias

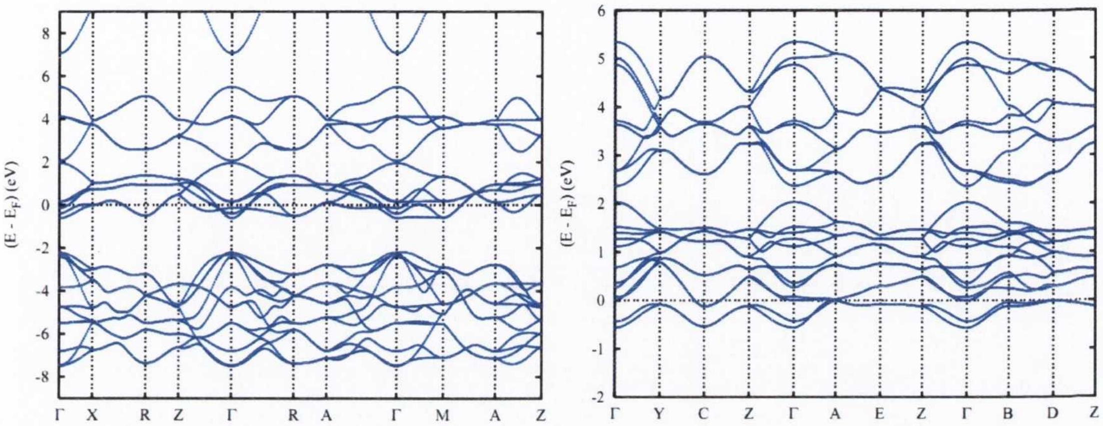

(a) Rutile $VO_2$ bandstructure.

(b) Monoclinic $VO_2$ bandstructure.

Figure 7.9: **(a)** Electronic bands of rutile $VO_2$ along selected symmetry lines within the first Brillouin zone of the simple tetragonal lattice. **(b)** Electronic bands of monoclinic $VO_2$ along selected symmetry lines within the simple monoclinic Brillouin zone. From Eyert *et al.* [50].

in absorption. For the $\mathbf{E}\|c$ these would be consist of primarily O $2p_x$ unoccupied states, thus equally favouring emission from occupied states of $p_y$ and $p_z$ symmetry at 90° in-plane. While for the $\mathbf{E}\perp c$ geometry it is primarily $p_z$ $\sigma^*$ unoccupied states selected in the intermediate state, favouring emission of $p_y$ and $p_x$ states. The calculated bandstructure for higher binding energies in monoclinic $VO_2$, Figure 7.9b, is not shown by Eyert [50]. The expectation may be that it is similar to the near isostructural $WO_2$ and $MoO_2$. That being the case, and with $k$-selectivity in the CB at $\sim 3$ eV above threshold, then emission at the bottom of the VB preferentially picks out the now more tightly bound V–O $d_{z^2}$–$p_z$ component. The increase in spectra weight at the bottom of the VB for the monoclinic $\mathbf{E}\|c_R$;XES$\|c_R$ in Figure 7.6(c) is therefore attributed to O $2p_z$ states. That it is not observed to the same degree for the rutile phase suggests that the O $p_z$ and $p_x$ states exhibit greater energy overlap when the monoclinic distortion is absent.

Focusing on one specific geometry, that of $\mathbf{E}\perp c_R$;XES$\perp c_R$, the XAS and RXES are shown in Figure 7.10, comparing both the monoclinic and rutile structural phases. The evolution of the resonant O $K$-edge VB emission features can be seen much more clearly in this figure. The excitation energies are indicated by the arrows on the absorption spectra, labelled A through H. Feature (ii) as described for Figure 7.6, is again observed as more prominent in the monoclinic phase, especially for the $\pi^*$ feature excitations C and D. In both structural phases it diminishes very quickly after D, observed as unpronounced with the small step in energy E and F, though it is still evident likely due to the 0.6 eV bandwidth of the incident X-rays still selecting some states attributed to D. Feature (ii) is obscured

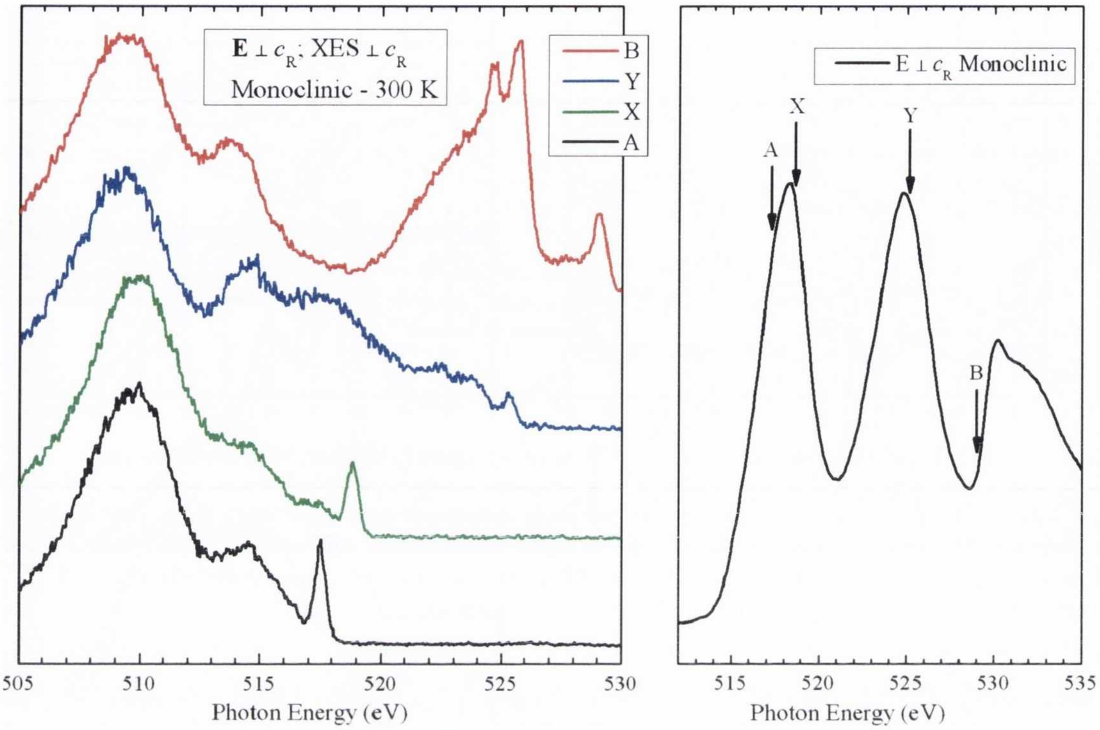

Figure 7.10: Vanadium $L$-edge RIXS waterfall graph of $VO_2$ in the $\mathbf{E}\perp c_R$;XES$\perp c_R$ scattering geometry only. Arrows in XAS panel on right gives excitation energies.

outright in the higher energy excitations G and H, and the peak of the emission is seen to shift its peak position for these energies.

Figure 7.10 iterates two spectra, A and B, from the monoclinic spectra in Figure 7.7, but with two more spectra (X and Y), with a focus on the V $L$-edge emission. The XAS scan is included in this figure with arrows to illustrate the excitation energies at which the emission was acquired. Elastic peaks are present at the excitation energies and significant spectral changes are observed between the resonant V $L$-edge spectra. Shin *et al.* [165] reported a $-6$ eV charge transfer loss feature in the vanadium $L$-edge RXES spectra of monoclinic $VO_2$. This was not observed in the spectra presented in Figure 7.10, though they are of higher resolution and lower noise than either of those from Shin *et al.* Further, though the spectra show considerable energy dependence at resonant energies, no clear energy position can be assigned to resonant loss features in this figure, such as for example what would be expected from $dd$-excitations, supporting the same assessment made by Schmitt *et al.* [167]. This indicates that the electronic structure of $VO_2$ is more band like than correlated [166], notwithstanding the difficulty in getting accurate calculations for the monoclinic $VO_2$ electronic structure.

## 7.5 Conclusions

Polarisation dependent X-ray absorption spectroscopy (XAS) and resonant X-ray emission spectroscopy (RXES) was performed on a single bulk crystal of $VO_2$, for two in-plane scattering geometries in both its monoclinic (room temperature) phase, and its rutile tetragonal ($> 340$ K) phase.

Many problems occurred in the repeated polarisation dependent measurements of these crystals that hindered the collection of a complete set of RXES data for both phases in the two measurement geometries, much of which can be attributed to the quality of the samples. In the first instance at BL8, a shard that was used for one of the measurement geometries, upon analysis was discovered to possess significant surface reduction and partially resembled $V_2O_3$.[†] In the second attempt at a complete dataset at the same beamline, a resetting of the piezo-electric controlled spectrometer entrance slit occurred before or during sample heating, resulting in all subsequent spectra being unresolved. The final attempt to complete the dataset with measurements in the rutile phase, cleaving the crystal prior to measurement, resulted in poor dichroism observed in the XAS and thus a single geometry could be relied upon. In the end however a sufficiently complete dataset was compiled between the measurements and presented in this chapter.

The XAS measurements made on the large crystal samples clearly indicated that they are indeed stoichiometric $VO_2$, and they do not resemble any of the other vanadium oxide absorption spectra reported by Schmitt [164]. Dichroism in O $K$-edge XAS was evident, however the splitting of the $d_{xy}$-hybridised bands in the $\mathbf{E}\|a_M$ spectrum [159–161] was not observed.

For the RXES spectra, a similar trend of resonant features were observed in the two scattering geometries on both sides of the MIT. The differences in polarisation, state and symmetry selectivity allowed insight into the electronic structure of the compound, such as a prominent $p_x$ band (feature (ii)) lying approximately 5 eV below the Fermi level and selected only for specific values of crystal momentum. The data suggests it possesses either an increased density of states, or increased separation from other bands in the monoclinic phase. This resonant polarisation dependent probe of valence band states not only allowed a greater understanding of the real space bonding and hybridisation of $VO_2$, but subsequently gave experimental insight into the differences and similarities between the electronic structure of the two phases, that may contribute in the future to a stronger understanding of the MIT.

---

[†] In this dataset it is only the $E\|c$ geometry that showed any contamination, the comparison between the rutile and monoclinic $E\perp c$ is still instructive. The entire set can be viewed in Figure A.4 in the appendix section, page 210.

# 8 Rutile and Anatase $TiO_2$, Ti $L$-edge

## 8.1 Introduction

Titanium(IV) oxide ($TiO_2$) is the most stable oxide of titanium, of which four naturally occurring structural polymorphs exist. In order of most to least common these are rutile (tetragonal), anatase (tetragonal), brookite (orthorhombic) and akaogiite (monoclinic). The rutile name is actually synonymous with the family of $MA_2$ compounds that share its particular structure, the structural class of compounds that this body of work is based upon. The different structures that compounds of this formula unit form are expected to possess differing electronic structures, surface structures and optical properties [173,174]. A well crystallised bulk single crystal of rutile for example has a band gap of approximately 3.0 eV, while for anatase it is closer to 3.2 eV [175].

$TiO_2$ is a compound with many potential applications; as with other transition metal oxides, much of the current applications relate to the surface properties and its application in the catalysis of redox reactions [175]. Both anatase and rutile are insulating in their stoichiometric forms, but readily develop concentrations of oxygen vacancies when heated to temperatures $> 1000°C$, becoming n-type semiconductors. This has fuelled research interest into a possible solar powered source of hydrogen [176]. These and other properties of titanates such as electrochromism, electromigration for memristive technology, and other applications that will be detailed in section 8.2, means a great deal of benefit could come about from an increased understanding of their electronic structure, making them very worthy of scientific research. Further, knowledge of the electronic structure of $TiO_2$ is important in its own right as it may lead to a greater understanding of numerous other titanate compounds such as $BaTiO_3$ and $SrTiO_3$.

Following work done by Kennedy on both rutile and anatase $TiO_2$, successfully probing the electronic structure and linear dichroism at the O $K$-edge [5], it was thought to be beneficial to further probe these materials at the Ti $L$-edges, as all previous studies did not appear to take account of the possible existence of natural linear dichroism. The goal of this investigation is to ascertain the presence of any natural linear dichroism, to measure the polarisation dependence of the material and explain it within the context of a comparative resonant X-ray spectroscopic study of the electronic structure of the formula-identical compounds. To accomplish this, a similar methodology to the O $K$-edge work by Kennedy [5] and indeed in the bulk of this thesis is used, but applied this time to the Ti $L$-edge. A molecular orbital picture of the bonding and structure of the compounds is taken as a starting point. With the benefit of electronic structure calculations, the axis-projected partial density of states (PDOS) of the conduction band (CB) is resolved from the X-ray absorption spectroscopy (XAS) and with special attention attributed to its polarisation dependence. Then using resonant X-ray emission spectroscopy (RXES) at differing scattering geometries, at different excitation energies the valence band (VB) PDOS is investigated, with the possibility of isolating the contributions of individual orbitals. This work is considered supplementary to the work undertaken in early chapters which focused on the O $K$-edge, probing the bonding nature of transition metal $MA_2$ compounds from a different perspective, that of the metal cation.

However for the cation, particularly in the case of $L_{3,2}$-edge spectroscopy of the first transition row, there cannot be a simple comparison of either the XAS or X-ray emission spectroscopy (XES) spectrum to the appropriate unoccupied or occupied PDOS, not just because of the spin orbit splitting of the $2p$ levels but especially because of the significant $\langle 2p|3d\rangle$ overlap integrals and matrix elements, to the point where the spectrum is dominated by atomic multiplet effects. Bandstructure effects are thus minimised. Nevertheless, the influence of chemical bonding and the anisotropic charge distribution around the metal cation, together with a lifting of degeneracy of both the $t_{2g}$ and $e_g$ orbitals in the tetragonally distorted octahedral environment should still be expected to give rise to natural linear dichroism in the Ti $L_{3,2}$-edge XAS and perhaps to a lesser degree in the Ti $L_{3,2}$-edge XES spectra of $TiO_2$.

This chapter presents the results of the electronic structure study of undoped anatase and rutile $TiO_2$. Polarisation dependent XAS and RXES study of the titanium $L$-edges was completed to study the Ti $3d$ PDOS, in the in-plane scattering geometry, i.e. with the spectrometer in the plane of the electric polarisation vector $\mathbf{E}$ and the propagation vector $\mathbf{k}$ of the incident light.

### 8.1.1 Previous Work and Motivation

Matsubara *et al.* [177] and Harada *et al.* [91] have previously performed polarisation dependent soft X-ray Raman scattering (SXRS) on rutile $TiO_2$, an alternative term for resonant inelastic X-ray scattering (RIXS) and RXES. Harada, while mentioning it, appears to disregard the importance of the crystal orientation in the interpretation of the spectra, while Matsubara does not even indicate what it was. Both ascertain that the important variable is whether the scattering geometry is "polarised" or "depolarised". This corresponds to a 70° grazing incidence onto a flat surface, with a 90° scattering geometry between the incident beam and the spectrometer axis. The "polarised" designation refers to the electric polarisation vector **E** being orthogonal to the plane created by the incident and scattered light, while in the depolarised it is contained within it. The nomenclature used in this thesis has referred to these geometries as out-of-plane and in-plane scattering respectively. In their experiments rather than an undulator capable of giving linear-vertical as well as linear-horizontal polarisation, the chamber, including sample and manipulator, was rotated about the beam axis in order to obtain these orientations, and thus the crystal was also rotated. From Harada [91] it is deduced that their polarised scattering geometry refers approximately to $\mathbf{E}\perp c$;XES$\|c$, while their depolarised configuration refers approximately to $\mathbf{E}\|c$;XES$\|c$. The latter of which is in-plane and was replicated in our measurements presented here.

The work of Harada *et al.* [91], although not discussing their Ti $L_{3,2}$-edge XAS in this fashion, appears to be the first report in the literature of what can be seen as natural linear dichroism at the Ti $L$-edge in $TiO_2$ where their "polarized" XAS spectrum is $\mathbf{E}\perp c$ and their "depolarized" XAS spectrum $\mathbf{E}\|c$. XAS of both rutile and anatase $TiO_2$ at the Ti $L_{3,2}$-edge was also carried out by van der Laan *et al.* [178]. The electron energy loss spectroscopy (EELS) study of Heiliger *et al.* [179], although repeating the natural linear dichroism presented in $TiO_2$ at the O $K$-edge, do not quite appear to have the resolution and signal necessary to describe the natural linear dichroism reported by Harada, or observed in this work.

Observations of the Ti $L$-edge XAS date back to EELS measurements of Grunes *et al.* [180] and the earlier ingenious work of Fischer [181] which incorporated measurements of the Ti $L_{\mathrm{III}}$, Ti $K$ and O $K$ XAS and XES spectra to empirically obtain an approximation to the molecular orbital picture here shown for $TiO_2$. However, the advent of 2nd generation synchrotrons and the application of the atomic multiplet method to the $2p-3d$ XAS of transition metal oxides give the first and clearest understanding of the $L_{3,2}$-edge XAS of $TiO_2$ [182,183]. These high resolution XAS spectra of $TiO_2$ agreed with contemporaneous EELS measurements of Brydson *et al.* [92,93]. Although de Groot remarked that the $D_{4h}$ symmetry inherent in $TiO_2$ results in a polarisation dependence of the spectrum and that using $D_{4h}$ symmetry in the atomic multiplet model could accurately describe the Ti $L_{3,2}$-edge XAS of $TiO_2$, it appears the details of this calculation, and perhaps of the polarisation dependent measurement of $TiO_2$, were never published [184].

The atomic multiplet method is well established now and can be used to describe all $2p^63d^N \rightarrow 2p^53d^{NH}$ XAS spectra as well as RXES spectra of transition metal oxides [15].The success of the atomic multiplet method relies only on the starting point of crystal field theory and the associated empirical parameters, e.g. with octahedral crystal fields ($O_h$), that of the crystal field splitting 10 Dq which splits the $t_{2g}$ and $e_g$ levels. For lower point group symmetries, such as $D_{4h}$, further parametrisation is required ($D_s$,$D_t$) describing the additional splittings between $d$-orbitals arising due to the distortion of the octahedral crystal field. Going to $D_{2h}$ introduces even more empirical parameters [185]. It has been argued that the atomic multiplet model precludes band structure effects from playing a role in the Ti $L_{3,2}$-edge XAS [15]. However ab initio methods are still being employed to model the Ti $L_{3,2}$-edge XAS employing density functional theory (DFT) methods with a great deal of recent success, albeit at a very significant computational cost [186] or complexity [187]. Very recent calculations using a first principles multichannel multiscattering method describe the situation whereby both multiplet type electron correlation effects and long-range bandstructure strongly influence the spectra [188]. However the atomic multiplet method remains the easiest and most accessible way in interpreting these spectra, particularly for $TiO_2$, though not without its own complexity. A code for carrying out these atomic multiplet calculations is readily available [189] and the methods are well described [15].

A recent summary of the progress in modelling $2p$ XAS spectra by multiplet and ab initio methods is soon to be available [190]. However to date, even with the latest theoretical methods, there is still no recognition of the aspect of natural linear dichroism that should be expected to be present in lower symmetries than $O_h$, particularly in $TiO_2$, rutile and anatase. The Ti $L$-edge XAS and RXES spectra are interpreted here in the light of both ab-initio DFT methods and atomic multiplet methods, but more directly informed by the molecular-orbital diagrams. The RXES or RIXS of $TiO_2$ is described also by the atomic multiplet approach as detailed for instance in Shin and Kotani [177,191]. They apply a complete group-theoretical approach to the description of the polarised and depolarised spectra reported by Harada *et al.* [91], Matsubara *et al.* [177] and Tezuka *et al.* [192], accurately describing the RIXS component – specifically the inelastic losses observed in the Ti $L$-edge RXES spectra. They acknowledge that longer cluster size calculations are required for the modelling of the normal XES (NXES) component, and such calculations are described [193]. The group theoretical selection rules distinguish between the depolarised and polarised RIXS spectra [177,191]. These selection rules are given by equations 8.1 (polarised) and 8.2 (depolarised):

$$\sum_{\gamma=x,y} A_{1g} \otimes T_{1u}(y) \otimes T_{1u}(\gamma) = A_{1g}, E_g, T_{1g}, T_{2g} \qquad \text{(Polarised)} \qquad (8.1)$$

$$\sum_{\gamma=x,y} A_{1g} \otimes T_{1u}(z) \otimes T_{1u}(\gamma) = T_{1g}, T_{2g} \qquad \text{(Depolarised)} \qquad (8.2)$$

Briefly explained using the notation from Kotani *et al.* [191], the ground state symmetry of $TiO_2$ is given by $A_{1g}$. The electric dipole transition operator, in the case of both the X-ray absorption and emission process, is represented by $T_{1u}$. In the final state the irreducible representations will be given by the product representation $A_{1g} \otimes T_{1u} \otimes T_{1u}$, but for the selection rules to be obtained for the polarised and depolarised† the scattering plane is chosen as $xz$, and thus the component of the dipole excitation operator is $T_{1u}(y)$ for the polarised and $T_{1u}(z)$ for the depolarised geometry. The final states allowed in RIXS(/RXES) are then given by equations 8.1 and 8.2.

Figure 8.1, reproduced from Kotani *et al.* [191], shows the mechanism by which the multiplet states can be explained, disregarding the effects of the spin-orbit splitting of the $2p$ states and the crystal field splitting of the $3d$ states, for simplicity. The ground state of $TiO_2$ is the bonding state between the $3d^0$ and $3d^1$ $L$ configurations. The bonding and anti-bonding states have $A_{1g}$ symmetry, as part of the $O_h$ symmetry group. The non-bonding $3d^1$ $L$ states include those with $T_{1g}$, $T_{2g}$, $E_g$ etc. symmetry.

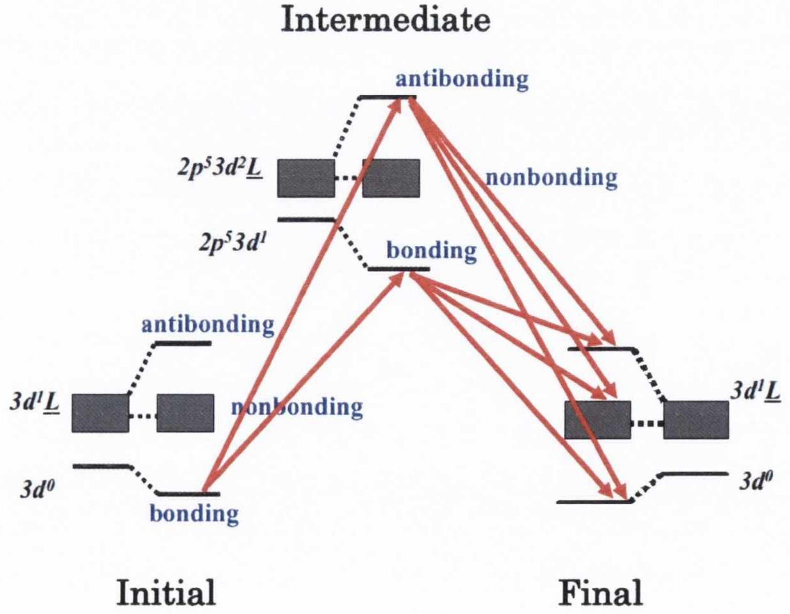

Figure 8.1: Schematic representation of the Ti $2p \rightarrow 3d \rightarrow 2p$ RIXS transition of $TiO_2$. From Kotani *et al.* [191]

---

† Out-of-plane and in-plane scattering geometries respectively.

The motivation behind this investigation was the contention that the orientation of the crystal axis plays a non-trivial role in the polarisation dependence of these compounds rather than purely being subject to the contrast of polarised versus depolarised scattering configuration, or out-of-plane versus in-plane. Thus all spectra presented in this chapter were measured in the same in-plane scattering geometry where any polarisation dependence can be attributed purely to the orientation of the crystal axes with respect to **E**. Unfortunately time did not allow for out-of-plane measurements to be obtained. Nevertheless, the effect or influence of bandstructure on Ti *L*-edge RXES can be discerned by contrasting the two in-plane scattering geometries without regard to the details of atomic multiplet transitions or depolarised versus polarised selection rules

## 8.2 Applications of Rutile and Anatase $TiO_2$

The applications of $TiO_2$ given in this section will particularly pertain to its electronic structure, optical properties and reactivity. The fields of current interest range from its use as a photocatalyst, photovoltaic material and photolytic medium for the evolution of hydrogen. It can also be used as an electronic material such as in dielectric logic gates or spintronic media. Recently, and with much interest, it has found employment as a memristive compound [194,195].

Due to its wide bandgap, it is suitable material in solar voltaics, allowing the creation of a photo-induced electron hole pair that can be spatially separated before recombining, such as in the dye sensitised Grätzel cell. Many other applications of $TiO_2$ rely rather on its surface properties, utilising it as a catalyst [196]. The foremost use however is as a pigment; up to 98% of the annual global production, exceeding 4 million tonnes, is used to make pigment for white paint, toothpaste, medicine tablets etc.

### 8.2.1 Memristors

The memristor (or memory resistor) has in the past been referred to as the missing fourth element of integrated circuitry. First theorised in 1971 by Leon Chua it was considered to have valuable circuit properties; for many years however nobody produced either a useful physical model or an example of a memristor. A 2008 Nature paper by Strukov *etal.* [194] however, entitled "The missing memristor found", announced the details behind the development of a switching memristor based on a thin film of titanium dioxide at Hewlett Packard (HP) labs. It has been suggested by HP that the development may extend the current Moore's Law[†] trend by decades. HP have announced the commercial availability of memristor technology within 18 months, at the time of writing, replacing current used technology in devices such as Flash, SSD, DRAM and SRAM.

---

[†] The observation that steady technological improvements in miniaturisation leads to a doubling of the density of transistors on new integrated circuits every 18 months.

A memristor is a passive two-terminal electrical component, where there is a functional relationship between the sense and magnitude of electric current and the resistance in a hysteretic fashion. When current flows through a memristive device in one direction, its electrical resistance increases; when it flows in the opposite direction its resistance decreases. When current is stopped, the device retains its last known resistance when it was active. This remembered resistance is kept upon restarting of charge flow, independent of the direction of that flow. As long as the time-interval of the current or its magnitude remains within certain bounds [197], the device maintains an approximately linear charge-resistance relationship.

This behaviour can be seen as a bi-product of the electrochromic behaviour of $TiO_2$; whereby the application of a sufficiently strong DC electric field causes a region of deeper colouring to emerge. This is caused by electromigration, the visibly darkened regions of the normally colourless crystal representing regions of high oxygen vacancy defect concentration. Further, the resistivity of the crystal in these reduced regions drops by some orders of magnitude. The dielectric field required to achieve such electromigration is far too high for use in commercial applications, for example with the size of crystal (mm) used in this work. However, in nanostructured $TiO_2$ films, the requisite dielectric fields can be obtained with comparative ease [198]. An example implementation is via a platinum electrode crossbar strategy that sandwiches the (in this case rutile) $TiO_2$ [199].

The action of $TiO_2$ based memristive technology has been recently studied by spatially selective near edge X-ray absorption fine structure (NEXAFS), or XAS, at the Ti *L*-edge [200]. Further NEXAFS, as well as measurements of a related nature such as RXES which also utilises linear polarised synchrotron soft X-rays, may well depend upon the results presented in this thesis in order to avoid a misinterpretation of variations observed, where these variations in fact are primarily related to the local crystal orientation.

## 8.3 Physical and Electronic Structure

Table 8.1 presents the structural parameters of both anatase and rutile $TiO_2$. The crystal structure of each of these compounds is illustrated in Figures 8.2 and 8.3. † Rutile, like the majority of the other compounds studied in this theses, is tetragonal with near octahedral symmetry of the metal cation and trigonal coordination of the oxygen anion. Similarly in

---

† In all structure illustrations, the orientation is chosen based on what the author believes best exhibits the structural details of the compound. The orientation is indicated by the *a*- *b*- and *c*-axes arrows, though it should be noted that for all rutile and anatase structures, the *a* and *b* labelled axes in these Figures are in fact equivalent, as they are both tetragonal unit cells.

| | **Anatase** | **Rutile** |
|---|---|---|
| Space Group | $I4_1/amd$ | $P4_2/mnm$ |
| $a$ (Å) | 3.784 | 4.593 |
| $c$ (Å) | 9.515 | 2.959 |
| Internal Parameter $u$ | 0.208 | 0.305 |
| Cell Volume (Å$^3$) | 136.3 | 62.5 |
| Molecule/Cell | 4 | 2 |
| Nearest $d_{M-O}$ (Å) | 1.934 | 1.949 |
| Nearest $d_{M-M}$ (Å) | 3.04 | 2.53 |
| Density (g/cm$^3$) | ~3.9 | ~4.23 |
| O–Ti–O bond angles | 77.7°<br>96.2° | 81.2°<br>90.0° |
| Symmetry Group | $D_{2d}$ | $D_{2h}$ |

Table 8.1: Anatase and rutile $TiO_2$ structural parameters and physical properties. Values from references: [40,116,201,202]

the anatase, the trigonal-planar coordination of the oxygen is distinctly visible in Figure 8.3, though the bond angles are more severe. From table 8.1 the bond angle difference for anatase is 18.5° whereas for rutile it is only 8.8°. This leads to a greater distortion of the anatase $TiO_6$ octahedra.

Often tetragonal structures are described by reference to their edge sharing octahedra. Figure 8.4 shows that for rutile structures there are two sets of orthogonal octahedra, each sharing two edges that form octahedral chains in the [001] direction. The octahedra share corners between sets of orthogonal chains. Conversely the pink shaded panel on the right of Figure 8.4 illustrates the anatase octahedra. These latter octahedra are more distorted than their rutile counterparts, with two opposing corners above and two below the equatorial plane of the octahedra. Each octahedron, rather than lying in a linear chain, shares edges with four neighbours and corners with four other neighbours. This results in a zigzag chain with a screw axis [174].

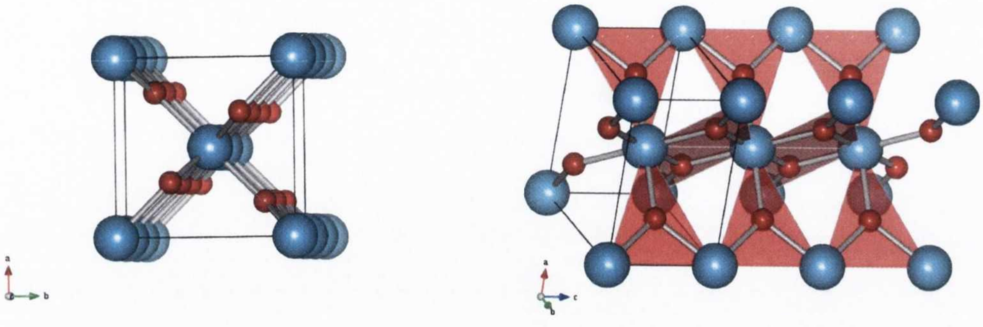

Figure 8.2: Three unit cells of rutile $TiO_2$ structure, contiguous along the *c*-axis, observed in two perspective orientations: along and parallel to the *c*-axis respectively. $Ti_3O$ trigonal planes are highlighted.

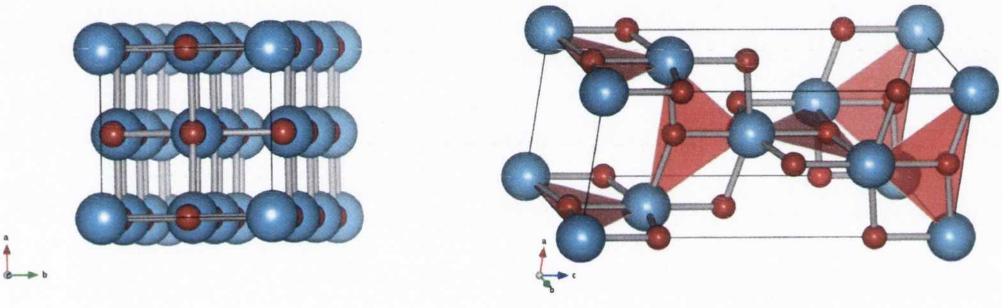

Figure 8.3: A single unit cell of anatase $TiO_2$ structure observed in two perspective orientations: down and parallel to the *c*-axis respectively. $Ti_3O$ trigonal planes are highlighted.

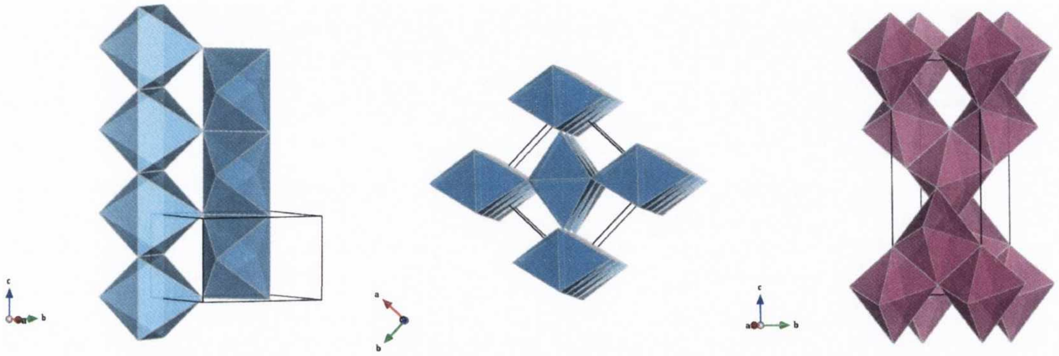

Figure 8.4: Two-edge-sharing octahedra of rutile $TiO_2$ forming chains in the [001] direction, shown in two orthogonal perspectives. On the right, shaded pink to demarcate the difference, are the anatase $TiO_2$ octahedra each sharing four edges.

### 8.3.1 Bonding in $TiO_2$

In the ionic model $TiO_2$, the cation has a $Ti^{4+}$ oxidation state, is considered a $d^0$ system. However with covalent bonding the rutile and anatase structures allow a partial occupancy of the $3d$ orbitals, reducing the electrostatic energy implied by a purely ionic situation. Therefore both ionic bonding, involving the transfer of charge from the Ti $3d$ and $4s$ orbitals to the O $2p$, and covalent bonding, associated with the hybridisation of the Ti $3d$ and O $2p$ orbitals play a role in the electronic structure of TiO$_2$ [5]. As documented in table 8.1, the nearest titanium-titanium distance is markedly larger in anatase than in rutile. Thus the Ti $3d$ $t_{2g}$ orbitals, that have their lobes directed away from the ligands, are more isolated in the anatase structure, while in the rutile structure some interaction is exhibited between neighbouring Ti cations [174].

Since the titanium cation is approximately octahedrally coordinated in both rutile and anatase TiO$_2$, it is correct as a first approximation to acknowledge the titanium $3d$ orbitals as being split, as with the other anions in this thesis, by an octahedral ($O_h$) crystal field into $t_{2g}$ and $e_g$ components. The chosen local coordinate system of the metal cation in rutile is the same as for other rutile and distorted-rutile (monoclinic) shaped compounds in this thesis, outlined in Chapter 3. To iterate for this structure, it is the natural coordinate system, where the local $z$ axis is co-linear with the apical axis of the TiO$_6$ octahedra, lying in the (001) plane. The $x$ and $y$ axes on the other hand are contained in the plane of the waist of the octahedron, roughly oriented toward the equatorial oxygen ligands.

However, due to the tetragonal distortion of the TiO$_6$ octahedron, not all Ti–O distances are equal, and the octahedron is stretched along the O–Ti–O direction perpendicular to the $c$-axis, thus defining the local $z$-axis. If this were all, then the point group symmetry of the cation would be reduced to $D_{4h}$ from $O_h$, lifting the degeneracy of the $e_g$ and of the $t_{2g}$ orbitals where the $d_{xy}$ orbital is separated. This was previously detailed in Table 3.1. In addition, though the four other Ti–O equatorial distances are the same, they are not arranged in a square but as a rectangle, with the shorter O–O edge being shared by successive octahedra along the $c$-axis, the longer O–O edge thus parallel to the $c$-axis. The point group symmetry of the cation is reduced further from $D_{4h}$ to $D_{2h}$ and the remaining two $t_{2g}$ orbitals are no longer degenerate.

The analogous local coordination for anatase Ti cation matches that chosen by Asahi *et al.* [174] as well as Thomas *et al.* [182] and is illustrated in Figure 8.6.. The anatase structure is visually quite different to rutile, though highly analogous. In a similar fashion the local $x$ and $y$ axes of lie in the (distorted) equatorial plane of the octahedron, each approximately toward a ligand oxygen, while the $z$ axis is parallel to the apical axis. In anatase however this apical Ti-O bond, and hence local $z$ axis is along the $\langle 001 \rangle$ directions. One effect of this relative 90° rotation of the octahedron when comparing rutile to anatase, is that now the $d_{z(y+x)}$ and $d_{z(y-x)}$ $t_{2g}$ orbitals both lie parallel to the $c$-axis, and are thus degenerate. Thus they will be referred to collectively as $d_{||}$ specifically for anatase.

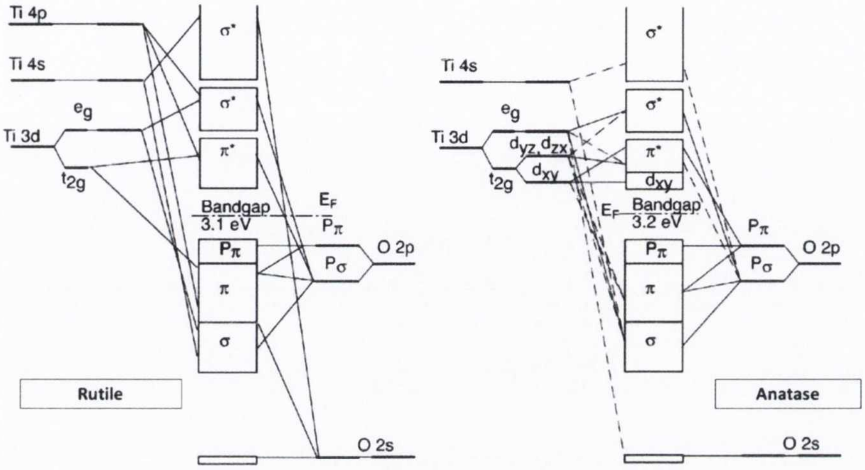

Figure 8.5: Molecular orbital diagram showing the $\sigma$ and $\pi$ bonding combinations in rutile and anatase $TiO_2$. Adapted from Thomas *et al.* [182]

All the Ti–O distances in the distorted equatorial plane of anatase are equal, with the O–O sides also equal. However the Ti–O distances along the long axis of the octahedron are longer, reducing the point group symmetry of the cation from $O_h$ to $D_{4h}$. This is reduced further to $D_{2d}$ [176] because of the two opposite pairings of ligand O in the equatorial plane bisecting the octahedron, and the cation site lying either above or below the plane. In rutile it is often convenient to approximate the point group symmetry to $D_{4h}$, if not even to $O_h$ [15,203]. In anatase the splitting into $D_{4h}$ cannot be ignored, but the $D_{2d}$ splitting can be overlooked in most instances. Some of these issues are important for the data to follow.

Figure 8.5 gives the molecular orbital (MO) diagrams for both rutile and anatase in the described local coordination. The immediate notable difference in the MO diagrams between the two structures is the splitting of the $t_{2g}$ orbital in the anatase structural phase. The distortion of the $TiO_6$ octahedra in the anatase structure gives rise to a lowering of the $d_{xy}$ orbital overlap and hence energy. This is analogous to the O $2p_y$ (labelled P$\pi$ in Figure 8.5) lying perpendicular to the $Ti_3O$ plane in the top of the valence band. Neither are significantly hybridised and thus remain largely uninvolved in any bonding-antibonding combinations. Similar attributes are observed in rutile $TiO_2$ but to a less significant extent [44]. Further contributing to this is the larger metal-metal distance of 5.35 Å in the lobe direction $\langle 110 \rangle$ of the $d_{xy}$ orbital in the less dense anatase, resulting in this orbital being quite isolated at the bottom of the conduction band. This contrasts with rutile, where the metal-metal distance along the [001] is only 2.96 Å, permitting the $d_{xy}$ orbital to provide metal-metal interaction.

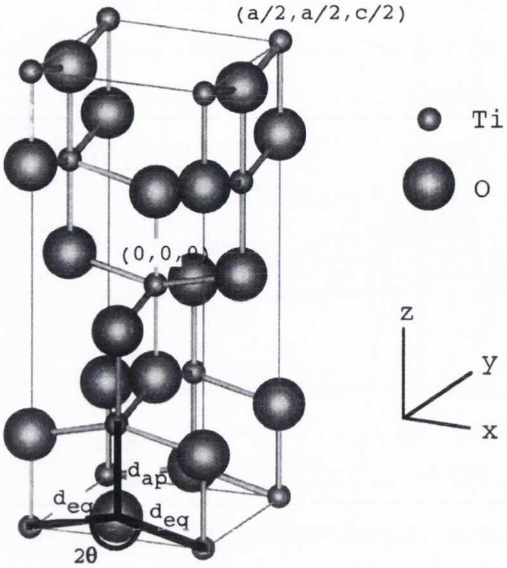

Figure 8.6: Primitive unit cell and definitions of the local metal coordination for $TiO_2$ in the anatase structure. Adapted from Asahi *et al.* [174]

## 8.4 Ti *L*-edge Spectroscopy and Analysis

Spectroscopy of the *L*-edge of metals differs from the *K*-edge of the oxygen and fluorine anions previously focused on in this these. The *K*-edge broadly refers to an electron transition involving the $n = 1$ energy level, and therefore always refers to the $1s$ shell.

Taking the example of the hydrogen atom or single electron atom, the transition from an static state $\Psi_i$ to final state $\Psi_f$, the quantum mechanical dipole matrix element [†] requires these initial and final wavefunctions to be of opposite parity or else the matrix element is zero and there is no transition. This parity alternates with increasing quantum number $l$ or orbital angular momentum quantum number.[‡] This leads to the dipole selection rule where for a transition to occur, the condition $\Delta l = \pm 1$ must be satisfied. Thus in the removal of a $1s$ core electron, or filling of a $1s$ core hole, the lowest energy allowed transition is with a $2p$ orbital. Since this is usually the only transition that can occur in the immediate energy locality, it allows an undisturbed probe of the valence and conduction band PDOS through either XAS or XES. [§]

Though the above holds fast for light atoms, for example the oxygen *K*-edge as explained in Chapter 2, the situation is usually more involved for n> 2. Electrons possess an inherent angular momentum, or spin ($s$),[¶] the vector sum of which with $l$ gives $j$, the total angular momentum quantum number. To conserve angular momentum for an emitted photon an additional $\Delta j = 0, \pm 1$ selection rule must also be satisfied, as well as the dipole transition selection rule $\Delta l = \pm 1$, where $j$ can be $l + s$, or $l - s$. The special case of a transition between $j = 0$ states however is not allowed.

---

[†] Given by equation 2.5 in Chapter 2 on page 11.

[‡] Where $l = 0, 1, 2, 3...$ for subshells $s, p, d, f...$

[§] For a detailed explanation of selection rules and spectroscopy see Chapter 2.

[¶] Distinct from the $s$ subshell.

The $L$-edge is defined as a transition involving the $n = 2$ energy level. In spectroscopic notation, excitation at the $L$-edge is divided further into the $L_1$ shell, $L_2$ and the $L_3$ shell referring to the $2s$ and $2p_{1/2}$ and $2p_{3/2}$ respectively. This energy splitting of the $p$ states is caused by the spin-orbit effect, the alignment (or anti-alignment) of the spins $s = 1/2$ with the orbital angular momentum $l = 1$. The filling of an $n = 2$ or $L$-edge core hole, and subsequent emission of a photon (or photoelectron), is further divided by the selection rule mentioned, $\Delta j = 0, \pm 1$ and labelled by non-systematic historical Greek-character notation.[†] Thus a transition from the $3d_{5/2}$ to $2p_{3/2}$ is $L\alpha_1$, $3d_{3/2}$ to $2p_{3/2}$ is $L\alpha_2$, and $3d_{3/2}$ to $2p_{1/2}$ is $L\beta_1$. Figure 2.3 on page 15 from Attwood [11], portrays an illustrated illustration of these transitions in an energy level diagram for copper. A further $L$ transition of note for this chapter is between the $3s$ and the $2p_{3/2}$ and $2p_{1/2}$, referred to as the $L1$ and $L\eta$ emission lines respectively. A more detailed discussion of the selection rules, allowed transitions and spectroscopic notation is given in Chapter 2.

The end result is that in both XAS and XES at the Ti $L$-edge in this case, a double representation of the Ti $3d$ PDOS is observed resulting from both $L_3$ and $L_2$ core hole excitations. In each case the separation is approximately 6 eV.

### 8.4.1 Dichroism at the Ti *L*-edge

The origin of natural linear dichroism in X-ray spectroscopy, with an emphasis on the anion $K$-edge, is discussed at length in Chapter 2. Here that discussion is boiled down to the relevant points concerning this chapter. For the $K$-edge, the $s$–$p$ polarisation dependent transition matrix element can be simplified in relation to the $p$ orbital shape, as along each orbital lobe axis a transition intensity of $1/3\ \mathcal{A}\mathcal{R}^2$ is observed [‡] when $\mathbf{E}$ is parallel to that lobe, and zero along the other two axes. This is visually represented in Figure 8.7 adapted from Stöhr and Siegmann [8]. From this figure the transition intensities for the $p$–$d$ transitions are similarly shown to be polarisation dependent. In this case however the orbitals are in a cloverleaf configuration. Thus for the $t_{2g}$ and $d_{x^2-y^2}$ cloverleaf orbitals, the transition intensities are given as $3/15\ \mathcal{A}\mathcal{R}^2$ for a $2p$ core hole oriented along either of the two axes that lie in the plane of the lobes, and zero for a core hole oriented perpendicular to the plane of the orbital [8]. The $d_{3z^2-r^2}$ (or simply $d_{z^2}$) orbital is a special case as illustrated in Figure 8.7, contributing to transitions along all axes.

---

[†] For the IUPAC systematic nomenclature equivalents see table A.2 in the Appendix on page 208.

[‡] Units of transition intensity are per orbital per spin, measured in $\mathcal{A}\mathcal{R}^2$, where $\mathcal{A}$ is the proportionality factor given by: $\mathcal{A} = 4\pi^2 \frac{e^2}{4\pi\epsilon_0 \hbar c} \hbar\omega$ and $\mathcal{R}$ is the radial dipole matrix element.

$$I(\theta) = I_{\|} \cos^2 \theta = \langle I \rangle \cos^2 \theta \tag{8.3}$$

Thus, whether a particular orbital is occupied or unoccupied will influence the contribution of that orbital to the core to valence XAS spectrum, but the choice of the projection of the core hole along a particular axis arises from the orientation of the electric field vector with the crystal axes.

In a more general sense the intensity of absorption can be written as a function of $\theta$, in this case referring to the angle of the $E$-vector with the axis of symmetry which will be labelled "$\|$", for example in a $p$-orbital which has a node perpendicular to this axis. The polarisation dependent intensity of absorption can be expressed by equation 8.3; thus it conforms to the ubiquitous cosine squared dependence, where $\langle I \rangle$ is the angle averaged intensity. It should be noted that this does not determine the charge distribution, only its projections along the local Cartesian coordinate axes.

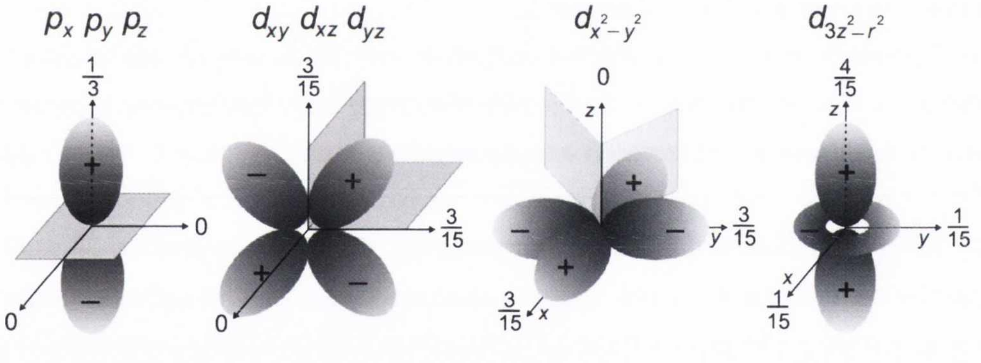

Figure 8.7: Polarisation dependent core to valence transition intensities for **E** along the natural principal coordinate axes. Listed are the intensities for the four basic symmetry cases at the $K$- and $L$-edges. [8]

### 8.4.2 Self Absorption Correction

An experimental problem arises in connection with analysis of any $L_{2,3}$-edge RXES spectrum, as due to the spin orbit splitting of the $2p$ level there is an energetic overlap of the Ti $L_3$ absorption edge with the Ti $L\beta_1$ emission. An $L\beta_1$ fluorescent photon from the filling of an $L_2$ core-hole is therefore energetic enough to potentially create an $L_3$ hole.[†] This is an example of self absorption. The probability of the self-absorption is proportional to the photoabsorption cross-section of the compound in question at that emission energy. The amount of self absorption observed in a given direction is then related to both the photoabsorption cross-section and the distance the photon must travel to escape. Further, at such resonant energies the $L_3$ XAS gives the direct relative probability of a transition, and hence photoionisation occurring at a chosen energy. These combined factors are considered enough to compensate for self absorption effects in emission spectra.

---

[†] See tables A.1 and A.2 in the appendix for explanation of spectral notation.

Varying the angle of incident of horizontal linear polarised radiation by rotating about [001] axis (maintaining an $\mathbf{E}\perp c$;XES$\perp c$ scattering geometry) onto the sample surface should yield no difference in emitted spectral weight in the absence of self absorption. Large intensity differences of the $L\beta_1$ emission peak are observed between near normal and near grazing incidences however, due to the differing average escape depth from the sample surface of the measured scattering photons. Soft X-ray emission is insensitive to sample charging, and thus it is a simple matter, using atomic absorption data, to estimate the average emission depth of our samples as a function of the surface orientation with with the direction of the incoming and outgoing light: [204]

$$\langle z\rangle = \cos\theta_i \cos\theta_o \frac{\int z \exp[-(\mu_i + \mu_o)z]dz}{\int \exp[-(\mu_i + \mu_o)z]dz} \tag{8.4}$$

Where $\mu_i$ and $\mu_o$ are the absorption coefficients for incoming and outgoing radiation energies respectively, for the compound in question. $\theta_i$ and $\theta_o$ are the incident and outgoing photon beam angles with respect to the surface normal.

To correct the fluorescent intensity it is not necessary to directly compute the emission depth, and the formula is simplified as for a 90° scattering geometry the angles of incident and outgoing radiation are related. Furthermore, since only relative intensity of emission is measured, the density component of the absorption coefficient cancels out leaving only the absorption cross section. The correction factor is thus given by equation 8.5 was reported in the literature by Müller *et al.* [204], but was not utilised in that publication. Jiménez-Mier *et al.* [205] employed the correction factor while investigating the Ti $L$-edge, using the cross section of metallic titanium. They later improved upon the method to include the contribution from the $L_3$ XAS via total electron yield (TEY) [206], whereby the well above threshold photoionisation cross-section per Ti atom is equated to the observed XAS signal at that energy, yielding the photoabsorption cross-sections across the whole of the $L_{3,2}$ XAS, due to the relative intensity recorded.

$$I(h\nu_o) = I_m(h\nu_o)\Big[1 + \frac{\sigma(h\nu_o)}{\sigma(h\nu_i)}\cot\theta\Big] \tag{8.5}$$

In the above self absorption correction formula 8.5, $I_m$ is the measured intensity at the outgoing emission energy $h\nu_o$ and $\theta$ is the angle of incidence onto the sample with respect to normal. $\sigma(h\nu_i)$ and $\sigma(h\nu_o)$ represent the absorption cross section for the incoming and outgoing photon energy. These were deduced in the following manner. First the absorption cross sections were obtained for the energies immediately above ($a$) and immediately below ($b$) the absorption edge features for each relevant subshell in elemental titanium and oxygen. These gave $\sigma_{\mathrm{O(a)}}, \sigma_{\mathrm{Ti(a)}}$ and $\sigma_{\mathrm{O(b)}}, \sigma_{\mathrm{Ti(b)}}$; where $\sigma_{\mathrm{Ti(a)}}$ further contained a $\Delta\sigma$ resulting from the added cross section of the Ti $2p$ absorption. The formula unit of $TiO_2$ means the (relative) total cross section is given by $\sigma = \sigma_{\mathrm{Ti}} + 2\sigma_{\mathrm{O}}$. The subshell cross section values were obtained from Yeh and Lindau [207]. The resultant values of $\sigma_{\mathrm{(a)}}$ and $\sigma_{\mathrm{(b)}}$ were matched to similar energy points on the measured TEY of the sample, and its arbitrary-unit $y$-axis was normalised to these points giving a graph of $\sigma$ versus energy. To match experimental parameters for RXES spectra, this absorption cross section graph was broadened by a Gaussian to an equivalent of a 0.4 eV monochromator resolution, yielding appropriate values for $\sigma(h\nu_i)$, while for $\sigma(h\nu_o)$ a 0.57 eV Gaussian broadening factor was then applied to account for the spectrometer slit resolution.

Figure 8.8 compares the corrected and uncorrected signals for two spectra at the same value of excitation energy for (001) anatase $TiO_2$ at the Ti $L$-edge. The left panel is at a 70° angle of incidence with respect to the surface normal, while the right panel is at 20°. Inset in both panels is a graph of the determined values of $\sigma(h\nu_o)$, the absorption cross section for the outgoing photons, created as previously described from the TEY and subshell photoabsorption cross section values from the literature. The arrow on the inset XAS graphs indicates the excitation energy, confirmed by the elastic features observed in emission. Clearly a significant modification to the spectra occurs for the region between 456 and 469 eV, which brackets or spans the main absorption features in the $L_{3,2}$ XAS. Similar results were found for emission whose excitation energy was in this region. Since the correction augments areas of low signal, it was required that the background of each spectrum to be fitted individually and removed, thus minimising artifacts from amplified noise. It should be noted that, particularly at excitation energies of low absorption cross-section, this correction factor can significantly reduce the apparent signal to noise ratio for regions of the emission spectra that are appreciably altered. Expanding on this; regions of low counts have lower statistics and are more affected by spectrometer noise, and since the self-absorption effectively amplifies certain parts of the signal, it will similarly amplify the associated noise.

A form of self absorption also occurred in the XAS spectra, whereby the normal incidence scans possess decreased intensity at the $L_2$ absorption edge and above when compared with grazing incidence scans. The average photon penetration depth is dependent upon the angle of incidence, and TEY is proportional to the photoemitted electrons ejected from

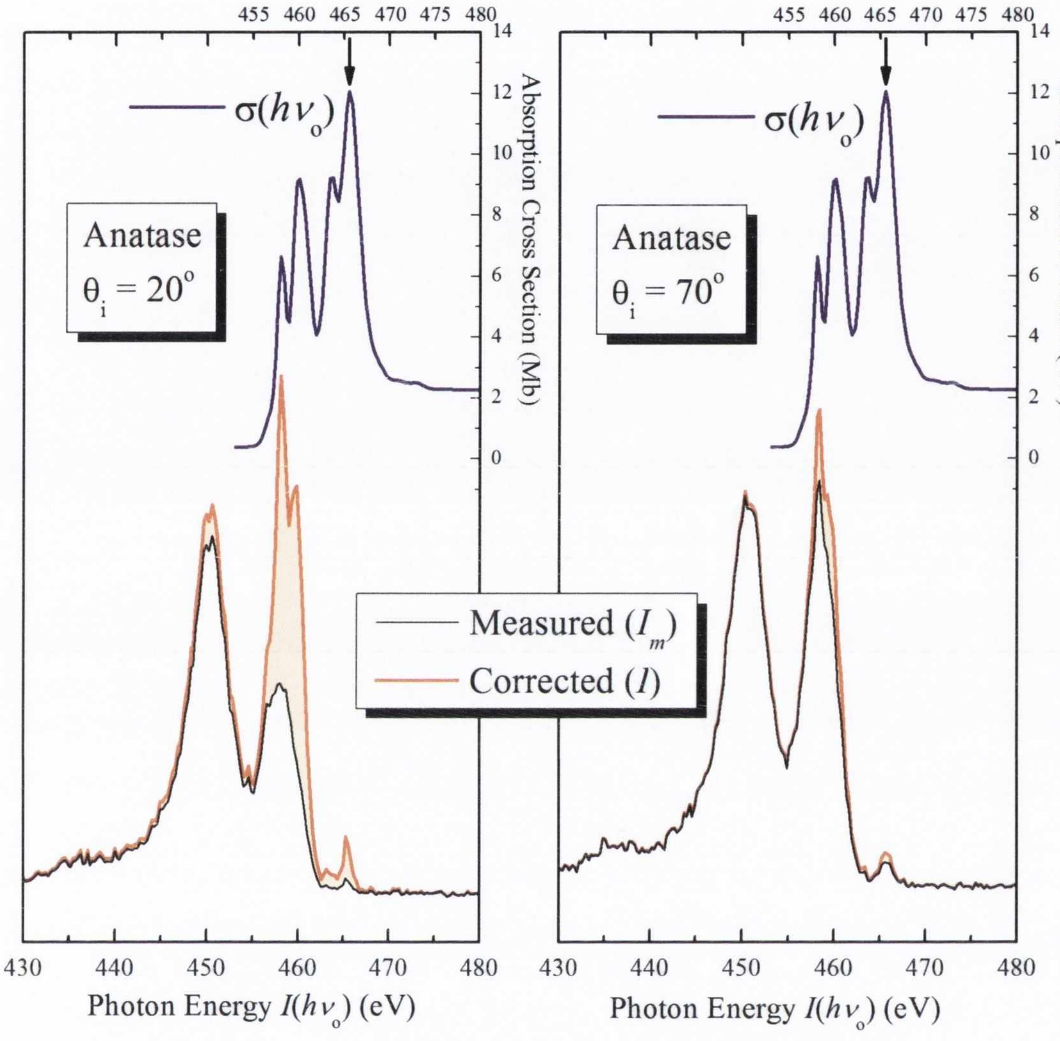

Figure 8.8: Comparison of uncorrected and corrected emission intensity for RXES at the Ti *L*-edge of anatase $TiO_2$ at 20° beam incidence for the left panel (grazing exit) and 70° beam incidence for the right panel(grazing incidence). Insets show outgoing absorption cross section $\sigma(h\nu_o)$ used for correction and determined from the TEY.

the sample surface, from an Auger decay process or otherwise. Thus the probability of an electron scattering and not being ejected depends upon the depth at which the electron is created and the electron-muon free path; in this case the contribution to the TEY signal from atoms near the surface is enhanced in grazing incidence measurements. Surface charging effects can also result on insulators effectively lowering the absorption intensity for time dependent beam exposure [208], this would act reduce the apparent step function in XAS as measurements are made with increasing energy. To compensate, a line was fitted to the difference in intensity between grazing and normal incidence XAS. Points were taken below threshold (nominally zero), in-between the features, and above the absorption features, and plotted against energy. The normal incidence absorption scan intensity was then multiplied by this line. This correction factor to the $L_{3,2}$ XAS then allows the difference in the intensity of features observed to be attributed purely to linear dichroism. Similarly, this double correction of self absorption applied to the RXES allows for the spectra to be compared for differences arising purely from spectroscopic origins.

All subsequent Ti $L$-edge emission and absorption spectra presented in this chapter have been corrected for self-absorption in the manner outlined where applicable.

## 8.5 Experimental Measurements

Soft X-ray measurements were carried out at beamline X1B in the National Synchrotron Light Source (NSLS) in Brookhaven National Laboratory (BNL) New York, as well as at Beamline 7.0.1 (BL7) at the Advanced Light Source (ALS) in Lawrence Berkeley National Laboratory (LBNL), California. Both are undulator beamlines equipped with a moveable selection of spherical grating monochromators. Both are also equipped with a Nordgren-type fluorescence spectrometers. More information on these beamlines is provided in Chapter 2.

XAS was measured in TEY and total fluorescence yield (TFY) mode, the former having a far superior signal to noise ratio for these materials. Monochromator resolution used in the acquisition of XAS spectra was approximately 0.15 eV. The X1B monochromator has a 1200 grooves per millimetre (gpm) diffraction grating that allows sub 0.1 eV absorption resolution at the expense of brightness, used for high resolution absorption scans. The Ti $L$-edge XAS was measured in $1^{st}$ order on the first grating of the Nordgren-type Gammadata XES300 spectrometer. The monochromator resolution used in emission measurement was approximately 0.4 eV. The XES spectrometer slit setting at BL7 was 7 $\mu$m, equivalent to 0.57 eV instrumental resolution, while at X1B the spectrometer resolution was approximately 0.65 eV. For Ti $L$-edge emission measurements at BL7 the medium energy grating (MEG) was used for the incident $x$-rays while the spectrometer grating 2 in $1^{st}$ order.

Emission spectra at the Ti $L$-edge were calibrated using the copper $L\alpha_{1,2}$, $L\beta_1$ and $L1$ emission lines in second order.

The Ti $L$-edge XAS monochromator energy was then rigidly shifted to match the Ti $L_3$-edge $t_{2g}$ peak energy as reported for rutile $TiO_2$ by Brydson *et al.* of 458.2 eV from EELS measurements [92,93], which we later confirmed by X-ray photoemission spectroscopy (XPS). The anatase Ti $L_3$-edge $t_{2g}$ peak was found to be $\sim$ 0.1 eV higher than that of rutile during XAS, thus it was rigidly shifted to 458.3 eV. Both of these values match those reported by Henderson *et al.* [209]

The spectrometer table at BL7 was set to a much wider energy range across the detector, leading to a lower pixel to photon energy ratio, or greater reciprocal dispersion, on the BL7 detector than at X1B. However, this allowed inclusion of the Ti $L1$ and $L\eta$ emission, which as well as giving a second polarisation dependent observation, also provides a useful intensity ($y$-axis) normalisation factor for the emission spectra.

## 8.6 Samples and Mounting

The single crystal rutile and anatase $TiO_2$ samples were purchased commercially, and were cut and polished from larger single crystals by SurfaceNet GmbH. The anatase crystal measured approximately $5 \times 5 \times 1$ mm, the orientation of its largest surface was (001). The single crystal rutile samples were a similar size of $5 \times 5 \times 0.5$ mm with both (100) large surfaces polished.

In each case samples were mounted flat on the sample plate. The rutile crystal was mounted with the [001] axis horizontal, in the plane of the plate, while the (001) anatase necessitated the $c$-axis being normal to the sample plate. Spatial constraints at X1B measurements ruled out azimuthal rotation; thus to access the two in-plane scattering geometries, $\mathbf{E}\|c$;XES$\|c$ and $\mathbf{E}\perp c$;XES$\perp c$, both samples were measured in near grazing ($\sim 70°$) and near normal ($\sim 20°$) incidence. At BL7 only the anatase was measured at both grazing and near normal incidences, while the rutile sample was azimuthally rotated, its polar angle putting it at $\sim 20°$ and $\sim 30°$ for $\|c$ and $\perp c$ measurements respectively.

## 8.7 Results and Discussion

### 8.7.1 XAS of $TiO_2$

The polarisation dependent Ti $L_{3,2}$ XAS of rutile and anatase $TiO_2$ measured in TEY mode is shown in Figure 8.9. These spectra were obtained at the X1B beamline at the NSLS, using the 1200 gpm monochromator grating with a nominal resolution of $<$ 100 meV. The shape and intensities of the features correspond well to results in the literature comparing both compounds [93,179,182,183,209,210], and for the anisotropic polarisation dependence in rutile [91].

The main four peak structure of the spectra can be explained by calculating the dipole transition probability from a ground state Ti $3d^0$ to the final state (intermediate state in RXES) $2p^5 3d^1$. The spin-orbit effect splits the spectrum into the $2p_{3/2}$ ($L_3$) and $2p_{1/2}$ ($L_2$) levels with a separation of approximately 6 eV. These are then further split in two again by the crystal field interaction into $t_{2g}$ and $e_g$ resulting in four main peaks in both compounds. In order of increasing energy they are the $L_3$ $t_{2g}$, $L_3$ $e_g$, $L_2$ $t_{2g}$ and $L_2$ $e_g$

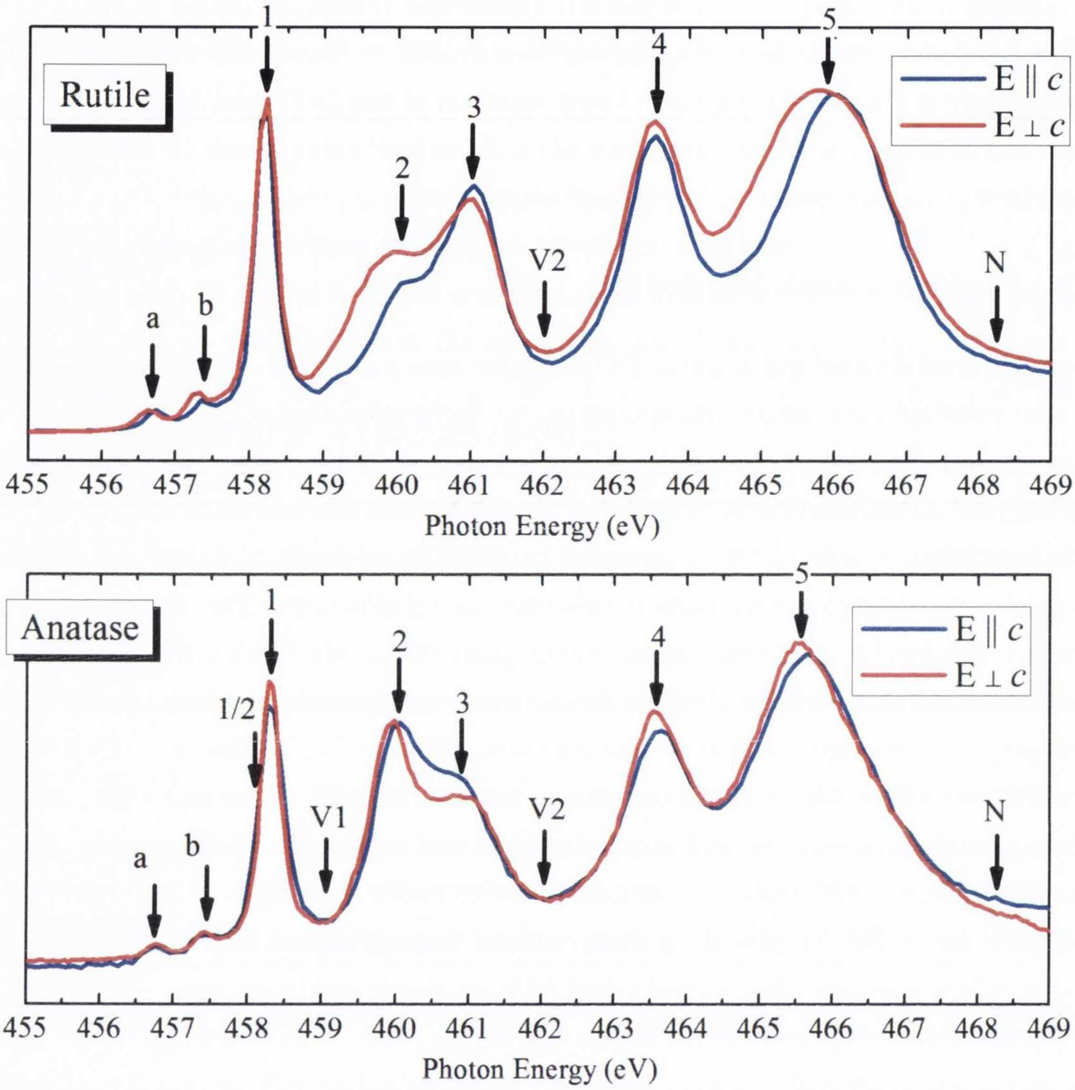

Figure 8.9: XAS of $TiO_2$ rutile and anatase at the Ti $L$-edge for $\mathbf{E}\|c$ and $\mathbf{E}\perp c$ measurement geometries. Arrows indicate RXES excitation energies.

features. None of these states are pure however and are instead labelled according to their main character. In both anatase and rutile an asymmetric broadening, or doubling, occurs in the $L_3$ $e_g$ peak which is thought to result from their respective distortion from octahedral symmetry [78,91,92] and thus a lifting of the $e_g$ degeneracy. This asymmetric peak, centred around 460 eV, is the main feature of difference between the rutile and anatase absorption, and serves as a fingerprint for the two structures. In anatase the lower energy side of the double $L_3$ $e_g$ feature is dominant, while the opposite is the case in rutile. Apart from the distortion of the octahedral field another possible explanation is a dynamic Jahn-Teller effect, where the electronic and vibrational states couple in the excited state [78,183].

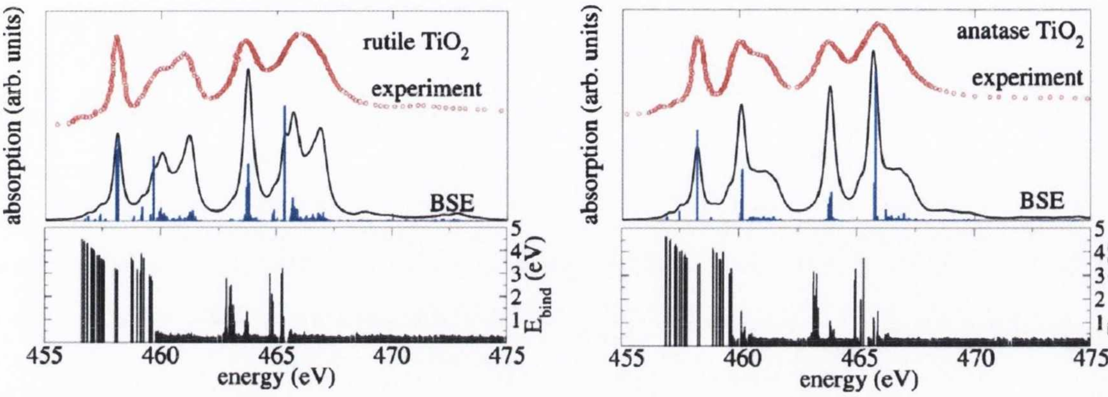

Figure 8.10: Calculated and experimental Ti $L_{3,2}$ edges in rutile and anatase TiO$_2$ with the BSE formalism. Adapted from Laskowski and Blaha [186]

The local density approximation (LDA) calculations failed to reproduce the splitting, and thus it was attributed to possible longer-range (non-local) interactions [211]. Recently however Laskowski and Blaha [186] utilised the Bethe-Salpeter equation (BSE), which operates within the many-body perturbation theory. This approach has been found to give very similar results as the standard DFT core-hole calculations for the $K$-edge CB PDOS in light elements [212]. Laskowski and Blaha used the BSE to calculate the $L_{2,3}$ absorption spectra of early $3d$ elements, including both rutile and anatase TiO$_2$ as shown in Figure 8.10. This method is demonstrated to be very successful at predicting the $L_3$ $e_g$ splitting, and hence shoulders visible in both anatase and rutile TiO$_2$, as well as the absorption spectra as a whole.

The rutile XAS, observed in the upper panel of Figure 8.9, was measured at $\theta = 0°$ normal incidence for the $\mathbf{E}\|c$ line, and at approximately $\theta = 70°$ grazing incidence for the $\mathbf{E}\perp c$ scan, making the latter only approximately $\perp c$. The XAS shows a marked dichroism, especially in the $L_3e_g$ region, the same region where the difference between the polymorphs is primarily exhibited. According to Harada *et al.* [91], in rutile TiO$_2$ the lower energy side of the $L_3e_g$ originates from the long Ti–O bonds ($d_{z^2}$), which are hybridised weaker than the shorter Ti–O bonds ($d_{x^2-y^2}$) that form the higher energy side of this double feature. In the chosen local metal ion coordination these would conform to the overlap of the $d_{z^2}$ and $d_{x^2-y^2}$ orbitals respectively. The relative increase in PDOS at the low energy side of the $L_3e_g$ peak was attributed to the long bonds (or $d_{z^2}$ orbital) being excited. Harada observed this same polarisation dependence for rutile XAS, though not to the same magnitude as the figure presented, which may be due to their $\sim 20°$ discrepancy in both geometries. In the presented spectra, the $d_{z^2}$ derived feature not only shows a contrast of intensity in the two measurement geometries, but the feature broadens, its average weight shifting to a lower energy in $\mathbf{E}\perp c$. This broadening trend, if not the double-peak feature, is mimicked in the

$L_2e_g$ peak, which shifts its average weight by approximately 0.25 eV. This is perhaps due to the excitation of purely $d_{z^2}$ attributed states in this low energy region.

This qualitative explanation of the observed dichroism described in the $e_g$ absorption features for rutile $TiO_2$ is, on first viewing, apparently not supported by the calculated rutile $TiO_2$ PDOS presented in appendix A.9. Here the average spectral weight of the Ti $3d_{z^2}$ unoccupied feature appears to lie at a slightly higher energy than the $d_{x^2-y^2}$. However, upon examination of the bandstructure character plots presented in Figure 8.11, a plausible explanation can be found. Figure 8.11 shows that while the $d_{z^2}$ and $d_{x^2-y^2}$ weightings are similar in energy, $d_{z^2}$ exhibits strong dispersion in the region of the $\Gamma$ point. This is likely due to the dumbbell shaped lobes of this orbital that hybridise strongly with the O $p_z$ in a $\sigma$-type overlap. The $\mathbf{E}\perp c$ scattering geometry favours the selection of the states parallel to the $z$-axis within the $d_{z^2}$ orbital, and hence the lower energy states around the $\Gamma$ point.

No publications appear to exist in the literature that probe the polarisation dependence of anatase $TiO_2$ at the Ti $L_{2,3}$ edges and thus this is the first such reported account. The anatase XAS in the lower panel of Figure 8.9 appears to experience a very similar dichroism as the rutile. Examining the crystal structure, illustrated in Figure 8.3, it is noted that the apical axis of the distorted octahedra lies along the [001] direction. This direction then contains the longer Ti–O $\sigma$-type bonds from the $3d_{z^2}$ $e_g$ orbital, and which should therefore show preferential excitation in the $\mathbf{E}\|c$ geometry. From the figure it is clear that the high energy side of the $L_3$ $e_g$ orbital experiences an increase in relative intensity in this geometry. The reason for this contrast with rutile is likely due to the reduced symmetry of the shorter equatorial Ti–O bonds in the anatase polymorph, which in turn reduces the degree of hybridisation of the $d_{x^2-y^2}$ with the O $2p$. This qualitatively explains the switching of the relative intensity of the $L_3$ $e_g$ double peak between rutile and anatase.

Apart from that the anatase does not exhibit the same uni-directional broadening of the $L_3$ or $L_3$ $e_g$ feature, as is the case for rutile. If the rutile broadening results from lower energy $d_{z^2}$ attributed states then it is possible the analogous states in anatase are contained within the main $e_g$ feature. If it partially due to $d_{z(x-y)}$ $t_{2g}$ states, then these may be suppressed in the $D_{2d}$ distortion of the lower density anatase structure. DFT electronic structure calculations of the PDOS and bandstructure are provided in order to assess these assertions. The explanation is more straightforward than for rutile; an inspection of the $e_g$ states in the calculated PDOS in appendix A.10 shows a trend between the $d_{z^2}$ and $d_{x^2-y^2}$ PDOS that corresponds well with the observed natural linear dichroism in absorption. The bandstructure character plots for anatase are included in Figure 8.12, where it can be inspected more closely, and clearly show the more dispersive $d_{x^2-y^2}$ states possess distinguishable spectral weight at a higher energy than the $d_{z^2}$ average.

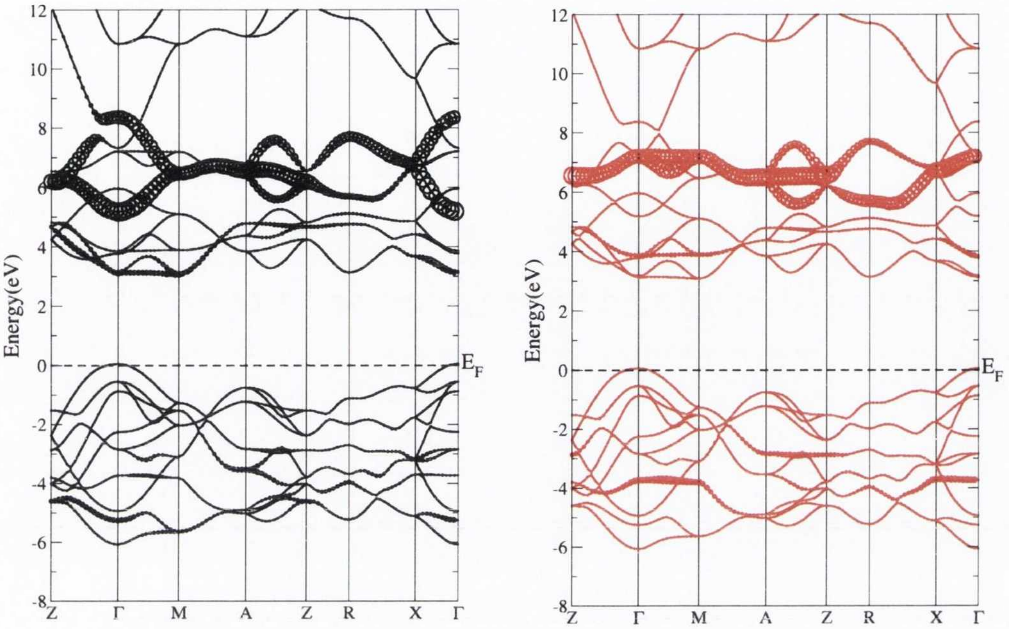

(a) Rutile $TiO_2$ $d_{z^2}$ (b) Rutile $TiO_2$ $d_{x^2-y^2}$

Figure 8.11: Electronic bandstructure character plots of rutile $TiO_2$ emphasising **(a)** the Ti $3d_{z^2}$ and **(b)** the Ti $3d_{z^2}$ weighted character of the bands in the CB.

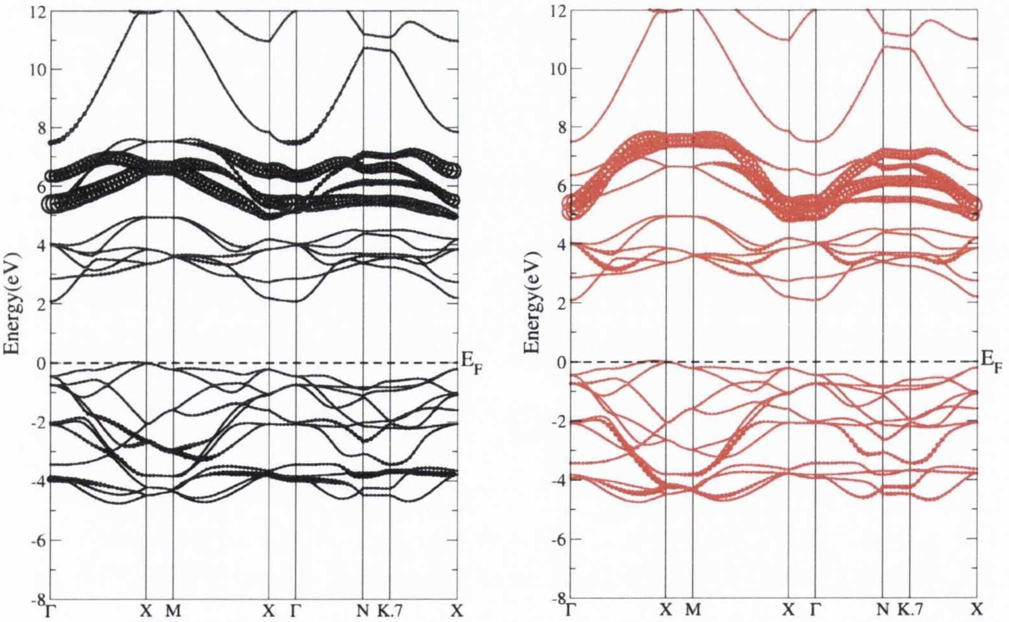

(a) Anatase $TiO_2$ $d_{z^2}$ (b) Anatase $TiO_2$ $d_{x^2-y^2}$

Figure 8.12: Electronic bandstructure character plots of anatase $TiO_2$ emphasising **(a)** the Ti $3d_{z^2}$ and **(b)** the Ti $3d_{z^2}$ weighted character of the bands in the CB.

### 8.7.2 Resonant X-ray Emission of $TiO_2$ $L$-edge

Presented in this section are the polarisation dependent resonant soft X-ray emission results from both rutile and anatase $TiO_2$ at the Ti $L_{2,3}$-edges. Two sets of data for each compound, in each geometry will be presented. First in each case will be that dataset acquired at the ALS which includes the lower energy emission $L1$ and $L\eta$ emission lines. Following this the NSLS, focused on a smaller energy range around the $L\alpha_{1,2}$ and $L\beta_1$ emission solely will be shown. Due to the more narrow range in these latter measurements, there was a higher reciprocal dispersion and an effectively higher resolution.

This chapter will start by presenting and discussing the rutile RXES first, as it is isostructural with many of the other compounds studied in this thesis. Then the anatase RXES will be addressed, with the results discussed in the context of the rutile results.

#### 8.7.2.1 Rutile RXES

Figure 8.13 gives a waterfall representation of the RXES spectra resulting from resonant excitations at the Ti $L$-edge for rutile $TiO_2$. The labels refer to the absorption feature corresponding to the excitation energy, which are given in Figure 8.9. Peaks resulting from elastic de-excitation are observed in some spectra, though elastically scattered photons are suppressed for in-plane scattering compared to out-of plane as, according to Harada *et al.* [91] and Matsubara *et al.* [177], they are technically forbidden. This is shown by the Kramers-Heisenberg formula† as well as group theoretical considerations [91,177] (equations 8.1 and 8.2). Here the final states with A1g, T1g, T2g, and Eg irreducible representations are allowed in the polarised (out-of-plane) configuration, but only those with T1g and T2g irreducible representations are allowed in the depolarized (in-plane) configuration [91].

Though Figure 8.13 illustrates continuous spectra, the left and right panels are divided to allow magnification of relative intensity of the $L\alpha_{1,2}$ and $L\beta_1$ features on the right, in this case by a factor of three over the $L1$ and $L\eta$ emission in the left panel.

There is a shared trend between these two sets of spectra, in that as they both exhibit a second feature only after the $L_2$ excitation energy is reached, showing the same dependence on spin orbit splitting. Tezuka *et al.* [192] previously observed the $L1$ emission in an RXES study of rutile $TiO_2$ and commented on a shoulder possibly resulting from a Ti $3s - 2p_{1/2}$ ($L\eta_1$) transition, in coincidence with the emergence of the $L\beta_1$ peak.‡ This is noted in spectrum (3). However, Tezuka's spectra did not show the same degree of structure as those presented here. Further, this is the first published polarisation dependent study of these emission peaks.

---

† See equation 2.5 in Chapter 2 for the Kramers-Heisenberg formula

‡ Excitation and emission peak notation explained in table A.2 on page 208

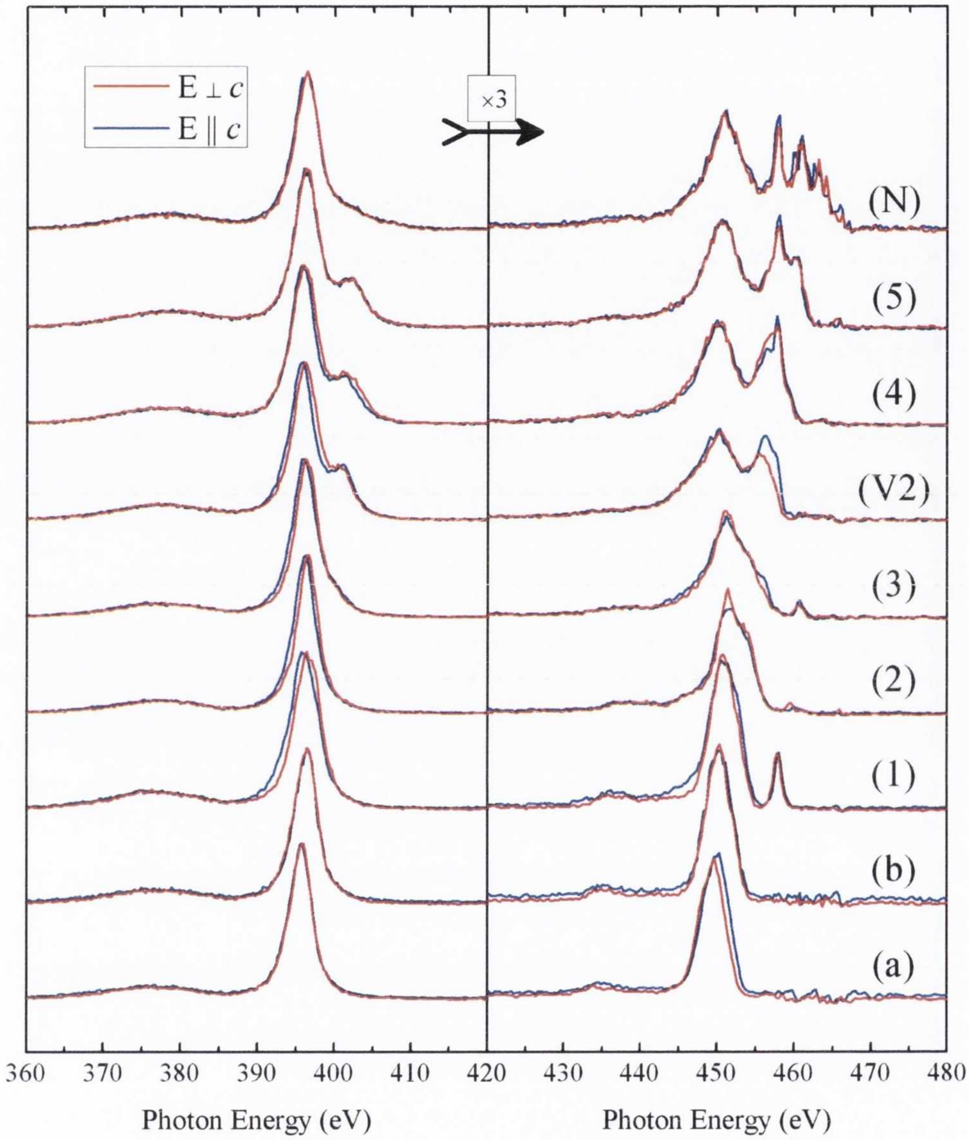

Figure 8.13: RXES of the Ti $L_{2,3}$-edges for rutile $TiO_2$ for two in-plane scattering geometries, $\mathbf{E}\|c$;XES$\|c$ and $\mathbf{E}\perp c$;XES$\perp c$, recorded at the ALS. The left panel shows the $L1$ and $L\eta$ emission, while the right panel shows the comparably amplified $L\alpha_{1,2}$ and $L\beta_1$. All spectra are corrected for self-absorption and normalised to the $L\beta_1$ peak maximum.

An anisotropy is observed between the two measurement geometries in the $L1$ emission, specifically between spectra (1) and (4) inclusive. Figure 8.14 separates these fluorescence spectra and shows them for a smaller energy range for closer examination. It is clear that there is a resonant trend in the peak position, and average spectral weight, of the $L\beta_1$ emission peak at 396.5 eV, as the excitation energy increases. It ranges between an energy minimum and maximum spanning 0.75 eV, which appear to be defined by the first two threshold (a) and (b) pre-peaks of the absorption. These are indicated by two lines drawn on each panel. This trend is a common feature of bandstructure dispersion as observed by RXES due to its crystal momentum selective nature. A prime example was shown by Carlisle *et al.* [17,213]† for graphite. The trend is mimicked for both measurement geometries but, as seen in Figure 8.13, there is a divergence between the spectra for the excitation at feature (1) and the four subsequent excitations, reconverging as the excitation approaches the ionisation continuum and is no longer **k**-selective.

In attempting to explain the dispersion of the features, it perhaps prudent to backtrack briefly at this point; de Groot and Kotani point out that in the case of transition metal (TM) $L_{2,3}$ absorption edges, the single particle approximation used to predict XAS spectral shape breaks down due to radial overlap of the excited core electron with the already partially filled valence $d$-shell in the final state, or state of RXES. The $L1$ RXES clearly begins as a $2p^6 3d^0 \rightarrow 2p^5 3d^1$ excitation in going from the initial to intermediate state, however the RXES is given by $2p^5 3d^1 \rightarrow 3s^1 3d^1$ [15], leaving a $3s$ hole in the final state. The $3s^1 3d^1$ final state means the single particle approximation breaks down for the same reason in described in $L_{2,3}$ XAS, making it less feasible to effectively describe the observed emission features in terms of the occupied $3s$ PDOS. Nevertheless, some of the features may be explained by the character of the excitation in the intermediate state, which in the threshold spectra more likely to select only a narrow range of crystal momentum.

So, at excitation (a) the very small peak of the intermediate state is clearly a $2p^5 3d^1$ state, but as the $d_{z^2}$ character bandstructure plot in Figure 8.11 clearly shows (at $\sim 3$ eV in the unoccupied states) it is a $2p^5 e_g(d_{z^2})$ intermediate state. Thus the $L1$ RXES is given by $2p^5 e_g(d_{z^2}) \rightarrow 3s^1 e_g(d_{z^2})$, i.e. the final state differs from the initial state in that there is a $3s$ hole and a $3d$ $e_g$ electron.

At excitation (b) the second very small peak of the intermediate $2p^5 3d^1$ state is, from the $d_{x^2-y^2}$ bandstructure character plot (at 4eV in the unoccupied states), most identifiable with a $2p^5$ $e_g$ $d_{x^2-y^2}$ intermediate state. Thus the L1 RXES is given by $2p^5 e_g(d_{x^2-y^2}) \rightarrow 3s^1 e_g(d_{x^2-y^2})$ and again the final state is $3s$ hole with a $3d$ $e_g$ electron.

The final state energies will be approximately at $-60$ eV as the binding energy of a $3s$ electron is $\sim 60$ eV. The character of the final state extra $3d$ electron will be that of the previously unoccupied CB states. Thus the first two spectra reflect for (a) – the $d_{z^2}$ $e_g$ orbital, and for (b) $d_{x^2-y^2}$ $e_g$ orbital. It is no coincidence that the difference in excitation energy between (a) and (b), $\sim 0.75$ eV, matches exactly that of the difference in their peak maxima. Any difference between them would have to gleaned by plotting them on a loss, or final state scale. This was done for both orientations (not shown), and no difference was

---

[†] The RXES Figure of graphite from these papers is reproduced in Figure 2.5 page 19

observed, an unsurprising result as although the $d_{z^2}$ $d_{x^2-y^2}$ in the unoccupied PDOS are not identical, they are nearly so. Any difference would be negligible within the experimental resolution and core hole broadening effects.

At excitation (1), the excitation energy is coincident with the very large and sharp $t_{2g}$ feature, dominated to a large degree by the $d_{xy}$ orbital but involving all $t_{2g}$ orbitals (again from consideration of the bandstructure plots). Thus the $L1$ RXES is given by $2p^5t_{2g} \rightarrow 3s^1t_{2g}$. The final state is now a $3s$ hole but with a $3d$ $t_{2g}$ electron. The $L1$ emission will be representative of the CB $t_{2g}$ orbital, which upon inspection in both orientations in Figure 8.14, is observed to be distinguishably different from that of (a) or (b) in both measurement geometries, exhibiting a broader width and possibly containing some unresolved structure as evidenced by the spectral shape difference between measurement geometries or dichroism.

For excitations (2) and (3) we return to final states of $e_g$ character, thus the spectra are expected to resemble again that of (a) and (b) which they do, reducing again in width and fine structure. However for excitation (2), we know that the $e_g$ orbitals contribute differently to the absorption in different geometries, as evidenced in Figure 8.9. The apparent dichroism in the $L1$ emission at excitation (2) suggests that this may also be evident here, where the states due to the "lobes" of the $d_{z^2}$ are emphasised in the $\mathbf{E}||c$;XES$||c$ due to dipole symmetry selection.

The $L\alpha_{1,2}$ and $L\beta_1$ RXES, as shown in the right panel in Figure 8.13, also displays a polarisation dependence. While the effective resolution is low, distinct differences are observed between the measurement geometries in spectra (a), (1), (3) and (V2). As stated, repeated measurements of the $L\alpha_{1,2}$ and $L\beta_1$ emission were taken with a higher resolution at the NSLS. These are graphed in Figure 8.15, and are normalised to the $L\alpha_{1,2}$ peaks. Comparing the spectra one can see the same dichroism apparent in excitations (1) and (3), though emphasised to a greater extent in the increased resolution. Since these measurements were acquired prior to the ALS data at a synchrotron of lower brightness, the (V2) excitation is not repeated.

$L\alpha_{1,2}$ and $L\beta_1$ RXES corresponds, in its simplest form, to a $2p^63d^0 \rightarrow 2p^53d^1$ excitation from ground state to intermediate state. Going from the intermediate to final state is a little more complex. Looking again at Figure 8.1 on page 171, the ground state of $TiO_2$ is the bonding state between the $(2p^6)3d^0$ and the $(2p^6)3d^1\underline{L}$ configurations, where the latter possesses a ligand hole. The $3d^1\underline{L}$ is represented as a box reflecting the range of possible $3d^1$ ligand hole energies for the $3d^1\underline{L}$. The wavefunction incorporating both of these characters will be either symmetric (bonding) or antisymmetric (antibonding), the bonding state being the "real" ground state and defining our starting position. The final state however may be varied due to this mixing, and the transitions to final states of $3d^1\underline{L}$ are responsible for

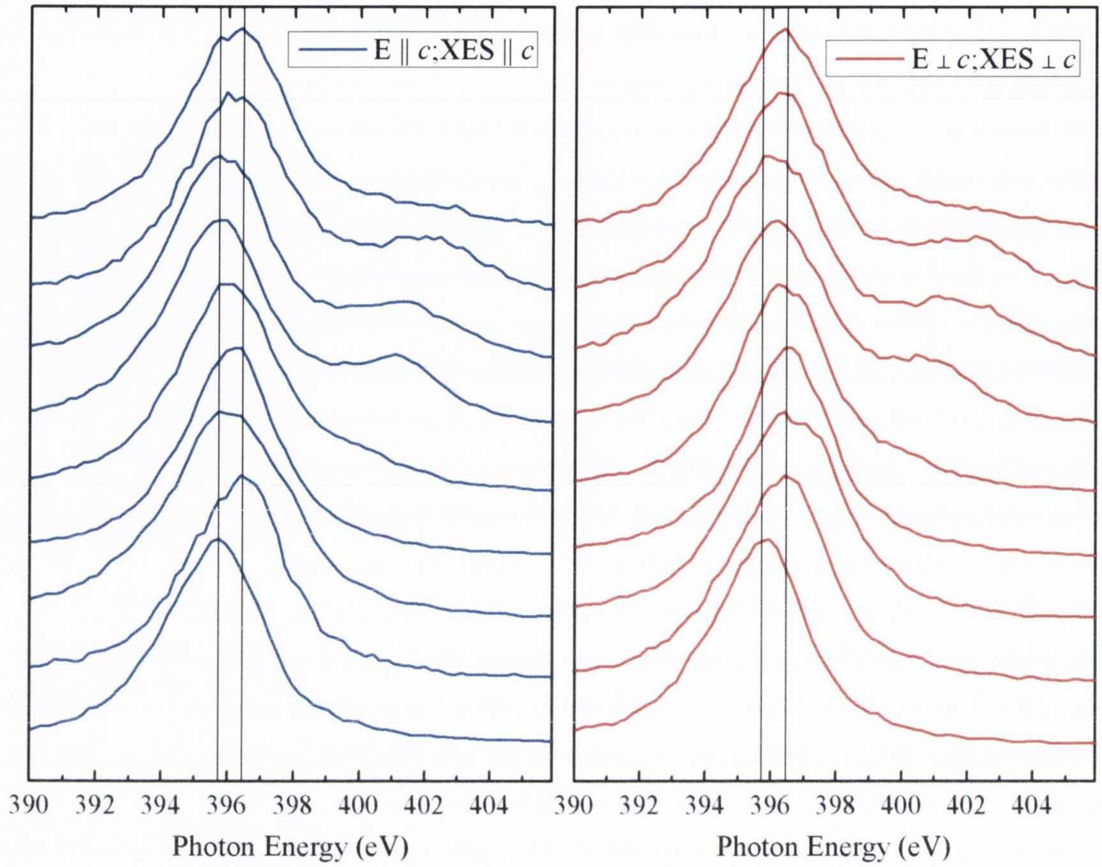

Figure 8.14: RXES of rutile TiO$_2$ for the $L1$ and $L\eta$ emission peaks, separated for the two measurement geometries. Lines show energy min and max of dispersion of the $L1$ peak.

RIXS loss (or Raman scattering) features whose energies range between -3 and -10 eV away from the excitation energy or elastic peak (zero loss). These features are studied in depth in the literature [177,186,191,192,205,206,214–216] and it is important to be aware of them during analysis.

There is a caveat to Figure 8.15 that requires mention. It is clear that some of the elastic peaks are not coincident between measurement geometries. Though the possibility of these not being true elastic features was entertained, a thorough inspection of the data revealed that, due to monochromator drift at X1B, some small error arose while attempting to repeat energy measurements in differing scattering geometries. After calibration of both monochromator and emission spectrometer, the designated elastic peaks were all found to match their corresponding excitation energy and are thus considered true elastic features. The small error occurred in the case of spectrum (a,b) and (2), and to a lesser extent in spectra (3) and (5). That some elastic peaks do line up is because not all of the spectra were acquired contiguously but rather over a number of shifts. Some of the observed dichroism, such as in spectrum (a,b), must therefore be attributed to this.

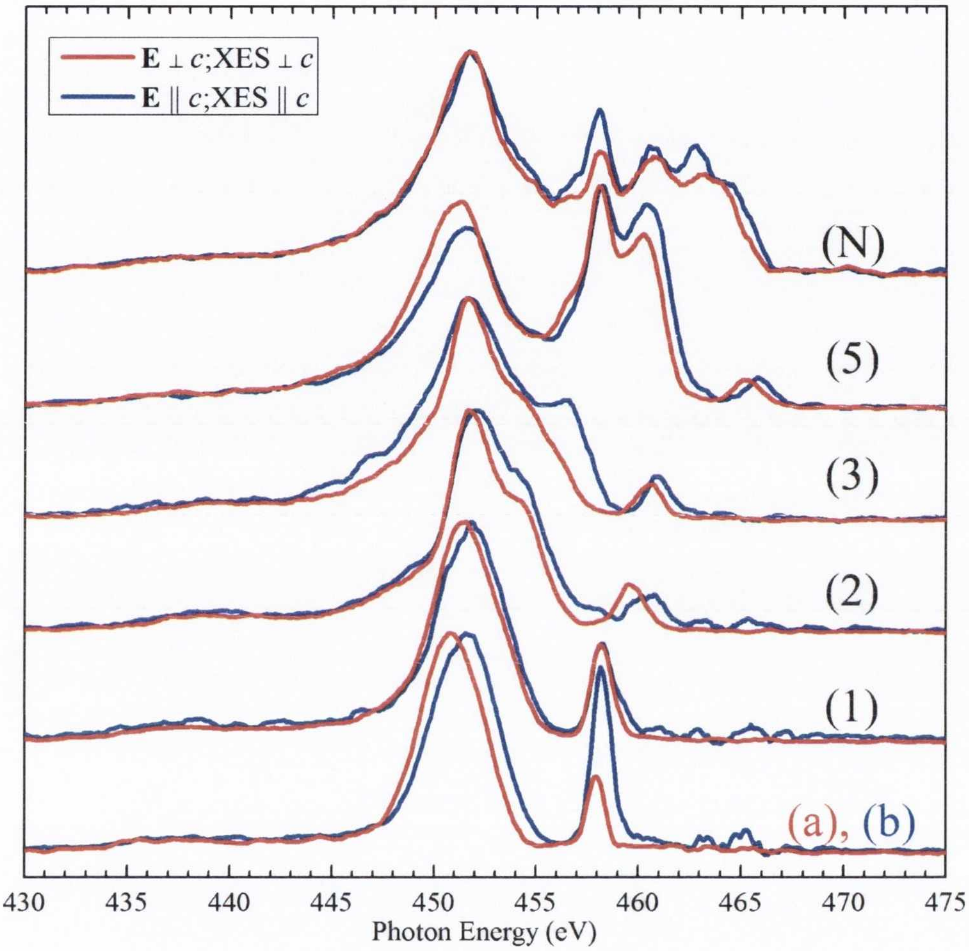

Figure 8.15: $L\alpha_{1,2}$ and $L\beta_1$ RXES for rutile TiO$_2$ for two in-plane scattering geometries, $\mathbf{E}\|c$;XES$\|c$ and $\mathbf{E}\perp c$;XES$\perp c$, recorded at the NSLS. Low signal to noise required a 9-point adjacent averaging. All spectra are corrected for self-absorption.

We now focus on the dichroism observed in (3), resulting from excitation into the $e_g$ derived states of $\sigma$, or $t_{2g}$ orbitals involved in Ti–O $\pi$ overlap. At the $K$-edge the linear structure of the orbital lobes prohibits emission propagating parallel to the axis of that lobe. Thus for $\mathbf{E}\|c$ excitation absorption into primarily $e_g$ states, intensity will favour a transition intensity for $d_{x2-y2}$:$d_{z2}$ with a ratio of 3:1. The $\mathbf{E}\perp c$ geometry on the other hand also favours a mixture of $d_{x2-y2}$ and $d_{z2}$, this time in a 3:5 intensity ratio.[†] The origin of these intensities and hence ratios is explained earlier in this chapter in section 8.4.1.

The measured radiative decay from these orbitals is then governed by the spectrometer's orientation with respect to the crystal. $e_g$ excitation with XES$\|c$ will favour $t_{2g}$ de-excitation from the $d_{z(y-x)}$ orbital as it lies in the (001) plane. For XES$\perp c$ the $t_{2g}$ will consist instead of $(d_{z(y+x)} + d_{xy})/2$. The strong shift of spectral weight of the $\mathbf{E}\|c$;XES$\|c$ (blue) spectrum (3) in Figure 8.15 (and to some degree in Figure 8.13) toward the VB is thus attributed not to $L\beta_1$ emission, but could instead be due to $d_{z(x-y)}$ states in the $L\alpha_{1,2}$ emission. The increase in spectral weight toward the bottom of the $L\alpha_{1,2}$ valence band in this spectrum could be attributed to $d_{z^2}$ states, preferentially excited into and recorded in this geometry. The $d_z$ states can be seen occupying the bottom of the VB in Figure 8.16.

---

[†] Intensity for $d_{z^2}$ in $\mathbf{E}\perp c$ is $\frac{4/15+1/15}{2}$, for $d_{x2-y2}$ it is $\frac{3/15}{2}$

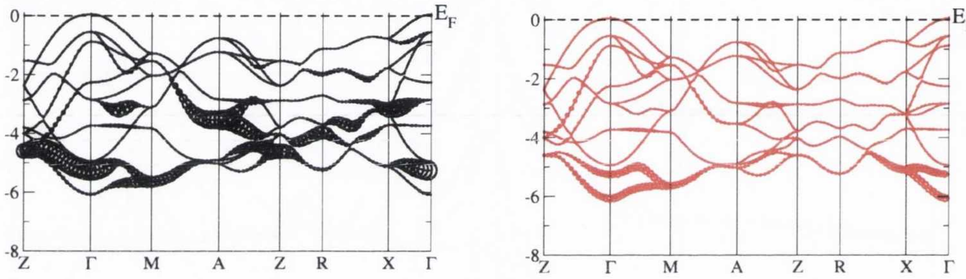

(a) Rutile TiO$_2$ VB $d_{z^2}$ (b) Rutile TiO$_2$ VB $d_{x^2-y^2}$

Figure 8.16: Electronic bandstructure character plots of rutile TiO$_2$ emphasising **(a)** the Ti $3d_{z^2}$ and **(b)** the Ti $3d_{z^2}$ weighted character of the bands in the VB. The comparatively reduced Ti $3d$ occupied PDOS required the weightings in the VB be amplified when compared to other bandstructure character plots presented in this thesis.

Spectrum (1) shows a similar increase of spectral weight towards the bottom of the valence band in the $\mathbf{E}\|c$;XES$\|c$ (blue) geometry in Figure 8.13 (though Figure 8.15 failed to show substantial evidence of this feature). This excitation corresponds primarily to the $t_{2g}$ peak, where $\mathbf{E}\|c$ preferentially allows excitation.

#### 8.7.2.2 Anatase RXES

Figure 8.17 gives a waterfall representation of the RXES spectra resulting from resonant excitations at the Ti $L$-edge for the anatase polymorph of TiO$_2$. Like the previous subsection presenting the rutile RXES, labels refer to the absorption feature corresponding to the excitation energy, which are given in Figure 8.9.

Like the rutile Ti $L1/L\eta$ emission shown in Figure 8.14, the left panel of Figure 8.17 follows a similar band dispersion RXES evolution. Though a subtle divergence is noted for the (V1) and peak position of (2), overall the $L1$ emission does not have the same degree of apparent dispersion as it does in the rutile, nor does it exhibit any notable dichroism between the two measured scattering geometries. There does however appear to be a structural dissimilarity in spectra (4) in the region straddling the $L1$ and $L\eta$ peaks, though it is

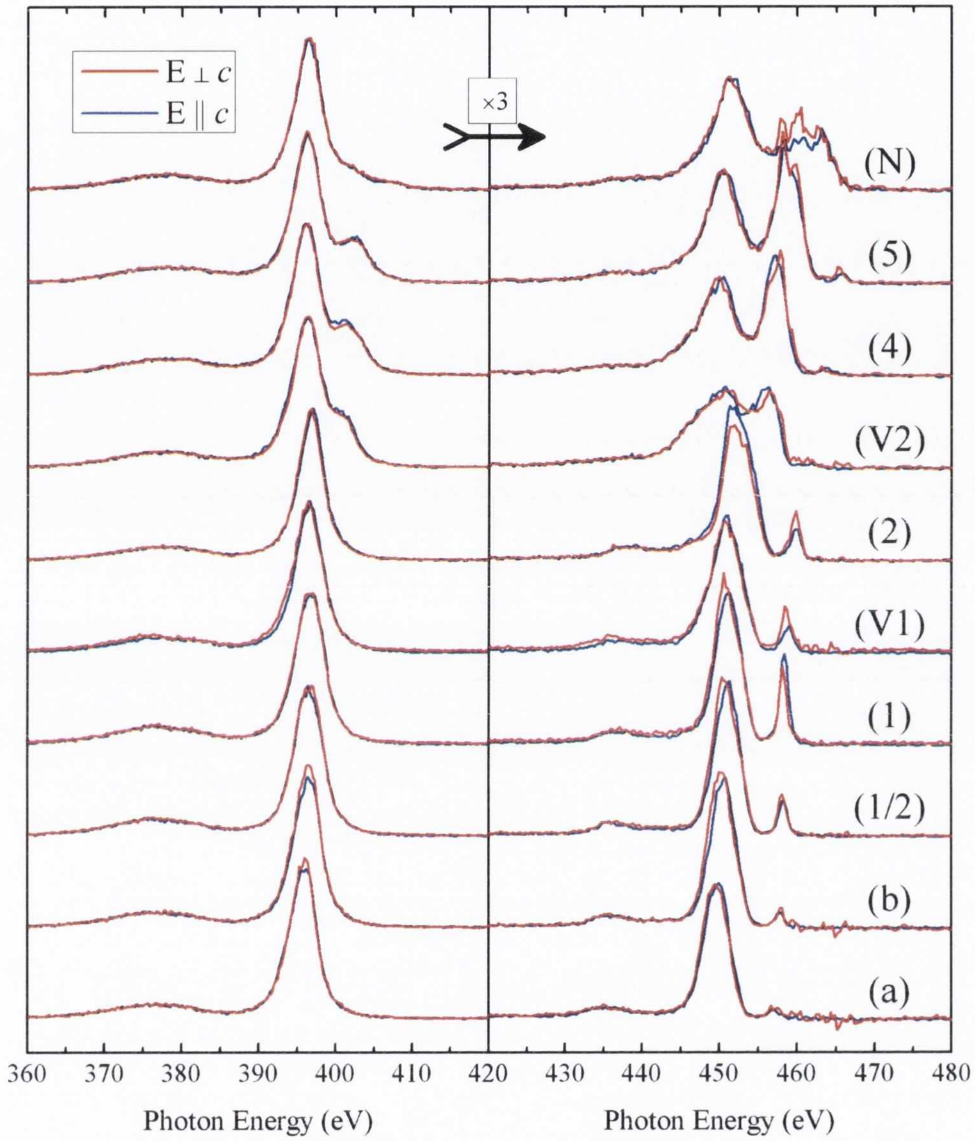

Figure 8.17: RXES of the Ti $L_{2,3}$-edges for anatase Ti$O_2$ for two in-plane scattering geometries, $\mathbf{E}\|c$;XES$\|c$ and $\mathbf{E}\perp c$;XES$\perp c$, recorded at the ALS. The left panel shows the $L1$ and $L\eta$ emission, while the right panel shows the comparably amplified $L\alpha_{1,2}$ and $L\beta_1$. All spectra are corrected for self-absorption and normalised to the $L\beta_1$ peak maximum.

unclear to which it belongs and there is not enough information to draw any conclusion here.

The anatase Ti $L\alpha_{1,2}$ and $L\beta_1$ RXES does not appear to exhibit much dichroism on first glance of Figure 8.17. However, the spectra that showed most dichroism in rutile, that of (3), was not (successfully) recorded for both measurement geometries during this beamtime and is not present. It was however recorded for the higher resolution NSLS run and is presented in Figure 8.18.

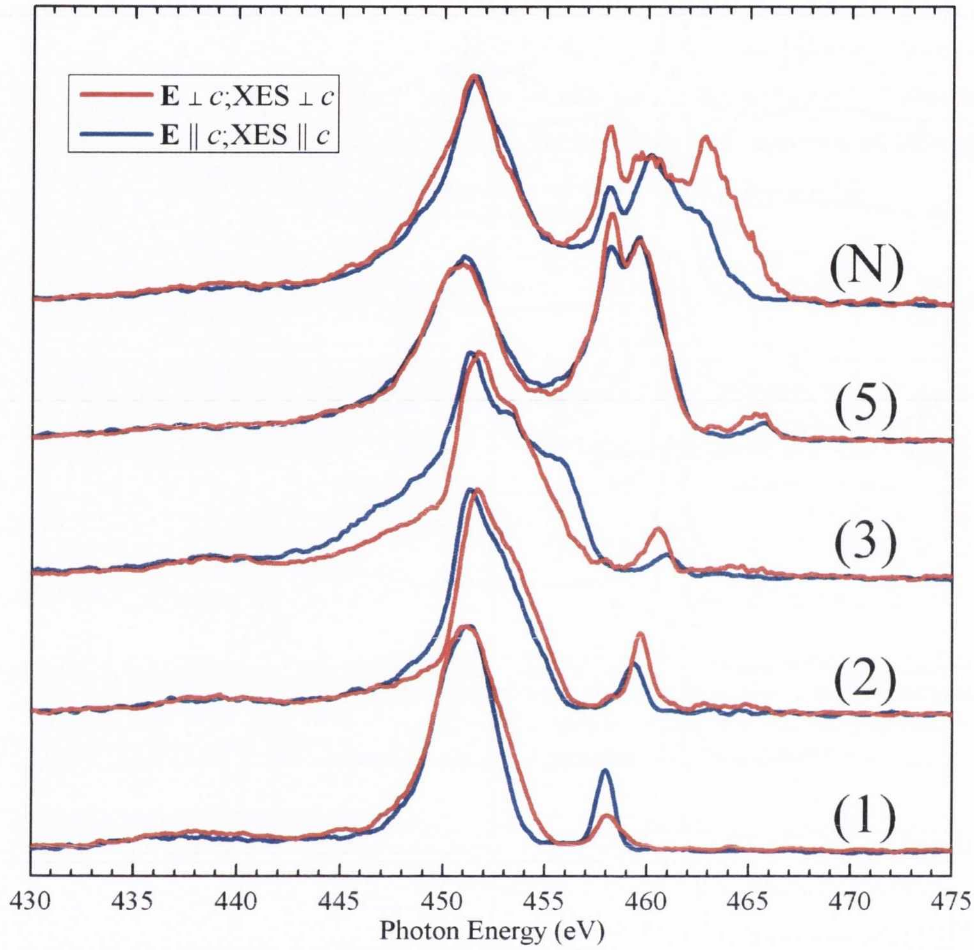

Figure 8.18: $L\alpha_{1,2}$ and $L\beta_1$ RXES for anatase TiO$_2$ for two in-plane scattering geometries, $\mathbf{E}\|c$;XES$\|c$ and $\mathbf{E}\perp c$;XES$\perp c$, recorded at the NSLS. Low signal to noise required a 9-point adjacent averaging. All spectra barring (1) are corrected for self-absorption.

Here the spectra excited at feature (3) show a surprisingly similar anisotropy to the rutile spectra excited in the analogous region. Again there is increase in spectral weight both at the top and bottom of the $L\alpha_{1,2}$ emission spectrum in the $\mathbf{E}\|c$;XES$\|c$ measurement geometry. Due to the effective swapping in position of the energy of the individual $e_g$ states in the conduction band, as seen by both the shape and polarisation dependence in absorption, it is logical to surmise that an analogous switching occurs in the valence band for the same reasons as stated in section 8.7.1.

By examining the structure of anatase (Figure 8.3) it is noted that in comparison with the rutile structure, the local octahedral coordinate axis of the cation in anatase is rotated by 90°, such that the apical bonds now lie along the [001] direction as opposed to in the

(001) plane. Thus resonant excitation into the $e_g$ derived feature (3) in the $\mathbf{E}\|c$ geometry now preferentially excites into the $d_{z^2}$ $e_g$ unoccupied states, and $\mathbf{E}\perp c$ into the $d_{x^2-y^2}$ $e_g$ states unoccupied states, the opposite of rutile. Emission measured with XES$\|c$ will be similarly switched for the two orientations. Thus the difference, or extra spectral weight at the top of the valence band of the $\mathbf{E}\|c$;XES$\|c$ (blue) $L\alpha_{1,2}$ spectrum (3) is now attributed to the $d_{\|}$ occupied states. Careful examination of the structure and positioning of these orbitals with respect to the $Ti_3O$ trigonal planes (Figure 8.3) strongly implies that these $d_{\|}$ orbitals will partially hybridise in a $\pi$-type manner with the O $2p_y$ orbital, which lies normal to said planes and whose occupied states are in the region of the VB max. The structure also implies a strong Ti–Ti overlap of the $d_{\|}$ orbitals with each other. This, along with the tightly bound O $2p_x$-hybridised Ti $3d_{x^2-y^2}$ occupied states, explains the observed shift of spectral weight towards the bottom of the valence band in the $\mathbf{E}\|c$;XES$\|c$ spectra (2) and (3). The calculated anatase PDOS in appendix A.10 supports these assertions, showing that the $d_{\|}$ states are essentially split between the top and bottom of the VB, as well as the tightly bound $d_{x^2-y^2}$ states.

## 8.8 Summary and Conclusions

$TiO_2$ is considered a technologically important compound, used throughout a range of technologies. This includes very promising applications in memristive technologies which offers the possibility of a leap beyond Moore's Law predictions.

Here, two polymorphs of $TiO_2$, rutile and anatase, were probed at the Ti $L$-edge via X-ray absorption and X-ray emission spectroscopy with the goal of probing the polarisation dependence of these compounds. The overlapping $L$-edges required a self absorption correction factor to be applied before analysis could take place.

This is the first report of polarisation dependent XAS and RXES of anatase $TiO_2$ at the Ti $L$-edge, and the first in-plane polarisation dependent report of rutile $TiO_2$. Previous work [91,177] on rutile $TiO_2$ focused on the "depolarised" versus "polarised" dependence, where the polarisation vector $\mathbf{E}$ was varied in and out of the plane of scattering, while the orientation of the crystal was given little emphasis. Here all RXES measurements were carried out in-plane and only the relative orientation of the crystal was varied.

Natural linear dichroism was observed in both polymorphs for using XAS and RXES. Analogous features and dichroism were observed in both the conduction and valence bands between the two compounds. Significant contrast in features in both the valence and conduction bands was observed for excitation into the $L_3$ $e_g$ feature, and thus this region comprised the bulk of the discussion. Careful examination of the structure and resultant molecular orbital effects, and subsequent comparison with electronic structure DFT calculations allowed interpretation of the resultant resonant anisotropic features, independently for both compounds.

# 9 Conclusions

The purpose of this concluding chapter is fourfold; (*i*) to reiterate the overall stated goal of this project, and evaluate the outcome (*ii*) to further consolidate the already shared theme of the individual chapters, summarising the knowledge obtained in each, (*iii*) to draw more general comparative conclusions and hypotheses, and finally (*iv*) to address continuing and possible future related work.

The rutile-type structure is the simplest and most common of $MA_2$ transition metal compounds and, given the variety of properties and applications this class of compounds possesses, can be considered the most important structural class of $MA_2$ compounds. From the experimental results presented in this thesis, as well as the supporting calculated electronic DOS, it has been shown here that the rhetorical question proposed in the introduction section of this thesis has indeed been fruitful. That is, using the symmetry and state selective characteristics of polarisation dependent, element-selective X-ray spectroscopic techniques, which had not been previously applied to tetragonal binary systems that exhibit natural linear dichroism, we have gained a new insight into and extended our principal understanding of both the electronic structure of, and bonding within the rutile-type class of crystal structures.

In this thesis, especially in comparing the calculated, axes-projected PDOS along chosen planes and directions, polarisation dependent XAS and RXES were demonstrated as extremely powerful tools for investigating the anisotropy in the chemical bonding and electronic structure in this class of compounds. The natural linear dichroism observed strongly implies that adoption of this structure is accompanied with striking a balance between the ionic transfer of electrons to the ligand ions, the covalent $\sigma$- and $\pi$-like interactions between the metal and ligand orbitals, as well as the metal-metal bonding. As with any systematic scientific investigation, some results were more scientifically satisfactory than others, fitting theory well. Where dichroism was not observed, explanations attributing its lack were postulated, whether down to the inherent nature of the compound, or due to experimental factors. Though the focus of this investigation has been on O $K$-edge measurements, the polarisation dependent F $K$-edge and metal $L$-edge measurements pushed the boundaries, rounding it off as a thorough exploration of the value of this approach, as well as a significantly more complete analysis into the bonding and electronic structure in this class of compounds.

The introductory results presented in this work include the O $K$-edge measurements of $IrO_2$. Like $TiO_2$ and $SnO_2$ reported by Kennedy [5], it represents an archetypal rutile compound, showing a distinctly anisotropic chemical bonding, particularly of the anion, and an interesting electronic structure with a strong energy separation of its $\pi$ ($\pi^*$) and $\sigma$ ($\sigma^*$) component states. This made it an ideal compound to be studied by polarisation dependent RXES. A marked polarisation dependence was observed in absorption and all emission, and a strong $\Omega$ (incident photon energy) dependence in resonant emission. Owing in no small part to the high quality spectra obtained from BL8 at the ALS, it was possible to entirely decouple the orthogonal components of the $IrO_2$ O $2p$ PDOS, the DFT calculated versions of which compared excellently.

Presented alongside the $IrO_2$ in Chapter 4 are results from another tetragonal rutile compound, $MnO_2$. This antiferromagnetic compound nominally possesses a $d^3$ metal compound, and is thus subject to exchange splitting. This splitting of the Mn valence spin$\uparrow$ and spin$\uparrow$ states results in an energy overlap between some nominally $t_{2g}$ and $e_g$ states when sampling for both spins, whereas these states would normally be distinct if split only by the crystal field. Though this relates to the metal valence states, the oxygen states are strongly hybridised with these in the CB, this meant that significantly biased state selection could not be achieved for the intermediate state of RXES, and thus a strongly reduced dichroism was observed. However, that which was observed appeared to conform to trends whose origin were postulated by the author. Planar projected DFT PDOS calculations are recommended to enlighten or support these assertions in the case of $MnO_2$.

The next chapter presented the F $K$-edge results from $MgF_2$ and $MnF_2$, both of pure rutile-tetragonal structure. The lack of valence $d$-orbitals in magnesium and hence in $MgF_2$ makes it an atypical compound in this study. Nevertheless, natural linear dichroism was manifest in the F $K$-edge due to the $sp^2$ environment in the rutile structure, where a small covalent interaction was still evident. From the calculations some hybridisation was apparent in the CB with the Mg $s$ and $p$ states. Simulated XAS matched the features, if not overall shape, of the experiment and a strong correlation was observed especially for the predicted dichroism. The resonant emission displayed consistent natural linear dichroism, and the NXES in both geometries conformed extremely well with the predicted shape and differences of the simulated spectra. This strong comparison allowed for difference spectra to be extracted that, like with the $IrO_2$, experimentally decoupled the orthogonal components of the F $2p$ occupied PDOS. Though the $MnF_2$ did not show notable dichroism in emission, the XAS did, and matched very well with the simulated axis-projected F $2p$ PDOS of the CB. While $\Omega$-dependence was observed and discussed for $MnF_2$, the reason for the disparity of calculated anisotropy with experiment remains unclear. Thus for $MnF_2$, repeated polarisation dependent NXES is suggested to rule out experimental errors and, assuming they are ruled out, further investigation into the VB DOS is advised.

$WO_2$ and $MoO_2$ constitute the primary distorted rutile (monoclinic) structures investigated in this thesis. They are both $d^2$, isostructural metallic conductors. The polarisation dependent O $K$-edge XAS and RXES were thus expected to be very similar, and were demonstrably so. The interest in these materials is derived from their structural similarity to the monoclinic phase of $VO_2$, and thus may provide clues or insights to the latter's electronic structure and its MIT. Spectroscopically the main feature of note in these compounds comes from the splitting of the $t_{2g}$ $d$ bands and their resultant oxygen hybridisation, which is observed in the XAS only for the $\mathbf{E}\|a$ orientation approximately 3 eV above the Fermi energy threshold for both compounds. Interestingly it is concurrent excitation at this energy that produces the most striking RXES dichroism, attributed to the strong site-selectivity and in the RXES state selection. While overall the $WO_2$ PDOS calculations for both the VB and CB compared very well with experiment, predicting the majority of dichroism, some small disparity exists. That the $MoO_2$[†] exhibits a compellingly similar pattern to the $WO_2$ experimental results implies a minor correction of the calculated conditions may be useful in authenticating the asserted interpretation.

Polarisation dependent resonant absorption and emission spectroscopy at the O $K$-edge was then presented for the two phases of bulk $VO_2$, by recording on either side of its MIT transition temperature (340 K), where the high temperature phase is rutile and metallic and the low temperature phase is monoclinic and semiconducting. As previously shown in the literature, natural linear dichroism was observed in XAS. However the previously reported feature in the monoclinic phase attributed to the $d_{\|}$ split $t_{2g}$ hybridised states, like that seen in $WO_2$ and $MoO_2$, was not definitively exhibited in our measurements. Though several experimental difficulties were encountered over numerous measurements, eventually a sufficiently complete RXES dataset was acquired. The dichroism and resonant evolution of emission spectra observed, as well as the differences between the two phases were discussed within a MO based approach. In spite of the extensive research already conducted into the electronic structure of this compound, the original knowledge acquired from the results may well play a contributing role in the goal of understanding the as yet controversial transition.

---

[†] For which no supporting calculations were produced, rather relying on previously published non-polarisation specialised calculations.

Some further time and analysis would be required to consolidate our interpretation of the $VO_2$ results in light of the earlier results in both $MoO_2$ and $WO_2$.

In the final results chapter XAS and RXES were performed on rutile and anatase $TiO_2$. In these experiments, the investigation into bonding was this time approached from the perspective of the metal cation, exploring the suspected possibility of a polarisation dependence in RXES at the metal $L$-edges. Self-absorption effects were compensated for post-acquisition, though this process reduced the signal-to-noise ratio of the $L_\beta$ features. XAS for both compounds revealed distinctive linear anisotropy in the $L_3$ $e_g$ states for both compounds, which for anatase appears to be the first report.

Resonant excitation at the energies coincident with this CB feature revealed an unambiguous dichroism in the RXES/RIXS that was analogous for both compounds. While RXES of anatase $TiO_2$ has been reported [214], this is the first reported polarisation dependent study, and the first account of in-plane natural linear dichroism in rutile $TiO_2$. Further, a dichroism was observed in the $L$-edge emission of rutile $TiO_2$. The discussion of the features was treated with reference to the DFT calculated PDOS and bandstructure, as well as in the light of atomic multiplet theory, albeit without supporting calculations. Although a band-like interpretation of Ti $L$-edge RXES has previously been reported [215], exploiting the dichroism inherent in a tetragonally distorted $TiO_6$ octahedron can give further insight into chemical bonding, even in the absence of detailed atomic multiplet calculations. In terms of natural linear dichroism this required a carefully altered approach to that of $K$-edge $1s-2p$, due to the nature of the largely atomic like $\langle 2p|3d\rangle$ overlap integrals and atomic multiplet interactions dominating the $2p-3d$ XAS, RXES and $2p-3s$ RXES. Nevertheless, a further insight into the contrast in chemical bonding between anatase and rutile is achieved.

Though there exist numerous other rutile-like compounds, this element-, symmetry- and state-selective, polarisation dependent study of the rutile class may be considered a comprehensive investigation, as it spans both metallic and insulating samples, distorted rutile compounds, and encompasses RXES from both the anion and the cation. Despite experimental hiccups expected in any boundary-pushing investigation, the project went beyond its initial targeted goals. The groundwork set by this project has paved the way for continuing work with this technique in the group here in Dublin. New experiments will be applied to defective $TiO_2$, as used in memristors. The ambition will be to probe the local defective electronic structure due to anion (oxygen) vacancies and cation (or $Ti^{3+}$) interstitials, and polarisation-dependent state-selective RXES and RIXS at both the anion and cation edges, exploiting any natural linear linear dichroism, will be a significant part of this new project.

In terms of the resonant X-ray emission spectroscopy technique, the next obvious step toward further exploring the electronic bandstructure of compounds such as those studied in this thesis, is to increase resolution of the spectra. There is a physical limit to the resolution it is possible to obtain, as determined by the uncertainty principal. However, instrumental broadening is still currently the largest obstacle in the path to detailed interpretation of the spectra. For high-resolution to be practical requires that the countrate be at least maintained if not improved, so that the time it takes to acquire spectra is not unreasonably increased, or the spectra statistics and signal-to-noise ratio is not compromised. Fourth-generation synchrotron facilites such as the NSLS-II at Brookhaven NY and MAX-IV in Lund Sweden, both under construction at the time of writing, will provide necessary brightness for this holy-grail of high resolution RXES. The other factor is creating a suitable beamline and spectrometer to record at such a high-resolution. The slit-grating emission spectrometer design in particular requires some engineering in order to accomplish this. One example of which is the 7 m long SAXES spectrometer of the ADRESS beamline at the Swiss Light Source, capable of high resolution RXES/RIXS, boasting a possible resolution of $\Delta 90$ meV for 1 keV photons. A similar spectrometer is planned for a soft X-ray emission beamline at the NSLS-II, and will be greater than 10 m in length. It is hoped that these next generation synchrotrons and high-resolution soft X-ray spectrometers will shed new light upon questions currently unanswerable with current achievable resolutions.

# A Appendix

## A.1 Excitation Nomenclature

| Level | Electron configuration | Level | Electron configuration | Level | Electron configuration |
|---|---|---|---|---|---|
| K | $1s^{-1}$ | $N_1$ | $4s^{-1}$ | $O_1$ | $5s^{-1}$ |
| $L_1$ | $2s^{-1}$ | $N_2$ | $4p_{\_}^{-1}$ | $O_2$ | $5p_{\_}^{-1}$ |
| $L_2$ | $2p_{\_}^{-1}$ | $N_3$ | $4p_{3/2}^{-1}$ | $O_3$ | $5p_{3/2}^{-1}$ |
| $L_3$ | $2p_{3/2}^{-1}$ | $N_4$ | $4d_{3/2}^{-1}$ | $O_4$ | $5d_{3/2}^{-1}$ |
| $M_1$ | $3s^{-1}$ | $N_5$ | $4d_{5/2}^{-1}$ | $O_5$ | $5d_{5/2}^{-1}$ |
| $M_2$ | $3p_{\_}^{-1}$ | $N_6$ | $4f_{5/2}^{-1}$ | $O_6$ | $5f_{5/2}^{-1}$ |
| $M_3$ | $3p_{3/2}^{-1}$ | $N_7$ | $4f_{7/2}^{-1}$ | $O_7$ | $5f_{7/2}^{-1}$ |
| $M_4$ | $3d_{3/2}^{-1}$ | | | | |
| $M_5$ | $3d_{5/2}^{-1}$ | | | | |

Figure A.1: Spectroscopic notation correspondence with electron configuration for shell excitations.

## A.2 Emission Nomenclature

| Siegbahn | IUPAC | Siegbahn | IUPAC | Siegbahn | IUPAC | Siegbahn | IUPAC |
|---|---|---|---|---|---|---|---|
| $K\alpha_1$ | $K$-$L_3$ | $L\alpha_1$ | $L_3$-$M_5$ | $L\gamma_1$ | $L_2$-$N_4$ | $M\alpha_1$ | $M_5$-$N_7$ |
| $K\alpha_2$ | $K$-$L_2$ | $L\alpha_2$ | $L_3$-$M_4$ | $L\gamma_2$ | $L_1$-$N_2$ | $M\alpha_2$ | $M_5$-$N_6$ |
| $K\beta_1$ | $K$-$M_3$ | $L\beta_1$ | $L_2$-$M_4$ | $L\gamma_3$ | $L_1$-$N_3$ | $M\beta$ | $M_4$-$N_6$ |
| $K\beta_2^{I}$ | $K$-$N_3$ | $L\beta_2$ | $L_3$-$N_5$ | $L\gamma_4$ | $L_1$-$O_3$ | $M\gamma$ | $M_3$-$N_5$ |
| $K\beta_2^{II}$ | $K$-$N_2$ | $L\beta_3$ | $L_1$-$M_3$ | $L\gamma'_4$ | $L_1$-$O_2$ | $M\zeta$ | $M_{4,5}$-$N_{2,3}$ |
| $K\beta_3$ | $K$-$M_2$ | $L\beta_4$ | $L_1$-$M_2$ | $L\gamma_5$ | $L_2$-$N_1$ | | |
| $K\beta_4^{I}$ | $K$-$M_2$ | $L\beta_5$ | $L_3$-$O_{4,5}$ | $L\gamma_6$ | $L_2$-$O_4$ | | |
| $K\beta_4^{II}$ | $K$-$N_5$ | $L\beta_6$ | $L_3$-$N_1$ | $L\gamma_8$ | $L_2$-$O_1$ | | |
| $K\beta_{4x}$ | $K$-$N_4$ | $L\beta_7$ | $L_3$-$O_1$ | $L\gamma'_8$ | $L_2$-$N_{6(7)}$ | | |
| $K\beta_5^{I}$ | $K$-$M_5$ | $L\beta'_7$ | $L_3$-$N_{6,7}$ | $L\eta$ | $L_2$-$M_1$ | | |
| $K\beta_5^{II}$ | $K$-$M_4$ | $L\beta_9$ | $L_1$-$M_5$ | $Ll$ | $L_3$-$M_1$ | | |
| | | $L\beta_{10}$ | $L_1$-$M_4$ | $Ls$ | $L_3$-$M_3$ | | |
| | | $L\beta_{15}$ | $L_3$-$N_4$ | $Lt$ | $L_3$-$M_2$ | | |
| | | $L\beta_{17}$ | $L_2$-$M_3$ | $Lu$ | $L_3$-$N_{6,7}$ | | |
| | | | | $Lv$ | $L_2$-$N_{6(7)}$ | | |

Figure A.2: Correspondence between the Siegbahn and the more intuitive systematic IUPAC notations describing electronic transitions and thus X-ray emission lines.

## A.3 $VO_2$ RXES, O $K$ Peak Normalisation

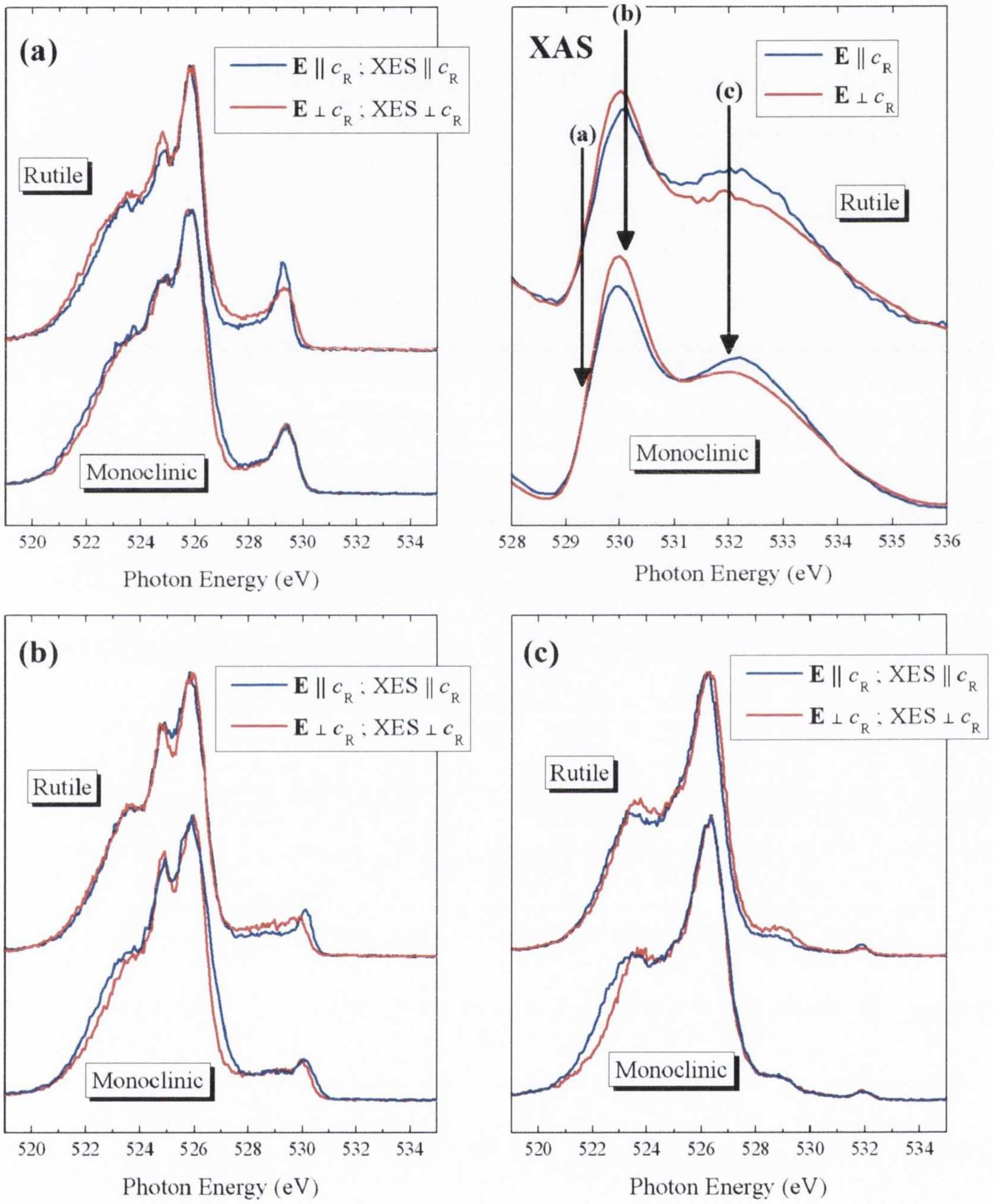

Figure A.3: Duplicate of Figure 7.6 page 158, with normalisation to O $K$-edge peak maxima, as consistent with the majority of RXES spectra presented in this thesis.

## A.4 $VO_2$ RXES, Contaminated

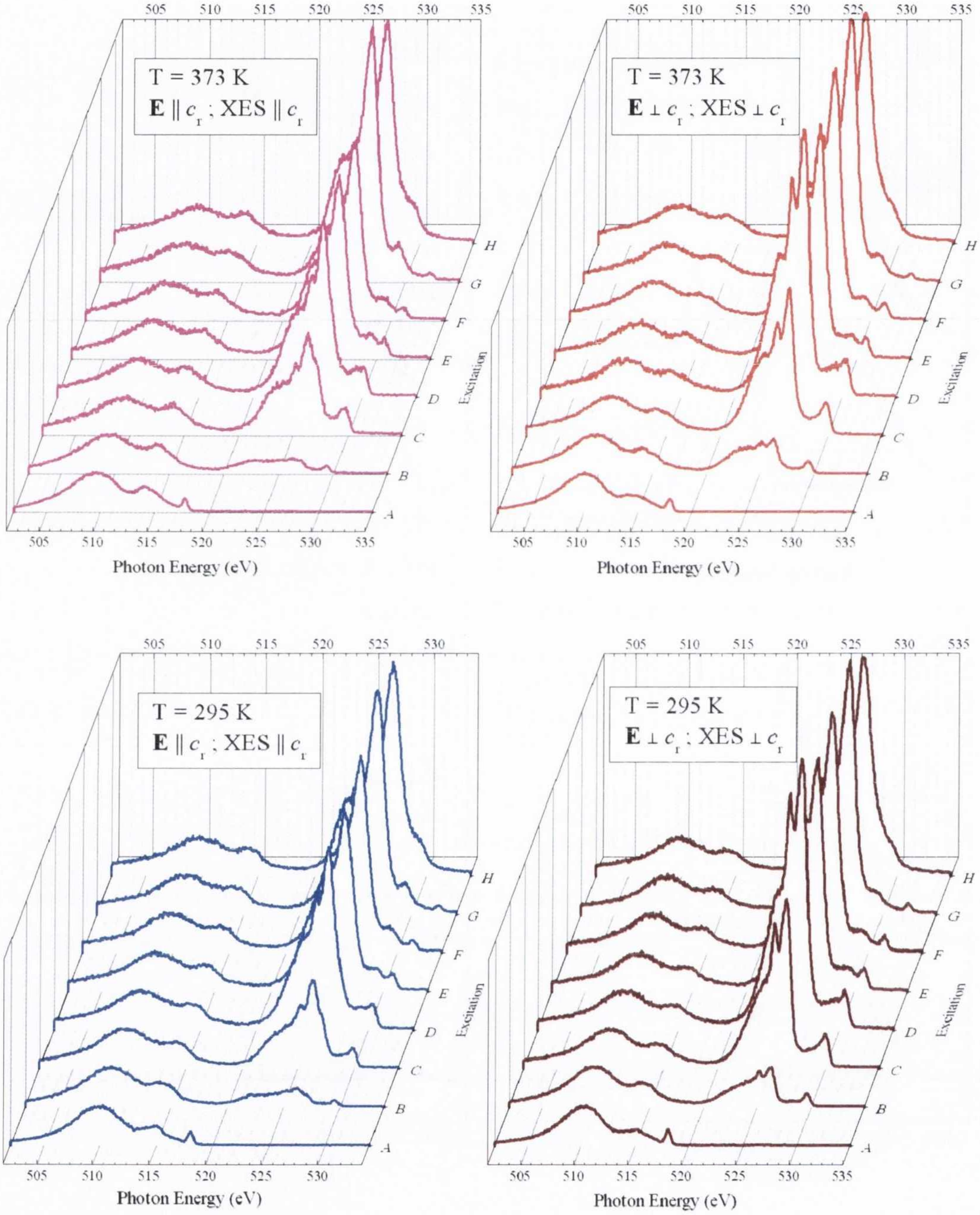

Figure A.4: O $K$-edge polarisation dependent RXES of $VO_2$ in both its metallic-rutile and monoclinic-semiconducting phases. $\mathbf{E}\|c$;XES$\|c$ measurement geometry sample contaminated by suspected $V_2O_3$ reduction.

## A.5 WO$_2$ O1 Weighted Bandstructures

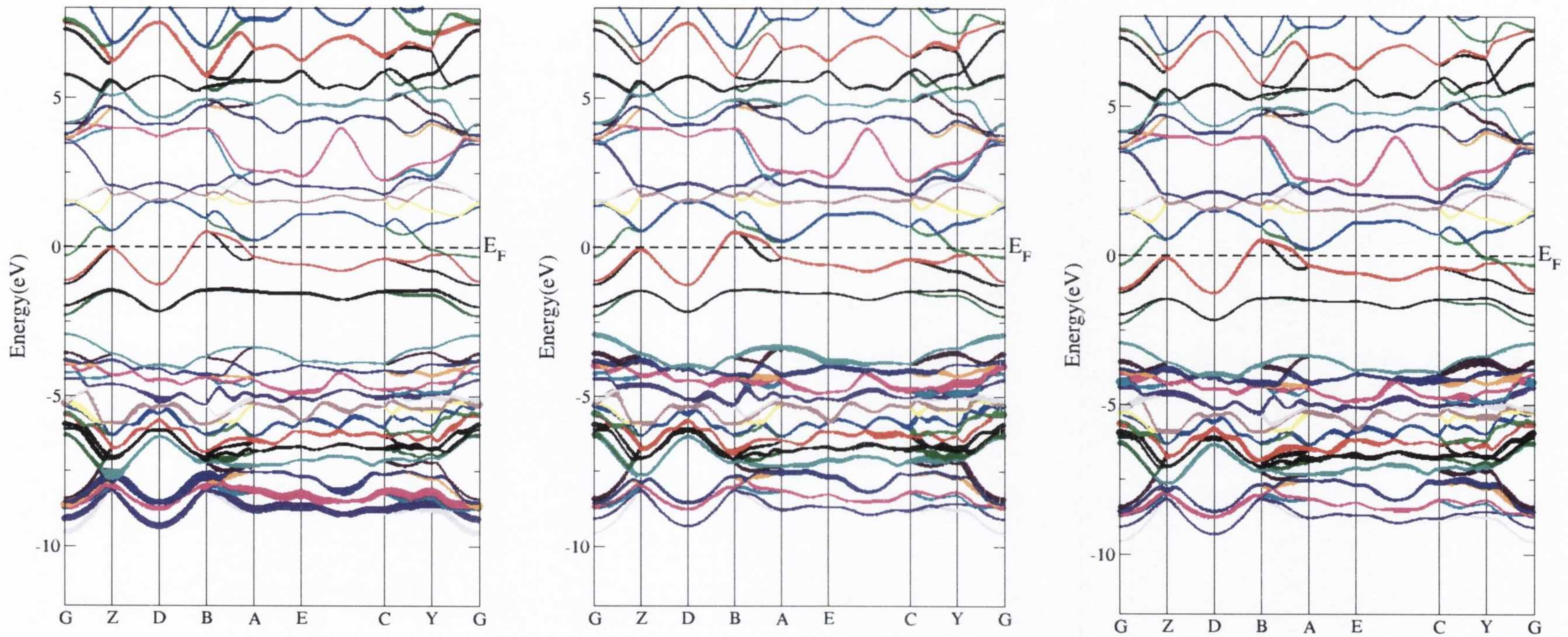

(a) O1 $2p_x$ (b) O1 $2p_y$ (c) O1 $2p_z$

Figure A.5: Bandstructure character plots of the O1 site for monoclinic WO$_2$ calculated by the DFT method through WIEN2K. The weightings represent PDOS for the **(a)** $2p_x$, **(b)** $2p_y$ and **(c)** $2p_z$ states on the O1 atomic site.

## A.6 $WO_2$ O2 Weighted Bandstructures

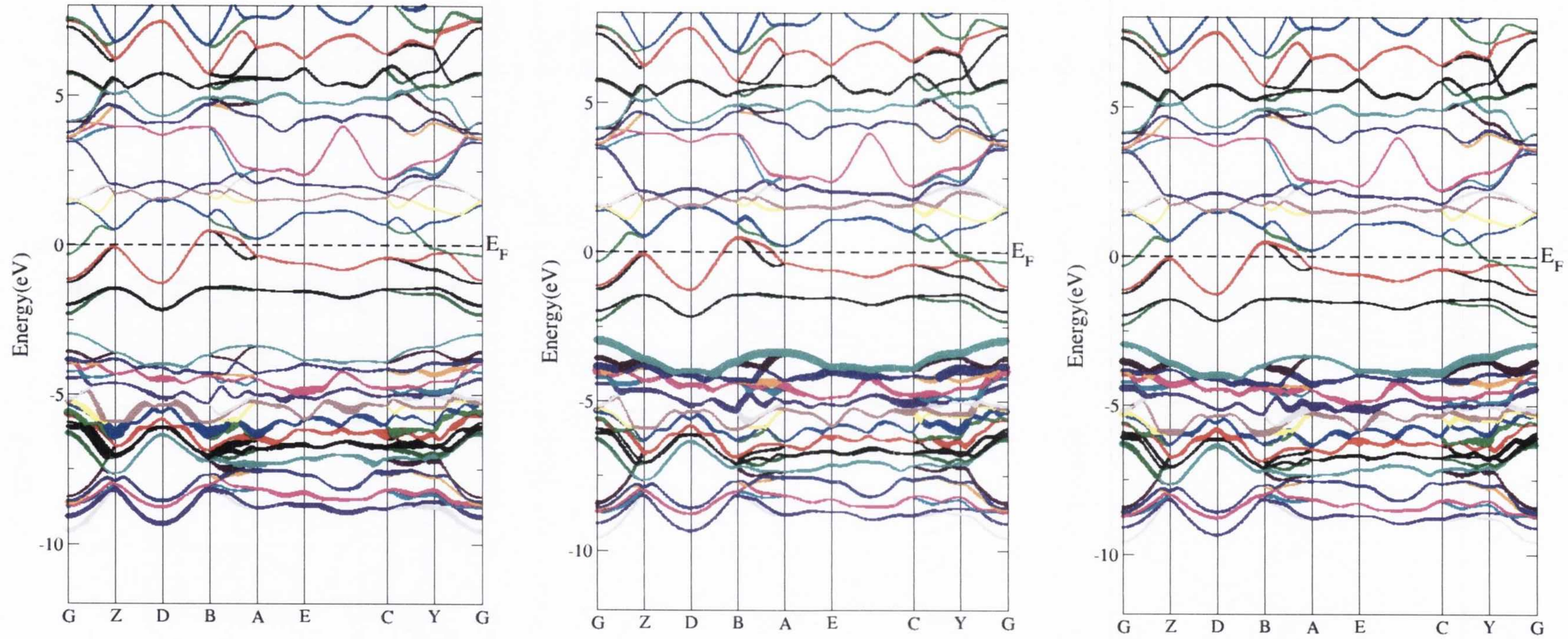

(a) O2 $2p_x$

(b) O2 $2p_y$

(c) O2 $2p_z$

Figure A.6: Bandstructure character plots of the O2 site for monoclinic $WO_2$ calculated by the DFT method through WIEN2K. The weightings represent PDOS for the **(a)** $2p_x$, **(b)** $2p_y$ and **(c)** $2p_z$ states on the O2 atomic site.

## A.7 WO$_2$ W 5$d$ $t_{2g}$ Weighted Bandstructures

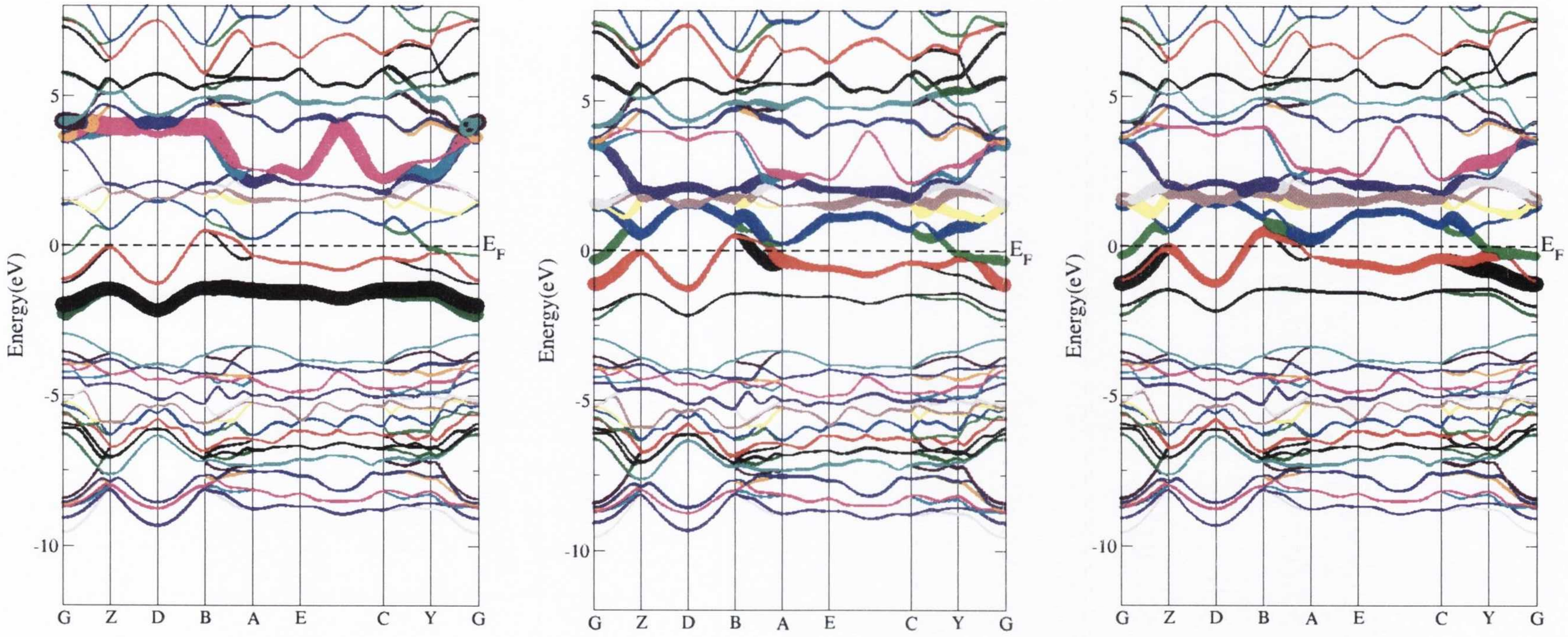

(a) W 5$d_{xy}$

(b) W 5$d_{xz}$

(c) W 5$d_{yz}$

Figure A.7: Bandstructure character plots of the W 5$d$ $t_{2g}$ orbitals for monoclinic WO$_2$ calculated by the DFT method through WIEN2K. The weightings represent PDOS for the **(a)** 5$d_{xy}$, **(b)** 5$d_{xz}$ and **(c)** 5$d_{yz}$ states on the W atomic site.

## A.8 WO$_2$ W 5$d$ $e_g$ Weighted Bandstructures

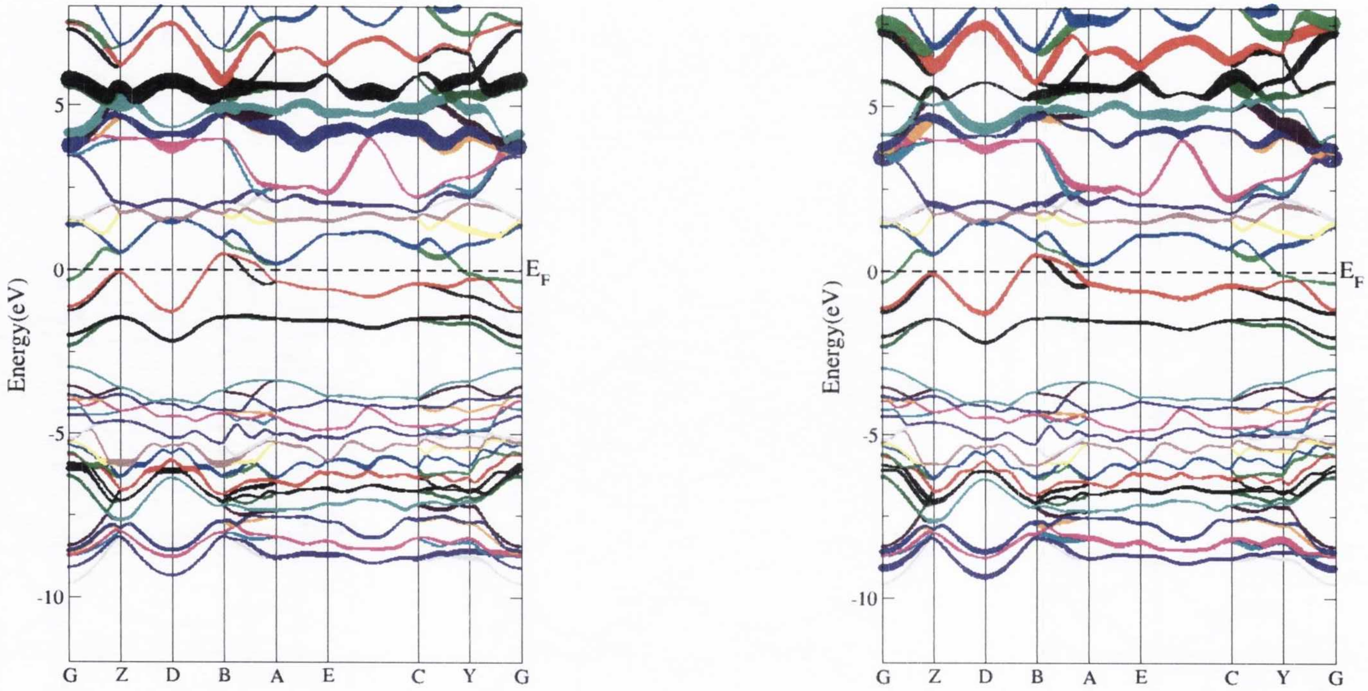

(a) W 5$d_{x^2-y^2}$

(b) W 5$d_{z^2}$

Figure A.8: Bandstructure character plots of the W 5$d$ $e_g$ orbitals for monoclinic WO$_2$ calculated by the DFT method through WIEN2K. The weightings represent PDOS for the **(a)** 5$d_{x^2-y^2}$ and **(b)** 5$d_{z^2}$ states on the W atomic site.

## A.9 Rutile TiO$_2$ PDOS

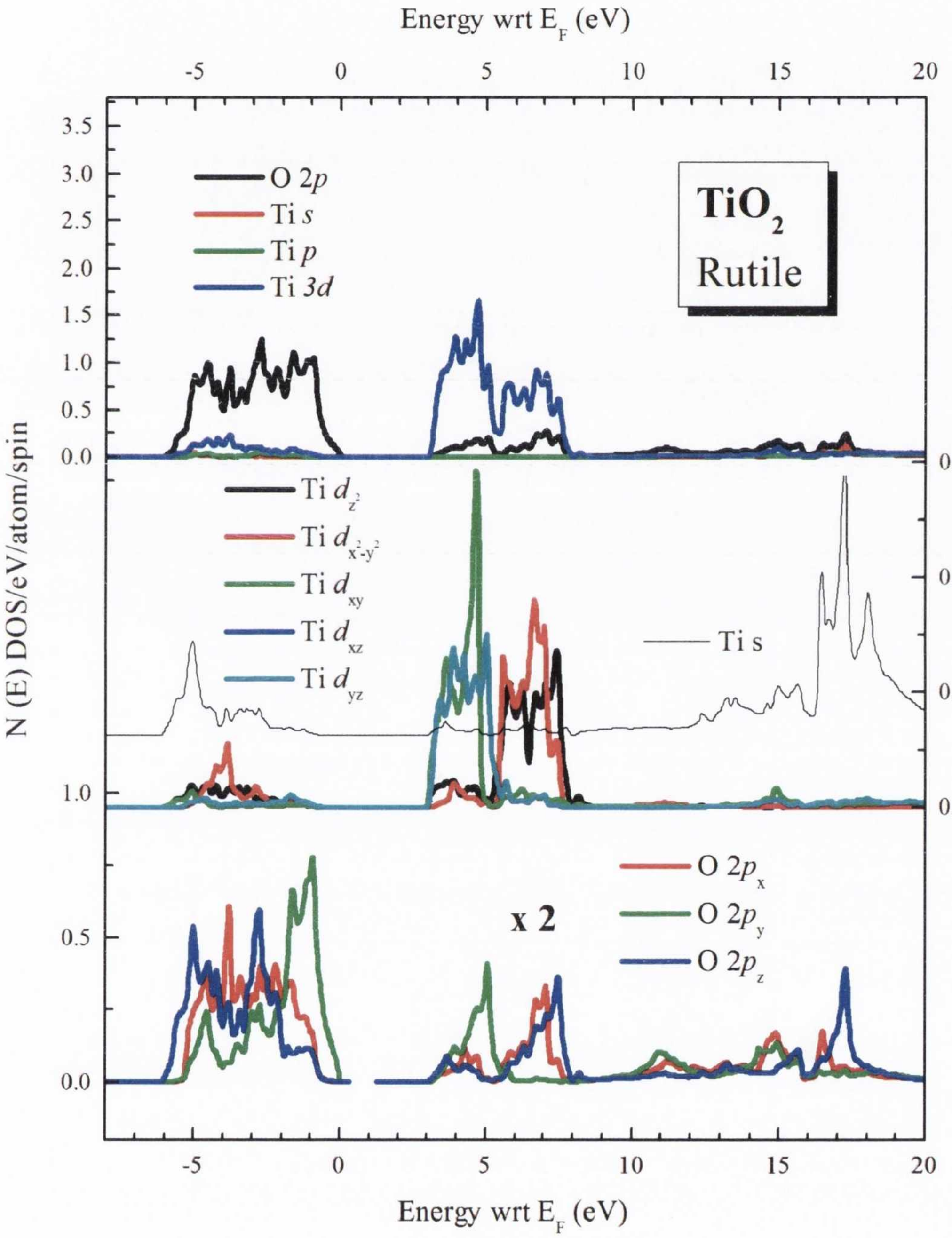

Figure A.9: Electronic structure calculations showing the PDOS of rutile TiO$_2$, calculated using DFT and the FP-LAPW approach implemented in WIEN2K..

## A.10 Anatase TiO$_2$ PDOS

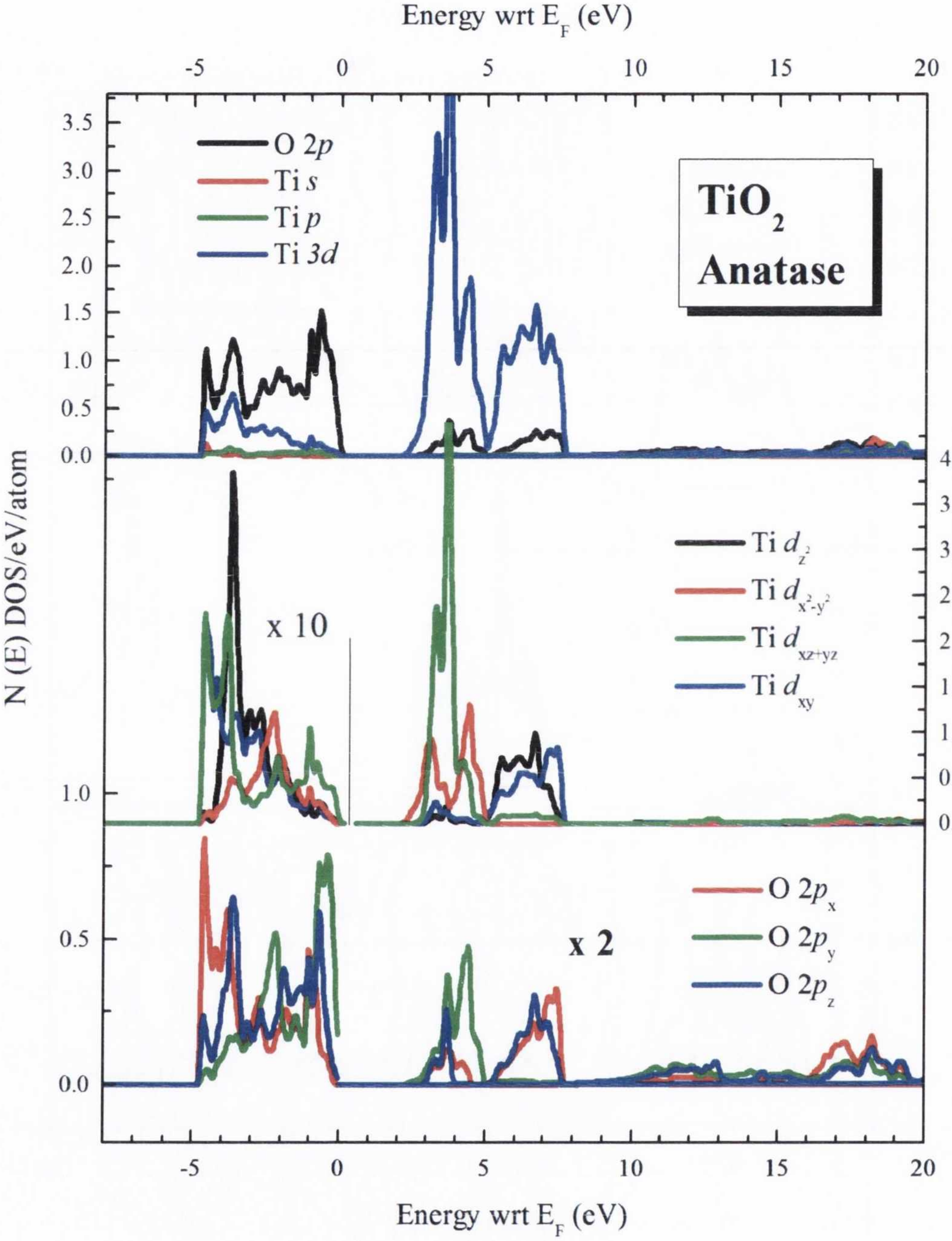

Figure A.10: Electronic structure calculations showing the PDOS of anatase TiO$_2$, calculated using DFT and the FP-LAPW approach implemented in WIEN2K.

# List of Abbreviations

| | |
|---|---|
| **ALS** | Advanced Light Source |
| **AF** | antiferromagnet |
| **ASW** | augmented spherical wave |
| **BL7** | Beamline 7.0.1 |
| **BL8** | Beamline 8.0.1 |
| **BNL** | Brookhaven National Laboratory |
| **BSE** | Bethe-Salpeter equation |
| **CB** | conduction band |
| **CFT** | crystal field theory |
| **CSFE** | crystal field stabilisation energy |
| **DFT** | density functional theory |
| **DMS** | dilute magnetic semiconductor |
| **DOS** | density of states |
| **EELS** | electron energy loss spectroscopy |
| **EXAFS** | extended X-ray absorption fine structure |
| **FP-LAPW** | full-potential linearised augmented planewave |
| **FWHM** | full-width half-maximum |
| **FY** | fluorescence yield |
| **GGA** | generalised gradient approximation |
| **gpm** | grooves per millimetre |

| | |
|---|---|
| **HAXPES** | hard X-ray photoemission spectroscopy |
| **HEG** | high energy grating |
| **HSE** | Heyd-Scuseria-Ernzerhof |
| **HP** | Hewlett Packard |
| **IP** | in-plane |
| **IR** | infra-red |
| **IUPAC** | International Union of Pure and Applied Chemistry |
| **LAPW** | linear augmented planewave |
| **LBNL** | Lawrence Berkeley National Laboratory |
| **LDA** | local density approximation |
| **LEED** | low energy electron diffraction |
| **MCP** | microchannel plate |
| **MEG** | medium energy grating |
| **MIT** | metal-to-insulator transition |
| **MO** | molecular orbital |
| **NEXAFS** | near edge X-ray absorption fine structure |
| **NSLS** | National Synchrotron Light Source |
| **NXES** | normal XES |
| **OOP** | out-of-plane |
| **PDOS** | partial density of states |
| **PES** | photoemission spectroscopy |
| **PLD** | pulsed laser deposition |
| **RAE** | resistive anode encoder |
| **RIXS** | resonant inelastic X-ray scattering |

| | |
|---|---|
| **RR** | resonance Raman |
| **RXES** | resonant X-ray emission spectroscopy |
| **SGM** | spherical grating monochromator |
| **SPEM** | scanning photoelectron microscopy |
| **STM** | scanning tunnelling microscopy |
| **SXE** | soft X-ray emission |
| **SXF** | soft X-ray fluorescence |
| **SXPS** | soft X-Ray photoelectron spectroscopy |
| **SXRS** | soft X-ray Raman scattering |
| **TEY** | total electron yield |
| **TFY** | total fluorescence yield |
| **TM** | transition metal |
| **UPS** | ultra-violet photoelectron spectroscopy |
| **UV** | ultra-violet |
| **VB** | valence band |
| **VUV** | vacuum ultra-violet |
| **XAFS** | X-ray absorption fine structure |
| **XAS** | X-ray absorption spectroscopy |
| **XES** | X-ray emission spectroscopy |
| **XPS** | X-ray photoemission spectroscopy |

# Presentations and Publications

## Conference Poster Presentations

**Conference:** 37th International Conference on Vacuum UltraViolet and X-ray Physics. Vancouver, Canada. (July 2010)
**Poster Title:** Symmetry Selective Resonant X-ray Emission Spectroscopy Study of Tungsten Dioxide ($WO_2$) at the O $K$-Edge.
**Authors:** Declan Cockburn, Brian Kennedy, Jonathan Denlinger, Russell G. Egdell and Cormac McGuinness.

**Conference:** 37th International Conference on Vacuum UltraViolet and X-ray Physics. Vancouver, Canada. (July 2010)
**Poster Title:** The Valence Band Electronic Structure of $RuO_2$ A Study of Chemical Bonding Through Polarisation Dependent Resonant Soft X-ray Emission.
**Authors:** Cormac McGuinness, Brian Kennedy, Declan Malachy Cockburn, Brendan J. Arnold, Jonathan D. Denlinger, Tanel Käämbre, and Russell G. Egdell.

**Conference:** 11th International Conference on Electronic Spectroscopy and Structure - ICESS-11. Nara, Japan. (October 2009)
**Poster Title:** Symmetry Selective Resonant X-Ray Emission Spectroscopy Study of Iridium Dioxide ($IrO_2$) at the O $K$-Edge.
**Authors:** Declan Cockburn, Brian Kennedy, Jonathan Denlinger, W. L. Yang, Y. S. Huang and Cormac McGuinness.

**Conference:** 11th International Conference on Electronic Spectroscopy and Structure - ICESS-11. Nara, Japan. (October 2009)
**Poster Title:** Measurement and Simulations of the Oxygen $K$-edge Resonant X-ray Emission Spectroscopy of Rutile Titanium Dioxide.
**Authors:** Brian Kennedy, Declan Cockburn, Brendan Arnold, Al Grogan, Tanel Käämbre, Jinghua Guo, Russell G. Egdell, P. Blaha and Cormac McGuinness.

## Activity Reports

**Report:** MAX-lab Activity Report 2012 .

**Title:** Symmetry and polarisation dependent resonant soft X-ray emission at the F $K$-edge in $MgF_2$.

**Authors:** D. Cockburn , B. Kennedy , C. McGuinness , A. Pietzsch and F. Hennies.

**Report:** MAX-lab Activity Report 2010.

**Title:** The valence band electronic structure of the distorted rutile-like $WO_2$ a study of chemical bonding via resonant soft X-ray emission at the O $K$-edge.

**Authors:** D. Cockburn, B. Kennedy, C. McGuinness, R. G. Egdell, A. Pietzsch and F. Hennies.

**Report:** MAX-lab Activity Report 2009.

**Title:** Symmetry and state-selective electronic structure of rutile-type $TiO_2$ investigated by polarisation dependent absorption and resonant soft X-ray emission spectroscopy at the oxygen $K$-edge.

**Authors:**B. Kennedy, C. McGuinness, B. Arnold, D. Cockburn, A. Grogan, R. G. Egdell, T. Käämbre and P. Blaha.

**Report:** MAX-lab Activity Report 2007.

**Title:** The valence band electronic structure of $RuO_2$ a study of chemical bonding through polarisation dependent resonant soft X-ray emission.

**Authors:** D. Cockburn , B. Kennedy , B. Arnold , C. McGuinness , R. G. Egdell and T. Käämbre.

## Papers

**Title:** Symmetry Selective Resonant X-Ray Emission Spectroscopy Study of Tungsten Dioxide ($WO_2$) at the O $K$-Edge

**Authors:** D. M. Cockburn, B. Kennedy, J. D. Denlinger, F. Hennies, A. Pietzch, R. G. Egdell and C. McGuinness.

**Status:** Draft manuscript - awaiting submission

**Title:** Polarization Dependent Spectroscopic Study of Rutile Iridium Dioxide ($IrO_2$) by Resonant X-ray Emission and X-ray Absorption Spectroscopy.

**Authors:** Declan M. Cockburn, Brian Kennedy, Jonathan Denlinger, W. L. Yang, Ying-Sheng Huang, Franz Hennies, Annette Pietzch, Cormac McGuinness.

**Status:** Draft manuscript - awaiting submission

**Title:** Polarization-dependent O $K$-edge RIXS of bulk $VO_2$.

**Authors:** Declan M. Cockburn, Brian Kennedy, Jonathan Denlinger, W. L. Yang, Russ Egdell, Cormac McGuinness.

**Status:** Draft manuscript (letter) - awaiting submission.

# List of Figures

2.1 After absorption of an X-ray photon the excited core hole will undergo decay. Two primary routes are shown. For low Z elements Auger decay is dominant, while for high Z elements fluorescent decay is dominant. Adapted from [7] . 8

2.2 Non radiative and radiative transition rates as a function of atomic number Z from page 6 in Attwood [11] . . . . . . . . . . . . . . . . . . . . . . . . . 12

2.3 Energy level diagram for copper showing spectroscopic notation for transitions allowed by the selection rules $\Delta l = \pm 1$ and $\Delta j = 0, \pm 1$. $n$ is the principal quantum number, $l$ is the orbital angular momentum quantum number and $j$ is the total angular momentum quantum number from the vector combination of spin and orbital angular momentum. Absorption edge nomenclature is shown to the right. From page 17 Attwood [11]. . . . . . . 15

2.4 Orbital symmetry selectivity in X-ray emission due to varying spectrometer position with respect the polarisation of the exciting photons. Geometries of maximum absorption and emission are illustrated for $p$ orbitals with either $\sigma$ or $\pi$ bonding symmetry in the left and right panel respectively. Black has orbital axis (**k**-vector) and bond direction (**E**-vector) in the plane of the page, for red the orbital axis (**E**-vector) alone is orthogonal to the page. Blue applies only to the photon, where **E** is parallel to the page but the **k** is orthogonal. Adapted from Gel'mukhanov and Ågren (Figure 32) [9]. . . . . . . . . . . . 16

2.5 Resonant and non resonant emission spectra from oriented graphite. Upper left panel is bandstructure aligned such that the energy axes match. The right panel is a schematic representation of the coherent resonant fluorescence. Only emission from the occupied states with the same crystal momentum (vertical line) is allowed. Adapted from Carlisle *et al.* [17] . . . . . . . . . . 19

2.6 Sketch of a synchrotron storage ring and a beamline. Bending magnets are shown at corners, while a straight-line section houses an undulator storage device. The tangential cone-shaped trajectory of the of light is also indicated. 21

2.7 Grazing incidence Rowland circle focusing geometry for a concave spherical grating, in a soft X-ray fluorescence (SXF) spectrometer. Radius of Rowland circle 2R is defined as the radius of curvature of the grating positioned at its centre point: 2R = $R_c$. Entrance slit and detector are also indicated lying on the circumference for optimal focus. . . . . . . . . . . . . . . . . . . . . . . . 22

2.8 Gammadata XES300/350 SXF Nordgren type spectrometer. (A) shows the sample, slit, grating-selector, gratings and detector layout. (B) details the detector; showing the deflector, microchannel plate (MCP) as well as the resistive anode encoder (RAE). (C) gives the relative orientation of the spherical gratings with respect to the slit. Diagram from Nordgren *et al.* [18] . . 24

2.9 End station and SXF spectrometer at the ALS beamline 8.0.1. Diagram adapted from Jia [21]. . . . . . . . . . . . . . . . . . . . . . . . . . . . . 25

2.10 End station and SXF spectrometer at the ALS beamline 8.0.1. Diagram adapted from Jia [21]. . . . . . . . . . . . . . . . . . . . . . . . . . . . . 26

3.1 Periodic table of rutile and rutile-like oxides and fluorides. The oxides have added annotation in parentheses: where M is metallic, S is semiconductor, F is ferromagnetic and AF is an antiferromagnet. Starred compounds are compounds that are in a distorted rutile, or monoclinic phase at room temperature. . . . . . . . . . . . . . . . . . . . . . . . . . . . . . . . . 30

3.2 (a)Adjacent edge-sharing octahedra in a typical rutile structure from Sorantin and Schwarz [44]. (b)Two unit cells of rutile $CrO_2$ contiguous along the *c*-axis. Alternating orientations of trigonal planes, all $\|c$, highlighted. . . 31

3.3 Defining the natural coordinate systems in a rutile geometry for (a) the cation and (b) the anion, adapted from Sorantin and Schwarz [44]. . . . . . . . . 33

3.4 *d* orbital shapes and orientation divided into two degenerate states by the octahedral crystal field: $t_{2g}$ and $e_g$. . . . . . . . . . . . . . . . . . . . . . . 34

3.5 3D visualisation of $e_g$ orbitals (a) $d_{z^2}$ and (c) $d_{x^2-y^2}$ . . . . . . . . . . . . . 34

3.5 continuation of 3D visualisation, this time for $t_{2g}$ orbitals (d) $d_{z^2}$ and the alternatively designated remaining (e) $d_{z(y+x)}$ and (f) $d_{z(y-x)}$. Adapted from Eyert *et al.* [50] . . . . . . . . . . . . . . . . . . . . . . . . . . . . 35

4.1 Rutile tetragonal $IrO_2$ crystal structure. Oxygen atoms in red, iridium in yellow. **a)** Two unit cells of $IrO_2$ showing the $c$-axis and the central metal cation in its octahedral coordination. **b)** Two unit cells of $IrO_2$, illustrating the alternating orthogonal arrangement of the $Ir_3O$ trigonal planes parallel to the $c$-axis. **c)** One unit-cell highlighting $2p_y$ orbital which hybridises in a $\pi$-like configuration with metal $t_{2g}$, shown perpendicular to the $Ir_3O$ $sp^2$ hybridised trigonal plane. . . . . . . . . . . . . . . . . . . . . . . . . . . 45

4.2 Electronic structure DFT DOS calculations for $IrO_2$ in the VB and CB, calculated by the FP-LAPW method. **a)** Total $IrO_2$ DOS. **b)** Component PDOS separated for O 2p, and the $t_{2g}$ and $e_g$ components of the Ir $5d$ states resulting from crystal field splitting. **c)** The orthogonal O$2p_x$, $2p_y$, $2p_z$ component PDOS for the natural coordination axes of the trigonally coordinated oxygen anion. . . . . . . . . . . . . . . . . . . . . . . . . . . . . . . . . . . . . . . 46

4.3 DFT calculations of Ir $5d$ PDOS in the VB and CB of $IrO_2$. **a)** Total Ir $5d$ PDOS. **b)** $e_g$ component states of Ir $5d$, $d_{z^2}$ and $d_{x^2-y^2}$. **c)** $t_{2g}$ component states of Ir $5d$, tetragonal distortion lifts degeneracy. $d_{z(y-x)}$ orbital in particular lies in the (001) plane, exhibiting significant $\pi$-like hybridisation with O $p_y$ (Figure 4.2c) in the region around $E_F$ . . . . . . . . . . . . . . . . . . 47

4.4 Partial molecular orbital diagram for manganese $d$ level splitting in $MnO_2$, note similar position of $t_{2g} \downarrow$ with $e_g \uparrow$ due to energetically similar crystal field and exchange splitting. Adapted from Kurata *et al.* [89] . . . . . . . . 50

4.5 Schematic drawing of the "polarized" versus "depolarized" experimental configuration, or out-of-plane versus in-plane scattering respectively, for a normal planar undulator. Adapted from Harada *et al.* [91] . . . . . . . . . . . . . . 52

4.6 **a)**Polarisation dependent O $K$-edge XAS of $IrO_2$ for $\mathbf{E} \parallel c$ and $\mathbf{E} \perp c$ incidence geometries measured in TEY mode.**b)** DFT calculated partial DOS of oxygen $2p$ CB PDOS projected along the local $x$-axis (blue) and along the direction bisecting the local $x$ and $y$ axes (red). . . . . . . . . . . . . . . . . . . . . . 56

4.7 Polarisation dependent O $K$-edge XAS of $MnO_2$ measured in TEY mode (top) for the $\mathbf{E} \parallel c$ and $\mathbf{E} \perp c$ incidence geometries. Compared below with, respectively, EELS from Kurata *et al.* [89], O $K$-edge fluorescence yield (FY) from Figueiredo *et al.* [79], and on the bottom XAS in the $\mathbf{E} \parallel c$ geometry measured in TFY mode. . . . . . . . . . . . . . . . . . . . . . . . . . 59

4.8 (Top) scanning photoelectron microscopy (SPEM) from (Tsai *et al.* [70]) and photoemission spectroscopy (PES) from (Daniels *et al.* [69]) compared with (middle) O $K$-edge in-plane (IP) polarisation dependent NXES of $\mathrm{IrO_2}$ taken at 555 eV excitation energy at BL7, and (bottom) out-of-plane (OOP) NXES-like RXES of the same from I511-3. . . . . . . . . . . . . . . . . . . 61

4.9 Polarisation dependent IP O $K$-edge RXES of $\mathrm{IrO_2}$. $\mathbf{E}\perp c$;XES$\perp c$ scattering geometry shown in red and the $\mathbf{E}\|c$;XES$\|c$ in blue. Labelled arrows on formerly presented, and geometrically associated XAS spectra (top) indicate resonant excitation energies. . . . . . . . . . . . . . . . . . . . . . . . . . . 63

4.10 IrO2 bandstructures. **(a)** Presents the unweighted calculated bandstructure for rutile $\mathrm{IrO_2}$. **(b)** $\mathrm{IrO_2}$ bandstructure weighted for O $2p_x$ DOS. **(b)** $\mathrm{IrO_2}$ bandstructure weighted for O $2p_y$ DOS. **(b)** $\mathrm{IrO_2}$ bandstructure weighted for O $2p_z$ DOS. . . . . . . . . . . . . . . . . . . . . . . . . . . . . . . . 67

4.11 Polarisation dependent OOP O $K$-edge RXES of $\mathrm{IrO_2}$. $\mathbf{E}\perp c$;XES$\|c$ scattering geometry shown in red and the $\mathbf{E}\|c$;XES$\perp c$ in blue. Labelled arrows on formerly presented, and geometrically associated XAS spectra (top) indicate resonant excitation energies. Due to relatively low signal to noise, a 5 point-adjacent averaging was applied to emission line spectra, while scatter points indicate raw recorded data. . . . . . . . . . . . . . . . . . . . . . . . . . 68

4.12 Difference spectra for IP $\mathrm{IrO_2}$ using NXES and compared with broadened DFT component VB PDOS. **a)** XES$\|c$ - XES$\perp c$ NXES compared $p_y$. **b)** XES$\perp c$ - XES$\|c$ NXES compared $p_x$. **c)** $\mathbf{E}\|c$;XES$\|c$ NXES subtracted from same geometry $\sigma^*$ resonant spectrum, compared with $p_y$ DFT. **d)** $\mathbf{E}\|c$;XES$\|c$ NXES subtracted from same geometry $\pi^*$ resonant spectrum, compared with $p_z$ DFT. . . . . . . . . . . . . . . . . . . . . . . . . . . . . . . . . . 70

4.13 Experimentally isolated anisotropic orthogonal components of O $2p$ VB DOS using polarisation dependent IP RXES of $\mathrm{IrO_2}$, compared with broadened DFT calculations of same. Blue lines indicate energy difference between O $2p_z$ and $p_x$ features. **a)** $\mathbf{E}\perp c$;XES$\perp c$ $\pi^*$ spectrum compared with $p_x$. **b)** $\mathbf{E}\|c$;XES$\|c$ $\sigma^*$ - $\pi^*$ difference spectrum compared with $p_y$. **c)** $\mathbf{E}\|c$;XES$\|c$ $\pi^*$ - $\sigma^*$ difference spectrum compared with $p_z$. . . . . . . . . . . . . . . . . . . 72

4.14 Polarisation dependent IP O $K$-edge RXES of $\mathrm{MnO_2}$. $\mathbf{E}\perp c$;XES$\perp c$ scattering geometry shown in red and the $\mathbf{E}\|c$;XES$\|c$ in blue. Labelled arrows on formerly presented and geometrically associated XAS spectra (top) indicate resonant excitation energies. . . . . . . . . . . . . . . . . . . . . . . . . . . 74

4.15 Figure adapted from Franchini *et al.* [76]. In black is an XPS spectrum of rutile $\beta$-$MnO_2$ obtained by Audi and Sherwood [77]. In comparison the red full line is the DFT calculated $d$-like DOS using the Heyd-Scuseria-Ernzerhof (HSE) method through VASP by Franchini *et al.* [76]. Three features can be observed. . . . . . . . . . . . . . . . . . . . . . . . . . . . . . . . . . 75

4.16 Polarisation dependent OOP O $K$-edge RXES of $MnO_2$. $\mathbf{E}\perp c$;XES$\|c$ scattering geometry shown in red and the $\mathbf{E}\|c$;XES$\perp c$ in blue. Labelled arrows on formerly presented and geometrically associated XAS spectra (top) indicate resonant excitation energies. Due to relatively low signal to noise, a 5 point-adjacent averaging was applied to emission line spectra, while scatter points indicate raw recorded data. . . . . . . . . . . . . . . . . . . . . . . . . . 77

5.1 $Mn_3F$ plane, containing $c$-axis, showing the relationship between spin and site for manganese and fluorine in $MnF_2$, adapted from Dufek *et al.* [99] . . 84

5.2 Doubled unit cell of $MnF_2$ showing spin alignment (spin↑ and spin↓) of the Mn atomic sites. Adapted from Dufek *et al.* [99] . . . . . . . . . . . . . . . . 84

5.3 PDOS of $MgF_2$. Top: compares the total $MgF_2$ DOS with the total F $2p$ PDOS. Middle: comparing the fluorine $s$ states with the magnesium $s$, $p$ and $d$ states. Bottom: fluorine $2p$ PDOS broken down into its coordinate components $p_x$ $p_y$ and $p_z$, inset shows $\sim 13$ times magnification of CB states. 86

5.4 PDOS of $MnF_2$. Top part: total fluorine $2p$ states compared to total manganese $s$ $p$ and $d$ components. Bottom part: fluorine $2p_x$, $p_y$ and $p_z$, inset shows $\sim 20$ times magnification of CB states. . . . . . . . . . . . . . . . . 89

5.5 Top panel shows XAS of $MgF_2$ at the fluorine $K$-edge for two measurement geometries $\mathbf{E}\perp c$ and $\mathbf{E}\|c$ measured in TFY compared with the simulated XAS for the two geometries, created from the $p_x$ and average $p_y + p_z$ calculated CB DOS respectively. These were then broadened by convolution with a Gaussian and Lorentzian concurrent with the instrumental and core-hole lifetime broadening. Bottom panel gives the raw FY XAS counts for the same measurements but graphed over a broader energy range. This is then contrasted with previous transmission XAS measurements obtained by Oizumi *et al.* [108]. . . . . . . . . . . . . . . . . . . . . . . . . . . . . . . . . . 93

5.6 XAS of $MnF_2$ compared to calculations and previous measurements from the literature. Top reproduces XAS measurements from Jiménez-Mier *et al.* [103] and Vinogradov *et al.* [102]. Middle shows XAS of $MnF_2$ at the fluorine $K$-edge for two measurement geometries $\mathbf{E}\perp c$ and $\mathbf{E}||c$ measured in TFY mode. Bottom are the simulated XAS for the two geometries, created from the fluorine $p_x$ and average $p_y + p_z$ calculated CB DOS respectively. These were then broadened by convolution with a Gaussian and Lorentzian concurrent with the instrumental and core-hole lifetime broadening. . . . . . . . . . . 96

5.7 Conduction band calculated PDOS for $MnF_2$ illustrating the detailed hybridisation or correspondence between the unoccupied F $2p$ and Mn $3d$ orbitals 97

5.8 Part **(a)** shows the total fluorine $2p$ VB DOS for $MgF_2$ broadened to simulate core-hole and instrumental broadening of XES, this is then shown split into its component $\pi$ and $\sigma$ states, the unbroadened calculation of each overlaid. Part **(b)** breaks this down further showing the simulated fluorine VB $p_x$, $p_y$ and $p_z$ components of the PDOS which should correspond to the emission. . 99

5.9 $MgF_2$ NXES and difference spectrum compared with theory. **(a)** compares the measured NXES on top in both measurement geometries, with the simulated NXES spectra below. The simulated spectra are a broadened addition of the $p_y+p_z$ for the XES$||c$, and $p_x+(p_y+p_z)/2$ for the XES$\perp c$ measurement geometry. The upper portion of part **(b)** shows the 3-point adjacent-average smoothed difference spectrum (line) and raw difference spectrum (triangles) created by the subtraction: XES$\perp c-$XES$||c\times 0.6$. Below is the comparison with the simulated $p_x$ component of emission. . . . . . . . . . . . . . . . . . 100

5.10 Part **(a)** shows the stepwise RXES measured in both in-plane geometries: $\mathbf{E}\perp c$;XES$\perp c$ and $\mathbf{E}||c$;XES$||c$ for $MgF_2$ at the fluorine $K$-edge. Part **(b)** is the XAS for the same crystal, numbered black arrows indicate the energies where emission was recorded. This is compared with the unbroadened calculated fluorine $p_x$, $p_y$ and $p_z$ CB components. Part **(c)** is a second difference spectrum created by subtracting 0.5× spectrum (4) from spectrum (1), both in the $\mathbf{E}||c$;XES$||c$ measurement geometry. This was then normalised and directly overlaid with the fluorine VB $p_y$ simulated component of emission. 102

5.11 $MgF_2$ calculated bandstructure. Greyed rectangles illustrate the first three RXES excitation bandwidths. Note yellow bands at the bottom of the CB are attributed to Mg $3s$. . . . . . . . . . . . . . . . . . . . . . . . . . . 103

5.12 $MgF_2$ difference spectra from previous Figures 5.9b and 5.10c compared directly, and contrasted below with the simulated $p_x$ and $p_y$ components of the F VB respectively. The Fermi energy is rigidly shifted to 675.2 eV. . . . . . 105

5.13 Part **(a)** shows the total fluorine $2p$ VB DOS for $MnF_2$ broadened to simulate core-hole and instrumental resolution of XES, this is then shown split into its component $\pi$ and $\sigma$ character states, the unbroadened calculation of each is overlaid. Part **(b)** breaks this down further showing the simulated fluorine VB $p_x$, $p_y$ and $p_z$ components of emission. . . . . . . . . . . . . . . . . . . . 106

5.14 Part **(a)** shows the RXES in the two in-plane measurement geometries: $\mathbf{E}\perp c$;XES$\perp c$ and $\mathbf{E}\| c$;XES$\| c$ for $MnF_2$ at the fluorine $K$-edge. Part **(b)** is the XAS for the same crystal, numbered black arrows indicating the energies where emission was recorded. This is compared with the unbroadened calculated fluorine $p_x$, $p_y$ and $p_z$ CB components. Part **(c)** contrasts NXES on top in both measurement geometries, with the simulated NXES spectra below. The simulated spectra are a broadened addition of the $p_y + p_z$ projected states for XES$\| c$, and $p_x + (p_y + p_z)/2$ for the XES$\perp c$ measurement geometry. The predicted dichroism is not observed in this crystal. . . . . . . 108

5.15 (a) The F $K$-edge calculated projected total densities for type A and type B "spin states" in the VB, divided further for $\sigma$ and $\pi$ character. Broadened to simulate experimental emission. (b): The F $K$-edge calculated densities for type A and type B states projected along $p_x$ (top) and half-way between the $p_z$ and $p_y$ (bottom) in the CB. Broadened to simulate experimental absorption parameters during RXES. . . . . . . . . . . . . . . . . . . . . . . . . 109

5.16 Top panel: $MnF_2$ NXES1 spectra from Figure 5.14 for the two measurement geometries compared with XES from Jiménez-Mier *et al.* [103] on an unoriented powder sample at approximately the same excitation energy of 700 eV. Bottom panel: Three sets of DFT calculations for the total fluorine $2p$ VB DOS. Top calculation from Jiménez-Mier *et al.* [103] middle is presented here, while the bottom is adapted from Dufek *et al.* [99] and is for type A (F1 $\uparrow$) states only, while the other two are averaged. All were calculated using the FP-LAPW method. The placement of $E_F$, and hence alignment of the emission spectra with the calculations was adopted from the method used by Jiménez-Mier *et al.* . . . . . . . . . . . . . . . . . . . . . . . . . . . . 111

6.1 Corner sharing parallel $W_3O$ trigonal planes along the crystal $a$-axis, shown in the $xy$ plane for the metal coordination, equivalent to the $xz$ plane of the oxygen. Differing bond angles and bond lengths exhibited for O1 (bottom) and O2 (top) sites. Oxygen $sp^2$ hybridised orbitals lobes are shown with respect to the metal $d_{xy}$. Metal–metal dimerisation is also illustrated along the $a$-axis by overlap of $d_{xy}$ orbitals in the O1 trigonal plane. A similar structural relationship, with the separation of oxygen into two distinct sites, is seen in $MoO_2$. . . . . . . . . . . . . . . . . . . . . . . . . . . . . . . . 117

6.2 **a)** Unit cell of monoclinic $WO_2$. Oxygen atoms shown in red, tungsten in grey. **b)** cropped and rotated slightly to emphasise one orientation of $W_3O$ trigonal planes, note average bond length is larger for O2. **c)** Cropped further and rotated 90° from b) to emphasise the W–W bonds along the $a$-axis, note the kink-like distortion and alternating bond length. . . . . . . . . . . . . . . 119

6.3 The $WO_2$ total DOS and W $5d$, O1 $2p$ and O2 $2p$ PDOS are shown in the upper panel as well as the W $5d$ $t_{2g}$ ($d_\perp$ and $d_\parallel$) and $e_g$ components In the two lower panels, the O $2p$ PDOS is decomposed into the projections $\parallel$ $a$-axis, $\perp$ $W_3O$ plane and the $a$-axis, and within the $W_3O$ plane and parallel to the W-apical oxygen bond direction. . . . . . . . . . . . . . . . . . . . . . . . . 121

6.4 Monoclinic structure of $MoO_2$. Differing O1 and O2 sights shown. Dimerised metal pairs highlighted with thicker bonds. The $abc$-axes for a hypothetical pure rutile $MoO_2$ structure is superimposed for clarity. Figure is adapted from Moosburger-Will *et al.* [130] . . . . . . . . . . . . . . . . . . . . . . 122

6.5 XAS of $MoO_2$ at the O $K$-edge at two orthogonal measurement geometries, $\mathbf{E}\parallel a$ and $\mathbf{E}\perp a$. Simultaneously recorded TEY and TFY are shown to highlight difference between bulk and surface sensitivity. These are compared with previous results acquired from Eyert *et al.* [52], though were originally published in a PhD thesis by Müller [131]. Here the black is for unoriented $MoO_2$. . . . . . . . . . . . . . . . . . . . . . . . . . . . . . . . . . . . . . . 128

6.6 Adapted from Moosburger-Will *et al.* [130] **a)** Partial calculated DOS of $MoO_2$ for Mo $4d$ $t_{2g}$ (red), $4d$ $e_g$ (green) and O $2p$ (blue). **b)** Partial DOS of Mo $4d$ $t_{2g}$ individual orbitals, where local coordinate frame of Mo cation is rotated by ~45° about the $z$-axis with respect to the natural coordinate frame used in this thesis. Thus $d_{x^2-y^2}$ in the rotated frame, as described by Moosburger-Will, is transformed into our $d_{xy}$ in the natural coordinate frame. Similarly their $d_{xz}$ and $d_{yz}$ are transformed into our $d_{z(x+y)}$ and $d_{z(x-y)}$ respectively. . . . . . . . . . . . . . . . . . . . . . . . . . . . . . . . . 129

6.7 XAS of $WO_2$ at the O $K$-edge at two orthogonal measurement geometries, $\mathbf{E}\|a$ and $\mathbf{E}\perp a$. Compared below these are the simulated XAS constructed from the calculated oxygen $2p$ CB PDOS for the $p_x$ and $(p_y + p_z)/2$ respectively. These were averaged between the O1 and O2 sites and broadened with a 0.2 eV Gaussian and 0.25 eV Lorentzian to simulate experimental resolution. 132

6.8 Waterfall graphs of $MoO_2$ emission spectra at the O $K$-edge in the two measurement geometries indicated: $\mathbf{E}\perp a$;XES$\perp a$ and $\mathbf{E}\|a$;XES$\|a$. Left panel shows the first four chosen RXES excitation energies labelled (a) through (d) as indicated by the correlating labels on the XAS in Figure 6.5. Right panel shows the next three resonant excitation energies as well as the normal emission on top. Scatter points represent recorded data while solid lines are after 5-point adjacent averaging. . . . . . . . . . . . . . . . . . . . . . . . . . 134

6.9 Electronic band structure along the high-symmetry points for $MoO_2$. The dashed line denotes the Fermi energy. From Scanlon *et al.* [140] . . . . . . 136

6.10 Comparison of polarisation dependent O $K$-edge RXES of $MoO_2$ at excitation (d) (top) with O $2p$ VB He I and He II ultra-violet photoelectron spectroscopy (UPS) from Gulino *et al.* [124] (middle), and two sets of O $2p$ VB DFT calculations from Scanlon *et al.* [140] as well as Moosburger-Will *et al.* [130] Lines on this figure show the position of the $d_{\|}(\sigma)$ and $d_{\perp}(\pi)$ features at approximately -1.5 eV and -0.5 eV respectively, with respect to the Fermi energy. . . . . . . . . . . . . . . . . . . . . . . . . . . . . . . . . . . . 137

6.11 Waterfall graphs of $WO_2$ emission spectra at the O $K$-edge in the two measurement geometries indicated: $\mathbf{E}\perp a$;XES$\perp a$ and $\mathbf{E}\|a$;XES$\|a$. Labels (a)-(e) are the RXES excitation energies as indicated by the correlating labels on the XAS in Figure 6.7. Top spectra are polarisation dependent NXES. Scatter points represent recorded data while solid lines are after 5-point adjacent averaging. . . . . . . . . . . . . . . . . . . . . . . . . . . . . . . . . . . . 139

6.12 Comparison of polarisation dependent O $K$-edge XES of $WO_2$ at excitation (c) as well as NXES (middle) with O $2p$ VB He I UPS from Jones *et al.* [125] (top), and VB DFT calculations presented in this thesis for the projection PDOS in the plane parallel and perpendicular to the monoclinic $a$-axis. Lines on this figure show the position of the $d_{\|}(\sigma)$ and $d_{\perp}(\pi)$ features at approximately -1.5 eV and -0.5 eV respectively, with respect to the Fermi energy. . 140

6.13 **(a)** Comparison of $WO_2$ VB $2p_z + 2p_y$ component calculated PDOS between O1 and O2. Components correspond to those probed in the XES$\|a$ emission measurement geometry. **(b)** Comparison of $WO_2$ CB $2p_x$ component calculated PDOS between O1 and O2, corresponding to $\mathbf{E}\|a$ excitation. Yellow area highlights bandwidth selected by excitation energy (c). . . . . . . . . . 143

7.1 One unit cell of $VO_2$ structure in the monoclinic phase showing the two oxygen sites, and with the rutile unit cells overlayed. From Eyert [50]. . . . 147

7.2 Calculated DFT PDOS of both rutile and monoclinic $VO_2$ showing the oxygen $2p$ total DOS in red, and the $t_{2g}$ and $e_g$ components of the vanadium $3d$ in black and blue respectively. Adapted from Eyert [50], Figures 11 and 23. 149

7.3 Calculated DFT PDOS of the vanadium $e_g$ and $t_{2g}$ components for both rutile and monoclinic $VO_2$, focusing primarily on the CB and region around the Fermi energy. The are divided into their component orbitals based on the local metal coordination detailed in Chapter 3. Adapted from Eyert [50], Figures 12 and 24. . . . . . . . . . . . . . . . . . . . . . . . . . . . 151

7.4 Polarisation dependent XAS at the O $K$-edge of $VO_2$ in the rutile and monoclinic phases. **(a)** TEY measured using the MEG at beamline 8.0.1 with a resolution of approximately 0.2 eV. **(b)** Similar results from the literature, adapted from Muller *et al.* [161]. **(c)** TEY taken using the high energy grating (HEG) at beamline 8.0.1 with a nominal resolution of approximately 0.1 eV. . . . . . . . . . . . . . . . . . . . . . . . . . . . . . . . . . . . 154

7.5 **(a)** Polarisation dependent TFY on monoclinic $VO_2$ at the O $K$-edge recorded simultaneously with the TEY in Figure 7.4(a). **(b)** High resolution TEY taken at both the V $L$- and O $K$-edges using the HEG at beamline 8.0.1. Arrows indicate areas dichroism in the vanadium edge of the monoclinic phase. 155

7.6 RXES spectra taken at the O $K$-edge threshold (a), the $\pi^*$ peak (b), and the $\sigma^*$ peak, as indicated by arrows on the XAS spectra in the upper right panel. Emission was recorded for the two labelled scattering geometries in both the rutile and monoclinic phases. The XES spectra are comparable in form with those observed for monoclinic $VO_2$ by Schmitt *et al.* as E7, E8 and E11 in their Figure 5 [167]. . . . . . . . . . . . . . . . . . . . . . . . . . . . 158

7.7 Waterfall RIXS (RXES) Figures for the $\mathbf{E}\perp c_R$;XES$\perp c_R$ scattering geometry only, for the O $K$-edge of $VO_2$ in both the rutile and monoclinic phases. XAS panel (top) shows arrows indicating excitation energies. . . . . . . . . . . 159

7.8 (**a**) Binding energy subtracted RXES at 530.1 eV excitation energy of monoclinic and rutile $VO_2$ compared with VB PES in the same structural phases. The PES is adapted from Koethe *et al.* (**b**) O $1s$ core-level hard X-ray photoemission comparison of a 10 nm $VO_2$ thin film in its monoclinic and rutile phases, adapted from Eguchi *et al.* [157] . . . . . . . . . . . . . . . . . . . . 162

7.9 (**a**) Electronic bands of rutile $VO_2$ along selected symmetry lines within the first Brillouin zone of the simple tetragonal lattice. (**b**) Electronic bands of monoclinic $VO_2$ along selected symmetry lines within the simple monoclinic Brillouin zone. From Eyert *et al.* [50]. . . . . . . . . . . . . . . . . . . . . . . 163

7.10 Vanadium $L$-edge RIXS waterfall graph of $VO_2$ in the $\mathbf{E}\perp c_R$;XES$\perp c_R$ scattering geometry only. Arrows in XAS panel on right gives excitation energies. 164

8.1 Schematic representation of the Ti $2p \rightarrow 3d \rightarrow 2p$ RIXS transition of $TiO_2$. From Kotani *et al.* [191] . . . . . . . . . . . . . . . . . . . . . . . . . . 171

8.2 Three unit cells of rutile $TiO_2$ structure, contiguous along the $c$-axis, observed in two perspective orientations: along and parallel to the $c$-axis respectively. $Ti_3O$ trigonal planes are highlighted. . . . . . . . . . . . . . . . . . . . . . . 175

8.3 A single unit cell of anatase $TiO_2$ structure observed in two perspective orientations: down and parallel to the $c$-axis respectively. $Ti_3O$ trigonal planes are highlighted. . . . . . . . . . . . . . . . . . . . . . . . . . . . . . . . . 175

8.4 Two-edge-sharing octahedra of rutile $TiO_2$ forming chains in the [001] direction, shown in two orthogonal perspectives. On the right, shaded pink to demarcate the difference, are the anatase $TiO_2$ octahedra each sharing four edges. . . . . . . . . . . . . . . . . . . . . . . . . . . . . . . . . . . . . . 175

8.5 Molecular orbital diagram showing the $\sigma$ and $\pi$ bonding combinations in rutile and anatase $TiO_2$. Adapted from Thomas *et al.* [182] . . . . . . . . . 177

8.6 Primitive unit cell and definitions of the local metal coordination for $TiO_2$ in the anatase structure. Adapted from Asahi *et al.* [174] . . . . . . . . . . 178

8.7 Polarisation dependent core to valence transition intensities for $\mathbf{E}$ along the natural principal coordinate axes. Listed are the intensities for the four basic symmetry cases at the $K$- and $L$-edges. [8] . . . . . . . . . . . . . . . . . . . 180

8.8 Comparison of uncorrected and corrected emission intensity for RXES at the Ti $L$-edge of anatase $TiO_2$ at 20° beam incidence for the left panel (grazing exit) and 70° beam incidence for the right panel(grazing incidence). Insets show outgoing absorption cross section $\sigma(h\nu_o)$ used for correction and determined from the TEY. . . . . . . . . . . . . . . . . . . . . . . . . . 183

8.9 XAS of $TiO_2$ rutile and anatase at the Ti $L$-edge for $\mathbf{E}||c$ and $\mathbf{E}\perp c$ measurement geometries. Arrows indicate RXES excitation energies. . . . . . . . . . 186

8.10 Calculated and experimental Ti $L_{3,2}$ edges in rutile and anatase $TiO_2$ with the BSE formalism. Adapted from Laskowski and Blaha [186] . . . . . . . . 187

8.11 Electronic bandstructure character plots of rutile $TiO_2$ emphasising **(a)** the Ti $3d_{z^2}$ and **(b)** the Ti $3d_{z^2}$ weighted character of the bands in the CB. . . 189

8.12 Electronic bandstructure character plots of anatase $TiO_2$ emphasising **(a)** the Ti $3d_{z^2}$ and **(b)** the Ti $3d_{z^2}$ weighted character of the bands in the CB. 189

8.13 RXES of the Ti $L_{2,3}$-edges for rutile $TiO_2$ for two in-plane scattering geometries, $\mathbf{E}||c$;XES$||c$ and $\mathbf{E}\perp c$;XES$\perp c$, recorded at the ALS. The left panel shows the $L1$ and $L\eta$ emission, while the right panel shows the comparably amplified $L\alpha_{1,2}$ and $L\beta_1$. All spectra are corrected for self-absorption and normalised to the $L\beta_1$ peak maximum. . . . . . . . . . . . . . . . . . . . 191

8.14 RXES of rutile $TiO_2$ for the $L1$ and $L\eta$ emission peaks, separated for the two measurement geometries. Lines show energy min and max of dispersion of the $L1$ peak. . . . . . . . . . . . . . . . . . . . . . . . . . . . . . 194

8.15 $L\alpha_{1,2}$ and $L\beta_1$ RXES for rutile $TiO_2$ for two in-plane scattering geometries, $\mathbf{E}||c$;XES$||c$ and $\mathbf{E}\perp c$;XES$\perp c$, recorded at the NSLS. Low signal to noise required a 9-point adjacent averaging. All spectra are corrected for self-absorption. . . . . . . . . . . . . . . . . . . . . . . . . . . . . . 195

8.16 Electronic bandstructure character plots of rutile $TiO_2$ emphasising **(a)** the Ti $3d_{z^2}$ and **(b)** the Ti $3d_{z^2}$ weighted character of the bands in the VB. The comparatively reduced Ti $3d$ occupied PDOS required the weightings in the VB be amplified when compared to other bandstructure character plots presented in this thesis. . . . . . . . . . . . . . . . . . . . . . . . 196

8.17 RXES of the Ti $L_{2,3}$-edges for anatase $TiO_2$ for two in-plane scattering geometries, $\mathbf{E}||c$;XES$||c$ and $\mathbf{E}\perp c$;XES$\perp c$, recorded at the ALS. The left panel shows the $L1$ and $L\eta$ emission, while the right panel shows the comparably amplified $L\alpha_{1,2}$ and $L\beta_1$. All spectra are corrected for self-absorption and normalised to the $L\beta_1$ peak maximum. . . . . . . . . . . . . . . . . . . . 197

8.18 $L\alpha_{1,2}$ and $L\beta_1$ RXES for anatase $TiO_2$ for two in-plane scattering geometries, $\mathbf{E}||c$;XES$||c$ and $\mathbf{E}\perp c$;XES$\perp c$, recorded at the NSLS. Low signal to noise required a 9-point adjacent averaging. All spectra barring (1) are corrected for self-absorption. . . . . . . . . . . . . . . . . . . . . . . . . . . 198

A.1 Spectroscopic notation correspondence with electron configuration for shell excitations. . . . . . . . . . . . . . . . . . . . . . . . . . . . . . . . . 207
A.2 Correspondence between the Siegbahn and the more intuitive systematic IUPAC notations describing electronic transitions and thus X-ray emission lines. . . . . . . . . . . . . . . . . . . . . . . . . . . . . . . . . . . . 208
A.3 Duplicate of Figure 7.6 page 158, with normalisation to O $K$-edge peak maxima, as consistent with the majority of RXES spectra presented in this thesis. . . . . . . . . . . . . . . . . . . . . . . . . . . . . . . . . . . . . 209
A.4 O $K$-edge polarisation dependent RXES of $VO_2$ in both its metallic-rutile and monoclinic-semiconducting phases. $\mathbf{E}\|c$;XES$\|c$ measurement geometry sample contaminated by suspected $V_2O_3$ reduction. . . . . . . . . . . . . . 210
A.5 Bandstructure character plots of the O1 site for monoclinic $WO_2$ calculated by the DFT method through WIEN2K. The weightings represent PDOS for the **(a)** $2p_x$, **(b)** $2p_y$ and **(c)** $2p_z$ states on the O1 atomic site. . . . . . . . 211
A.6 Bandstructure character plots of the O2 site for monoclinic $WO_2$ calculated by the DFT method through WIEN2K. The weightings represent PDOS for the **(a)** $2p_x$, **(b)** $2p_y$ and **(c)** $2p_z$ states on the O2 atomic site. . . . . . . . 212
A.7 Bandstructure character plots of the W $5d$ $t_{2g}$ orbitals for monoclinic $WO_2$ calculated by the DFT method through WIEN2K. The weightings represent PDOS for the **(a)** $5d_{xy}$, **(b)** $5d_{xz}$ and **(c)** $5d_{yz}$ states on the W atomic site. 213
A.8 Bandstructure character plots of the W $5d$ $e_g$ orbitals for monoclinic $WO_2$ calculated by the DFT method through WIEN2K. The weightings represent PDOS for the **(a)** $5d_{x^2-y^2}$ and **(b)** $5d_{z^2}$ states on the W atomic site. . . . 214
A.9 Electronic structure calculations showing the PDOS of rutile $TiO_2$, calculated using DFT and the FP-LAPW approach implemented in WIEN2K.. . . . . . 215
A.10 Electronic structure calculations showing the PDOS of anatase $TiO_2$, calculated using DFT and the FP-LAPW approach implemented in WIEN2K. . . 216

# References

[1] Sang-Wook Cheong. Transition metal oxides: The exciting world of orbitals. *Nature Materials*, 6(12):927–928, December 2007.

[2] Y. Matsumoto, R. Takahashi, M. Murakami, T. Koida, X. J. Fan, T. Hasegawa, T. Fukumura, M. Kawasaki, S. Y. Koshihara, and H. Koinuma. Ferromagnetism in Co-doped $TiO_2$ rutile thin films grown by laser molecular beam epitaxy. *Japanese Journal of Applied Physics: Part 2 - Letters*, 40(11B):L1204–L1206, 2001.

[3] S. B. Ogale, R. J. Choudhary, J. P. Buban, S. E. Lofland, S. R. Shinde, S. N. Kale, V. N. Kulkarni, J. Higgins, C. Lanci, J. R. Simpson, N. D. Browning, S. Das Sarma, H. D. Drew, R. L. Greene, and T. Venkatesan. High temperature ferromagnetism with a giant magnetic moment in transparent Co-doped $SnO_{2-\delta}$. *Physical Review Letters*, 91(7):077205, 2003.

[4] C.B. Fitzgerald, M. Venkatesan, A.P. Douvalis, S. Huber, J.M.D. Coey, and T. Bakas. $SnO_2$ doped with Mn, Fe or Co: Room temperature dilute magnetic semiconductors. *Journal of Applied Physics*, 95(11, Part 2):7390–7392, JUN 1 2004. 9th Joint Magnetism and Magnetic Materials Conference / International Magnetics Conference, Anaheim, CA, JAN 05-09, 2004.

[5] Brian Kennedy. *Resonant Soft X-ray Spectroscopic Studies of Certain Transition Metal Oxides.* PhD thesis, University of Dublin, Trinity College., 2011.

[6] Joachim Stöhr. *NEXAFS Spectroscopy.* Springer, 1992.

[7] Lars-Åke Näslund. *Oxygen 1s x-ray absorption spectroscopy of liquid water and aqueous solutions.* PhD thesis, Uppsala Universitet, 2002.

[8] J. Stöhr and H. C. Siegmann. *Magnetism, From Fundamentals to Nanoscale Dynamics.* Springer, 2006.

[9] F. Gel'mukhanov and H. Ågren. Resonant X-ray Raman scattering. *Physics Reports-Review Section of Physics Letters*, 312(3-6):91–244, 1999.

[10] A Kotani and S Shin. Resonant inelastic x-ray scattering spectra for electrons in solids. *Reviews of Modern Physics*, 73(1):203–246, JAN 2001.

[11] D.T. Attwood. *Soft x-rays and extreme ultraviolet radiation: principles and applications*. Cambridge University Press, 2000.

[12] M. O. Krause. Atomic radiative and radiationless yields for K and L shells. *Journal of Physical and Chemical Reference Data*, 8(2):307–327, 1979.

[13] S. Tanaka, K. Okada, and A. Kotani. Theory of X-Ray Emission in High-Tc Superconductors. *Journal of the Physical Society of Japan*, 58(3):813–816, 1989.

[14] Luuk J. P. Ament, Michel van Veenendaal, Thomas P. Devereaux, John P. Hill, and Jeroen van den Brink. Resonant inelastic x-ray scattering studies of elementary excitations. *Review of Modern Physics*, 83:705–767, June 2011.

[15] F. de Groot and A. Kotani. *Core level spectroscopy of solids*, volume 6. CRC, 2008.

[16] S.M. McMurry. *Quantum mechanics*. Addison-Wesley, 1994.

[17] J.A. Carlisle, E.L. Shirley, E.A. Hudson, L.J. Terminello, T.A. Callcott, J.J. Jia, D.L. Ederer, R.C.C. Perera, and F.J. Himpsel. Probing the graphite band structure with resonant soft-x-ray fluorescence. *Physical Review Letters*, 74(7):1234–1237, 1995.

[18] J. Nordgren, G. Bray, S. Cramm, R. Nyholm, J. E. Rubensson, and N. Wassdahl. Soft-X-Ray Emission-Spectroscopy Using Monochromatized Synchrotron Radiation. *Review of Scientific Instruments*, 60(7):1690–1696, 1989.

[19] J. A. R. Samson. *Techniques of Vacuum Ultraviolet Spectroscopy*. Wiley, 1967.

[20] T. Learmonth. *Soft x-ray spectroscopic studies of quasi-low dimensional and strongly correlated materials*. PhD thesis, Boston University, 2008.

[21] J. J. Jia, T. A. Callcott, J. Yurkas, A. W. Ellis, F. J. Himpsel, M. G. Samant, J. Stohr, D. L. Ederer, J. A. Carlisle, E. A. Hudson, L. J. Terminello, D. K. Shuh, and R. C. C. Perera. First Experimental Results From IBM/Tenn/Tulane/LLNL/LBL Undulator Beamline at the Advanced Light-Source. *Review of Scientific Instruments*, 66(2):1394–1397, 1995.

[22] E. Hoyer, J. Chin, K. Halbach, W.V. Hassenzahl, D. Humphries, B. Kincaid, H. Lancaster, and D. Plate. The U5.0 Undulator For the Advanced Lightsource. *Review of Scientific Instruments*, 63(1, Part 2A):359–362, JAN 1992.

[23] G. Bray S. Cram R. Nyholm J.E. Rubensson and N. Wassdahl J. Nordgren. Soft x-ray emission spectroscopy using monochromatized synchrotron radiation. *Review of Scientific Instruments*, 60(7):1690–1696, 1989.

[24] R. Denecke, P. Vaterlein, M. Bassler, N. Wassdahl, S. Butorin, A. Nilsson, J. E. Rubensson, J. Nordgren, N. Martensson, and R. Nyholm. Beamline I511 at MAX II, capabilities and performance. *Journal of Electron Spectroscopy and Related Phenomena*, 103:971–977, 1999.

[25] J. H. Guo, N. Wassdahl, P. Skytt, S. M. Butorin, L. Duda, C. J. Englund, and J. Nordgren. End Station for Polarization and Excitation-energy Selective Soft-X-ray Fluorescence Spectroscopy. *Review of Scientific Instruments*, 66(2, Part 2):1561–1563, FEB 1995.

[26] K. J. Randall, J. Feldhaus, W. Erlebach, A. M. Bradshaw, W. Eberhardt, Z. Xu, Y. Ma, and P. D. Johnson. Soft x-ray spectroscopy beam line on the NSLS X1 undulator: Optical design and first performance tests. *Review of Scientific Instruments*, 63(1):1367–1370, 1992.

[27] S. Krinsky and J. M. Wang. Longitudinal Instabilities of Long Gaussian Bunches. *IEEE Transactions On Nuclear Science*, 30(4):2495–2497, 1983.

[28] C. T. Chen and F. Sette. Performance of the Dragon Soft-x-ray Beamline. *Review of Scientific Instruments*, 60(7):1616–1621, July 1989.

[29] A. F. Wells. *Structural Inorganic Chemistry*. Oxford, 1984.

[30] L. Vegard. Results of crystal analysis. *Phil. Mag*, 32:65–96, 1916.

[31] W. H. Baur and A. A. Khan. Rutile-Type Compounds .4. $SiO_2$, $GeO_2$ and a Comparison with Other Rutile-Type Structures. *Acta Crystallographica Section B-Structural Crystallography and Crystal Chemistry*, B 27(NOV15):2133, 1971.

[32] D. B. Rogers, R. D. Shannon, A. W. Sleight, and J. L. Gillson. Crystal Chemistry of Metal Dioxides with Rutile-Related Structures. *Inorganic Chemistry*, 8(4):841, 1969.

[33] W. Gonschorek and R. Feld. Neutron diffraction study of the thermal and oxygen position parameters in rutile. *Zeitschrift für Kristallographie*, 161(1-2):1–5, 1982.

[34] John B. Goodenough. Metallic Oxides. *Progress in Solid State Chemistry*, 5:145–399, 1971.

[35] John B. Goodenough. The two components of the crystallographic transition in $VO_2$. *Journal of Solid State Chemistry*, 3(4):490 – 500, 1971.

[36] W. H. Baur. Rutile-type compounds. V. Refinement of $MnO_2$ and $MgF_2$. *Acta Crystallographica Section B-Structural Crystallography and Crystal Chemistry*, 32(7):2200–2204, 1976.

[37] L. F. Mattheiss. Electronic-Structure of $RuO_2$, $OsO_2$, and $IrO_2$. *Physical Review B*, 13(6):2433–2450, 1976.

[38] M. Gupta, AJ Freeman, and DE Ellis. Electronic structure and lattice instability of metallic $VO_2$. *Physical Review B*, 16(8):3338, 1977.

[39] E. Caruthers and L. Kleinman. Energy Bands of Semiconducting $VO_2$. *Physical Review B*, 7(8):3760, 1973.

[40] JK Burdett, T Hughbanks, GJ Miller, JW Richardson, and JV Smith. Structural electronic relationships in inorganic solids - powder neutron-diffraction studies of the rutile and anatase polymorphs of titanium-dioxide at 15 and 295-K. *Journal of the American Chemical Society*, 109:3639–3646, 1987.

[41] J. K. Burdett. Structural-electronic Relationships in Rutile. *Acta Crystallographica Section B: Structural Science*, 51(Part 4):547–558, 1995.

[42] J. K. Burdett. Electronic Control of the Geometry of Rutile and Related Structures. *Inorganic Chemistry*, 24(14):2244–2253, 1985.

[43] A. A. Bolzan, C. Fong, B. J. Kennedy, and C. J. Howard. Structural studies of rutile-type metal dioxides. *Acta Crystallographica Section B: Structural Science*, 53(3):373–380, 1997.

[44] P. I. Sorantin and K. Schwarz. Chemical Bonding in Rutile-Type Compounds. *Inorganic Chemistry*, 31(4):567–576, Feb 19 1992.

[45] G.L. Meissler and D.A. Tarr. *Inorganic Chemistry: International Edition*. Pearson Higher Education, 2010.

[46] SD Mo and WY Ching. Electronic and Optical-properties of 3 Phases of Titanium-dioxide - Rutile, Anatase, and Brookite. *Physical Review B*, 51(19):13023–13032, MAY 15 1995.

[47] K. M. Glassford and J. R. Chelikowsky. Electronic and Structural-Properties of $RuO_2$. *Physical Review B*, 47(4):1732–1741, Jan 15 1993.

[48] Donald S. Pearson Ralph G. Dunn, Thomas M. McClure. *Some aspects of crystal field theory.* Harper & Row, 1965.

[49] J. Kunes, P. Novak, P. M. Oppeneer, C. Konig, M. Fraune, U. Rudiger, G. Guntherodt, and C. Ambrosch-Draxl. Electronic structure of $CrO_2$ as deduced from its magneto-optical Kerr spectra. *Physical Review B*, 65(16):art. no. 165105, 2002.

[50] V Eyert. The metal-insulator transitions of $VO_2$: a band theoretical approach. *Annalen Der Physik*, 11(9):650–702, NOV 2002.

[51] V. Eyert. The metal-insulator transition of $NbO_2$: An embedded Peierls instability. *Europhysics Letters*, 58(6):851–856, Jun 2002.

[52] V Eyert, R Horny, KH Hock, and S Horn. Embedded Peierls instability and the electronic structure of $MoO_2$. *Journal of Physics-Condensed Matter*, 12(23):4923–4946, JUN 12 2000.

[53] D. P. Romanov and V. N. Skrobot. Distortions of octahedra in rutile-type structures of transition element dioxides. *Glass Physics and Chemistry*, 35(5):518–524, 2009.

[54] S. Biermann, A. Poteryaev, A.I. Lichtenstein, and A. Georges. Dynamical singlets and correlation-assisted Peierls transition in $VO_2$. *Physical Review Letters*, 94(2), JAN 21 2005.

[55] P Hohenberg and W Kohn. Inhomogeneous Electron Gas. *Physical Review B*, 136(3B):B864, 1964.

[56] W. Kohn and L.J. Sham. Self-consistent equations including exchange and correlation effects. *Physical Review*, 140(4A):1133–1138, 1965.

[57] P. Blaha, K. Schwarz, G.K.H. Madsen, D. Kvasnicka, and J. Luitz. WIEN2K, *An Augmented Plane Wave + Local Orbitals Program for Calculating Crystal Properties.* Karlheinz Schwarz, Techn. Universität Wien, Austria, 2001.

[58] S. Cottenier. *Density Functional Theory and the family of (L)APW-methods: a step-by-step introduction.* Instituut voor Kern- en Stralingsfysica, K. U. Leuven, Belgium, 2002.

[59] Ulf von Barth and Günter Grossmann. Dynamical effects in x-ray spectra and the final-state rule. *Physical Review B*, 25(8):5150–5179, Apr 1982.

[60] X.L. Zhou, Z.G. Ye, X.Z. Hua, A.H. Zou, and Y.H. Dong. Electrocatalytic activity and stability of Ti/$IrO_2$ + $MnO_2$ anode in 0.5 M NaCl solution. *Journal of Solid State Electrochemistry*, 14(7):1213–1219, 2010.

[61] W. D. Ryden, A. W. Lawson, and C. C. Sartain. Temperature Dependence of Resistivity of $RuO_2$ And $IrO_2$. *Physics Letters A*, A 26(5):209, 1968.

[62] W. D. Ryden and A. W. Lawson. Magnetic Susceptibility of $IrO_2$ and $RuO_2$. *Journal of Chemical Physics*, 52(12):6058, 1970.

[63] G. Beni and J. L. Shay. Electrochromism in Anodic Iridium Oxide-films. *Applied Physics Letters*, 33(2):208–210, 1978.

[64] S. Hackwood, G. Beni, M. A. Bosch, K. Kang, L. M. Schiavone, and J. L. Shay. New Process For Optical Information-storage. *Physical Review B*, 26(12):7073–7075, 1982.

[65] J. J. Lin, S. M. Huang, Y. H. Lin, T. C. Lee, H. Liu, X. X. Zhang, R. S. Chen, and Y. S. Huang. Low temperature electrical transport properties of $RuO_2$ and $IrO_2$ single crystals. *Journal of Physics-Condensed Matter*, 16(45):8035–8041, Nov 17 2004.

[66] F.A. Frame, T.K. Townsend, R.L. Chamousis, E.M. Sabio, T. Dittrich, N.D. Browning, and F.E. Osterloh. Photocatalytic Water Oxidation with Nonsensitized $IrO_2$ Nanocrystals under Visible and UV Light. *Journal of the American Chemical Society*, 2011.

[67] R. S. Chen, H. M. Chang, Y. S. Huang, D. S. Tsai, S. Chattopadhyay, and K. H. Chen. Growth and characterization of vertically aligned self-assembled $IrO_2$ nanotubes on oxide substrates. *Journal of Crystal Growth*, 271(1-2):105–112, Oct 15 2004.

[68] G. K. Wertheim and H. J. Guggenheim. Conduction-Electron Screening in Metallic Oxides - $IrO_2$. *Physical Review B*, 22(10):4680–4683, 1980.

[69] R. R. Daniels, G. Margaritondo, C. A. Georg, and F. Levy. Electronic States of Rutile Dioxides - $RuO_2$, $IrO_2$, and $Ru_xIr_{1-x}O_2$. *Physical Review B*, 29(4):1813–1818, 1984.

[70] H. M. Tsai, P. D. Babu, C. W. Pao, J. W. Chiou, J. C. Jan, K. P. K. Kumar, F. Z. Chien, W. F. Pong, M. H. Tsai, C. H. Chen, L. Y. Jang, J. F. Lee, R. S. Chen, Y. S. Huang, and D. S. Tsai. Comparison of electronic structures of $RuO_2$ and $IrO_2$ nanorods investigated by x-ray absorption and scanning photoelectron microscopy. *Applied Physics Letters*, 90(042108):3, Jan 2007.

[71] L. Atanasoska, R. Atanasoski, and S. Trasatti. XPS and AES study of mixed layers of $RuO_2$ and $IrO_2$. *Vacuum*, 40(1-2):91–94, 1990.

[72] J. H. Xu, T. Jarlborg, and A. J. Freeman. Self-Consistent Band-Structure of the Rutile Dioxides $NbO_2$, $RuO_2$, and $IrO_2$. *Physical Review B*, 40(11):7939–7947, Oct 15 1989.

[73] J. S. de Almeida and R. Ahuja. Electronic and optical properties of $RuO_2$ and $IrO_2$. *Physical Review B*, 73(16):165102, Apr 2006.

[74] B.A. Hamad. First-principle calculations of structural and electronic properties of rutile-phase dioxides ($MO_2$), M= Ti, V, Ru, Ir and Sn. *The European Physical Journal B-Condensed Matter and Complex Systems*, 70(2):163–169, 2009.

[75] SL Suib. Sorption, catalysis, separation design. *Chemical Innovation*, 30(3):27–33, MAR 2000.

[76] C. Franchini, R. Podloucky, J. Paier, M. Marsman, and G. Kresse. Ground-state properties of multivalent manganese oxides: Density functional and hybrid density functional calculations. *Physical Review B*, 75(19), MAY 2007.

[77] A.A. Audi and P.M.A. Sherwood. Valence-band x-ray photoelectron spectroscopic studies of manganese and its oxides interpreted by cluster and band structure calculations. *Surface And Interface Analysis*, 33(3):274–282, MAR 2002.

[78] F. M. F. de Groot, M. Grioni, J. C. Fuggle, J. Ghijsen, G. A. Sawatzky, and H. Petersen. Oxygen 1s X-ray Absorption Edges of Transition-metal Oxides. *Physical Review B*, 40(8):5715–5723, September 1989.

[79] M. O. Figueiredo and J. P. Mirao. Soft X-ray absorption at the O $K$-edge in rutile-type natural oxides. *Nuclear Instruments & Methods in Physics Research Section B: Beam Interactions With Materials and Atoms*, 238(1-4):314–318, August 2005.

[80] H Sato, T Enoki, M Isobe, and Y Ueda. Transport properties and magnetism of a helically Hund-coupled conductor: beta-$MnO_2$. *Physical Review B*, 61(5):3563–3569, FEB 1 2000.

[81] H Sato, Y Kawamura, T Ogawa, Y Murakami, H Ohsumi, M Mizumaki, and N Ikeda. Critical phenomena in helical magnet beta-$MnO_2$: X-ray magnetic scattering study. *Physica B-Condensed Matter*, 329(Part 2):757–758, MAY 2003.

[82] H Sato, K Wakiya, T Enoki, T Kiyama, Y Wakabayashi, H Nakao, and Y Murakami. Magnetic structure of beta-$MnO_2$: X-ray magnetic scattering study. *Journal of the Physical Society of Japan*, 70(1):37–40, JAN 2001.

[83] M Regulski, R Przenioslo, I Sosnowska, and JU Hoffmann. Short and long range magnetic ordering in beta-$MnO_2$ - A temperature study. *Journal of the Physical Society of Japan*, 73(12):3444–3447, DEC 2004.

[84] Zhang Jia, Duan Yuping, Jing Hui, Li Xiaogang, and Liu Shunhua. The morphology and electromagnetic properties of $MnO_2$ obtained in 8 T high magnetic field. *Journal of Crystal Growth*, 312(19):2788–2794, SEP 15 2010.

[85] J. P. Perdew, K. Burke, and M. Ernzerhof. Generalized gradient approximation made simple. *Physical Review Letters*, 77(18):3865–3868, Oct 28 1996.

[86] A Yoshimori. A New Type of Antiferromagnetic Structure in The Rutile Type Crystal. *Journal of the Physical Society of Japan*, 14(6):807–821, 1959.

[87] M Regulski, R Przenioslo, I Sosnowska, and JU Hoffmann. Incommensurate magnetic structure of beta-$MnO_2$. *Physical Review B*, 68(17), NOV 2003.

[88] M Zhuang and JW Halley. Self-consistent tight-binding method for the prediction of magnetic spin structures in solids: Application to $MnF_2$ and $MnO_2$. *Physical Review B*, 64(2), JUL 1 2001.

[89] H. Kurata and C. Colliex. Electron-energy-loss Core-edge Structures in Manganese Oxides. *Physical Review B*, 48(4):2102–2108, 1993.

[90] Y.S. Huang. Growth and Characterization of $IrO_2$ Single Crystals. *Chinese Journal of Physics*, 25(1):232, 1987.

[91] Y. Harada, T. Kinugasa, R. Eguchi, M. Matsubara, A. Kotani, M. Watanabe, A. Yagishita, and S. Shin. Polarization dependence of soft-x-ray Raman scattering at theLedge of $TiO_2$. *Physical Review B*, 61(19):12854–12859, 2000.

[92] R. Brydson, H. Sauer, W. Engel, J. M. Thomas, E. Zeitler, N. Kosugi, and H. Kuroda. Electron-Energy Loss and X-ray Absorption-Spectroscopy of Rutile and Anatase - A Test of Structural Sensitivity. *Journal of Physics-Condensed Matter*, 1(4):797–812, Jan 1989.

[93] R. Brydson, H. Sauer, W. Engel, and F. Hofer. Electron Energy-Loss near-Edge Structures at the Oxygen K-Edges of Titanium(IV) Oxygen Compounds. *Journal of Physics: Condensed Matter*, 4(13):3429–3437, 1992.

[94] F. M. F. de Groot. High-resolution X-ray emission and X-ray absorption spectroscopy. *Chemical Reviews*, 101(6):1779–1808, 2001.

[95] M. Lui, A. R. King, J. P. Kotthaus, P. K. Hansma, and V. Jaccarino. Observation of Antiferromagnetic-resonance in Epitaxial-films of $MnF_2$. *Physical Review B*, 33(11):7720–7723, June 1986.

[96] M. Lui, C. A. Ramos, A. R. King, and V. Jaccarino. Antiferromagnetic Standing-spin-wave Resonance in Epitaxial-films of $MnF_2$. *Journal of Applied Physics*, 67(9), May 1990.

[97] J. W. Stout. Absorption Spectrum of Manganous Fluoride. *Journal of Chemical Physics*, 31(3):709–719, 1959.

[98] Xinxin Li, Jun Lu, Guochun Peng, Linpei Jin, and Shuo Wei. Solvothermal synthesis of $MnF_2$ nanocrystals and the first-principle study of its electronic structure. *Journal of Physics and Chemistry of Solids*, 70(3-4):609–615, March 2009.

[99] P. Dufek, K. Schwarz, and P. Blaha. Electronic and Magnetic-structure of $MnF_2$ and $NiF_2$. *Physical Review B*, 48(17):12672–12681, November 1993.

[100] K. Yamasaki, T. Fujikawa, and S. I. Nakai. Short-range-order Full Multiple-scattering Approach To the Fluorine K-edge XANES of $MnF_2$. *Journal of the Physical Society of Japan*, 58(8):2962–2967, August 1989.

[101] S. Nakai, A. Kawata, M. Ohashi, M. Kitamura, C. Sugiura, T. Mitsuishi, and H. Maezawa. Core-exciton Absorption in the F $K$-absorption Spectra of 3d Transition-metal Fluorides. *Physical Review B*, 37(18):10895–10897, June 1988.

[102] AS Vinogradov, SI Fedoseenko, SA Krasnikov, AB Preobrajenski, VN Sivkov, DV Vyalikh, SL Molodtsov, VK Adamchuk, C. Laubschat, and G. Kaindl. Low-lying unoccupied electronic states in $3d$ transition-metal fluorides probed by NEXAFS at the F $1s$ threshold. *Physical Review B*, 71(4):045127, 2005.

[103] J. Jimenez-Mier, G. Herrera-Perez, P. Olalde-Velasco, G. Carabali, E. Chavira, P. de la Mora, W. L. Yang, J. Denlinger, A. Moewes, and R. Wilks. Electron dynamics of transition metal compounds studied with resonant soft x-ray scattering. *Revista Mexicana De Fisica*, 57(1):6–13, February 2011.

[104] Chikara Sugiura. *$K\alpha$* X-Ray Emission Spectra and *$K$* X-RayAbsorption-Edge Structures of Fluorine in $3d$ Transition-Metal Difluorides. *Journal of the Physical Society of Japan*, 60(8):2710–2717, 1991.

[105] J. Kawai, T. Yamamoto, Y. Harada, and S. Shin. Fluorine K alpha X-ray fluorescence spectra of $MnF_2$ excited at threshold. *Solid State Communications*, 105(6):381–385, February 1998.

[106] J. Jimenez-Mier, D. L. Ederer, and T. Schuler. X-ray Raman scattering at the manganese L edge of $MnF_2$: Valence emission of $Mn^{2+}$. *Physical Review A*, 72(5):052502, November 2005.

[107] M. Taguchi, J. C. Parlebas, T. Uozumi, A. Kotani, and C. C. Kao. K$\beta$ resonant x-ray emission spectra in $MnF_2$. *Physical Review B*, 61(4):2553–2560, January 2000.

[108] H. Oizumi, T. Fujikawa, M. Ohashi, H. Maezawa, and S. Nakai. F *$K$* XANES Studies of Alkaline-earth Fluorides. *Journal of the Physical Society of Japan*, 54(10):4027–4033, 1985.

[109] C. Sugiura, W. Konishi, S. Shoji, and S. Kojima. Fluorine K-alpha X-ray-emission Spectra of $MgF_2$, $CaF_2$, $SrF_2$ and $BaF_2$. *Journal of the Physical Society of Japan*, 59(11):4049–4053, November 1990.

[110] M. Catti, A. Pavese, R. Dovesi, C. Roetti, and M. Causà. Quantum-mechanical Hartree-Fock self-consistent-field study of the elastic constants and chemical bonding of $MgF_2$ (sellaite). *Physical Review B*, 44(8):3509–3517, Aug 1991.

[111] G. Vidalvalat, J. P. Vidal, C. M. E. Zeyen, and K. Kurkisuonio. Neutron-diffraction Study of Magnesium Fluoride Single-crystals. *Acta Crystallographica Section B: Structural Science*, 35(JUL):1584–1590, 1979.

[112] K. Hämäläinen, C.-C. Kao, J. B. Hastings, D. P. Siddons, L. E. Berman, V. Stojanoff, and S. P. Cramer. Spin-dependent x-ray absorption of MnO and $MnF_2$. *Physical Review B*, 46(21):14274–14277, Dec 1992.

[113] J. Hegarty, B. A. Wilson, W. M. Yen, T. J. Glynn, and G. F. Imbusch. Shift and broadening of optical transitions in $Mn_2$: Zn. *Physical Review B*, 18:5812–5815, Nov 1978.

[114] M. Pompa, A. M. Flank, P. Lagarde, J. C. Rife, I. Stekhin, M. Nakazawa, H. Ogasawara, and A. Kotani. Experimental and theoretical comparison between absorption,

total electron yield, and fluorescence spectra of rare-earth $M_5$ edges. *Physical Review B*, 56(4):2267–2272, Jul 1997.

[115] D. J. Bristow and G. M. Bancroft. Vibrational broadening in fluorine $1s$ hole states and the $a_{1g}$ valence orbital of xenon hexafluoride: structure of xenon hexafluoride and heats of formation of unusual cations. *Journal of the American Chemical Society*, 105(17):5634–5638, 1983.

[116] A. Ferreira da Silva, I. Pepe, C. Persson, J. Souza de Almeida, C. Moyses Araujo, R. Ahuja, B. Johansson, C. Y. An, and J. H. Guo. Optical properties of oxide compounds PbO, $SnO_2$ and $TiO_2$. *Physica Scripta*, T109:180–183, 2004.

[117] LS Roman, R Valaski, CD Canestraro, ECS Magalhaes, C Persson, R Ahuja, EF da Silva, I Pepe, and AF da Silva. Optical band-edge absorption of oxide compound $SnO_2$. *Applied Surface Science*, 252(15):5361–5364, MAY 30 2006.

[118] Carla D. Canestraro, Lucimara S. Roman, and Clas Persson. Polarization dependence of the optical response in $SnO_2$ and the effects from heavily F doping. *Thin Solid Films*, 517(23):6301–6304, OCT 1 2009.

[119] A. V. Soldatov, T. S. Ivanchenko, A. P. Kovtun, S. Della Longa, and A. Bianconi. Spin-dependent Mn $K$-edge XANES of MnO and $MnF_2$: Full multiple-scattering analysis. *Physical Review B*, 52:11757–11762, Oct 1995.

[120] G Deconninck and S Van Den Broek. Solid state effects on F and Na K$\alpha$ X-ray satellite structure. *Journal of Physics C: Solid State Physics*, 13(17):3329, 1980.

[121] O. Benka and M. Uda. Molecular-orbital Model For the Chemical Effect on the $K$ X-ray Spectrum of Fluorine. *Physical Review Letters*, 56(1):54–57, January 1986.

[122] J. E. Rubensson, M. Eisebitt, S.and Nicodemus, T. Boske, and W. Eberhardt. Electron Correlation in $CaF_2$ Studied in Threshold-excited Soft-x-ray Fluorescence. *Physical Review B*, 50(13):9035–9045, October 1994.

[123] A. Kikas, T. Kmbre, V. Kisand, A. Saar, K. Kooser, E. Nmmiste, and I. Martinson. Resonant inelastic X-ray scattering at the K edge of oxygen and fluorine in insulators. *Journal of Electron Spectroscopy and Related Phenomena*, 144-147(0):845 – 848, 2005. Proceeding of the Fourteenth International Conference on Vacuum Ultraviolet Radiation Physics.

[124] A. Gulino, S. Parker, F. H. Jones, and R. G. Egdell. Influence of metal-metal bonds on electron spectra of $MoO_2$ and $WO_2$. *Journal of the Chemical Society-Faraday Transactions*, 92(12):2137–2141, 1996.

[125] F. H. Jones, R. G. Egdell, A. Brown, and F. R. Wondre. Surface structure and spectroscopy of $WO_2(012)$. *Surface Science*, 374(1-3):80–94, 1997.

[126] N. Jiang and J. C. H. Spence. Electron energy-loss spectroscopy of the O $K$ edge of $NbO_2$, $MoO_2$, and $WO_2$. *Physical Review B*, 70(24):245117, 2004.

[127] O. Y. Khyzhun. XPS, XES and XAS studies of the electronic structure of tungsten oxides. *Journal of Alloys and Compounds*, 305(1-2):1–6, 2000.

[128] T Schroeder, J Zegenhagen, N Magg, B Immaraporn, and HJ Freund. Formation of a faceted $MoO_2$ epilayer on Mo(112) studied by XPS, UPS and STM. *Surface Science*, 552(1-3):85–97, MAR 10 2004.

[129] O. Yu. Khyzhun, V. L. Bekenev, and Yu. M. Solonin. Electronic structure of face-centred cubic $MoO_2$: A comparative study by the full potential linearized augmented plane wave method, X-ray emission spectroscopy and X-ray photoelectron spectroscopy. *Journal of Alloys and Compounds*, 459(1-2):22–28, JUL 14 2008.

[130] Judith Moosburger-Will, Joerg Kuendel, Matthias Klemm, Siegfried Horn, Philip Hofmann, Udo Schwingenschloegl, and Volker Eyert. Fermi surface of $MoO_2$ studied by angle-resolved photoemission spectroscopy, de Haas-van Alphen measurements, and electronic structure calculations. *Physical Review B*, 79(11), MAR 2009.

[131] O. Müller. PhD thesis, Universität Augsburg, 1996.

[132] A. A. Balandin and I. D. Rozhdestvenskaya. Some catalytic properties of molybdenum trioxide and dioxide. *Russian Chemical Bulletin*, 8:1804–1810, 1959. 10.1007/BF00914749.

[133] A. Katrib, P. Leflaive, L. Hilaire, and G. Maire. Molybdenum based catalysts. I. $MoO_2$ as the active species in the reforming of hydrocarbons. *Catalysis Letters*, 38:95–99, 1996. 10.1007/BF00806906.

[134] MC Kim and KL Kim. A role of molybdenum and shape selectivity of catalysts in simultaneous reactions of hydrocracking and hydrodesulfurization. *Korean Journal of Chemical Engineering*, 13(1):1–6, JAN 1996.

[135] US Ozkan, RE Gooding, and BT Schilf. Partial oxidation of C-5 hydrocarbons to maleic and phthalic anhydrides over molybdate-based catalysts. *Heterogeneous Hydrocarbon Oxidation*, 638:178–191, 1996.

[136] M Kitao, S Yamada, Y Hiruta, N Suzuki, and K Urabe. Electrochromic Absorption-Spectra Modulated By the Composition Of $WO_3/MoO_3$ Mixed Films. *Applied Surface Science*, 33-4:812–817, SEP 1988.

[137] M. P. Zach, K. Inazu, K. H. Ng, J. C. Hemminger, and R. M. Penner. Synthesis of Molybdenum Nanowires with Millimeter-Scale Lengths Using Electrochemical Step Edge Decoration. *Chemistry of Materials*, 14(7):3206–3216, 2002.

[138] D. J. Palmer and P. G. Dickens. Tungsten Dioxide - Structure Refinement by Powder Neutron-Diffraction. *Acta Crystallographica Section B-Structural Crystallography and Crystal Chemistry*, 35(SEP):2199–2201, 1979.

[139] B G Brandt and A C Skapski. A Refinement of Crystal Structure of Molybdenum Dioxide. *Acta Chemica Scandinavica*, 21(3):661, 1967.

[140] D. O. Scanlon, G. W. Watson, D. J. Payne, G. R. Atkinson, R. G. Egdell, and D. S. L. Law. Theoretical and Experimental Study of the Electronic Structures of $MoO_3$ and $MoO_2$. *Journal of Physical Chemistry C*, 114(10):4636–4645, 2010.

[141] L. Bendor and L. E. Conroy. Similarity between Tungsten Bronzes and Dioxides of W and Mo. *Israel Journal of Chemistry*, 7(5):713, 1969.

[142] H. Paulin. Diploma Thesis. Master's thesis, Universität Augsburg, 1996.

[143] T. Learmonth, C. McGuinness, P. A. Glans, B. Kennedy, J. S. John, J. H. Guo, M. Greenblatt, and K. E. Smith. Resonant soft x-ray inelastic scattering and soft x-ray emission study of the electronic structure of alpha-$MoO_3$. *Physical Review B*, 79(3):035110, 2009.

[144] V Eyert. Basic notions and applications of the augmented spherical wave method. *International Journal Of Quantum Chemistry*, 77(6):1007–1031, MAY 5 2000.

[145] D. Cockburn, B. Kennedy, J. D. Denlinger, W. L. Yang, Y. S. Huang, and C. McGuinness. Polarisation dependent spectroscopic study of rutile Iridium Dioxide ($IrO_2$) by resonant x-ray emission and x-ray absorption spectroscopy. Unpublished, submitted to PRB, 2011.

[146] C. B. Stagarescu, X. Su, D. E. Eastman, K. N. Altmann, F. J. Himpsel, and A. Gupta. Orbital character of O-2p unoccupied states near the Fermi level in $CrO_2$. *Physical Review B*, 61(14):R9233–R9236, 2000.

[147] Masatoshi Imada, Atsushi Fujimori, and Yoshinori Tokura. Metal-insulator transitions. *Reviews of Modern Physics*, 70:1039–1263, Oct 1998.

[148] D. B. Mcwhan, M. Marezio, J. P. Remeika, and P. D. Dernier. X-ray-diffraction Study of Metallic $VO_2$. *Physical Review B*, 10(2):490–495, 1974.

[149] M. Marezio, B. Mcwhan, P. D. Dernier, and J. P. Remeika. Structural Aspects of Metal-insulator Transitions in Cr-doped $VO_2$. *Physical Review B-solid State*, 5(7):2541, 1972.

[150] D Adler. Mechanisms For Metal-nonmetal Transitions in Transition-metal Oxides and Sulfides. *Reviews of Modern Physics*, 40(4):714, 1968.

[151] Serena A. Corr, Daniel P. Shoemaker, Brent C. Melot, and Ram Seshadri. Real-space investigation of structural changes at the metal-insulator transition in $VO_2$. *Physical Review Letters*, 105(5):056404, July 2010.

[152] Tao Yao, Xiaodong Zhang, Zhihu Sun, Shoujie Liu, Yuanyuan Huang, Yi Xie, Changzheng Wu, Xun Yuan, Wenqing Zhang, Ziyu Wu, Guoqiang Pan, Fengchun Hu, Lihui Wu, Qinghua Liu, and Shiqiang Wei. Understanding the Nature of the Kinetic Process in a $VO_2$ Metal-Insulator Transition. *Physical Review Letters*, 105(22):226405, November 2010.

[153] Jamie M. Booth and Philip S. Casey. Anisotropic structure deformation in the $VO_2$ metal-insulator transition. *Physical Review Letters*, 103(8):086402, August 2009.

[154] L. Braicovich, G. Ghiringhelli, L. H. Tjeng, V. Bisogni, C. Dallera, A. Piazzalunga, W. Reichelt, and N. B. Brookes. Neutral $3d$ excitations in insulating $VO_2$ as seen with resonant inelastic x-ray scattering at the V $L_{3,2}$ edges. *Physical Review B*, 76:125105, Sep 2007.

[155] N. F. Mott. The Transition to the Metallic State. *Philosophical Magazine*, 6(62):287–309, 1961.

[156] R. M. Wentzcovitch, W. W. Schulz, and P. B. Allen. $VO_2$ - Peierls Or Mott-Hubbard - A View From Band Theory. *Physical Review Letters*, 72(21):3389–3392, May 1994.

[157] R. Eguchi, M. Taguchi, M. Matsunami, K. Horiba, K. Yamamoto, Y. Ishida, A. Chainani, Y. Takata, M. Yabashi, D. Miwa, Y. Nishino, K. Tamasaku, T. Ishikawa, Y. Senba, H. Ohashi, Y. Muraoka, Z. Hiroi, and S. Shin. Photoemission evidence for a Mott-Hubbard metal-insulator transition in $VO_2$. *Physical Review B*, 78:075115, Aug 2008.

[158] M. W. Haverkort, Z. Hu, A. Tanaka, W. Reichelt, S. V. Streltsov, M. A. Korotin, V. I. Anisimov, H. H. Hsieh, H. J. Lin, C. T. Chen, D. I. Khomskii, and L. H. Tjeng. Orbital-assisted metal-insulator transition in $VO_2$. *Physical Review Letters*, 95(19):196404, November 2005.

[159] M. Abbate, F.M.F. de Groot, J.C. Fuggle, Y.J. Ma, C.T. Chen, F. Sette, A. Fujimori, Y. Ueda, and K. Kosuge. Soft X-ray-absorption Studies of the Electronic-Structure Changes Through the $VO_2$ Phase-transition. *Physical Review B*, 43(9):7263–7267, MAR 15 1991.

[160] T. C. Koethe, Z. Hu, M. W. Haverkort, C. Schüßler-Langeheine, F. Venturini, N. B. Brookes, O. Tjernberg, W. Reichelt, H. H. Hsieh, H.-J. Lin, C. T. Chen, and L. H. Tjeng. Transfer of Spectral Weight and Symmetry across the Metal-Insulator Transition in $VO_2$. *Physical Review Letters*, 97:116402, Sep 2006.

[161] O. Muller, E. Goering, J.P. Urbach, T. Weber, H. Paulin, M. Klemm, M.L. denBoer, and S. Horn. Metal-insulator transition of $VO_2$. A XANES investigation of the O $K$ edge of $VO_2$. *Journal De Physique IV*, 7(C2, Part 1):533–534, APR 1997. 9th International Conference on X-Ray Absorption Fine Structure, Grenoble, France, Aug 26-30, 1996.

[162] R Zimmermann, R Claessen, F Reinert, P Steiner, and S Hfner. Strong hybridization in vanadium oxides: evidence from photoemission and absorption spectroscopy. *Journal of Physics: Condensed Matter*, 10(25):5697, 1998.

[163] Dmitry Ruzmetov, Sanjaya D. Senanayake, and Shriram Ramanathan. X-ray absorption spectroscopy of vanadium dioxide thin films across the phase-transition boundary. *Physical Review B*, 75:195102, May 2007.

[164] Thorsten Schmitt. *Resonant Soft X-ray Emission Spectroscopy of Vanadium Oxides and Related Compounds.* PhD thesis, Uppsala Universitet, 2004.

[165] S. Shin, A. Agui, M. Watanabe, M. Fujisawa, Y. Tezuka, and T. Ishii. Soft-X-ray-fluorescence and inelastic-light-scattering studies of solids. *Journal of Electron Spectroscopy and Related Phenomena*, 79(0):125 – 130, 1996. Proceedings of the 11th International Conference on Vacuum Ultraviolet Radiation Physics.

[166] E. Z. Kurmaev, V. M. Cherkashenko, Yu M. Yarmoshenko, St Bartkowski, A. V. Postnikov, M. Neumann, L. C. Duda, J. H. Guo, J. Nordgren, V. A. Perelyaev, and W. Reichelt. Electronic structure of $VO_2$ studied by x-ray photoelectron and x-ray emission spectroscopies. *Journal of Physics: Condensed Matter*, 10:4081, 1998.

[167] T. Schmitt, L. C. Duda, A. Augustsson, J. H. Guo, J. Nordgren, J. E. Downes, C. McGuinness, K. E. Smith, G. Dhalenne, A. Revcolevshci, M. Klemm, and S. Horn. Resonant soft X-ray emission spectroscopy of $V_2O_3$, $VO_2$ and $NaV_2O_5$. *Surface Review and Letters*, 9(2):1369–1374, 2002.

[168] G. Andersson. Studies on Vanadium Oxides .2. the Crystal Structure of Vanadium Dioxide. *Acta Chemica Scandinavica*, 10(4):623–628, 1956.

[169] J. M. Longo and Kierkegaard P. A Refinement of Structure of $VO_2$. *Acta Chemica Scandinavica*, 24(2):420, 1970.

[170] M. M. Qazilbash, A. A. Schafgans, K. S. Burch, S. J. Yun, B. G. Chae, B. J. Kim, H. T. Kim, and D. N. Basov. Electrodynamics of the vanadium oxides $VO_2$ and $V_2O_3$. *Physical Review B*, 77:115121, Mar 2008.

[171] RM Bowman and JM Gregg. $VO_2$ thin films: growth and the effect of applied strain on their resistance. *Journal of Materials Science: Materials in Electronics*, 9(3):187–191, 1998.

[172] L. F. J. Piper, A. DeMasi, S. W. Cho, A. R. H. Preston, J. Laverock, K. E. Smith, K. G. West, J. W. Lu, and S. A. Wolf. Soft x-ray spectroscopic study of the ferromagnetic insulator $V_{0.82}Cr_{0.18}O_2$. *Physical Review B*, 82:235103, Dec 2010.

[173] A Amtout and R Leonelli. Optical-properties of rutile near its fundamental-band gap. *Physical Review B*, 51(11):6842–6851, MAR 15 1995.

[174] R Asahi, Y Taga, W Mannstadt, and AJ Freeman. Electronic and optical properties of anatase $TiO_2$. *Physical Review B*, 61(11):7459–7465, MAR 15 2000.

[175] U Diebold. The surface science of titanium dioxide. *Surface Science Reports*, 48(5-8):53–229, 2003.

[176] L. Vayssieres, editor. *On solar hydrogen and nanotechnology*. Wiley, 2009.

[177] Masahiko Matsubara, Takayuki Uozumi, Akio Kotani, Yoshihisa Harada, and Shik Shin. Polarization Dependence of Resonant X-Ray Emission Spectra in Early Transition Metal Compounds. *Journal of the Physical Society of Japan*, 69(5):1558–1565, 2000.

[178] G. van der Laan. Polaronic satellites in x-ray-absorption spectra. *Physical Review B*, 41:12366–12368, Jun 1990.

[179] Christian Heiliger, Frank Heyroth, Frank Syrowatka, Hartmut S. Leipner, Igor Maznichenko, Kalevi Kokko, Wolfram Hergert, and Ingrid Mertig. Orientation-dependent electron-energy-loss spectroscopy of $TiO_2$: A comparison of theory and experiment. *Phys. Rev. B*, 73:045129, Jan 2006.

[180] L. A. Grunes, R. D. Leapman, C. N. Wilker, R. Hoffmann, and A. B. Kunz. Oxygen $K$ near-edge fine structure: An electron-energy-loss investigation with comparisons to new theory for selected $3d$ Transition-metal oxides. *Phys. Rev. B*, 25:7157–7173, Jun 1982.

[181] David W. Fischer. X-Ray Band Spectra and Molecular-Orbital Structure of Rutile $TiO_2$. *Phys. Rev. B*, 5:4219–4226, Jun 1972.

[182] A. G. Thomas, W. R. Flavell, A. K. Mallick, A. R. Kumarasinghe, D. Tsoutsou, N. Khan, C. Chatwin, S. Rayner, G. C. Smith, R. L. Stockbauer, S. Warren, T. K. Johal, S. Patel, D. Holland, A. Taleb, and F. Wiame. Comparison of the electronic structure of anatase and rutile $TiO_2$ single-crystal surfaces using resonant photoemission and x-ray absorption spectroscopy. *Physical Review B*, 75(3), JAN 2007.

[183] F. M. F. de Groot, J. C. Fuggle, B. T. Thole, and G. A. Sawatzky. $L_{2,3}$ X-ray absorption edges of $d^0$ compounds: $K^+$, $Ca^{2+}$, $Sc^{3+}$, and $Ti^{4+}$ in $O_h$ (octahedral) symmetry. *Physical Review B*, 41:928–937, Jan 1990.

[184] F. M. F. de Groot, B. T. Thole, and G. A. Sawatzky.

[185] M. W. Haverkort. *Spin and orbital degrees of freedom in transition metal oxides and oxide thin films studied by soft x-ray absorption spectroscopy.* PhD thesis, University of Cologne, 2005.

[186] Robert Laskowski and Peter Blaha. Understanding the $L_{2,3}$ x-ray absorption spectra of early $3d$ transition elements. *Phys. Rev. B*, 82:205104, Nov 2010.

[187] Hidekazu Ikeno, Frank M F de Groot, Eli Stavitski, and Isao Tanaka. Multiplet calculations of L 2,3 x-ray absorption near-edge structures for 3dtransition-metal compounds. *Journal of Physics: Condensed Matter*, 21(10):104208, 2009.

[188] Peter Krüger. Multichannel multiple scattering calculation of $L_{2,3}$-edge spectra of $tio_2$ and $srtio_3$: Importance of multiplet coupling and band structure. *Phys. Rev. B*, 81:125121, Mar 2010.

[189] Eli Stavitski and Frank M.F. de Groot. The CTM4XAS program for EELS and XAS spectral shape analysis of transition metal L edges. *Micron*, 41(7):687 – 694, 2010.

[190] F. M. F. de Groot. $2p$ XAS new developments.

[191] A. Kotani. Resonant inelastic X-ray scattering in d and f electron systems. *The European Physical Journal B - Condensed Matter and Complex Systems*, 47:3–27, 2005. 10.1140/epjb/e2005-00303-4.

[192] Y Tezuka, S Shin, A Agui, M Fujisawa, and T Ishii. Resonant soft X-ray emission study of rutile $TiO_2$. *Journal of the Physical Society of Japan*, 65(1):312–317, JAN 1996.

[193] T. Idé and A. Kotani. Interplay between Raman and Fluorescence-Like Components in Resonant X-ray Emission Spectra of Degenerate $d^0$ and $d^1$ Systems. *Journal of the Physical Society of Japan*, 69(6):1895–1906, 2000.

[194] D. B. Strukov, G. S. Snider, D. R. Stewart, and R. S. Williams. The missing memristor found. *Nature*, 453:80–83, May 2008.

[195] K Szot, M Rogala, W Speier, Z Klusek, A Besmehn, and R Waser. $TiO_2$ a prototypical memristive material. *Nanotechnology*, 22(25):254001, 2011.

[196] X. Han, Q. Kuang, M. Jin, Z. Xie, and L. Zheng. Synthesis of titania nanosheets with a high percentage of exposed (001) facets and related photocatalytic properties. *Journal of the American Chemical Society*, 131(9):3152–3153, 2009.

[197] J. M. Tour and T. He. Electronics: The fourth element. *Nature*, 453:42–43, May 2008.

[198] John R. Jameson, Yoshiaki Fukuzumi, Zheng Wang, Peter Griffin, Koji Tsunoda, G. ingmar Meijer, and Yoshio Nishi. Field-programmable rectification in rutile $TiO_2$ crystals. *Applied Physics Letters*, 91(11), SEP 10 2007.

[199] Hua Gui Yang, Cheng Hua Sun, Shi Zhang Qiao, Jin Zou, Gang Liu, Sean Campbell Smith, Hui Ming Cheng, and Gao Qing Lu. Anatase $TiO_2$ single crystals with a large percentage of reactive facets. *Nature*, 453(7195):638–U4, MAY 29 2008.

[200] John Paul Strachan, J. Joshua Yang, Ruth Muenstermann, Andreas Scholl, Gilberto Medeiros-Ribeiro, Duncan R. Stewart, and R. Stanley Williams. Structural and chemical characterization of $TiO_2$ memristive devices by spatially-resolved NEXAFS. *Nanotechnology*, 20(48), DEC 2 2009.

[201] C M Freeman, J M Newsam, S M Levine, and C R A Catlow. Inorganic crystal-structure prediction using simplified potentials and experimental unit cells - application to the polymorphs of titanium-dioxide. *Journal of Materials Chemistry*, 3(5):531–535, MAY 1993.

[202] B Jiang, JM Zuo, N Jiang, M O'Keeffe, and JCH Spence. Charge density and chemical bonding in rutile, $TiO_2$. *Acta Crystallographica Section A*, 59(Part 4):341–350, JUL 2003.

[203] F. M. F. de Groot, J. C. Fuggle, B. T. Thole, and G. A. Sawatzky. 2 $p$ x-ray absorption of 3 $d$ transition-metal compounds: An atomic multiplet description including the crystal field. *Physical Review B*, 42:5459–5468, Sep 1990.

[204] D. R. Mueller, D. L. Ederer, J. vanEk, W. L. OBrien, Q. Y. Dong, J. J. Jia, and T. A. Callcott. Soft-x-ray emission and the local p-type partial density of electronic states in $Y_2O_3$: Experiment and theory. *Physical Review B*, 54(21):15034–15039, December 1996.

[205] J. Jimenez-Mier, J. van Ek, D. L. Ederer, T. A. Callcott, J. J. Jia, J. Carlisle, L. Terminello, A. Asfaw, and R. C. Perera. Dynamical behavior of x-ray absorption and scattering at the L edge of titanium compounds: Experiment and theory. *Physical Review B*, 59(4):2649–2658, January 1999.

[206] J. Jimenez-Mier, U. Diebold, D. L. Ederer, T. A. Callcott, M. Grush, and R. C. Perera. Decay channels for the Ti ($2p_{1/2}$) core hole excitations in $TiO_2$ observed by x-ray Raman scattering. *Physical Review B*, 65(18):184105, May 2002.

[207] J.J. Yeh and I. Lindau. Atomic subshell photoionization cross sections and asymmetry parameters: $1 \leq Z \leq 103$. *Atomic Data and Nuclear Data Tables*, 32(1):1 – 155, 1985.

[208] AJ Achkar, TZ Regier, H. Wadati, Y.J. Kim, H. Zhang, and DG Hawthorn. Bulk sensitive x-ray absorption spectroscopy free of self-absorption effects. *Physical Review B*, 83(8):081106, 2011.

[209] G. S. Henderson, X. Liu, and M. E. Fleet. A Ti *L*-edge X-ray absorption study of Ti-silicate glasses. *Physics and Chemistry of Minerals*, 29:32–42, 2002. 10.1007/s002690100208.

[210] R Ruus, A Kikas, A Saar, A Ausmees, E Nommiste, J Aarik, A Aidla, T Uustare, and I Martinson. Ti 2p and O 1s X-ray absorption of $TiO_2$ polymorphs. *Solid State Communications*, 104(4):199–203, OCT 1997.

[211] J. P. Crocombette and F. Jollet. Ti 2*p* X-ray-absorption in Titanium Dioxides ($TiO_2$) - the influence of the Cation Site Environment. *Journal of Physics-Condensed Matter*, 6(49):10811–10821, December 1994.

[212] W. Olovsson, I. Tanaka, T. Mizoguchi, P. Puschnig, and C. Ambrosch-Draxl. All-electron Bethe-Salpeter calculations for shallow-core x-ray absorption near-edge structures. *Phys. Rev. B*, 79:041102, Jan 2009.

[213] J.A. Carlisle, S.R. Blankenship, L.J. Terminello, J.J. Jia, T.A. Callcott, D.L. Ederer, R.C.C. Perera, and F.J. Himpsel. Crystal-momentum-resolved electronic structure of solids using resonant soft-X-ray fluorescence spectroscopy. *Journal of Electron Spectroscopy and Related Phenomena*, 110-111(0):323 – 334, 2000.

[214] A. Augustsson, A. Henningsson, S. M. Butorin, H. Siegbahn, J. Nordgren, and J.-H. Guo. Lithium ion insertion in nanoporous anatase $TiO_2$ studied with RIXS. *The Journal of Chemical Physics*, 119(7):3983–3987, 2003.

[215] L. D. Finkelstein, E. Z. Kurmaev, M. A. Korotin, A. Moewes, B. Schneider, S. M. Butorin, J-H. Guo, J. Nordgren, D. Hartmann, M. Neumann, and D. L. Ederer. Band approach to the excitation-energy dependence of x-ray fluorescence of $TiO_2$. *Phys. Rev. B*, 60:2212–2217, Jul 1999.

[216] Y. Tezuka, N. Nakajima, and O. Morimoto. Detailed measurement of Ti 2*p* resonant X-ray Raman scattering of $TiO_2$ and its polarization dependence measurements. *Journal of Electron Spectroscopy and Related Phenomena*, 184(36):216 – 219, 2011.